



# **NAVAL POSTGRADUATE SCHOOL**

**MONTEREY, CALIFORNIA**

## **THESIS**

**EFFECT OF OCEAN INTERANNUAL VARIABILITY ON  
ACOUSTIC PROPAGATION IN THE PHILIPPINE SEA  
AND SOUTH CHINA SEA**

by

Albert Mahendro Yudono

June 2017

Thesis Advisor:

Peter C. Chu

Co-Advisor:

Tetyana Margolina

**Approved for public release. Distribution is unlimited.**

THIS PAGE INTENTIONALLY LEFT BLANK

<b>REPORT DOCUMENTATION PAGE</b>			<i>Form Approved OMB No. 0704-0188</i>	
Public reporting burden for this collection of information is estimated to average 1 hour per response, including the time for reviewing instruction, searching existing data sources, gathering and maintaining the data needed, and completing and reviewing the collection of information. Send comments regarding this burden estimate or any other aspect of this collection of information, including suggestions for reducing this burden, to Washington headquarters Services, Directorate for Information Operations and Reports, 1215 Jefferson Davis Highway, Suite 1204, Arlington, VA 22202-4302, and to the Office of Management and Budget, Paperwork Reduction Project (0704-0188) Washington, DC 20503.				
<b>1. AGENCY USE ONLY</b> (Leave blank)		<b>2. REPORT DATE</b> June 2017		<b>3. REPORT TYPE AND DATES COVERED</b> Master's thesis
<b>4. TITLE AND SUBTITLE</b> EFFECT OF OCEAN INTERANNUAL VARIABILITY ON ACOUSTIC PROPAGATION IN THE PHILIPPINE SEA AND SOUTH CHINA SEA			<b>5. FUNDING NUMBERS</b>  NRP-W7A19	
<b>6. AUTHOR(S)</b> Albert Mahendro Yudono				
<b>7. PERFORMING ORGANIZATION NAME(S) AND ADDRESS(ES)</b> Naval Postgraduate School Monterey, CA 93943-5000			<b>8. PERFORMING ORGANIZATION REPORT NUMBER</b>	
<b>9. SPONSORING / MONITORING AGENCY NAME(S) AND ADDRESS(ES)</b> CDR Benjamin A. Jones, OPNAV-N2N6E benjamin.a.jones@navy.mil			<b>10. SPONSORING / MONITORING AGENCY REPORT NUMBER</b>	
<b>11. SUPPLEMENTARY NOTES</b> The views expressed in this thesis are those of the author and do not reflect the official policy or position of the Department of Defense or the U.S. Government. IRB number ____N/A____.				
<b>12a. DISTRIBUTION / AVAILABILITY STATEMENT</b> Approved for public release. Distribution is unlimited.			<b>12b. DISTRIBUTION CODE</b>	
<b>13. ABSTRACT (maximum 200 words)</b>  Effect of interannual variability of temperature and salinity on acoustic propagation in the Philippine Sea and South China Sea is investigated using the Navy's climatological (T, S) dataset [i.e., Generalized Digital Environmental Model (GDEM)] and the Synoptic Monthly Gridded World Ocean Database (SMG-WOD) data from January 1960 to December 2014, and an open source acoustic model (BELLHOP). The multi-year averaged monthly (T, S) profiles calculated from the SMG-WOD agree quite well with the GDEM with slight difference in upper layers, especially in thermoclines. The interannual variability of the transmission loss (TL) is identified using the BELLHOP model with the sound speed profiles calculated from the SMG-WOD and GDEM. Less TL was found in the convergence paths modelled from the SMG-WOD. Interannual (3-7 years) variabilities were found in each decade. The TL does not show strong interannual variabilities over the convergence paths; however, the interannual variability will affect the TL between the convergence paths, in the formation of surface duct, sound channels and bottom bounce. The SMG-WOD data is more suitable to assess the interannual variability effect on the acoustic propagation.				
<b>14. SUBJECT TERMS</b> interannual variability, Philippine Sea, South China Sea, thermohaline characteristics, sound speed, form of merit, acoustic transmission loss			<b>15. NUMBER OF PAGES</b> 213	
			<b>16. PRICE CODE</b>	
<b>17. SECURITY CLASSIFICATION OF REPORT</b> Unclassified	<b>18. SECURITY CLASSIFICATION OF THIS PAGE</b> Unclassified	<b>19. SECURITY CLASSIFICATION OF ABSTRACT</b> Unclassified	<b>20. LIMITATION OF ABSTRACT</b> UU	

NSN 7540-01-280-5500

Standard Form 298 (Rev. 2-89)  
Prescribed by ANSI Std. Z39-18

THIS PAGE INTENTIONALLY LEFT BLANK

**Approved for public release. Distribution is unlimited.**

**EFFECT OF OCEAN INTERANNUAL VARIABILITY ON ACOUSTIC  
PROPAGATION IN THE PHILIPPINE SEA AND SOUTH CHINA SEA**

Albert Mahendro Yudono  
Lieutenant, Indonesian Navy  
B.S., Indonesia's School for Naval Technology (STTAL), 2014

Submitted in partial fulfillment of the  
requirements for the degree of

**MASTER OF SCIENCE IN METEOROLOGY  
AND PHYSICAL OCEANOGRAPHY**

from the

**NAVAL POSTGRADUATE SCHOOL  
June 2017**

Approved by: Peter C. Chu  
Thesis Advisor

Tetyana Margolina  
Co-Advisor

Peter C. Chu  
Chair, Department of Oceanography

THIS PAGE INTENTIONALLY LEFT BLANK

## **ABSTRACT**

Effect of interannual variability of temperature and salinity on acoustic propagation in the Philippine Sea and South China Sea is investigated using the Navy's climatological (T, S) dataset (i.e., Generalized Digital Environmental Model [GDEM]) and the Synoptic Monthly Gridded World Ocean Database (SMG-WOD) data from January 1960 to December 2014, and an open source acoustic model (BELLHOP). The multi-year averaged monthly (T, S) profiles calculated from the SMG-WOD agree quite well with the GDEM with slight difference in upper layers, especially in thermoclines. The interannual variability of the transmission loss (TL) is identified using the BELLHOP model with the sound speed profiles calculated from the SMG-WOD and GDEM. Less TL was found in the convergence paths modelled from the SMG-WOD. Interannual (3-7 years) variabilities were found in each decade. The TL does not show strong interannual variabilities over the convergence paths; however, the interannual variability will affect the TL between the convergence paths, in the formation of surface duct, sound channels and bottom bounce. The SMG-WOD data is more suitable to assess the interannual variability effect on the acoustic propagation.

THIS PAGE INTENTIONALLY LEFT BLANK



## TABLE OF CONTENTS

<b>I.</b>	<b>INTRODUCTION.....</b>	<b>1</b>
<b>A.</b>	<b>MOTIVATION .....</b>	<b>1</b>
<b>B.</b>	<b>BACKGROUND .....</b>	<b>1</b>
<b>C.</b>	<b>THESIS OBJECTIVES AND OUTLINE.....</b>	<b>6</b>
<b>II.</b>	<b>DATA .....</b>	<b>9</b>
<b>A.</b>	<b>SOUND SPEED IN THE WATER COLUMN .....</b>	<b>9</b>
<b>1.</b>	<b>GDEM .....</b>	<b>9</b>
<b>2.</b>	<b>SMG-WOD .....</b>	<b>10</b>
<b>B.</b>	<b>OCEAN FLOOR CHARACTERISTICS .....</b>	<b>13</b>
<b>1.</b>	<b>Bathymetry .....</b>	<b>13</b>
<b>2.</b>	<b>Ocean Bottom Sediments .....</b>	<b>14</b>
<b>C.</b>	<b>GEOACOUSTIC PARAMETERS.....</b>	<b>15</b>
<b>III.</b>	<b>METHODS .....</b>	<b>17</b>
<b>A.</b>	<b>COMPOSITE ANALYSIS.....</b>	<b>17</b>
<b>B.</b>	<b>EMPIRICAL ORTHOGONAL FUNCTIONS (EOF) ANALYSIS .....</b>	<b>18</b>
<b>C.</b>	<b>GEOGRAPHICAL LOCATIONS .....</b>	<b>19</b>
<b>D.</b>	<b>BELLHOP .....</b>	<b>19</b>
<b>IV.</b>	<b>SEASONAL VARIABILITY .....</b>	<b>23</b>
<b>A.</b>	<b>SPICINESS.....</b>	<b>23</b>
<b>1.</b>	<b>MULTI-YEAR MONTHLY AVERAGE OF SMG-WOD .....</b>	<b>24</b>
<b>2.</b>	<b>GDEM MONTHLY SPICINESS .....</b>	<b>29</b>
<b>B.</b>	<b>SOUND SPEED.....</b>	<b>31</b>
<b>1.</b>	<b>MULTI-YEAR MONTHLY AVERAGE OF SMG-WOD .....</b>	<b>31</b>
<b>2.</b>	<b>GDEM MONTHLY SOUND SPEED .....</b>	<b>34</b>
<b>C.</b>	<b>UNDERWATER SOUND PROPAGATION AND SOUND SPEED PROFILES (SSP). .....</b>	<b>37</b>
<b>D.</b>	<b>SOUND SPEED PROFILES (SSP). .....</b>	<b>43</b>
<b>1.</b>	<b>Point A.....</b>	<b>44</b>
<b>2.</b>	<b>Point B.....</b>	<b>45</b>
<b>3.</b>	<b>Point C.....</b>	<b>46</b>
<b>4.</b>	<b>Point D.....</b>	<b>47</b>
<b>5.</b>	<b>Point E.....</b>	<b>48</b>
<b>6.</b>	<b>Point F .....</b>	<b>49</b>

	7.	Point G .....	50
	8.	Point H .....	51
E.		MEAN DECADEAL TEMPERATURE AND SALINITY .....	54
	1.	Point A.....	54
	2.	Point B.....	56
	3.	Point C.....	58
	4.	Point D.....	60
	5.	Point E.....	62
	6.	Point F .....	64
	7.	Point G .....	66
	8.	Point H .....	68
F.		MEAN TRANSMISSION LOSS-GDEM .....	70
	1.	Transmission Loss Point A.....	70
	2.	Transmission Loss Point B.....	72
	3.	Transmission Loss Point C.....	74
	4.	Transmission Loss Point D.....	76
	5.	Transmission Loss Point E.....	78
	6.	Transmission Loss Point F .....	80
	7.	Transmission Loss Point G .....	82
	8.	Transmission Loss Point H .....	84
G.		GDEM AND SMG-WOD COMPARISON .....	86
	1.	Point A.....	86
	2.	Point B.....	87
	3.	Point C.....	88
	4.	Point D.....	89
	5.	Point E.....	90
	6.	Point F .....	91
	7.	Point G .....	92
	8.	Point H .....	93
V.		INTERANNUAL VARIABILITY.....	95
A.		TIME VARIATIONS OF (T, S, SSP) PROFILES .....	95
	1.	Temperature.....	95
	2.	Salinity .....	102
	3.	Sound Speed .....	110
B.		EOF ANALYSIS .....	118
C.		TRANSMISSION LOSS DUE TO SHORT-TERM INTER ANNUAL VARIABILITY .....	141
	1.	Point A.....	142
	2.	Point B.....	144

3.	Point C.....	146
4.	Point D.....	148
5.	Point E.....	149
6.	Point F.....	151
7.	Point G .....	153
8.	Point H .....	155
VI.	CONCLUSIONS .....	157
	APPENDIX. ADDITIONAL GDEM MONTHLY SPICINESS FIGURES.....	161
	LIST OF REFERENCES .....	183
	INITIAL DISTRIBUTION LIST .....	189

THIS PAGE INTENTIONALLY LEFT BLANK

## LIST OF FIGURES

Figure 1.	Salinity (psu) along the 137°E line of Longitude in June 2000 Observed by RV “Ryofu Maru” Operated by the Japan Meteorological Agency (2000). Image from <i>ICES Journal of Marine Science</i> , vol. 64, no. 7 (2007).....	2
Figure 2.	Pacific Western Boundary Currents. Source: Hu et al. (2015). .....	4
Figure 3.	(a) La Niña, (b) Normal, and (c) El Niño Conditions. Source: Lynne D. Talley et al. (2011). .....	5
Figure 4.	A Plot of Southern Oscillation Index (SOI) Derived from Pressure Measurements at Tahiti and Darwin. Source: NOAA NCEI, <a href="https://www.ncdc.noaa.gov/teleconnections/enso/indicators/soi/">https://www.ncdc.noaa.gov/teleconnections/enso/indicators/soi/</a> . .....	5
Figure 5.	Sea Surface Temperature (upper panels) and Sea Surface Temperature Anomalies (lower panels) during Two Phases of ENSO. Source: NOAA, National Weather Service Climate Prediction Center (2005).....	6
Figure 6.	Bathymetry of the Philippine Sea and the South China Sea.....	14
Figure 7.	Bottom Sediment Types of the Philippine Sea and South China Sea. White Circles Denote Locations Chosen for Acoustic Propagation Modeling as Described in Chapter IV .....	15
Figure 8.	The Input and Output for the BELLHOP Model. Source: Porter (2011). .....	20
Figure 9.	SMG-WOD Multi-year Monthly Average Spiciness at the Surface. ....	25
Figure 10.	SMG-WOD Multi-year Monthly Average Spiciness at 100 m. ....	26
Figure 11.	SMG-WOD Multi-year Monthly Average Spiciness at 400 m. ....	27
Figure 12.	SMG-WOD Multi-year Monthly Average Spiciness at 1000 m. ....	28
Figure 13.	GDEM Monthly Spiciness at the Surface.....	29
Figure 14.	GDEM Monthly Spiciness at 100 m.....	30
Figure 15.	SMG-WOD Multi-year Monthly Average Sound Speed at the Surface. ....	32
Figure 16.	SMG-WOD Multi-year Monthly Average Sound Speed at 100 m.....	33

Figure 17.	GDEM Monthly Sound Speed at the Surface. ....	35
Figure 18.	GDEM Monthly Sound Speed at 100 m. ....	36
Figure 19.	Ocean Layers. Source: FAS (2017). ....	38
Figure 20.	An Example of Acoustic Path for a Negative SSP Gradient. Source: (FAS, 2017). The Corresponding SSP Is Shown in the Left Panel. ....	39
Figure 21.	An Example of Acoustic Path for a Positive SSP Gradient. Source: (FAS, 2017). The Corresponding SSP is Shown in the Left Panel.....	39
Figure 22.	Surface Duct. Source: (FAS, 2017). ....	40
Figure 23.	An Example of a Shadow Zone (sonic layer). Source: (FAS, 2017). The Corresponding SSP is Shown In the Left Panel. ....	40
Figure 24.	Sound Channel. Source: (FAS, 2017).....	41
Figure 25.	Convergence Zone. Source: FAS (2017). ....	41
Figure 26.	Bottom Bounce. Source: FAS (2017). ....	42
Figure 27.	Points from A through H.....	43
Figure 28.	Mean Sound Speed Profiles (Point A). ....	44
Figure 29.	Mean Sound Speed Profiles (Point B). ....	45
Figure 30.	Mean Speed Profiles (Point C). ....	46
Figure 31.	Mean Sound Speed Profiles (Point D). ....	47
Figure 32.	Mean Sound Speed Profiles (Point E). ....	48
Figure 33.	Mean Sound Speed Profiles (Point F).....	49
Figure 34.	Mean Sound Speed Profiles (Point G). ....	50
Figure 35.	Mean Sound Speed Profiles (Point H). ....	51
Figure 36.	SMG-WOD January Mean Decadal T-S Diagram (Point A). ....	54
Figure 37.	SMG-WOD July Mean Decadal T-S Diagram (Point A). ....	55
Figure 38.	SMG-WOD January Mean Decadal T-S Diagram (Point B).....	56
Figure 39.	SMG-WOD July Mean Decadal T-S Diagram (Point B). ....	57

Figure 40.	SMG-WOD January Mean Decadal T-S Diagram (Point C).....	58
Figure 41.	SMG-WOD July Mean Decadal T-S Diagram (Point C). ....	59
Figure 42.	SMG-WOD January Mean Decadal T-S Diagram (Point D). ....	60
Figure 43.	SMG-WOD July Mean Decadal T-S Diagram (Point D). ....	61
Figure 44.	SMG-WOD January Mean Decadal T-S Diagram (Point E).....	62
Figure 45.	SMG-WOD July Mean Decadal T-S Diagram (Point E).....	63
Figure 46.	SMG-WOD January Mean Decadal T-S Diagram (Point F).....	64
Figure 47.	SMG-WOD July Mean Decadal T-S Diagram (Point F).....	65
Figure 48.	SMG-WOD January Mean Decadal T-S Diagram (Point G). ....	66
Figure 49.	SMG-WOD July Mean Decadal T-S Diagram (Point G). ....	67
Figure 50.	SMG-WOD January Mean Decadal T-S Diagram (Point H). ....	68
Figure 51.	SMG-WOD July Mean Decadal T-S Diagram (Point H). ....	69
Figure 52.	TL Point A. ....	71
Figure 53.	TL Point B.....	73
Figure 54.	TL Point C.....	75
Figure 55.	TL Point D. ....	77
Figure 56.	TL Point E.....	79
Figure 57.	TL Point F.....	81
Figure 58.	TL Point G. ....	83
Figure 59.	TL Point H. ....	85
Figure 60.	Point A January (upper) and July (lower).....	87
Figure 61.	Point B January (upper) and July (lower). ....	88
Figure 62.	Point C January (upper) and July (lower). ....	89
Figure 63.	Point D January (upper) and July (lower).....	90
Figure 64.	Point E January (upper) and July (lower). ....	91

Figure 65.	Point F January (upper) and July (lower). .....	92
Figure 66.	Point G January (upper) and July (lower). .....	93
Figure 67.	Point H January (upper) and July (lower). .....	94
Figure 68.	Temporal Variability of SMG-WOD Temperature at point A. ....	96
Figure 69.	Temporal Variability of SMG-WOD Temperature at point B. ....	96
Figure 70.	Temporal Variability of SMG-WOD Temperature at point C. ....	97
Figure 71.	Temporal Variability of SMG-WOD Temperature at point D. ....	98
Figure 72.	Temporal Variability of SMG-WOD Temperature at point E. ....	99
Figure 73.	Temporal Variability of SMG-WOD Temperature at point F. ....	100
Figure 74.	Temporal Variability of SMG-WOD Temperature at point G. ....	101
Figure 75.	Temporal Variability of SMG-WOD Temperature at point H. ....	102
Figure 76.	Temporal Variability of SMG-WOD Salinity at point A. ....	103
Figure 77.	Temporal Variability of SMG-WOD Salinity at point B. ....	104
Figure 78.	Temporal Variability of SMG-WOD Salinity at point C. ....	105
Figure 79.	Temporal Variability of SMG-WOD Salinity at point D. ....	106
Figure 80.	Temporal Variability of SMG-WOD Salinity at point E. ....	107
Figure 81.	Temporal Variability of SMG-WOD Salinity at point F. ....	108
Figure 82.	Temporal Variability of SMG-WOD Salinity at point G. ....	109
Figure 83.	Temporal Variability of SMG-WOD Salinity at point H. ....	110
Figure 84.	Temporal Variability of SMG-WOD Sound Speed at Point A. ....	111
Figure 85.	Temporal Variability of SMG-WOD Sound Speed at Point B. ....	112
Figure 86.	Temporal Variability of SMG-WOD Sound Speed at Point C. ....	113
Figure 87.	Temporal Variability of SMG-WOD Sound Speed at Point D. ....	114
Figure 88.	Temporal Variability of SMG-WOD Sound Speed at Point E. ....	115
Figure 89.	Temporal Variability of SMG-WOD Sound Speed at Point F. ....	116



Figure 90.	Temporal Variability of SMG-WOD Sound Speed at Point G.....	117
Figure 91.	Temporal Variability of SMG-WOD Sound Speed at Point H.....	118
Figure 92.	Point A: Eigenvalues and Mode Variance. ....	119
Figure 93.	Point B: Eigenvalues and Mode Variance. ....	120
Figure 94.	Point C: Eigenvalues and Mode Variance. ....	120
Figure 95.	Point D: Eigenvalues and Mode Variance. ....	121
Figure 96.	Point E: Eigenvalues and Mode Variance. ....	121
Figure 97.	Point F: Eigenvalues and Mode Variance.....	122
Figure 98.	Point G: Eigenvalues and Mode Variance. ....	122
Figure 99.	Point H: Eigenvalues and Mode Variance.....	123
Figure 100.	The First Four EOFs of Point A.....	123
Figure 101.	EOF Coefficients of Sound Speed of Point A. ....	124
Figure 102.	The First Four EOFs of Point B.....	126
Figure 103.	Coefficients of Sound Speed of Point B. ....	126
Figure 104.	The First Four EOFs of Point C.....	128
Figure 105.	Coefficients of Sound Speed of Point C. ....	128
Figure 106.	The First Four EOFs of Point D.....	130
Figure 107.	Coefficients of Sound Speed of Point D. ....	130
Figure 108.	The First Four EOFs of Point E. ....	132
Figure 109.	Coefficients of Sound Speed of Point E. ....	133
Figure 110.	The First Four EOFs of Point F. ....	135
Figure 111.	Coefficients of Sound Speed of Point F.....	135
Figure 112.	The First Four EOFs of Point G.....	137
Figure 113.	Coefficients of Sound Speed of Point G. ....	137
Figure 114.	The First Four EOFs of Point H.....	139

Figure 115.	Coefficients of Sound Speed of Point H .....	139
Figure 116.	TL for 1960–1967 (upper panels), 1975–1978 (middle panels) and 2005–2008 (lower panels) for Point A in January (left column) and July (right column).....	142
Figure 117.	TL for 1960–1967 (upper panels), 1975–1978 (middle panels) and 2005–2008 (lower panels) for Point B in January (left column) and July (right column).....	144
Figure 118.	TL for 1962–1965 (upper panels), 1975–1978 (middle panels) and 2005–2008 (lower panels) for Point C in January (left column) and July (right column).....	146
Figure 119.	TL for 1961–1965 (upper panels) and 2005–2008 (lower panels) for Point D in January (left column) and July (right column). ....	148
Figure 120.	TL for 1962–1966 (upper panels) and 1969–1972 (lower panels) for Point E in January (left column) and July (right column). ....	149
Figure 121.	TL for 1960–1963 (upper panels), 1998–2002 (middle panels) and 2010–2013 (lower panels) for Point F in January (left column) and July (right column).....	151
Figure 122.	TL for 1960–1967 (upper panels), 1997–2001 (middle panels) and 2009–2012 (lower panels) for Point G in January (left column) and July (right column).....	153
Figure 123.	TL for 1964–1969 (upper panels), 1997–2001 (middle panels) and 2009–2012 (lower panels) for Point G in January (left column) and July (right column).....	155

## LIST OF TABLES

Table 1.	GDEM Depth Layers Source: NAVO (2009).....	10
Table 2.	Datasets and the Instruments Types that contributes to the WOD13 Database. Adapted from Boyer et al. (2013). .....	11
Table 3.	Sediments Parameters for the HFEVA Bottom Sediment Types (NAVO, 2016), and their Properties. ....	16
Table 4.	Selected Geographical Locations.....	19
Table 5.	Sound Speed and Spiciness at the Surface in June. ....	31
Table 6.	Sound Speed and Spiciness at the surface in December.....	31
Table 7.	Sound Speed and Spiciness at 100 m depth in June. ....	32
Table 8.	Sound Speed and Spiciness at 100 m depth in December. ....	33
Table 9.	GDEM Sound Speed and Spiciness at the Surface in June. ....	34
Table 10.	GDEM Sound Speed and Spiciness at the Surface in December. ....	34
Table 11.	GDEM Sound Speed and Spiciness at 100 m depth in June. ....	34
Table 12.	GDEM Sound Speed and Spiciness at 100 m depth in December. ....	34
Table 13.	Possible Propagation Types and Maximum Variations.....	53
Table 14.	Variances of First Four EOF Modes.....	119
Table 15.	EOF Analysis at Point A.....	124
Table 16.	EOF Analysis at Point B.....	127
Table 17.	EOF Analysis at Point C.....	129
Table 18.	EOF Analysis at Point D.....	131
Table 19.	EOF Analysis at Point E.....	133
Table 20.	EOF Analysis at Point F.....	136
Table 21.	EOF Analysis at Point G.....	138
Table 22.	EOF Analysis at Point H.....	140

THIS PAGE INTENTIONALLY LEFT BLANK

## LIST OF ACRONYMS AND ABBREVIATIONS

ASW	anti-submarine warfare
CTD	conductivity temperature depth
DBDB-V	Digital bathymetric Database-Variable resolution version
ENSO	El Nino/La Nina and the Southern Oscillation
EOF	empirical orthogonal function
GDEM	generalized digital environmental model
HDF	Hierarchical Data Format
ITF	Indonesian through flow
MC	Mindanao Current
MCM	mine countermeasures
MODAS	Modular Ocean Data Assimilation System
NEC	north equatorial current
NL	noise level
NOAA	National Oceanic and Atmospheric Administration
NODC	National Oceanographic Data Center
NPTW	north Pacific tropical water
NPIW	north Pacific intermediate water
NOVA	National Oceanic Atmospheric Administration
OSD	ocean spectral decomposition
PAGASA	Philippine Atmospheric, Geophysical and Astronomical Services Administration
PC	principal component
PDO	Pacific decadal oscillation
NPGO	north Pacific gyre oscillation
SEC	south equatorial current
SL	source level
SMG-WOD	synoptic monthly gridded-world ocean atlas
SOI	southern oscillation index
SPTW	south Pacific tropical water
SSP	sound speed profile

SST	sea surface temperature
TL	transmission loss
TS	target strength
TSW	tropical surface water
USW	undersea warfare
WOD13	World Ocean Database 2013

## **ACKNOWLEDGEMENTS**

Thank you very much for my thesis advisor Professor Peter C. Chu and co-advisor Dr. Tetyana Margolina. Without their patience, support and excellent knowledge, completing this thesis would have been difficult.

Thank you very much for my program officer, CDR Paula Travis, for her support throughout my education.

And so much love to my family, for all of their support and prayers.

THIS PAGE INTENTIONALLY LEFT BLANK



# **I. INTRODUCTION**

## **A. MOTIVATION**

The Philippine Sea and the South China Sea are strategic areas for the Navy operations because through this region almost half of the world's sea based trade is held (Review of maritime transport, 2011). They are the main gateway to the Malacca Strait, which is one of the busiest straits in the world. Securing the sea trade has been one of the main tasks of any Navy since centuries ago. A healthy and secure trade will definitely support a good economy, and a good economy will eventually give an indirect effect to support the defense security among nations. The United States and countries around the Philippine Sea and South China Sea are now facing an emerging challenge especially from China as a powerful force of economy and military in the world nowadays. China had built a strong submarine base in Hainan Island that is located at the northern part of the South China Sea. Submarines from this base can easily reach the South China Sea and the Philippine Sea. To achieve the undersea warfare (USW) dominance, a strong knowledge of the underwater acoustic characteristics in the region is essential. Since the underwater acoustic is the best known method for the undersea detections, this knowledge is fundamental to optimize various kinds of underwater sensors. It is also required for developing beneficial USW tactics at a certain position and time in the region. The underwater acoustic propagation is highly impacted by the oceanographic characteristics such as surface condition, temperature, salinity, pressure, and bottom characteristics.

## **B. BACKGROUND**

Temperature and salinity (i.e., water mass characteristics) control the sound speed. The main water masses of the Philippine Sea and South China Sea are the North Pacific Tropical Water (NPTW), the South Pacific Tropical Water (SPTW), and the North Pacific Intermediate Water (NPIW). Water mass characteristics, formation mechanisms, and spatial distribution are described in Qu et al., 1998 based on long-term observations in the Western Pacific and in the Philippine Sea. Figure 1 shows the large-

scale distribution of these water masses in the vertical section of the salinity field. NPTW and SPTW are located in the thermocline; NPIW is located in the intermediate layer.

The South Pacific Tropical Water (SPTW) is identified by a salinity maximum at the  $\sigma_\theta = 25.0$  kg/m<sup>3</sup> surface. SPTW is located in the equatorial Pacific, southward of 50°N. Its salinity exceeds 35.25 psu. The primary formation mechanism is the subduction in the main subtropical gyre (Qu et al., 1998).

The North Pacific Tropical Water (NPTW) is identified by a salinity maximum at the  $\sigma_\theta = 24.0$  kg/m<sup>3</sup> surface. Its salinity is lower than the salinity of SPTW, 34.75-35.25 psu. It is also formed by the subduction of the denser water in the region of high evaporation at about 20°N, 140°E–160°W (Qu et al., 1998). Between 10° and 25°N, the North Equatorial Current (NEC) transports this water mass westward from the formation site. NPTW follows the NEC path as it separates into Kuroshio and the Mindanao Current. It can also be traced as far as in the Indian Ocean (Katsura and Oka, 2013).

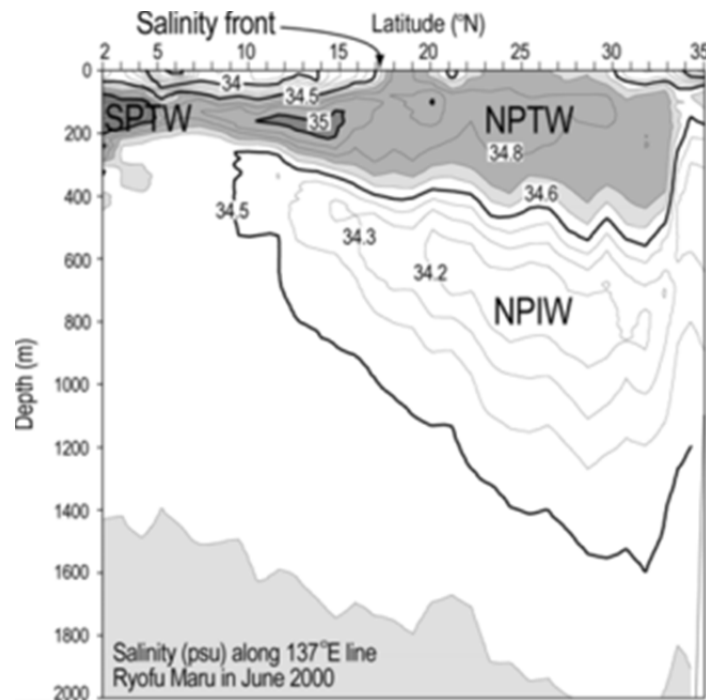


Figure 1. Salinity (psu) along the 137°E line of Longitude in June 2000 Observed by RV “Ryofu Maru” Operated by the Japan Meteorological Agency (2000). Image from *ICES Journal of Marine Science*, vol. 64, no. 7 (2007).

NPIW is located at  $\sigma_\theta = 26.5\text{-}26.8 \text{ kg/m}^3$  surfaces (Qu et al., 1998). Its salinity is below 34.4 psu. Unlike other water masses, NPIW does not get its characteristics at the ocean surface. It is formed by mixing of fresh water from subpolar regions, and salty Oyashio and Kuroshio water (Talley et al., 2011). NPIW circulates within the North Pacific Subtropical gyre but can also be detected in the vertical section of the tropical Philippine Sea. (Qu et al., 1998).

Ocean currents change temperature and salinity and in turn vary the sound speed. A detailed review of the Pacific Western Boundary currents can be found in Hu et al. (2015). As explained by Hu et al. (2015) the main currents in the western tropical Pacific are North Equatorial Current (NEC), Kuroshio, and the Mindanao Current (MC) (Figure 2). This current system is an important part of both the global thermohaline circulation and wind-driven circulation. The buoyancy-driven thermohaline component of the circulation connects the western Pacific with the Indian Ocean by the Indonesian through flow (ITF). The wind-driven circulation in the western Pacific is mostly meridional, and connects the equatorial and subtropical regions.

As explained by Hu et al. (2015) the western Pacific circulation exhibits strong seasonal, intraseasonal, interannual, and decadal variability, which is connected to the atmospheric forcing variability and affects it. Buoyancy fluxes, which are connected to monsoon winds and precipitation, cause the change in location of the NEC separating into the Mindanao Current and Kuroshio. The western Pacific circulation is also affected by ENSO. According to Hu et al. (2015), during the El Nino the NEC bifurcation moves to the north, NEC and the Mindanao current get stronger, the Equatorial Undercurrent intensifies in the western part. At the same time, the Kuroshio and ITF get weaker. Qu et al. (1998) found out that the interannual variability of the Kuroshio extension is correlated to ENSO but lags 1.5 years behind it.

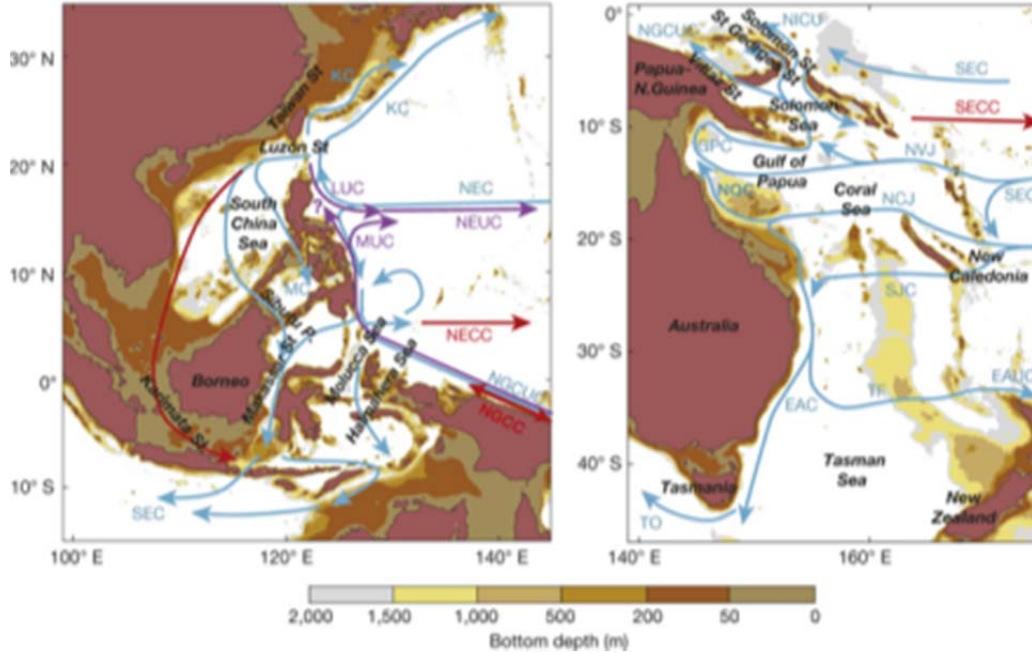


Figure 2. Pacific Western Boundary Currents. Source: Hu et al. (2015).

Variability of temperature and salinity at different scales will affect the sound propagation variations. In the region of the western Philippine Sea and South China Sea, a wide range of variability is observed, including intra-seasonal (20-30 days), seasonal, monthly-to-interannual, interannual (3-7 years), and interdecadal (10-30 years) time-scales (Talley et al., 2011). The region is characterized by tropical climate with high temperature and humidity. Seasonal variability of air temperature and precipitation is driven by monsoons with three seasons: the rainy season (June-November), the cool dry season (December-February), and the hot dry season (March-May) (PAGASA, 2016). May is the warmest month, and January, the coolest (Coronas, 1920).

The dominant pattern of interannual variability is the El Nino Southern Oscillation (ENSO), which has two quasi-periodic states, El Nino and La Nina (Talley et al., 2011). As illustrated by Talley et al. (2011) the ENSO normal conditions, which are observed between the two extreme states, are dominated by trade winds. The easterly winds push the warm surface water westward. This causes the elevated sea surface height in the western part of the ocean, and the intense coastal upwelling in the eastern part. As explained by Talley et al. (2011) the structure of the temperature field during the normal

conditions is characterized by the cold tongue in the eastern Pacific, and the westward decline of the thermocline. The La Nina is a stronger version of the normal conditions. During the El Nino state, the trade winds weaken and the thermocline becomes more level (Figure 3).

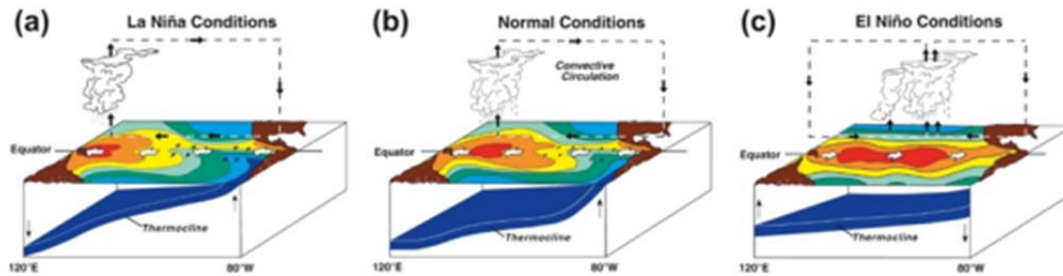


Figure 3. (a) La Niña, (b) Normal, and (c) El Niño Conditions. Source: Lynne D. Talley et al. (2011).

The Southern Oscillation Index (SOI) is used to characterize the ENSO event and available at the NOAA National Centers for Environmental Information website <https://www.ncdc.noaa.gov/>. It is a normalized monthly difference of pressures between two locations: Tahiti and Darwin. Large negative values of SOI correspond to the El Nino phase; large positive values indicate the La Nina phase (Figure 4).

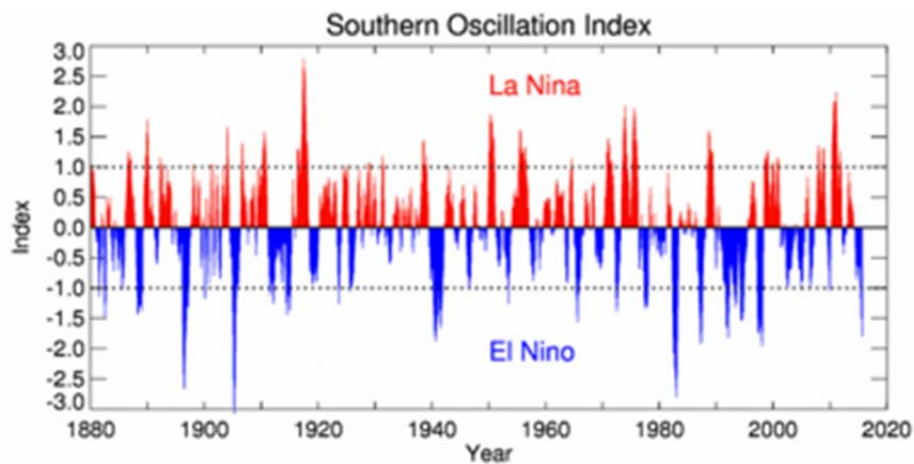


Figure 4. A Plot of Southern Oscillation Index (SOI) Derived from Pressure Measurements at Tahiti and Darwin. Source: NOAA NCEI, <https://www.ncdc.noaa.gov/teleconnections/enso/indicators/soi/>.

Sea surface temperature is a strong indicator of ENSO conditions (Figure 5). For example, there is an increase of the sea surface temperature of about  $0.5^{\circ}\text{C}$  -  $2^{\circ}\text{C}$  at some part of the Philippine Sea during a strong La Nina. At the same time, there is an increase of the sea surface temperature at the Luzon strait and South China Sea of about  $1^{\circ}\text{C}$  -  $3^{\circ}\text{C}$  (bottom right panel of Figure 5).

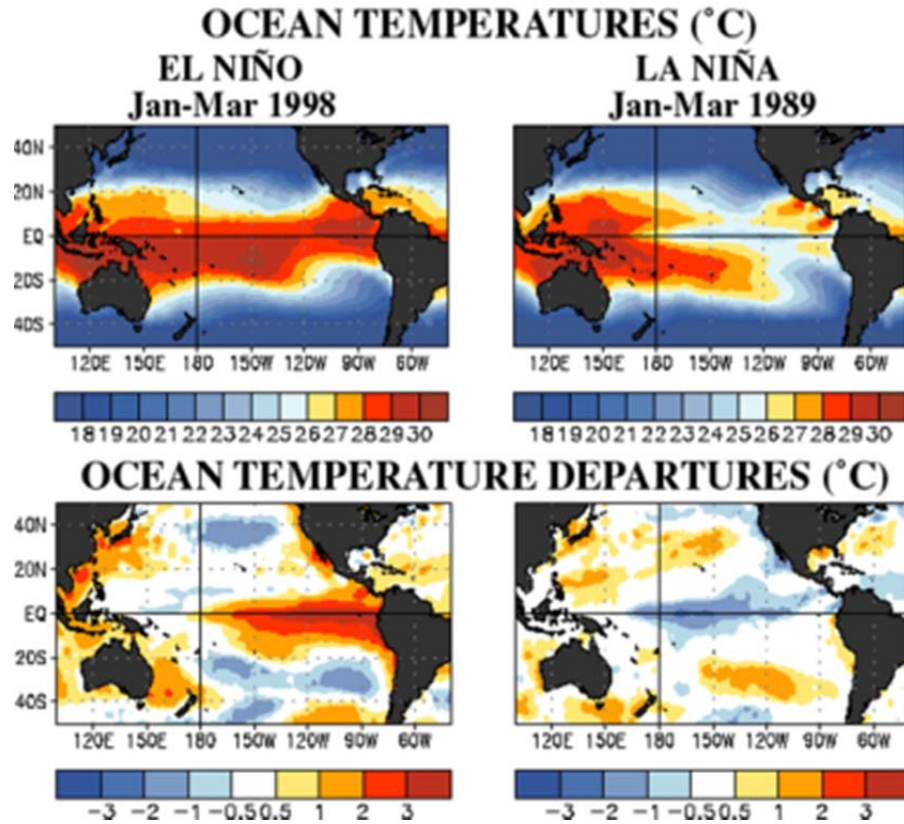


Figure 5. Sea Surface Temperature (upper panels) and Sea Surface Temperature Anomalies (lower panels) during Two Phases of ENSO. Source: NOAA, National Weather Service Climate Prediction Center (2005).

### C. THESIS OBJECTIVES AND OUTLINE

The objective of this thesis is to determine the effect of (T, S) (or thermohaline) interannual variability on acoustic propagation in Philippine Sea and South China Sea. Recently, a Synoptic Monthly Gridded World Ocean Database (SMG-WOD) with horizontal resolution of  $1^{\circ}$  world-wide and  $0.25^{\circ}$  in several regional seas and 1 month time increment from January 1960-December 2014 has been established at Naval

Postgraduate School (NPS) and quality controlled by the NOAA/NCEI scientists. This dataset can be openly downloaded at the NOAA website: at <https://data.nodc.noaa.gov/cgi-bin/iso?id=gov.noaa.nodc:0140938>. With this dataset interannual (T, S) variability and in turn sound speed variability can be identified. Using an openly available underwater acoustic ray tracing model BELLHOP, along with the GDEM, and SMG-WOD data the effect of T,S (or thermohaline) interannual variability on acoustic propagation can be determined.

These data and approach to investigate the effect of seasonal and interannual variability on variations of acoustic propagation, was previously applied to the Yellow Sea (McDonald, 2016), and the Mediterranean Sea (Kucukosmanoglu, 2016). Further development is now applied to the specific region of the Philippine Sea, and South China Sea.

The remainder of this thesis is organized as follows:

Chapter II presents the databases that are used for this thesis: GDEM, SMG-WOD and geoacoustic parameters in the research area for BELLHOP acoustic propagation model input.

Chapter III describes the methods that are used for this thesis: composite analysis to separate seasonal and interannual variability, empirical orthogonal function (EOF) to get interannual variability with dominant variances, geoacoustic parameters of the ocean bottom, and basic explanation of the acoustic ray tracing model - BELLHOP.

Chapter IV discusses the impact of climate change on acoustic transmission at eight representative locations using the BELLHOP acoustic model with climatological mean (T, S) profiles GDEM (without interannual variability) and SMG-WOD (with interannual variability) from January 1960 to December 2014.

Chapter V provides thesis conclusions, and offers recommendations for future research regarding the effect of ocean interannual variability on acoustic propagation.

THIS PAGE INTENTIONALLY LEFT BLANK



## **II. DATA**

To model acoustic propagation at a specific location of the World Ocean, the following environmental information is required: sound speed profiles, bathymetry and geoacoustic characteristics of the ocean floor along the propagation path (see for example, Porter 2011). In this thesis, two databases were used to characterize sound speed distribution in the water column, Generalized Digital Environment Model (GDEM) (Carnes, 2004) and Synoptic Monthly Gridded Database (SMG-WOD) (Chu and Fan, 2016). These datasets have different temporal and spatial resolution, as described below. Digital Bathymetric Data Base Variable Resolution DBDB-V (NAVO, 2009) was used for the ocean bathymetry. Geoacoustic information, including sediment density, sound attenuation coefficient and sound speed in sediments, was determined from published data (Hamilton and Bachman, 1982) based on the sediment type (Bottom Sediment Type database, NAVO 2003).

### **A. SOUND SPEED IN THE WATER COLUMN**

#### **1. GDEM**

GDEM is the Navy climatological monthly fields of temperature and salinity. Carnes (2004) states that, “Development of GDEM at the Naval Oceanographic Office began in 1975 and culminated in the first release to the Navy community in 1984. The first release contained only the North Atlantic Region, but by 1991 most of the world’s oceans were included.” The GDEM dataset is unclassified and approved for public release. In this thesis, GDEM-V3.0 (NAVO, 2009) was used.

As explained by Carnes (2004) GDEM-V 3.0 was processed from temperature and salinity profiles extracted from the Master Oceanographic Observational Data Set (MOODS) in 1995, and contains climatological monthly temperature, salinity, and standard deviations of temperature and salinity at 78 unevenly distributed depth levels down to 6600 m (Table 1). The horizontal resolution is 0.25 degree in both latitude and longitude (Carnes, 2004).

Table 1. GDEM Depth Layers Source: NAVO (2009).

Layer	Depth (m)	Layer	Depth (m)	Layer	Depth (m)	Layer	Depth (m)
1	0	21	85	41	400	61	3200
2	2	22	90	42	500	62	3400
3	4	23	95	43	600	63	3600
4	6	24	100	44	700	64	3800
5	8	25	110	45	800	65	4000
6	10	26	120	46	900	66	4200
7	15	27	130	47	1000	67	4400
8	20	28	140	48	1100	68	4600
9	25	29	150	49	1200	69	4800
10	30	30	160	50	1300	70	5000
11	35	31	170	51	1400	71	5200
12	40	32	180	52	1500	72	5400
13	45	33	190	53	1600	73	5600
14	50	34	200	54	1800	74	5800
15	55	35	220	55	2000	75	6000
16	60	36	240	56	2200	76	6200
17	65	37	260	57	2400	77	6400
18	70	38	280	58	2600	78	6600
19	75	39	300	59	2800		
20	80	40	350	60	3000		

## 2. SMG-WOD

Three-dimensional (3D) SMG-WOD is a database created at NPS and quality controlled by NOAA/NCEI scientists (Chu and Fan, 2016). It can be freely downloaded from the NOAA/NCEI, and provides 3D world ocean gridded monthly temperature and salinity data, from January 1945 to December 2014. The SMG-WOD is based on

WOD13 profiles (Boyer et al. 2013) using the Optimal Spectral Decomposition (OSD) (Chu and Fan 2016) and has global coverage for [180°E-180°W, 80°N-80°S].

The WOD13 database as noted by Boyer et al. (2013) contains a “collection of scientifically quality-controlled ocean profile and plankton data that includes measurements of temperature, salinity, oxygen, phosphate, nitrate, silicate, chlorophyll, alkalinity, pH, pCO<sub>2</sub>, TCO<sub>2</sub>, Tritium,  $\Delta^{13}\text{Carbon}$ ,  $\Delta^{14}\text{Carbon}$ ,  $\Delta^{18}\text{Oxygen}$ , Freon, Helium,  $\Delta^3\text{Helium}$ , Neon, and plankton.”

The WOD13 datasets are grouped based on their similar method of data acquisition, for example the low resolution data such as the data from bottle and low resolution CTD will be grouped in the same dataset. Each datasets will also be given a three-letter notation for naming the output data files (Boyer et al. 2013). Table 2 lists the WOD13 datasets and the instrument sources that contribute data.

Table 2. Datasets and the Instruments Types that contributes to the WOD13 Database. Adapted from Boyer et al. (2013).

<b>DATASET</b>	<b>SOURCE</b>	<b>INFORMATION</b>
OSD	Bottle, low-resolution Conductivity-Temperature-Depth (CTD), low-resolution XCTD data, and plankton data	Ocean Station Data (OSD) historically referring to the data taken from stationary research ship to a certain depths using reversing thermometers and bottles. The low resolution here means that the data only have a limited number of measurements along the vertical profile.
CTD	High-resolution Conductivity-Temperature-Depth (CTD) data and high-resolution XCDT data	High-resolution here means that the data recorded at a high frequency for each each depth or pressure, and the data usually are binned in 1 to 5 m depth interval.
MBT	Mechanical Bathythermograph (MBT) data, Digital Bathythermograph (DBT), micro-BT	Bathythermograph is an instrument to measure the temperature in the upper part of the ocean (last U.S. version reached a maximum depth of 295 m). The mechanical is the older version, followed by the digital

<b>DATASET</b>	<b>SOURCE</b>	<b>INFORMATION</b>
		version, and the latest micro version can record the depth-temperature pairs at high vertical or temporal resolution.
XBT	Expendable (XBT) data	XBT is a torpedo shaped devices with attached to a spool of copper wire to send the data collected from each depths (depth calculated as a function of time since it launched to the water).
SUR	Surface only data ( bucket, thermosalinograph)	The focus is for the sub-surface profile data, this data treated as an additional source for WOD13.
APB	Autonomous Pinniped Bathythermograph – Time-Temperature-Depth recorders attached to elephant seals	The sensor instruments are attached to marine mammals. The data from these instrumented animals could potentially fill the gap for the difficult location such as in the ice covered waters. Using the instrumented animals are less expensive than using a traditional instruments such as XBT (Boehlert et al., 2001).
MRB	Moored buoy data from TAO (Tropical Atmosphere-Ocean), PIRATA (moored array in the tropical Atlantic). MARNET, and TRITON (Japan-JAMSTEC)	This device platform is anchored or stabilized to measure the oceanographic and atmospheric data in a small area for a certain geographic location. The measurement devices can be attached at subsurface levels on the chain of the platform.
PFL	Profiling float data	This is a device drifting in a certain predetermined depth level, and will resurface to send data at a set time intervals.
DRB	Drifting buoy data from surface buoys with thermistor chains	This platform is drifting following the ocean currents, at the surface or at a certain shallow depths.
UOR	Undulating Oceanographic Recorder data from a Conductivity/Temperature/	This device also called as a towed CTD, towed behind a vessel and will go up and

<b>DATASET</b>	<b>SOURCE</b>	<b>INFORMATION</b>
	Depth probe mounted on a towed undulating vehicle	down on the water column.
GLD	Glider data	The data collected from a reusable autonomous underwater vehicle (AUVs), designed to glide up and down in the water column to collect data.

The optical spectral decomposition (OSD) method (Chu et al., 2015, 2016) allows assimilating oceanographic measurements from irregularly spaced locations onto a regular grid. Unlike the optimal interpolation approach, the OSD method does not require knowledge or assumptions on statistical properties of the analyzed fields (Chu et al., 2016). The method uses basis functions, which are not calculated from the observations but depend on the lateral boundary conditions (Chu et al., 2015).

The SMG-WOD has  $1^{\circ} \times 1^{\circ}$  horizontal resolution and 28 vertical levels using 10 meters, 20 meters, 25 meters, 50 meters, 100 meters, 250 meters and 250 meters of depth interval from surface to 3000 meters water depth (Chu et al. 2003a,b; 2004; 2015). The SMG-WOD spatial resolution is the same as for WOD13. However, unlike WOD13 and GDEM climatology, it contains synoptic monthly fields.

## **B. OCEAN FLOOR CHARACTERISTICS**

### **1. Bathymetry**

Bathymetry data of the Philippine Sea and the South China Sea were extracted from the NAVO database “Digital Bathymetric Database-Variable resolution (DBDB-V) version 5.4” (NAVO, 2006), level 0 data (unclassified). DBDB-V has four resolutions of bathymetry data: 2, 1, 0.5, and 0.1 arc-minutes. In this research we used the 2 minute resolution data, which provide a complete global coverage (McDonald, 2016).

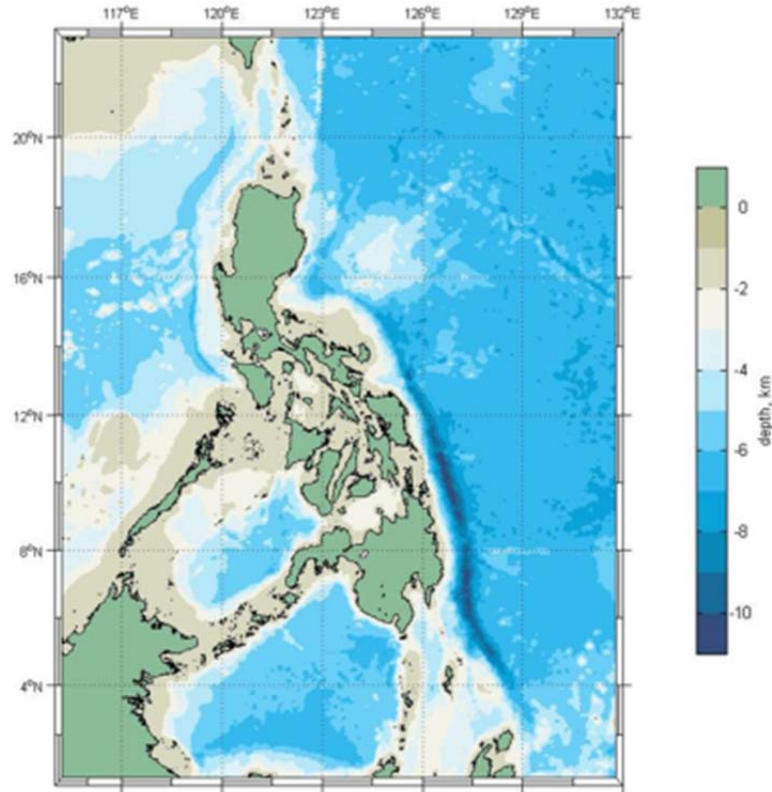


Figure 6. Bathymetry of the Philippine Sea and the South China Sea

## 2. Ocean Bottom Sediments

The unclassified Bottom Sediment Type database of The Naval Oceanographic Office was used in this thesis. It has four sediment databases: Enhanced, Standard, Reduced, and High-Frequency Environmental Acoustics (HFEVA). The last three databases are reclassified Enhanced database, have different nomenclatures, and have different purposes. This thesis used HFEVA sediment dataset, which is “designed specifically for high-frequency acoustic prediction” (NAVO, 2006). It is arranged into 23 standards “standard sediment types,” based on sediment mixture and grain-size” (NAVO, 2006).

Bottom Sediment Type Database contains the sediments data with two spatial resolutions: a 5-minute resolution data with the worldwide coverage, and 6-second resolution data for selected areas (NAVO 2003).

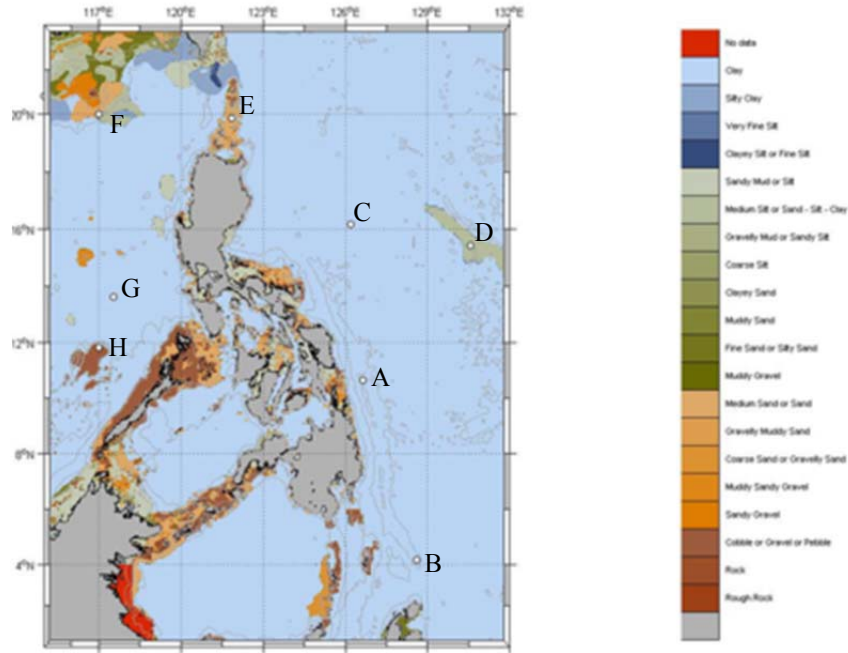


Figure 7. Bottom Sediment Types of the Philippine Sea and South China Sea. White Circles Denote Locations Chosen for Acoustic Propagation Modeling as Described in Chapter IV

### C. GEOACOUSTIC PARAMETERS

The following geoacoustic parameters are required to model sound propagation in a water column with a specific bottom sediment type: compressional sound speed in sediment, attenuation coefficient, and sediment density (Porter, 2011). After the sediment types have been extracted from the Bottom Sediment Type database, estimates of the geoacoustic parameters have been derived from empirical dependencies published by Hamilton (1980) and Hamilton and Bachman (1982). Table 3 shows the geoacoustic parameter estimates for the HFEVA sediment classes.

Table 3. Sediments Parameters for the HFEVA Bottom Sediment Types (NAVO, 2016), and their Properties.

<b>HFEVA code</b>	<b>HFEVA sediment type</b>	<b>Compressed Sound Speed, m/s</b>	<b>Sediment density, g/cm<sup>3</sup></b>	<b>Attenuation, dB/λ</b>
1	Rough Rock	2300	2.21	0.009
2	Rock	2300	2.21	0.009
3	Cobble or Gravel or Pebble	2736	2.5	0.009
4	Sandy Gravel	2032	2.492	0.009
5	Very Coarse Sand	2032	2.492	0.009
6	Muddy Sandy	2032	2.492	0.009
7	Gravel Coarse Sand or Gravelly Sand	1836	2.034	0.978
8	Gravelly Muddy Sand	1836	2.034	0.978
9	Medium Sand or Sand	1749	1.941	0.41
10	Muddy Gravel	1749	1.941	0.41
11	Fine Sand or Silty Sand	1646	1.772	0.549
12	Muddy Sand	1702	1.856	0.391
13	Very Fine Sand	1702	1.856	0.391
14	Clayey Sand	1702	1.856	0.391
15	Coarse Silt	1652	1.771	0.786
16	Gravelly Mud or Sandy Silt	1652	1.771	0.786
17	Medium Silt or Sand-Silt-Clay	1579	1.596	0.462
18	Sandy Mud or Silt	1615	1.74	0.477
19	Fine Silt or Clayey Silt	1549	1.488	0.477
20	Sandy Clay	1495	1.296	0.171
21	Very Fine Silt	1520	1.421	0.285
22	Silty Clay	1520	1.421	0.285
23	Clay	1493	1.414	0.097



### III. METHODS

To find out how environmental variability effects acoustic propagation in the Philippine Sea and South China Sea, a number of locations were chosen with different oceanography and bottom sediments. Then GDEM monthly mean was compared to multi-year averages calculated for SMG-WOD data. To separate the observed variability into seasonal and interannual parts, a composite analyses (Chu et al. 1997; 1998; Chu 2011) was applied to SMG-WOD sound speed profiles. After that, the interannual values were analyzed by the Empirical Orthogonal Functions (Hannachi, 2004) and correlated to the Southern Oscillation Index (SOI) (NOAA NCEI, 2017), Pacific Decadal Oscillation (PDO) index (Talley et al., 2011), and North Pacific Gyre Oscillation (NPGO) index (Talley et al., 2011). The acoustic transmission loss was calculated for the chosen locations through the BELLHOP ray-tracing model (Porter, 2011) using GDEM and SMG-WOD sound speed profiles. In this chapter we describe the main methods used in this thesis.

#### A. COMPOSITE ANALYSIS

The composite analysis was developed by (Chu et al. 1997; 1998; Chu 2011). It decomposes an oceanographic field into parts with different scales of variability. A sound speed profile is denoted as  $C(z_i, \tau_k, t_l)$ , where  $z$  is depth,  $\tau$  is year,  $t$  is month. Then the following values were calculated:

- Multi-year monthly average

$$\bar{C}(z_i, t_l) = \frac{1}{\Delta\tau} \sum_{k=1960}^{2014} C(z_i, \tau_k, t_l)$$

In Eq. (1)  $\Delta\tau=55$ , and the multi-year average is calculated for years 1960–2014.

- Total mean

$$\bar{\bar{C}}(z_i) = \frac{1}{12} \sum_{l=1}^{12} \bar{C}(z_i, t_l)$$

- Climatological monthly anomaly

$$\tilde{C}(z_i, t_l) = \bar{C}(z_i, t_l) - \bar{\bar{C}}(z_i)$$

- Synoptic monthly anomaly

$$\hat{C}(z_i, \tau_k, t_l) = C(z_i, \tau_k, t_l) - \bar{C}(z_i, t_l)$$

The synoptic monthly anomaly is a departure of each synoptic monthly sound speed profile at a specific location from the corresponding multi-year monthly average. It characterizes the interannual variability of the sound speed field in this location. Then apply the EOF method to select dominant variability patterns. Note that before applying the EOF analysis the  $\hat{C}(z_i, \tau_k, t_l)$  array was rearranged into a two-dimensional matrix with one dimension for depth and another dimension for time (Kucukosmanoglu, 2016).

## B. EMPIRICAL ORTHOGONAL FUNCTIONS (EOF) ANALYSIS

The EOF analysis can be applied to a meteorological or oceanographic field that depends on both space and time to separate the spatial and temporal variability of this field, and to select the spatial modes, which contribute most to the temporal variability of this field. A detailed description of the EOF method can be found, for example in (Hannachi, 2004).

In this thesis the EOF analysis was applied to the synoptic monthly anomalies of the sound speed profiles.  $\hat{C}(z, t)$  at each location were decomposed into the following linear combination:

$$\hat{C}(z, t) = \sum_{n=1}^N A_n(t) \Phi_n(z)$$

An important feature of the EOF approach is that the resulting coefficients  $A_n(t)$  depend only on time, and the EOF modes  $\Phi_n(z)$  depend only on depth. The modes and coefficients are arranged by their contribution to the total variability of the analyzed field (Chu et al., 1998). This means that the first mode contributes most variability. Overall,  $N = 30$  modes were calculated when it was possible by the profile depth. Only several

first modes were analyzed because they contribute most to the interannual variability of the total sound speed field.

### C. GEOGRAPHICAL LOCATIONS

The specific locations for the analysis were chosen to reflect different bathymetry, oceanographic conditions (different water masses), and bottom sediments. Since acoustic propagation was modeled for the mid-frequency sound source (3500 Hz), it is important to provide the acoustic model with geoacoustic parameters for the ocean bottom. (Computational Ocean Acoustic, 2011).

The bottom sediments for the Philippine Sea and the South China Sea are shown in Figure 7. This figure also shows the locations chosen for the analysis. The geographical coordinates, water depth and the type of bottom sediments are summarized in Table 4.

Table 4. Selected Geographical Locations.

Location	Latitude (N)	Longitude (E)	Depth (m)	Bottom Sediment
A	10°30'	126°40'	9.079	Clay
B	4°14.7'	128°32.7'	6.608	Clay
C	16°13.2'	126°15.1'	4.361	Clay
D	15°26.9'	130°35.5'	5.314	Coarse Silt
E	19°47.7'	121°48'	1.321	Muddy Sandy Gravel
F	20°	117°	1.464	Muddy Sandy Gravel
G	13°37.8'	117°	4.045	Clay
H	11°48'	117°	50	Cobble or Gravel or Pebble

### D. BELLHOP

The BELLHOP model is a ray-tracing model, which predicts transmission loss from a sound source in the ocean. It is an open source model, which is unclassified and can be used unrestricted. It allows a range-dependent environment, including ocean bathymetry, sediment distribution and sound speed in the water column to be modeled (Porter, 2011). The BELLHOP is implemented in Fortran, but the Fortran code can be compiled into an executable file and ran within the Matlab environment.

The BELLHOP model was run for a single-frequency sound source with two output options. First, a ray tracing option was used to obtain the transmission loss along the ray path, and to compare how the climatological and synoptic environmental models affect the energy propagation. Then, an eigenray option was used to calculate the transmission loss at a specific location of a receiver. See Figure 8.

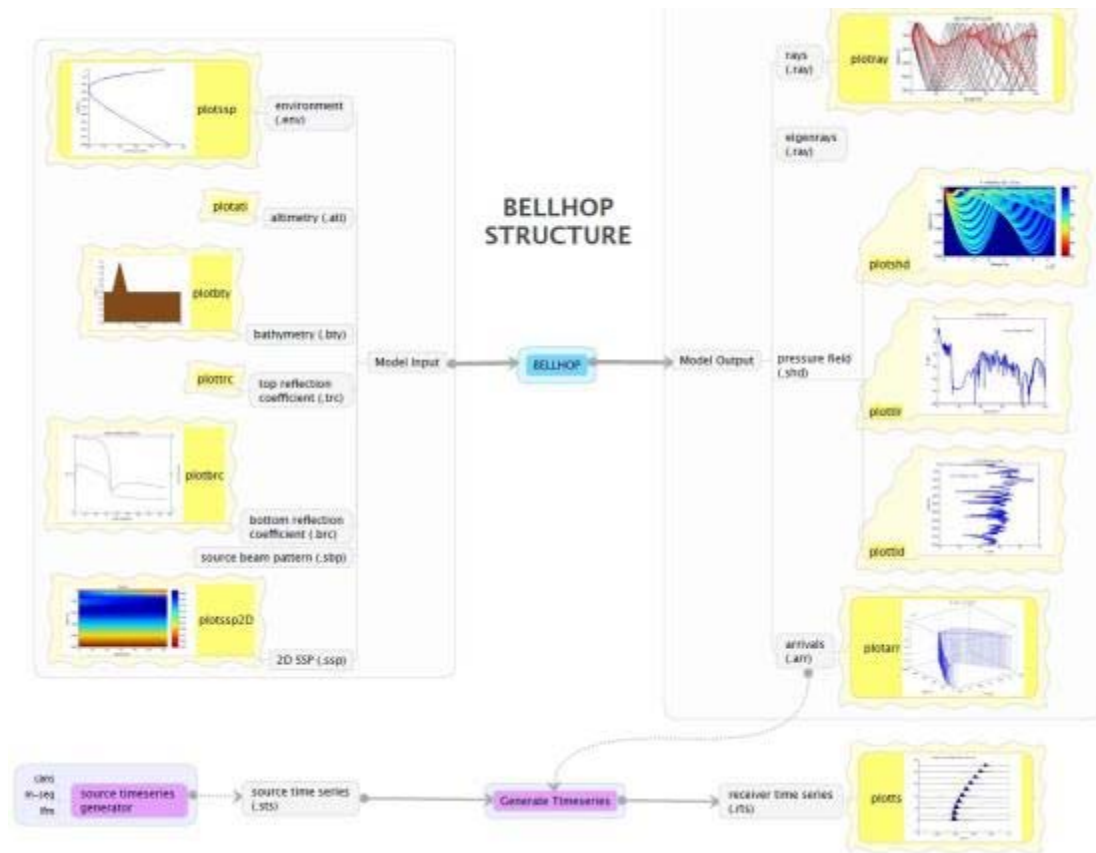


Figure 8. The Input and Output for the BELLHOP Model. Source: Porter (2011).

For the BELLHOP acoustic propagation model, 3500 Hz of acoustic frequency was used, with the sound source located at 40 m depth, using the GDEM and SMG-WOD databases to find the significant effect of the interannual variability for the acoustic propagation. The reason to choose the 3500 Hz for sound source frequency because this is a common frequency used for active sonar detection, 2–10 kHz is used to find and track underwater targets at distances of tens of kilometers. This frequency range is called “mid-frequency sonars,” or may be called “low frequency sonars” in the other countries.

(DOSITS, 2017). The 40 meters depth is a common depth where the active sonar detection from surface ships (using towed sonar) and submarine took place. The region between 0–100 meters will have more significant variability for the acoustic propagation that will create some tactical advantages and disadvantages for the underwater detection.

THIS PAGE INTENTIONALLY LEFT BLANK

## IV. SEASONAL VARIABILITY

In this chapter the seasonal variability in the oceanographic conditions in the Philippine Sea and South China Sea are described. To characterize the ocean state, the sea water spiciness is used, which allow to account for variations of both temperature and salinity at potential density surfaces (Munk, 1981). The seasonal variability in the region as captured by GDEM monthly mean fields were compared with the multi-year monthly averages calculated for the SMG-WOD dataset.

### A. SPICINESS

Based on Munk (1981),  $\pi$  is defined as ‘spiciness’. High spiciness corresponds to high temperature and salinity of the ocean water (Flament, 2002). Spiciness is constructed using potential density with reference to the surface  $p_{\text{ref}}=0$  (Flament, 2002). Following Fofonoff (1985) the given solution is.

$$\frac{\partial_{\theta}\pi}{\partial_{\theta}\rho} + \frac{\partial_s\pi}{\partial_s\rho} = 0 \quad (1)$$

$$\mu(\theta, s) = \tan^{-1} \partial_s \pi / \partial_s \rho \quad (2)$$

$$\pi(\theta, S) = \sum_{i=0}^5 \sum_{j=0}^4 b_{(ij)} \theta^i (s - 35)^j \quad (3)$$

Where  $b_{ij}$  are found by minimizing the weighted mean square error in equation (1) and  $\mu \approx 1$ , as stated in Flament (2002).

In the ocean the speed of acoustic propagation is not constant. The speed of the sound through water mainly is a function of three factors, which are temperature, depth and salinity. Since variations of temperature and salinity have opposite effect on density, the same density in different water masses within the water columns is possible. That is why spiciness variability is important to determine the variability of the acoustic propagation based on the sound speed profile variability.

To calculate the sound speed we can use the nine-term algorithm developed by Mackenzie (1981):

$$c(D, S, T) = 1448.96 + 4.591T - 5.304 \times 10^{-2}T^2 + 2.374 \times 10^{-4}T^3 + 1.340(S-35) + 1.630 \times 10^{-2}D + 1.675 \times 10^{-7}D^2 - 1.025 \times 10^{-2}T(S-35) - 7.139 \times 10^{-13}TD^3$$

T = temperature in degrees Celsius

S = salinity in parts per thousand

D = depth in meters

Range of validity: temperature 2 to 30 °C, salinity 25 to 40 parts per thousand and depth 0 to 8000 m. Source: NPL, 2000.

The Philippine Sea is a key region to connect the North Pacific subtropics to the equator in the Southside (Li, 2012). Most of the subtropical water in the North Pacific subtropics has to flow to the western boundary that is passing the Philippine Sea and has intrusions to the South China Sea through Luzon strait before going to the equator (Li, 2012), the continuous global circulations causing spiciness fluctuation and anomaly along the Philippine Sea and South China Sea.

In the Philippine Sea the fluctuation of the thermocline mainly is from the NEC, which brings mainly the spicy (warm/salty) NPTW (Li, 2012; Tsuchiya 1968). The water mass from the NEC bifurcates to the north via Kuroshio and to the south via Mindanao current (MC), the two currents are potentially important for generating the spiciness anomalies (Schneider, 2000; Kilpatrick et al., 2011).

## **1. MULTI-YEAR MONTHLY AVERAGE OF SMG-WOD**

Mean Spiciness in the Philippine Sea and South China Sea shows significant variability, both at temporal (seasonal) and spatial (regional) scales. It can be characterized by how strong spiciness decreases with depth. Figures 9, 10, 11, and 12 show the SMG-WOD multi-year monthly average at surface (0m), 100 m, 400 m, and 1000 m depth.

There is a strong decrease in spiciness from surface to 100 m during summer, especially in June. Maximum value ( $5.6 \text{ m}^3/\text{kg}$ ) is found at the surface of the Philippine Sea, decreasing with depth of around 100 m to the ( $4.9 \text{ m}^3/\text{kg}$ ). It also decreases in the South China Sea, from ( $5.1 \text{ m}^3/\text{kg}$ ) to ( $3.2 \text{ m}^3/\text{kg}$ ) at 100 m.



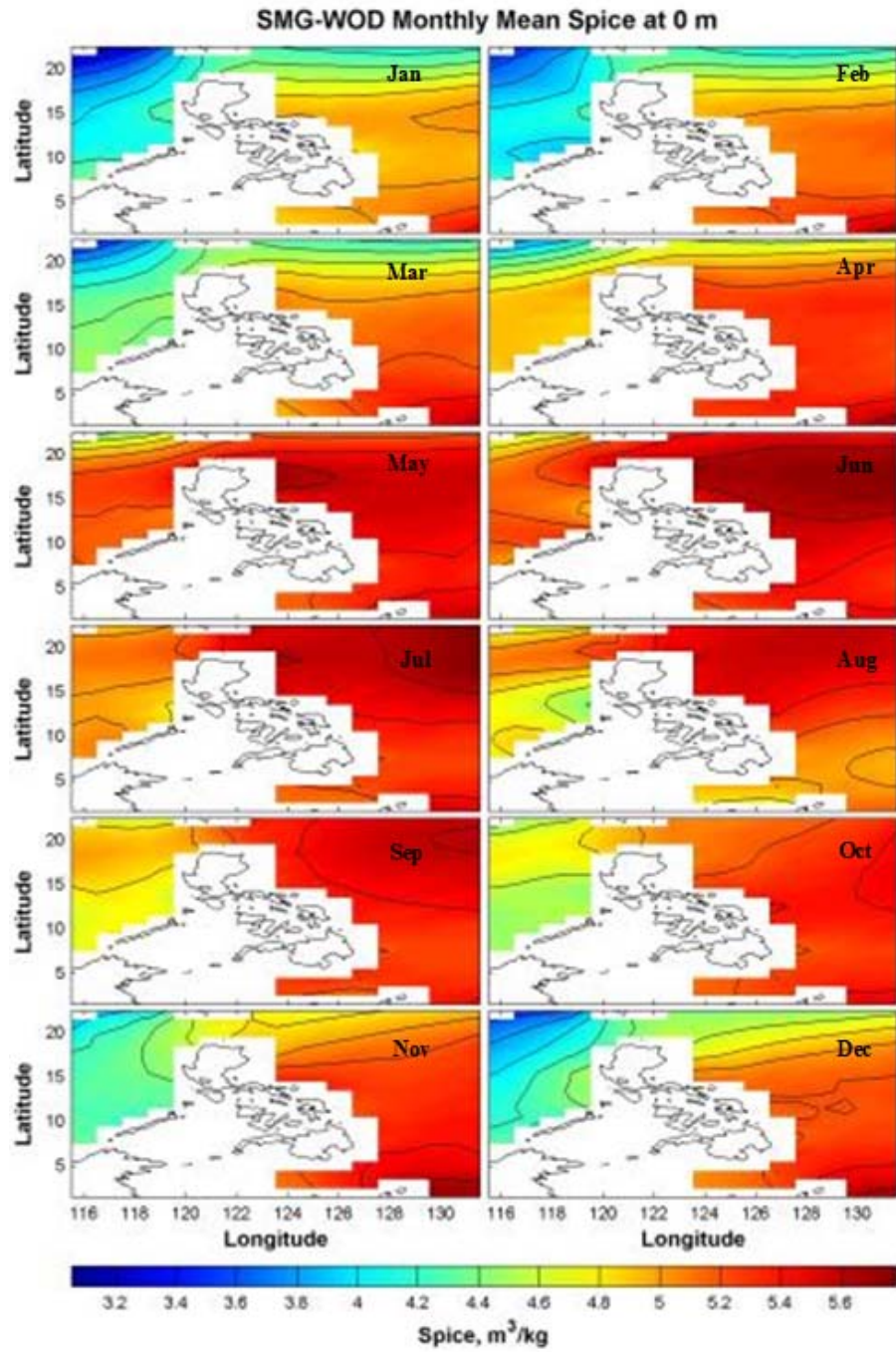


Figure 9. SMG-WOD Multi-year Monthly Average Spiciness at the Surface.

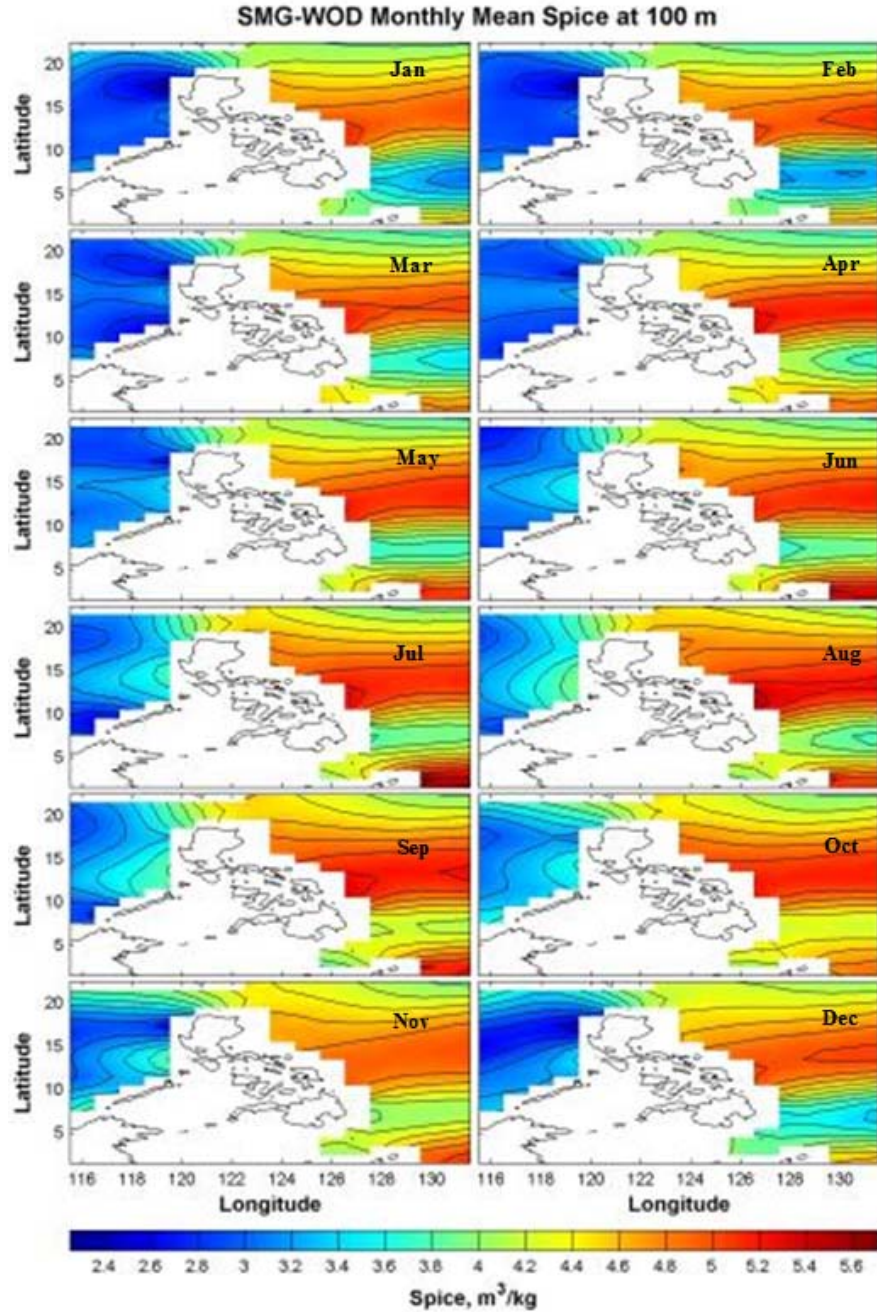


Figure 10. SMG-WOD Multi-year Monthly Average Spiciness at 100 m.

In November, maximum value ( $5.6 m^3/kg$ ) is found on the surface of the Philippine Sea, decreasing with depth of around 100 m to  $4.7 m^3/kg$ . It also decreases significantly in the South China Sea, from ( $5.2 m^3/kg$ ) to ( $2.8 m^3/kg$ ) around 100 meters depth. The main reason why rainy and dry seasons show different variations in

temperature because the surface water gets warmer in the rainy season due the great heating. Conversely, it gets cooler in the dry seasons.

NPTW lies between the surface water to about 400 meters, NPIW lies below the NPTW to about 1400 m depth (Kim, 2007). SMG-WOD Multi-year Monthly Average Spiciness is plotted at 400 meters in Figure 11.

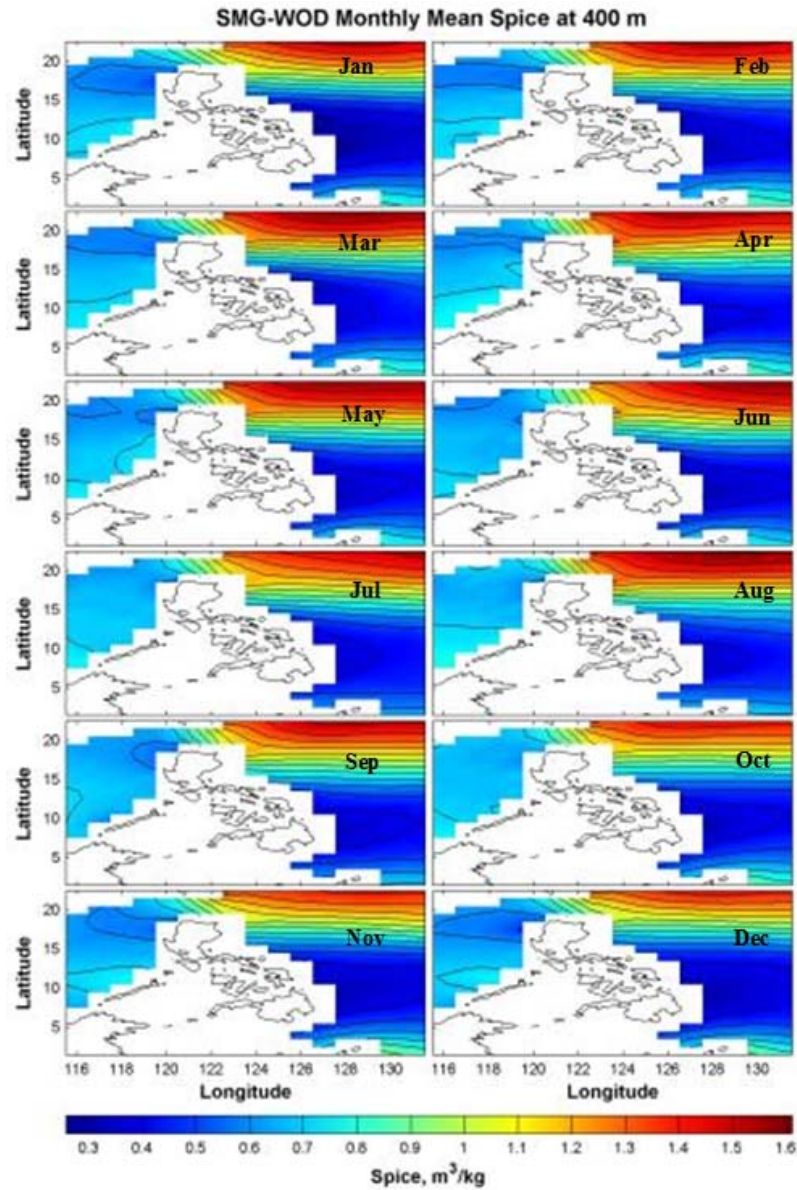


Figure 11. SMG-WOD Multi-year Monthly Average Spiciness at 400 m.



The spiciness decreases significantly at a depth of 400 meters relative to the surface. Oppositely, to the situations at the surface, the minimum values are found in the July in the Philippine Sea. At 400 meters depth, it is approximately  $0.7 \text{ m}^3/\text{kg}$ . The maximum values ( $1.5 \text{ m}^3/\text{kg}$ ) are seen in August. High salinity and temperature, referring high spiciness, is the signature of NPTW.

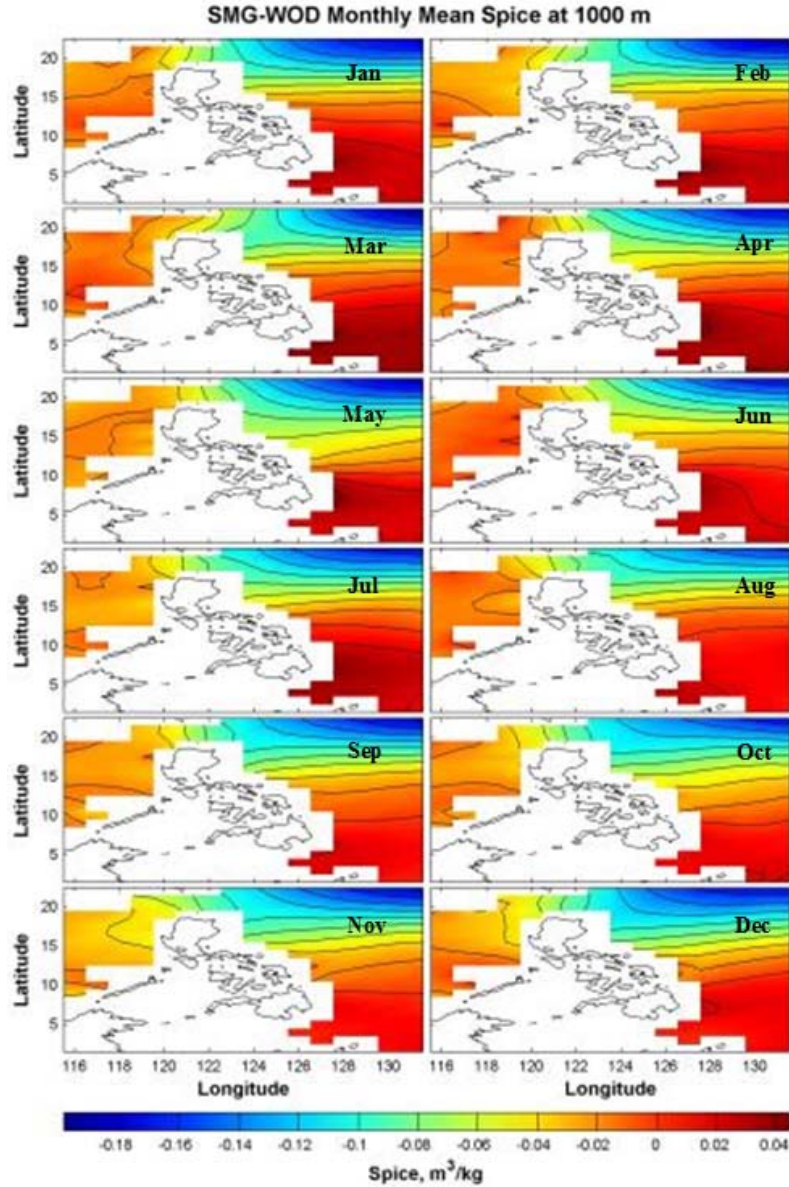


Figure 12. SMG-WOD Multi-year Monthly Average Spiciness at 1000 m.

SMG-WOD Multi-year Monthly Average Spiciness is plotted at 1000 m depth in order to analyze the Deep Water (Figure 12). The maximum values are found in the Philippine Sea, eastern part of the Mindanao Island in May. They are approximately ( $0.04 \text{ m}^3/\text{kg}$ ). The minimum values are found in northeastern part of the Luzon Island, about  $-0.14 \text{ m}^3/\text{kg}$  in August.

## 2. GDEM MONTHLY SPICINESS

GDEM monthly mean fields of Spiciness are analyzed at the same depths in order to compare the two models. Figure 13 shows GDEM Monthly mean Spiciness at the surface and Figure 14 shows GDEM Monthly mean Spiciness at 100 m depth.

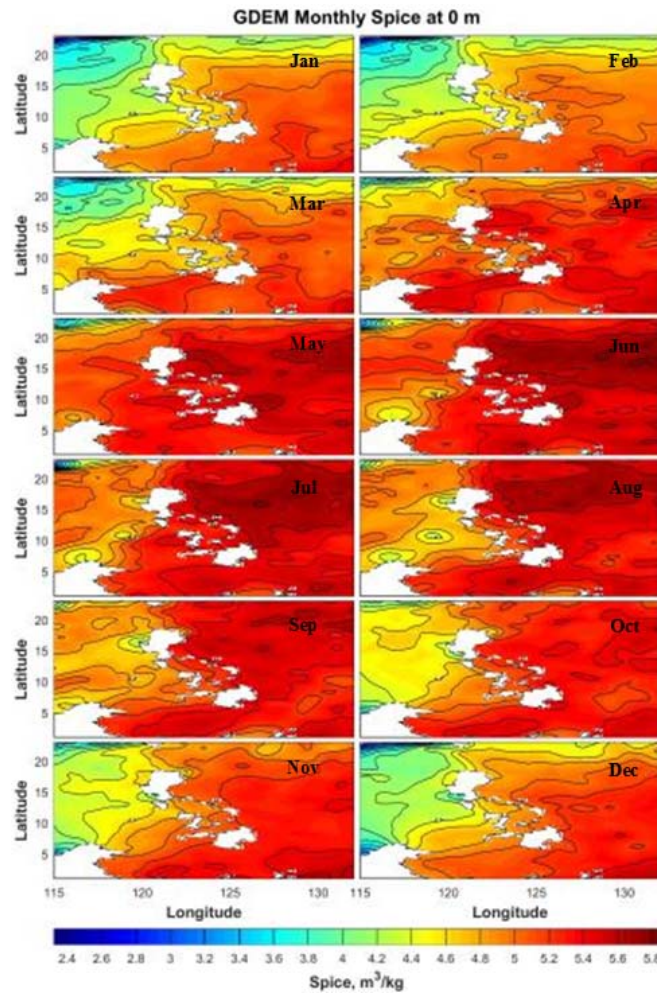


Figure 13. GDEM Monthly Spiciness at the Surface.

Maximum value ( $5.8 \text{ m}^3/\text{kg}$ ) is found in June at the surface of the Philippine Sea, decreasing with depth of around 100 meters to ( $2.3 \text{ m}^3/\text{kg}$ ) in February in the South China Sea. There is a slight difference between the two models in values.

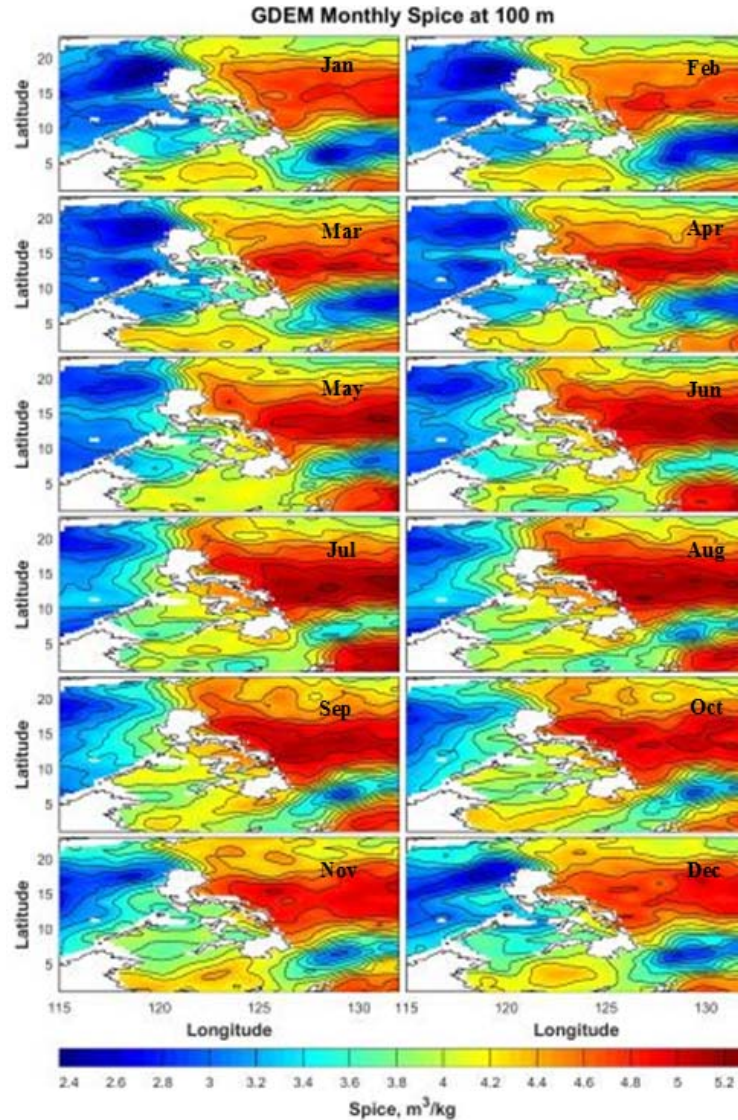


Figure 14. GDEM Monthly Spiciness at 100 m.

Since GDEM has higher vertical and horizontal resolution than SMG-WOD, SMG-WOD has some difficulties to resolve the shallow coastal waters due to limited vertical resolution. It is clearly seen that SMG-WOD spiciness values are not provided in coastal waters. However, GDEM provides all spiciness values clearly in coastal waters.

SMG-WOD has a very good agreement with GDEM in deep waters. The appendix provides an additional collection of spiciness figures and it was confirmed that the Philippine Sea is spicier than the South China Sea in all months.

## B. SOUND SPEED

Considering the strategic importance of the Philippine Sea and the South China Sea more comprehensive studies regarding the sound speed profile are needed. One of the purposes of this thesis is to provide sound speed profiles study in these region that have large seasonal and regional variation due to variation of spiciness.

### 1. MULTI-YEAR MONTHLY AVERAGE OF SMG-WOD

The images of the SMG-WOD monthly average sound speed are displayed to show the relation between spiciness and sound speed. Figure 15 shows SMG-WOD monthly mean sound speed at the surface, and SMG-WOD monthly mean sound speed at 100 meters is provided in Figure 16. Additional results are provided in Appendix B.

In the southern part of the Philippine Sea, sound speed is higher than in the South China Sea. The maximum surface sound speed (1542m/s) is found in the Philippine Sea where highest spiciness ( $5.6 \text{ m}^3/\text{kg}$ ) exists in June. Tables 5 to 8 shows these results.

Table 5. Sound Speed and Spiciness at the Surface in June.

Region	Spiciness	Sound Speed
Philippine Sea	$5.6 \text{ m}^3/\text{kg}$	1542m/s
South China Sea	$4.9 \text{ m}^3/\text{kg}$	1541 m/s.

Table 6. Sound Speed and Spiciness at the surface in December.

Region	Spiciness	Sound Speed
Philippine Sea	$5.5 \text{ m}^3/\text{kg}$	1541 m/s
South China Sea	$4.3 \text{ m}^3/\text{kg}$	1540 m/s.



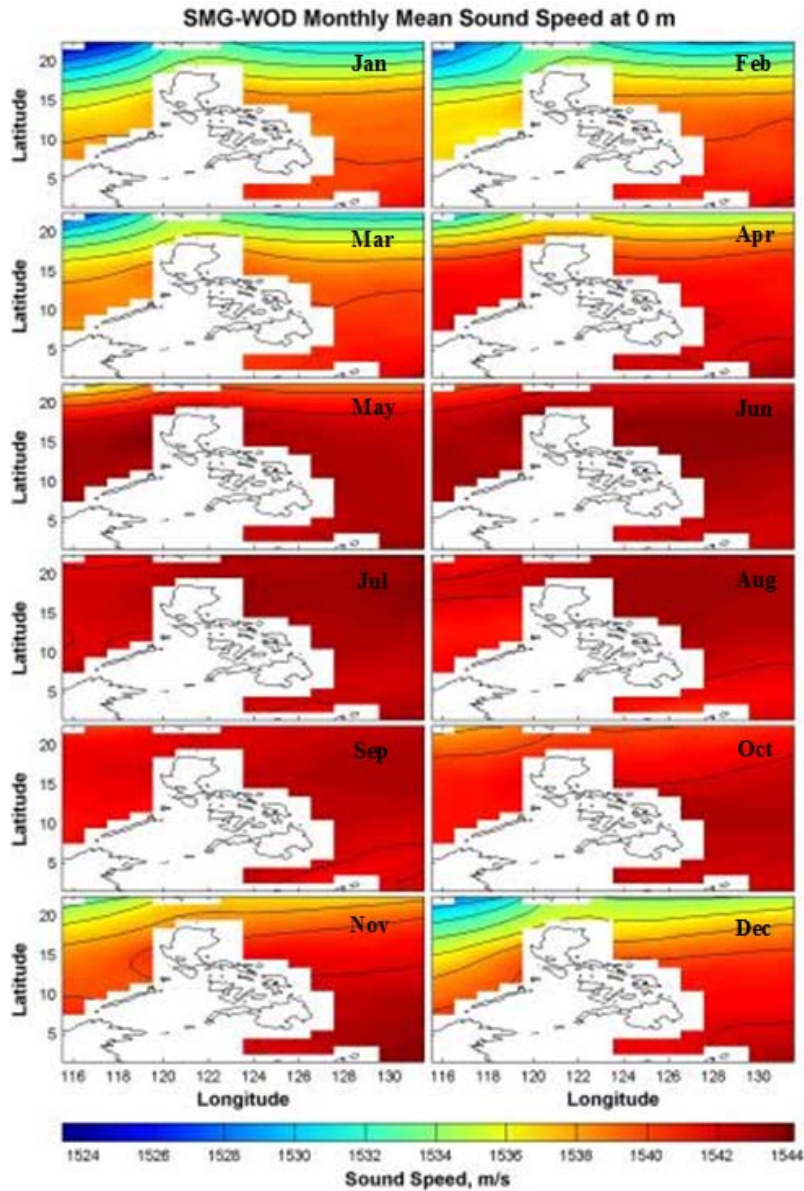


Figure 15. SMG-WOD Multi-year Monthly Average Sound Speed at the Surface.

Table 7. Sound Speed and Spiciness at 100 m depth in June.

Region	Spiciness	Sound Speed
Philippine Sea	$5.3 \text{ m}^3/\text{kg}$	1539 m/s
South China Sea	$3.3 \text{ m}^3/\text{kg}$	1530 m/s.



Table 8. Sound Speed and Spiciness at 100 m depth in December.

Region	Spiciness	Sound Speed
Philippine Sea	$5.0 \text{ m}^3/\text{kg}$	1537 m/s
South China Sea	$3.4 \text{ m}^3/\text{kg}$	1528 m/s.

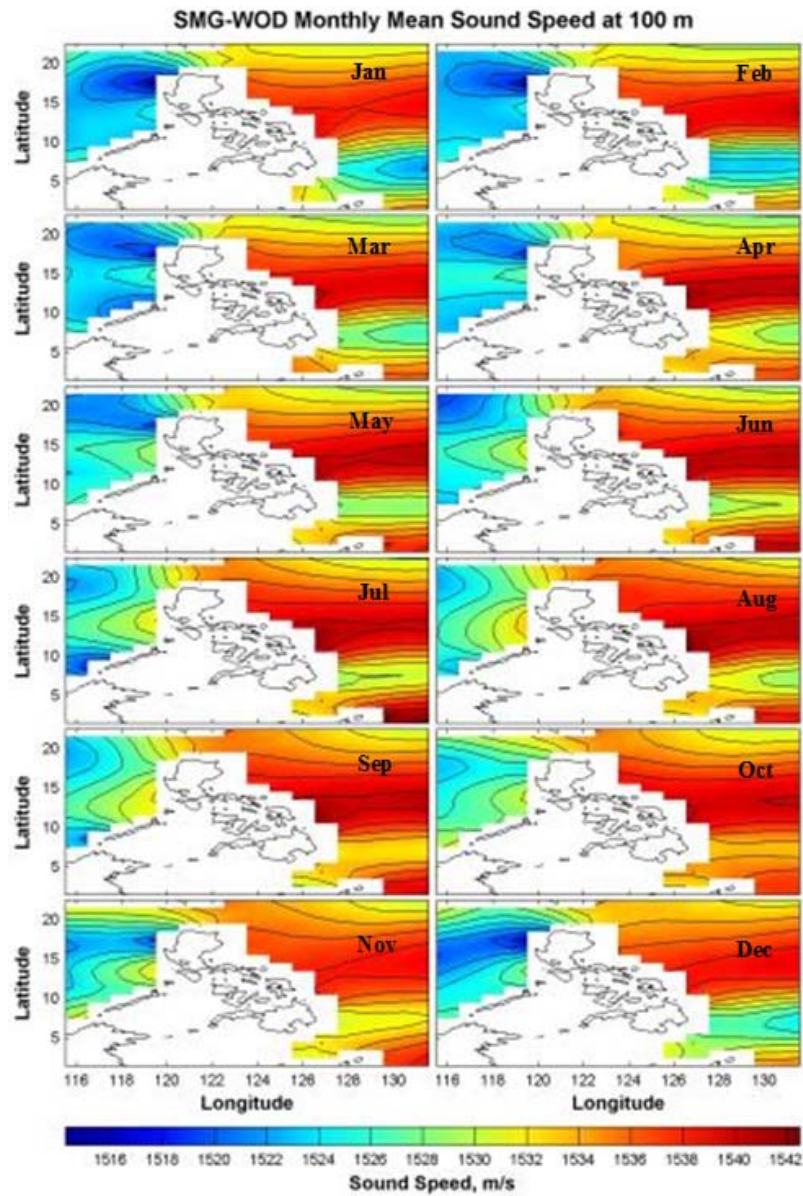


Figure 16. SMG-WOD Multi-year Monthly Average Sound Speed at 100 m.

## 2. GDEM MONTHLY SOUND SPEED

GDEM monthly sound speed was analyzed at the same depths to compare the two models with each other. GDEM monthly sound speed at the surface is provided in Figure 17, and GDEM monthly sound speed at 100 meters is provided in Figure 18. Additional results are provided in Appendix C.

The maximum surface sound speed (1544 m/s) is found in the Philippine Sea. Tables 9 to 12 shows these results.

Table 9. GDEM Sound Speed and Spiciness at the Surface in June.

Region	Spiciness	Sound Speed
Philippine Sea	$5.7 \text{ m}^3/\text{kg}$	1544m/s
South China Sea	$5.2 \text{ m}^3/\text{kg}$	1542 m/s.

Table 10. GDEM Sound Speed and Spiciness at the Surface in December.

Region	Spiciness	Sound Speed
Philippine Sea	$5.4 \text{ m}^3/\text{kg}$	1541 m/s
South China Sea	$4.9/\text{kg}$	1539 m/s.

Table 11. GDEM Sound Speed and Spiciness at 100 m depth in June.

Region	Spiciness	Sound Speed
Philippine Sea	$5.1 \text{ m}^3/\text{kg}$	1539 m/s
South China Sea	$4.2 \text{ m}^3/\text{kg}$	1531 m/s.

Table 12. GDEM Sound Speed and Spiciness at 100 m depth in December.

Region	Spiciness	Sound Speed
Philippine Sea	$5.0 \text{ m}^3/\text{kg}$	1538 m/s
South China Sea	$4.2 \text{ m}^3/\text{kg}$	1534 m/s.

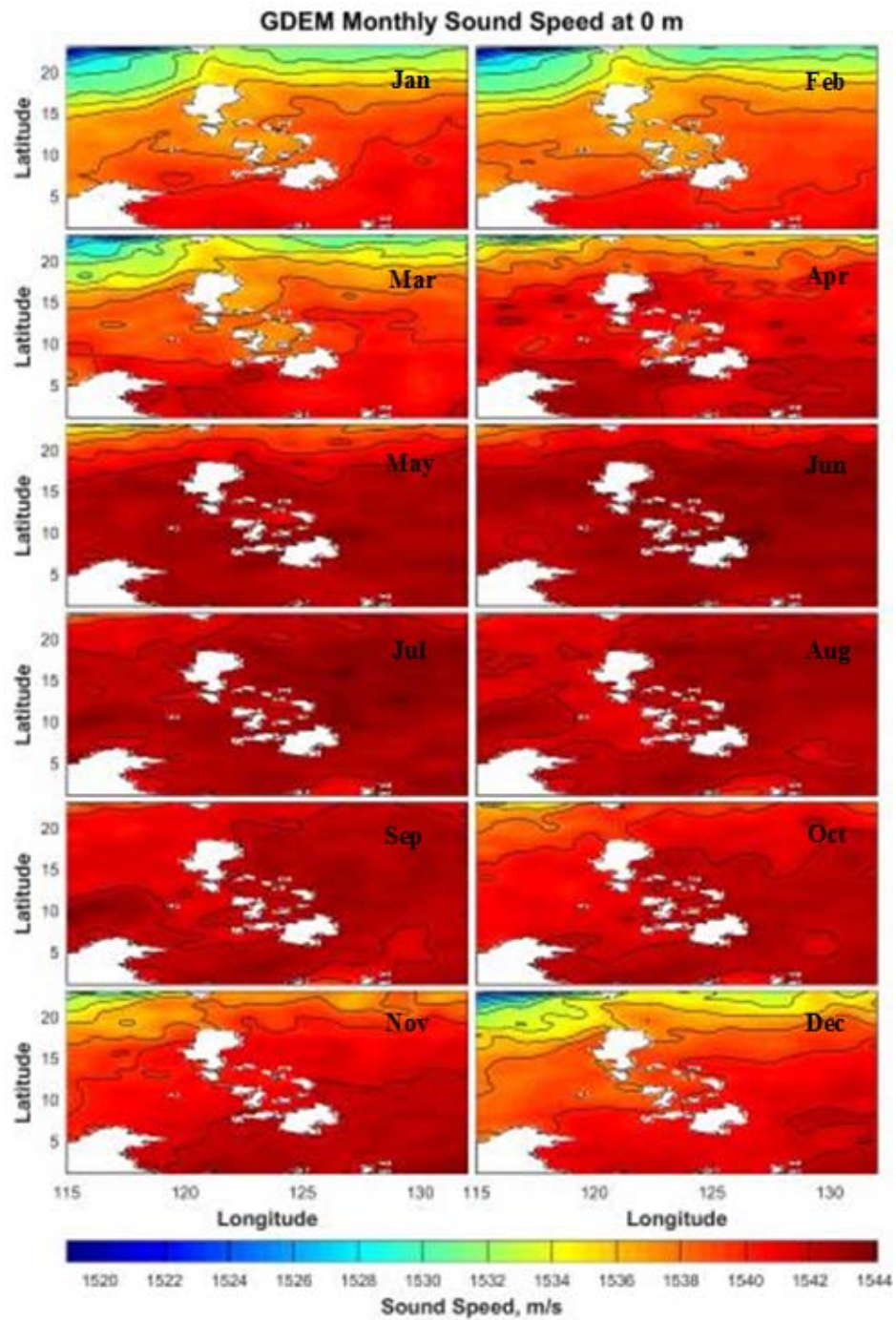


Figure 17. GDEM Monthly Sound Speed at the Surface.



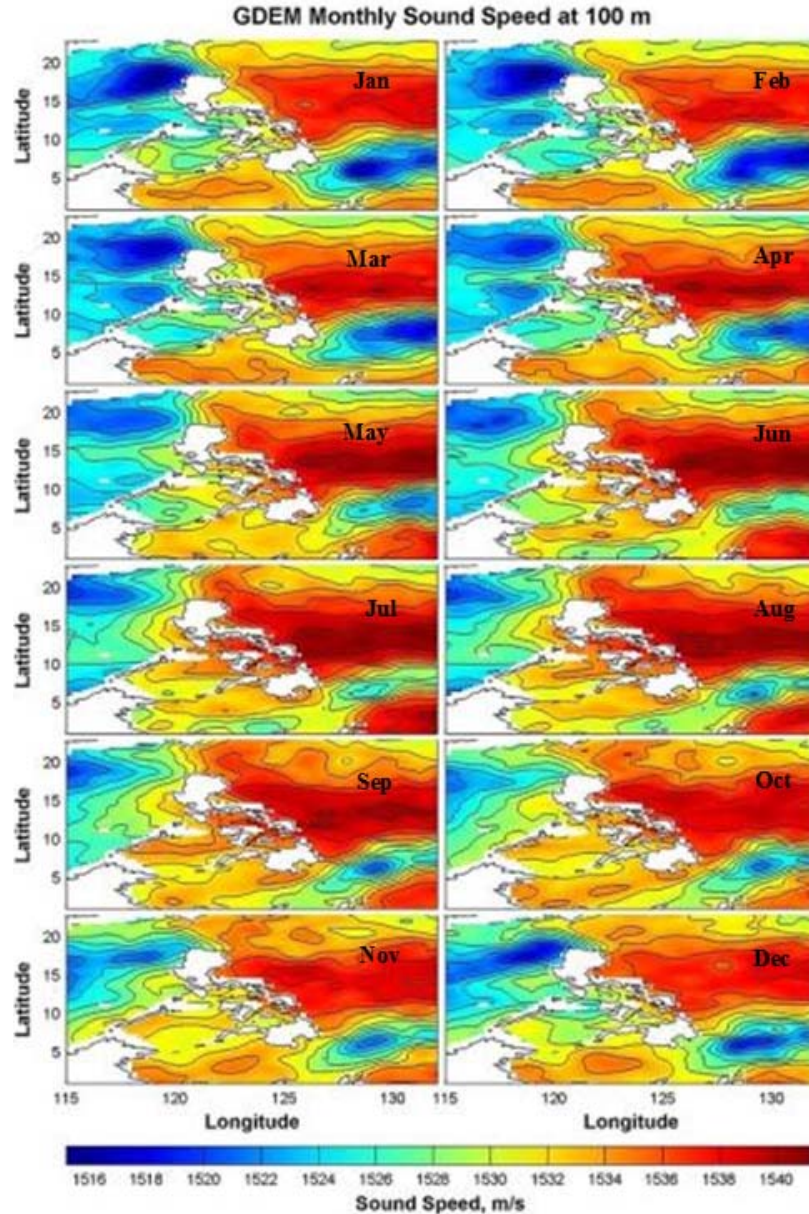


Figure 18. GDEM Monthly Sound Speed at 100 m.

The maximum sound speed is found in the region where maximum spiciness exists and where the pressure does not dominate. Then we can use the spiciness variable to compare the water masses in the region.

Comparing both data results, the sound speeds calculated from the multi-year averaged SMG-WOD (T, S) data are consistent with that calculated from the GDEM (T, S) data.

### C. UNDERWATER SOUND PROPAGATION AND SOUND SPEED PROFILES (SSP).

Sound is basically a mechanical disturbance that travels through a fluid (Medwin, 2005). Sound propagation in water is a more complex phenomenon than in air, because water is more viscous, has more heat capacity and conductivity, moreover in a natural condition like the ocean it will be even more complex (FAS, 2017).

In the 1940s during World War II, the sound speed variations and their effects on acoustic propagation were studied for the first time. It is not easy to locally measure the sound speed but it is more feasible to measure the parameters affecting the sound speed, which are temperature, salinity and pressure. A good first model was developed by Medwin (1975), but it was limited to 1000 meters in depth (USNA, 2017). A more accurate model has been developed based on Chen and Millero (1977), and it is used as United Nations Educational, Scientific and Cultural Organization (UNESCO) standard reference model.

$$C=c_0 + c_1P + c_2P^2 + c_3P^3 + AS + BS^2 + CS^2$$

P=Pressure from Leroy formula

$$A=A_0 + A_1P + A_2P^2 + A_3P^3$$

$$B=-1.922 \times 10^{-2} - 4.42 \times 10^{-5}t + (7.3637 \times 10^{-5} + 1.7945 \times 10^{-7}t)P$$

$$C=-7.9836 \times 10^{-6}P + 1.727 \times 10^{-3}$$

t=temperature (°C)

z=depth (m)

S=salinity (PSU) Source: (USNA, 2017).

To predict the acoustic propagation path the Sound Speed Profile (SSP) was used, which is the common profile of the sound speed through the depth of the ocean. It can be obtained from a measuring tool such as an expendable Bathy Thermograph (XBT).

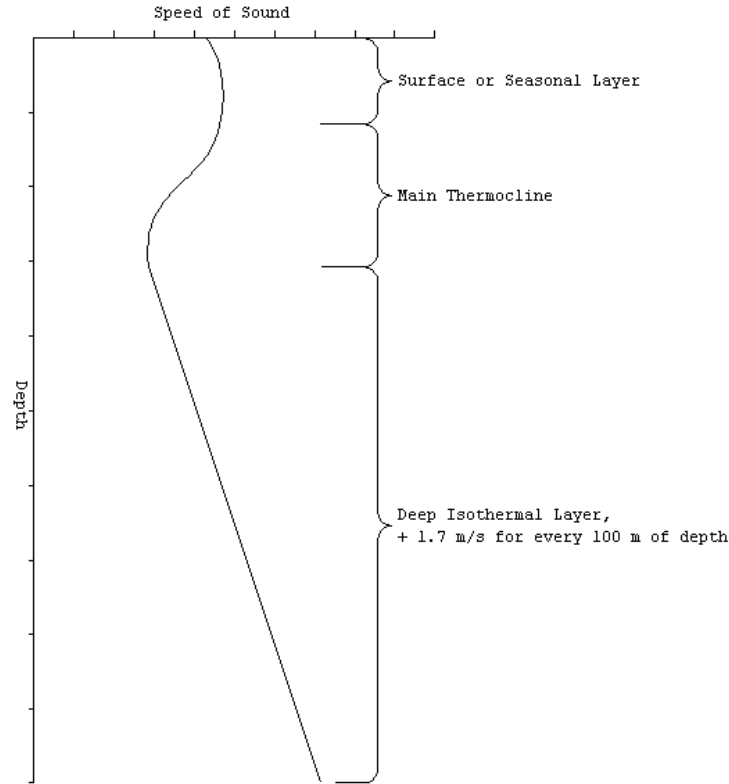


Figure 19. Ocean Layers. Source: FAS (2017).

The acoustic propagation obeys the principal of Snell's law

$$n_1 \sin \theta_1 = n_2 \sin \theta_2,$$

Which explains the refraction angle ( $\theta_1$ ) of a ray of light from an area of smaller refractive index ( $n_1$ ) (e.g., air) to an area of higher reflective index ( $n_2$ ) (e.g., water), then the refracted angle ( $\theta_2$ ) will become smaller because the speed of light is smaller in the denser medium like water. In the contrary the sound speed will be higher in a denser medium, which is higher spiciness and pressure.

As the acoustic rays goes deeper it will be affected by refraction, which is characterized by the index of refraction (in accordance to Snell's law). When the sound rays goes to a medium with a slower sound speed it will tend to deflect downward (Figure 20) (FAS, 2017).

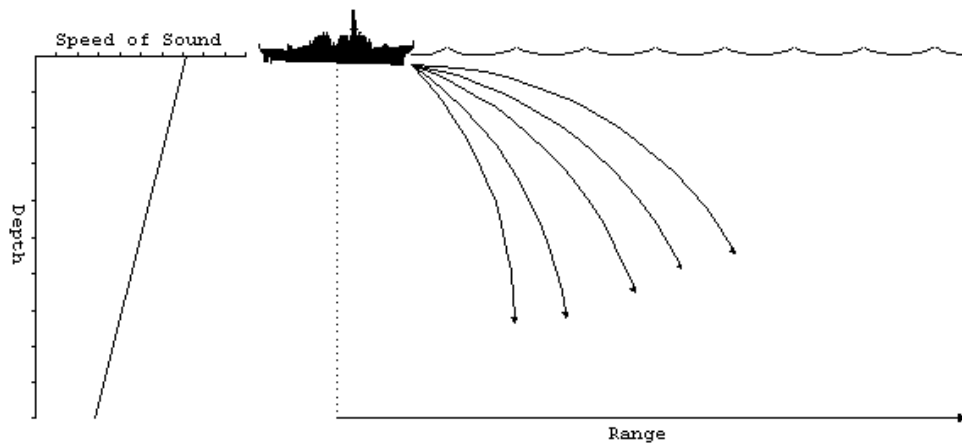


Figure 20. An Example of Acoustic Path for a Negative SSP Gradient. Source: (FAS, 2017). The Corresponding SSP Is Shown in the Left Panel.

A positive gradient will make an opposite effect: as the rays go deeper they tend to be deflected upward (Figure 21).

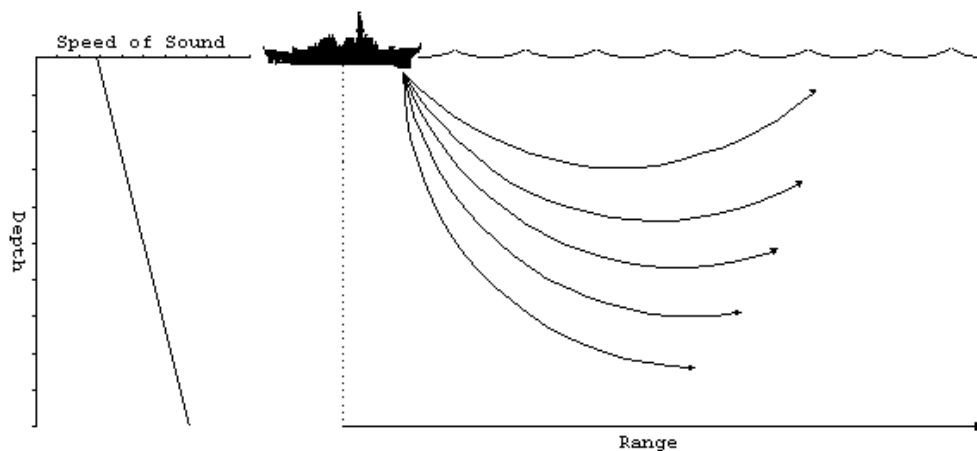


Figure 21. An Example of Acoustic Path for a Positive SSP Gradient. Source: (FAS, 2017). The Corresponding SSP Is Shown in the Left Panel.

All sound rays are getting deflected upward, and then deflected downward when they reach the surface. The process will be continuous, which means that the sound rays get trapped, because of the occurrence of a relatively small layer below the surface. This effect is called surface duct (FAS, 2017).

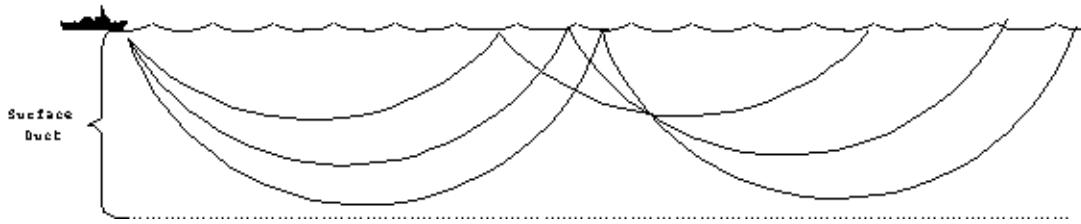


Figure 22. Surface Duct. Source: (FAS, 2017).

Figure 23 shows a combination of positive SSP gradient in the upper layer of the water column and negative SSP gradient below it. This SSP will create a shadow zone for a submarine to hide from Sound Navigation and Ranging (SONAR) detection. The depth of the maximum sound speed is called the layer depth (LD) (FAS, 2017).

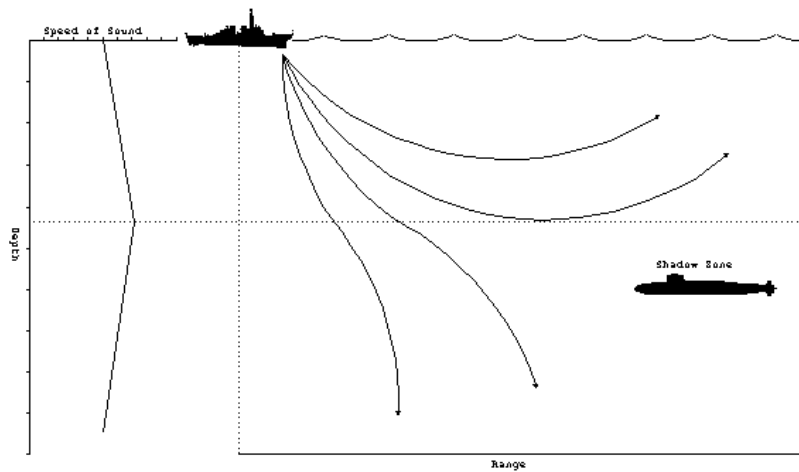


Figure 23. An Example of a Shadow Zone (sonic layer). Source: (FAS, 2017). The Corresponding SSP is Shown In the Left Panel.

For the combination of negative SSP gradient on top of the positive SSP gradient (Figure 24) will create a sound channel. In the sound channel the sound rays will be deflected upward and then downward back to the middle. When a sound source is located at the sound channel axis, the sound gets trapped and can travel long distances within the sound channel (FAS, 2017).



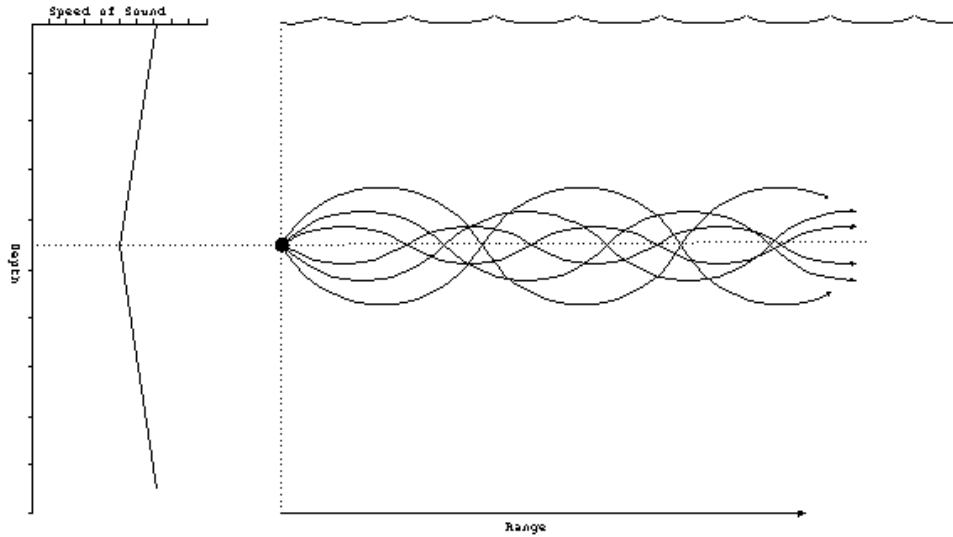


Figure 24. Sound Channel. Source: (FAS, 2017).

Another type of propagation is the convergence zone (Figure 25). The sound rays are deflected upwards by the positive gradient SSP at the deep isothermal layer. A convergence zone needs a minimum 200 m of depth excess from the lower boundary of the sound channel. The convergence zone tends to be at large distances, typically 20–30 nm from the sound source, and it is possible to have multiple convergence zones occurring at regular intervals (FAS, 2017).

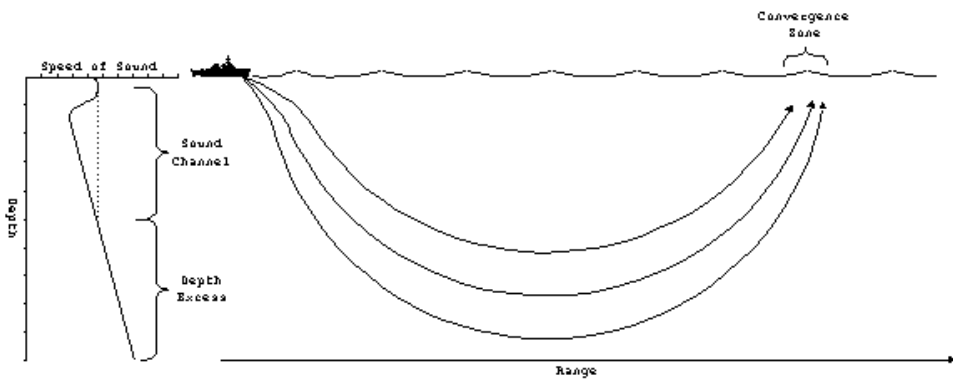


Figure 25. Convergence Zone. Source: FAS (2017).

Another type of sound propagation is when the sound rays are reflected from the ocean bottom, this will also depends on the types of the bottom sediments, and this is called the bottom bounce propagation (Figure 26).

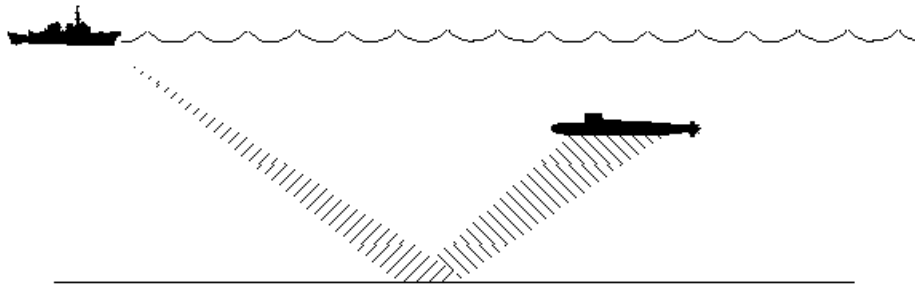


Figure 26. Bottom Bounce. Source: FAS (2017).

In the Philippine Sea and the South China Sea we can expect all of the sound propagation types to occur because it has the deep water area and the shallow water area, and the high seasonal variability near the surface layer.

#### **D. SOUND SPEED PROFILES (SSP).**

The total and monthly mean over SMG-WOD and GDEM are calculated at the points of interest in Figure 27. Eight points, from A to H, are selected in the Philippine and South China Sea.

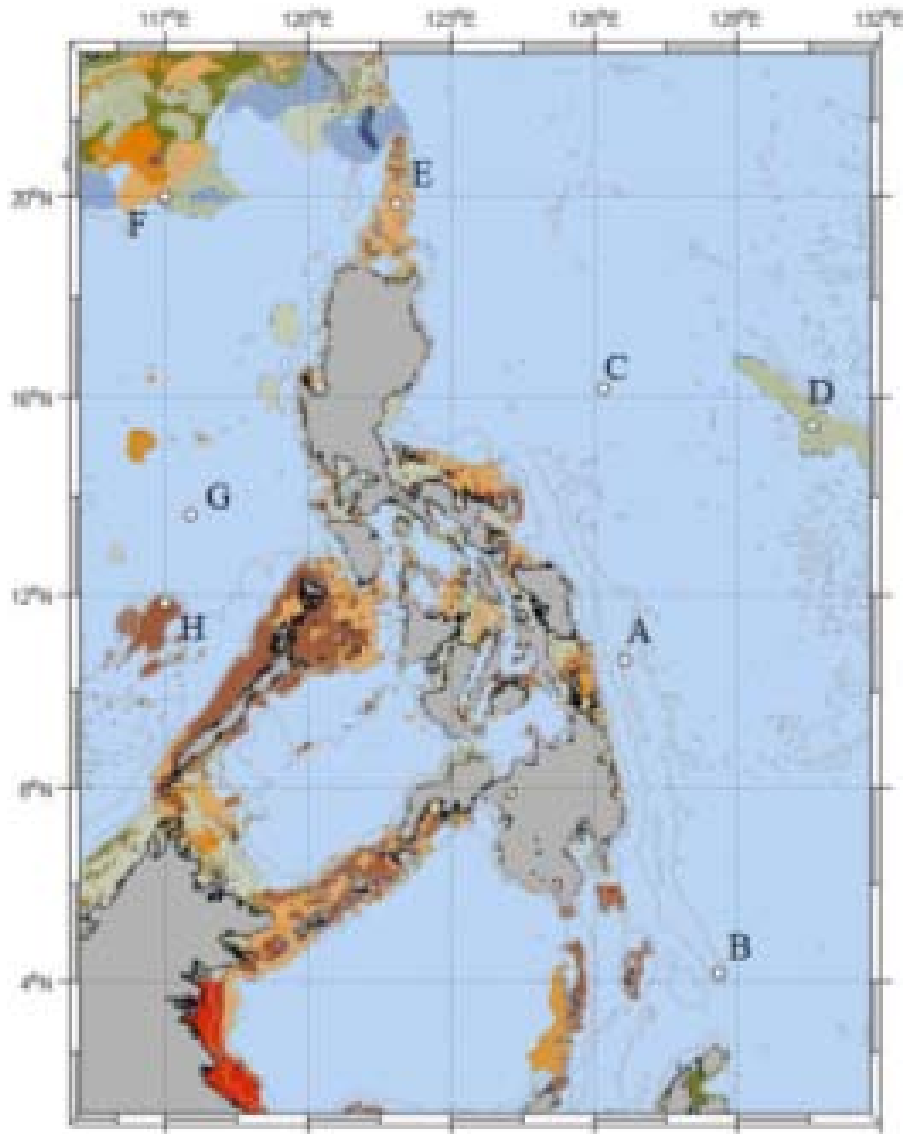


Figure 27. Points from A through H.

## 1. Point A

At the surface, the Mindanao current brings the warm and salty water to increase the sound speed. It is possible to see sound channel at a depth of 900 meters and convergence zones along all seasons. The greatest variance between monthly mean and total mean exist in the upper layers, particularly from January through March. The greatest variance is about 4 m/s in January, February and March. In the dry season, there is more difference between monthly mean and total mean in the surface layer. The monthly and total means are plotted in Figure 28.

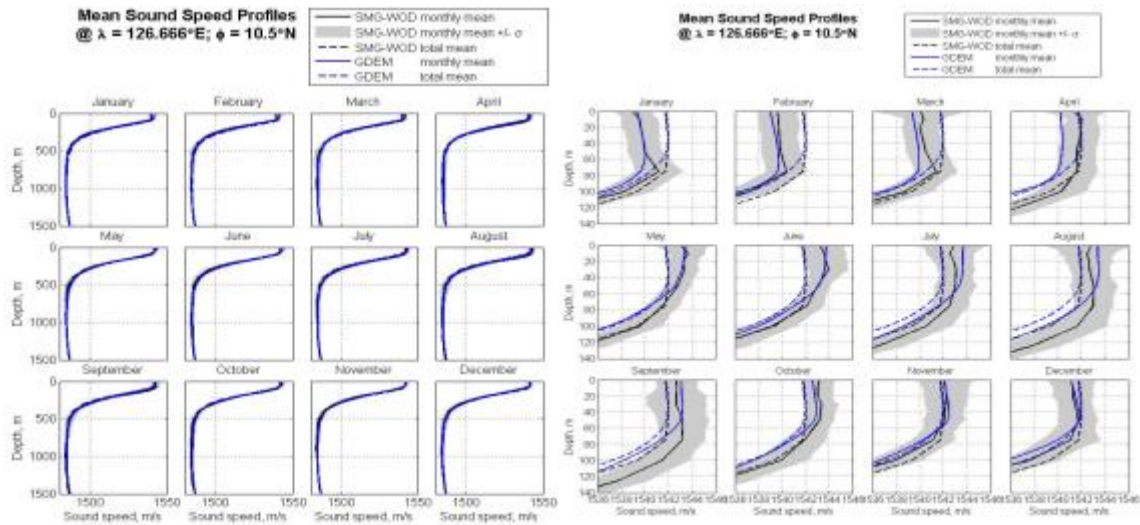


Figure 28. Mean Sound Speed Profiles (Point A).

## 2. Point B

As for point A, the Mindanao current brings the warm and salty water to increase the sound speed at the surface for point B. The sound channel is at a depth of 1000 meters, and convergence zones are expected to exist during all seasons. The greatest variance between monthly mean and total mean exist in the upper layers, particularly from January through March. The greatest variance is about 4 m/s in January, February and March. In the dry season, there is more difference between monthly mean and total mean in the surface layer. The monthly and total means are plotted in Figure 29.

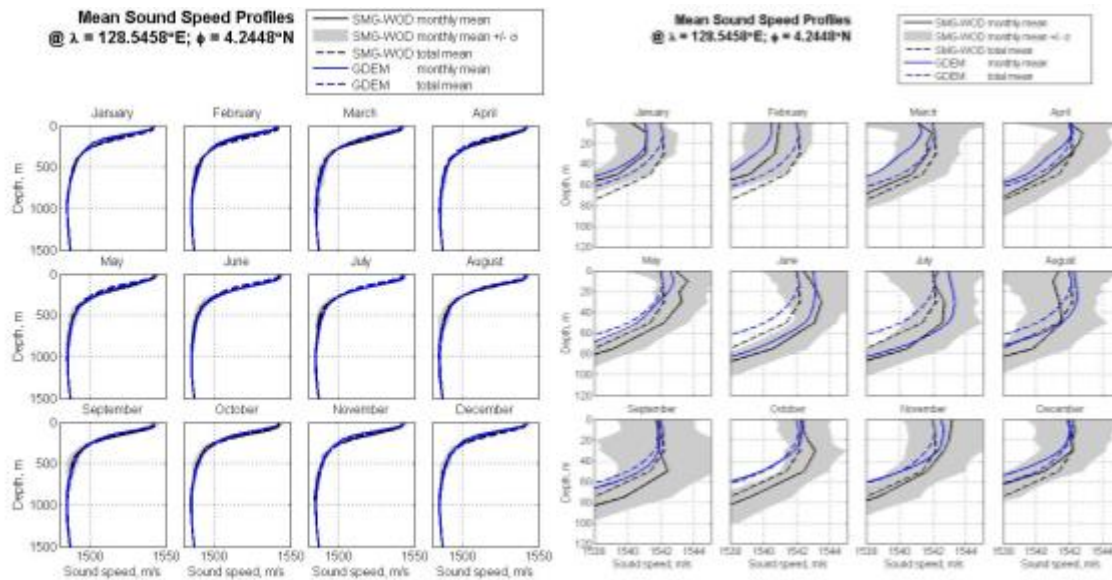


Figure 29. Mean Sound Speed Profiles (Point B).

### 3. Point C

At the surface, the Kuroshio Current brings the warm and salty water to increase the sound speed, and will intensify at rainy season. It is possible to see sound channel at a depth of 1000 meters and convergence zones along all seasons. The greatest variance between monthly mean and total mean exist in the upper layers, particularly from January through March. The greatest variance is about 3 m/s in January, February and March. In the dry season, there is more difference between monthly mean and total mean in the surface layer. The monthly and total means are plotted in Figure 30.

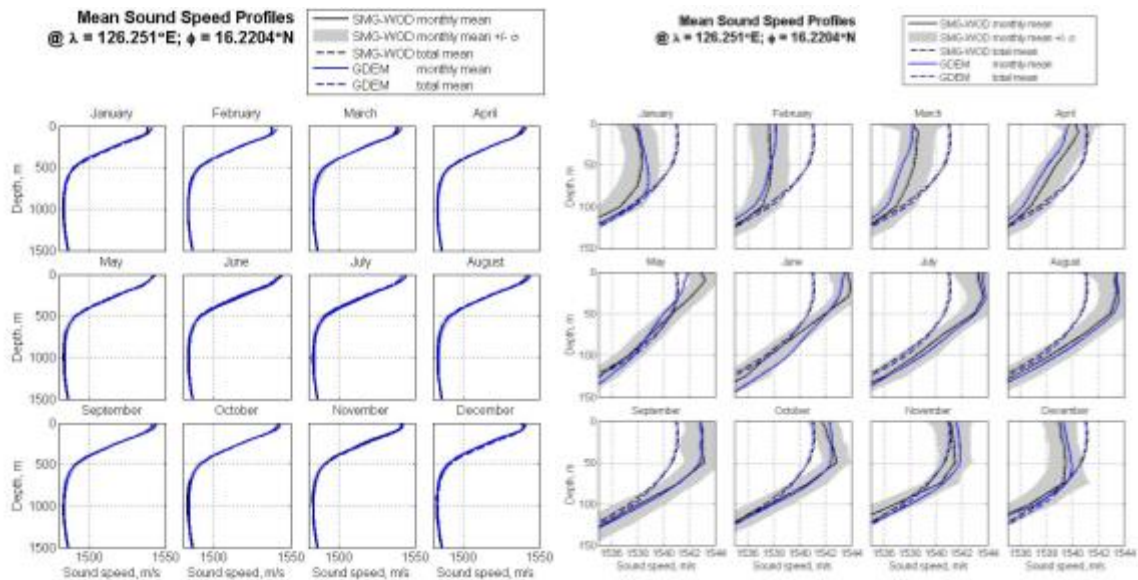


Figure 30. Mean Speed Profiles (Point C).

#### 4. Point D

At the surface, the North Equator Current brings the warm and salty water to increase the sound speed. It is possible to see sound channel at a depth of 1000 meters and convergence zones along all seasons. The greatest variance between monthly mean and total mean exist in the upper layers, particularly from January through March. The greatest variance is about 3 m/s in January, February and March. In the dry season, there is more difference between monthly mean and total mean in the surface layer. The monthly and total means are plotted in Figure 31.

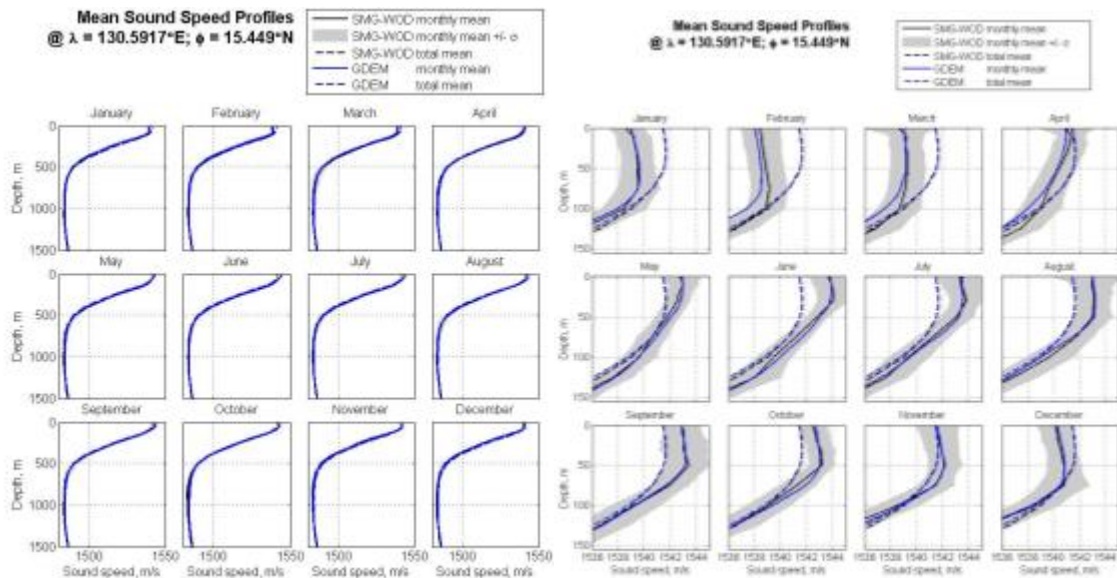


Figure 31. Mean Sound Speed Profiles (Point D).

## 5. Point E

At the surface, the Kuroshio Current brings the warm and salty water to increase the sound speed. It is possible to see sound channel at a depth of 1000 meters and convergence zones along all seasons. The greatest variance between monthly mean and total mean exist in the upper layers, particularly from January through March, and June through August. The greatest variance is about 4 m/s. In the dry season, there is more difference between monthly mean and total mean in the surface layer. The monthly and total means are plotted in Figure 32.

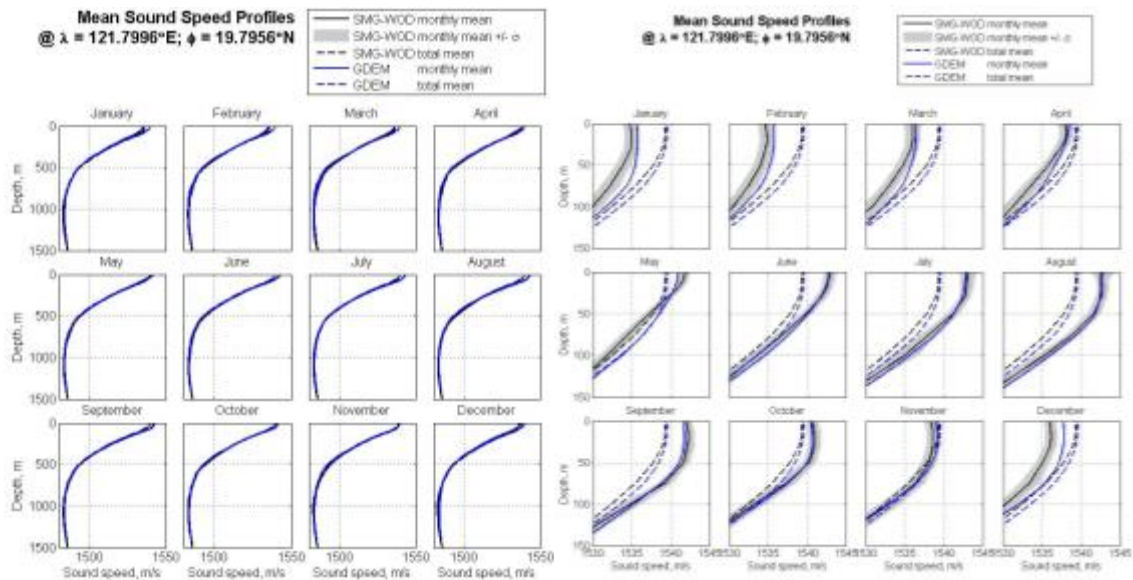


Figure 32. Mean Sound Speed Profiles (Point E).



## 6. Point F

At the surface, the intrusion from the North Equatorial Current through the Luzon strait current brings the warm and salty water to increase the sound speed. It is possible to see sound channel at a depth of 1000 meters and convergence zones along all seasons. The greatest variance between monthly mean and total mean exist in the upper layers, particularly from January through March. The greatest variance is about 6 m/s in January, February and March. In the dry season, there is more difference between monthly mean and total mean in the surface layer. The monthly and total means are plotted in Figure 33.

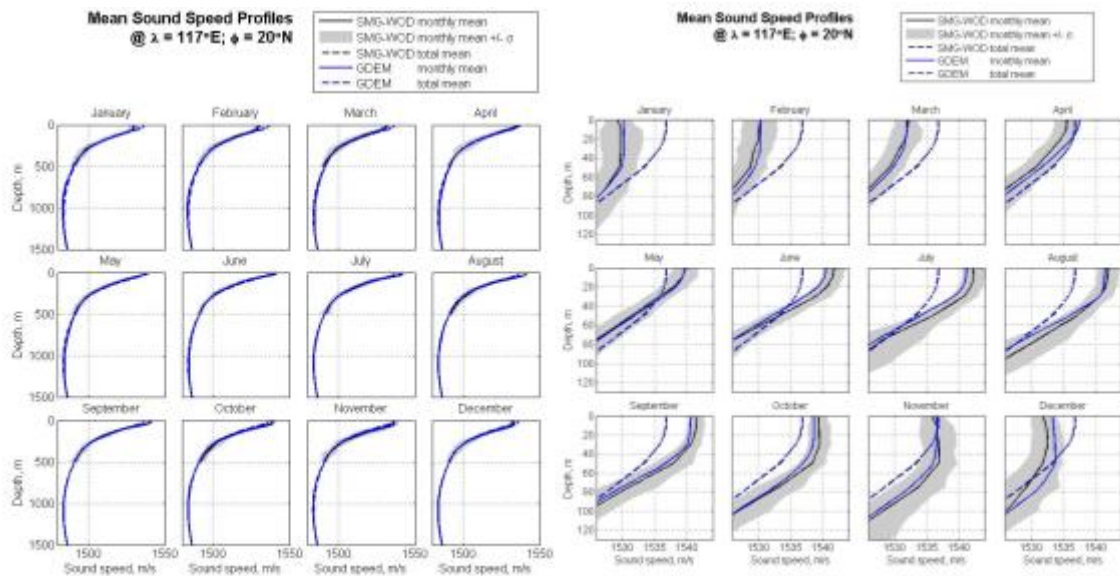


Figure 33. Mean Sound Speed Profiles (Point F).

## 7. Point G

At the surface, the intrusion from the North Equatorial Current through the Luzon strait current brings the warm and salty water to increase the sound speed. It is possible to see sound channel at a depth of 1000 meters and convergence zones along all seasons. The greatest variance between monthly mean and total mean exist in the upper layers, particularly from January through March. The greatest variance is about 3 m/s in January, February and March. In the dry season, there is more difference between monthly mean and total mean in the surface layer. The monthly and total means are plotted in Figure 34.

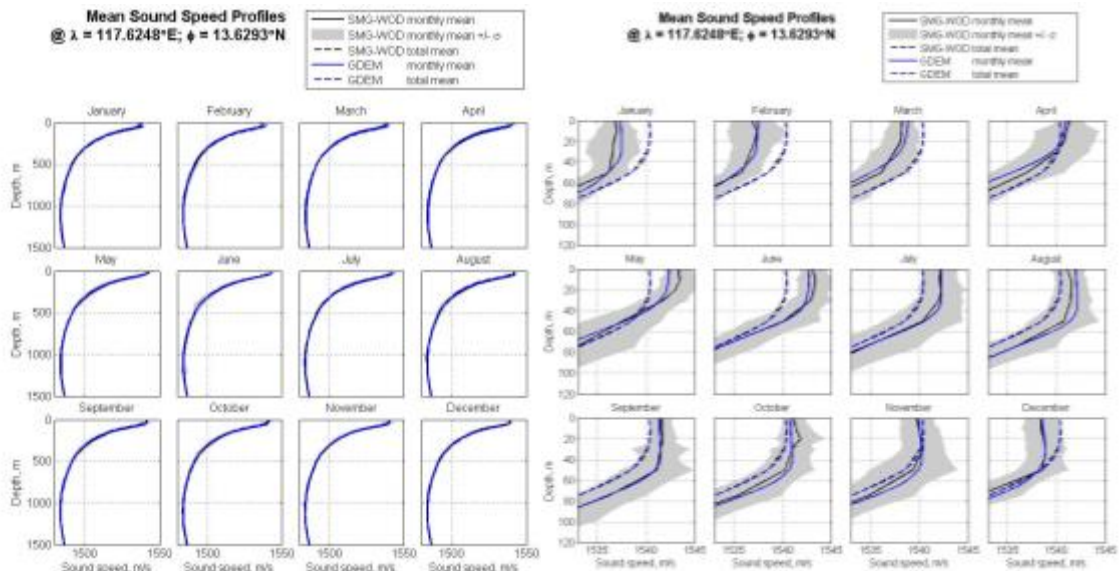


Figure 34. Mean Sound Speed Profiles (Point G).

## 8. Point H

At the surface, the intrusion from the North Equatorial Current through the Luzon strait current brings the warm and salty water to increase the sound speed. The greatest variance between monthly mean and total mean exist in the upper layers, particularly from January through March. The greatest variance is about 3 m/s in January, February and March. In the dry season, there is more difference between monthly mean and total mean in the surface layer. The depth at this point is very shallow and has obstructions from the bathymetric feature. The monthly and total means are plotted in Figure 35.

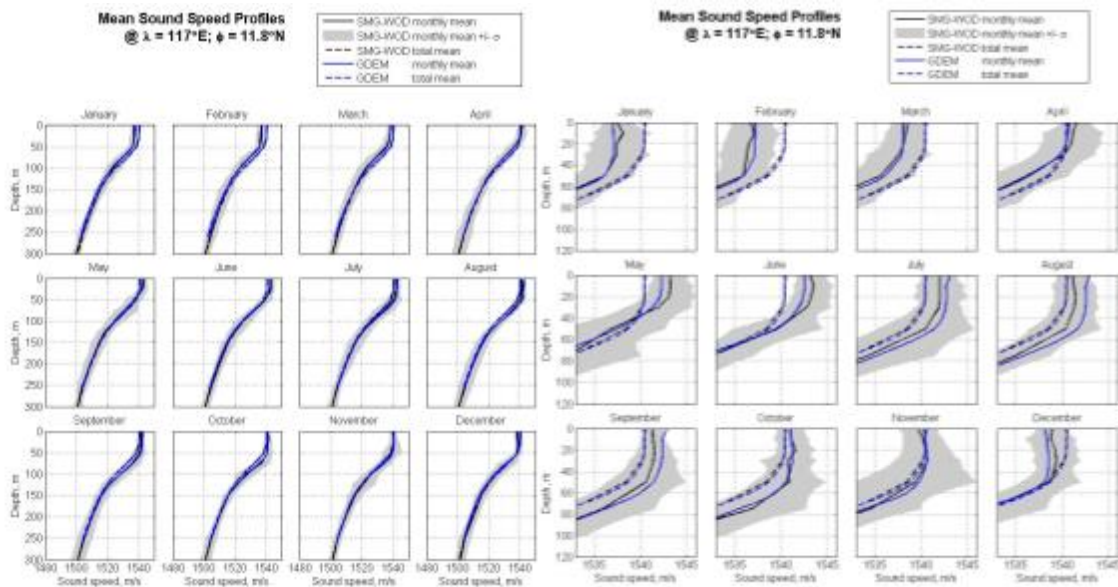


Figure 35. Mean Sound Speed Profiles (Point H).

During the dry season (December–May) the surface layer exhibit a lower monthly mean sound speed than the total mean sound speed due to lower temperatures at the surface layer to approximately 50 to 90 meters depth. Conversely, at rainy season (June–November) the surface layer exhibits a higher monthly mean sound speed than the total mean sound speed due to higher temperature at the surface layer to approximately 50 to 90 meters depth. Then, the sound speed continues to exhibit a negative gradient until the axis of the sound channel at approximately 1000 m depth where the minimum sound speed (1483 m/s) exists, except for the shallower point the minimum sound speed is

about 1500 m/s. Beneath the sound channel, layering about 900 to 1500 meters, the sound speed shows a weak positive gradient due to increase in pressure. SMG-WOD SSP monthly mean and GDEM monthly mean are in good agreement in surface layers and isothermal deep layers. Below the surface layers to a depth of 200 meters, SMG-WOD SSP monthly mean is about 1 m/s higher than GDEM monthly mean, this case possibly due to resolution difference between two datasets. The SMG-WOD standard deviation is small, which means that synoptical SSPs tend to be close to the mean.

Table 13 summarizes expected acoustic propagation types and months when maximum seasonal variations occur. It shows that maximum variance in the Philippine Sea and South China Sea occurs in January through March, and also June through August in the Luzon strait.

Table 13. Possible Propagation Types and Maximum Variations.

Location	Region	Depth (m)	Month	Possible Propagation Type	Maximum Variation
A	Philippine Sea	9.079	All season	Sound Channel (900 meters)	January - March
			January - March	Weak Surface Duct (50 meters)	
B	Philippine Sea	6.608	All season	Sound Channel (1000 meters)	January - March
C	Philippine Sea	4.361	All season	Sound Channel (1000 meters)	January - March
			December - January	Weak Surface Duct (50 meters)	
D	Philippine Sea	5.314	All season	Sound Channel (1100 meters)	January - March
			January - February	Weak Surface Duct (50 meters)	
E	Luzon Strait	1.321	All season	Sound Channel (1100 meters)	January - March June - August
F	South China Sea	1.464	All season	Sound Channel (1000 meters)	January - March
G	South China Sea	4.045	All season	Sound Channel (1000 meters)	January - March
			December	Weak Surface Duct (25 meters)	
H	South China Sea	50	December-February	Weak Surface Duct (50 meters)	January - March

## E. MEAN DECADAL TEMPERATURE AND SALINITY

The potential temperature ( $\Theta$ ) and salinity ( $S$ ) diagrams were plotted for January and July as the two characteristic months of the dry and rainy seasons for each point so we can see the decadal seasonal variability in 1960–2014 time periods by using the SMG-WOD data. Figures 36–51 show potential temperature-salinity diagrams with isopycnals and lines of equal spiciness, which are orthogonal to the isolines of equal potential density.

### 1. Point A

Figure 36 shows the oscillation of the thermocline from the highest spiciness in 1960–1969 time period consecutively going lower to 1970–1979, 1980–1989 to the lowest in 1990–1999 and then increasing again from 2000–2009 to 2010–2014 time period. The January dry season shows higher salinity but with a lower temperature.

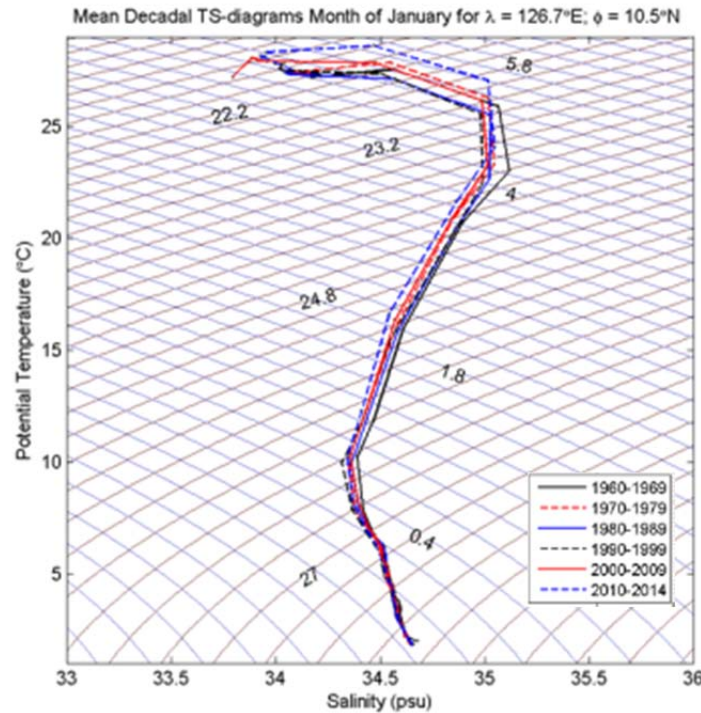


Figure 36. SMG-WOD January Mean Decadal T-S Diagram (Point A).

Figure 37 shows the oscillation of the thermocline from the lowest spiciness in 1960–1969 time period consecutively going higher to 1970–1979 to the high spiciness in 1980–1989 and then decrease to 1990–1999 and then increase again from 2000–2009 to the highest in 2010–2014 time period. The July rainy season shows higher temperature but with a lower salinity.

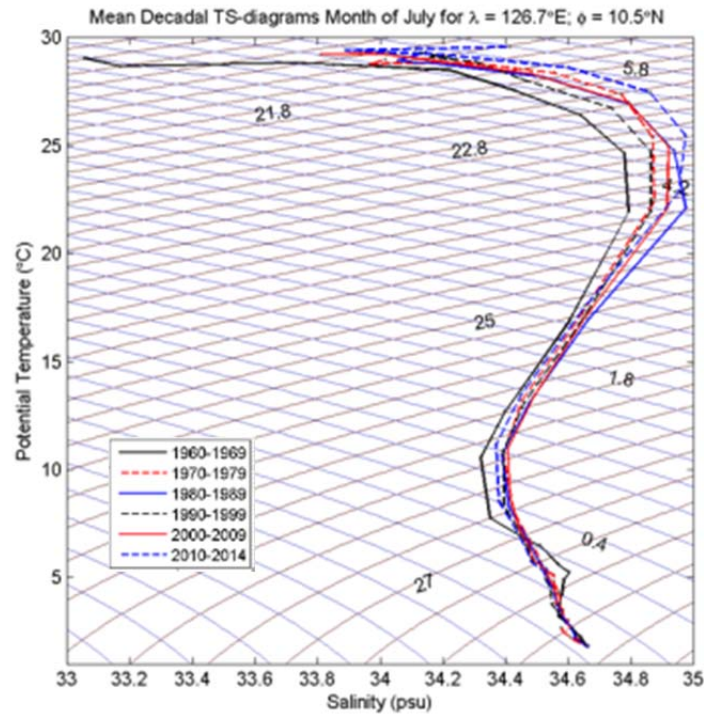


Figure 37. SMG-WOD July Mean Decadal T-S Diagram (Point A).



## 2. Point B

Figure 38 shows the oscillation of the thermocline from the highest spiciness in 1960–1969 time period consecutively going lower to 1970–1979, 1980–1989 to the lowest in 1990–1999 and then increasing again from 2000–2009 to 2010–2014 time period. The January dry season shows higher salinity but with a lower temperature.

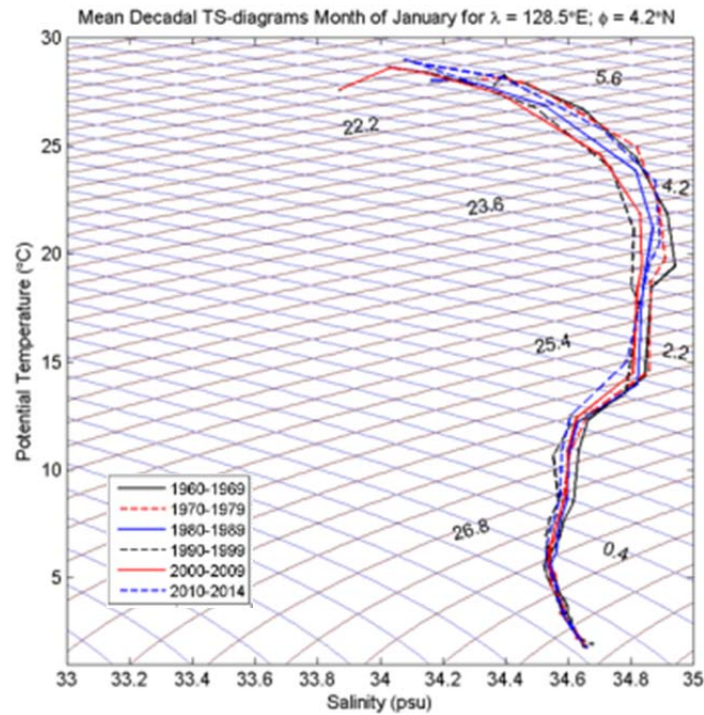


Figure 38. SMG-WOD January Mean Decadal T-S Diagram (Point B).



Figure 39 shows the oscillation of the thermocline from the lowest spiciness in 1960–1969 time period consecutively going higher to 1970–1979 to the high spiciness in 1980–1989 and then decrease to 1990–1999 and then increase again from 2000–2009 to the highest in 2010–2014 time period. The July rainy season shows higher temperature but with a lower salinity.

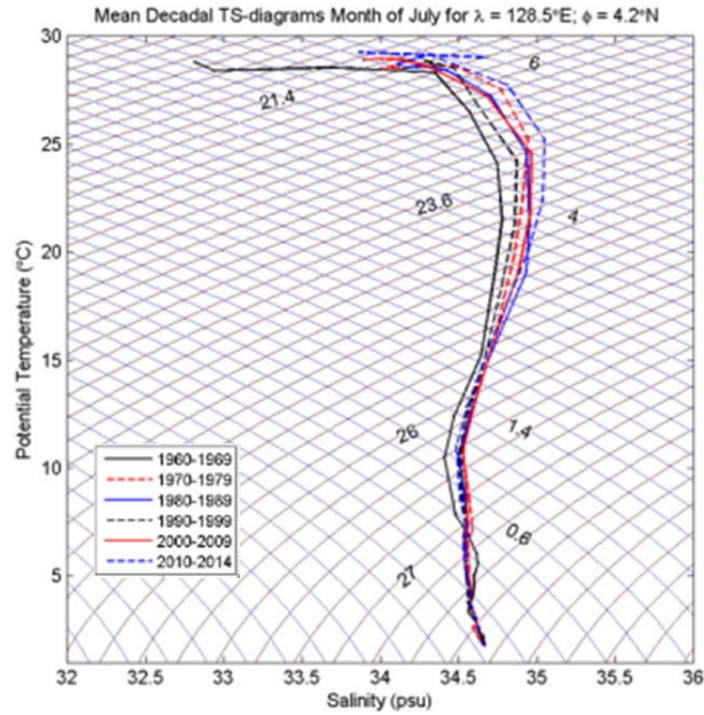


Figure 39. SMG-WOD July Mean Decadal T-S Diagram (Point B).

### 3. Point C

Figure 40 shows the oscillation of the thermocline from the highest spiciness in 1960-1969 time period going lower to 1970-1979, increasing in 1980-1989, decreasing again in 1990-1999 consecutively decreasing in 2000-2009 to the lowest in 2010-2014 time period. The January dry season shows higher salinity but with a lower temperature.

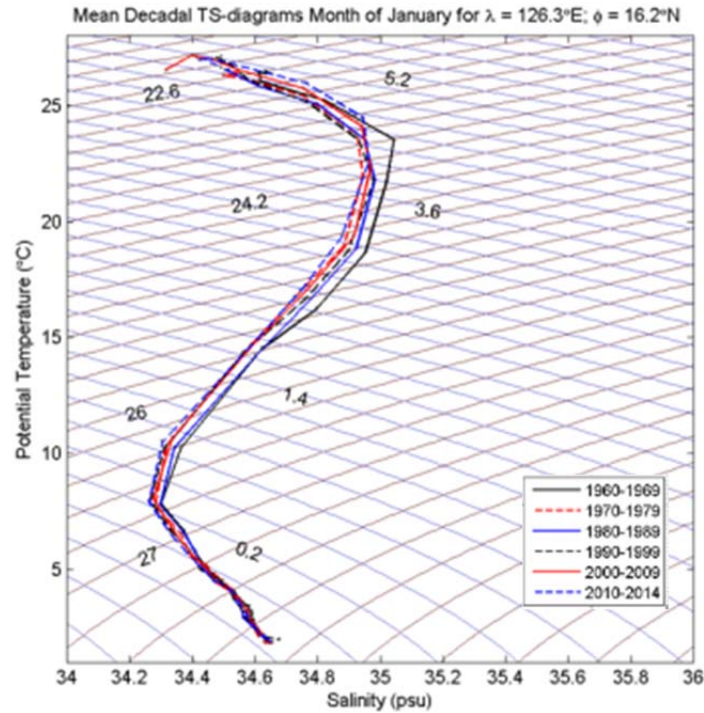


Figure 40. SMG-WOD January Mean Decadal T-S Diagram (Point C).

Figure 41 shows the oscillation of the thermocline from the lowest spiciness in 1960–1969 time period consecutively going higher to 1970–1979 to the high spiciness in 1980–1989 and then decrease to 1990–1999 and then increase again from 2000–2009 to the highest in 2010–2014 time period. The July rainy season shows higher temperature but with a lower salinity.

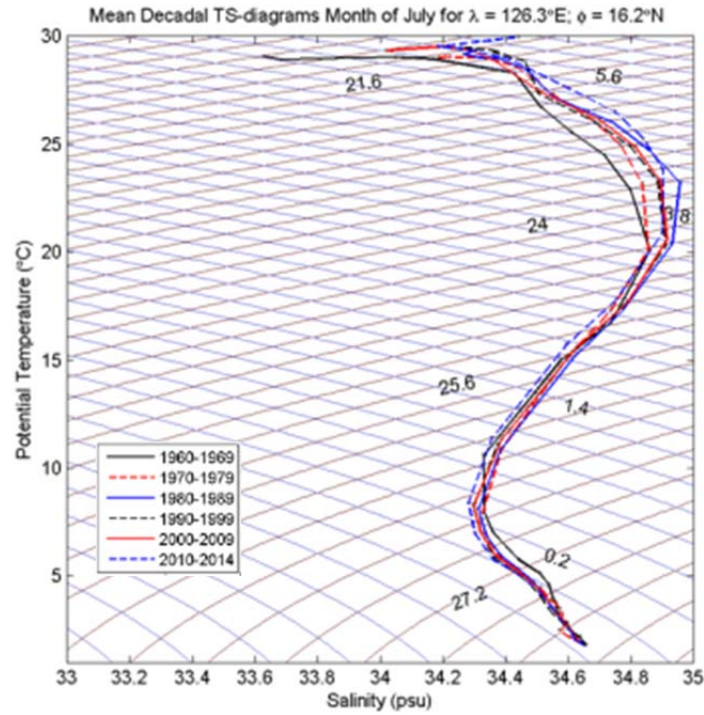


Figure 41. SMG-WOD July Mean Decadal T-S Diagram (Point C).

#### 4. Point D

Figure 42 shows the oscillation of the thermocline from the highest spiciness in 1960–1969 time period going lower to 1970–1979, increasing in 1980–1989, decreasing again in 1990–1999 consecutively decreasing in 2000–2009 to the lowest in 2010–2014 time period. The January dry season shows higher salinity but with a lower temperature.

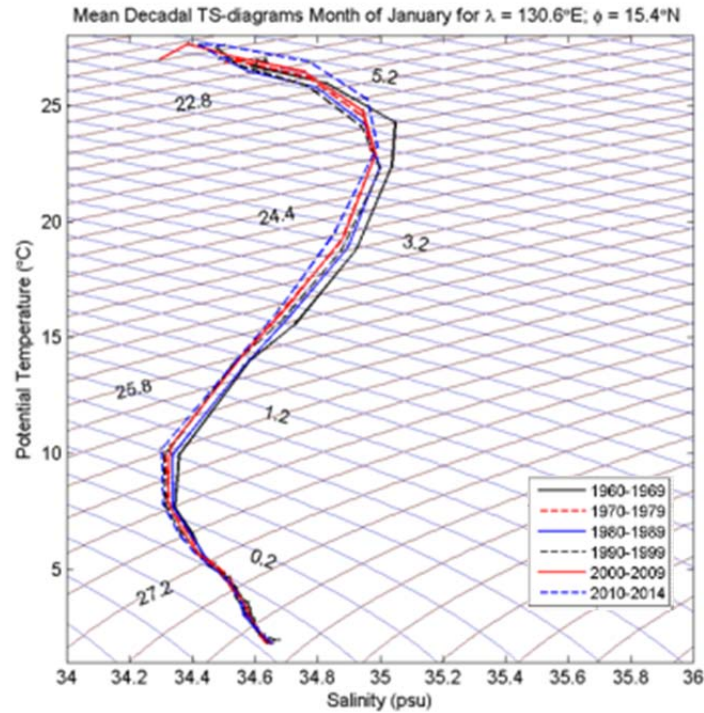


Figure 42. SMG-WOD January Mean Decadal T-S Diagram (Point D).

Figure 43 shows the oscillation of the thermocline from the lowest spiciness in 1960–1969 time period consecutively going higher to 1970–1979 to the high spiciness in 1980–1989 and then decrease to 1990–1999 and then increase again from 2000–2009 to the highest in 2010–2014 time period. The July rainy season shows higher temperature but with a lower salinity.

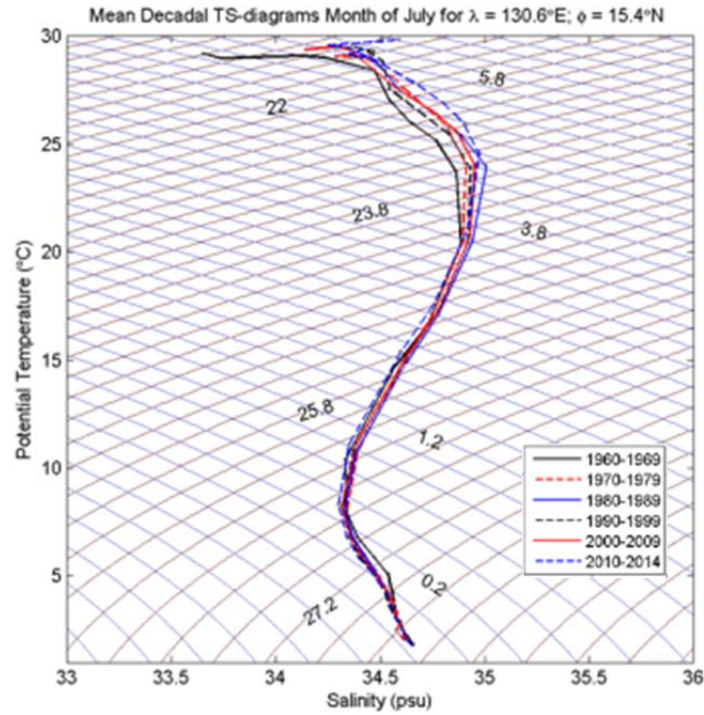


Figure 43. SMG-WOD July Mean Decadal T-S Diagram (Point D).



## 5. Point E

Figure 44 shows the oscillation of the thermocline from the highest spiciness in 1960–1969 time period going lower to 1970–1979, increasing in 1980–1989, decreasing again in 1990–1999 consecutively decreasing in 2000–2009 to the lowest in 2010–2014 time period. The January dry season shows higher salinity but with a lower temperature.

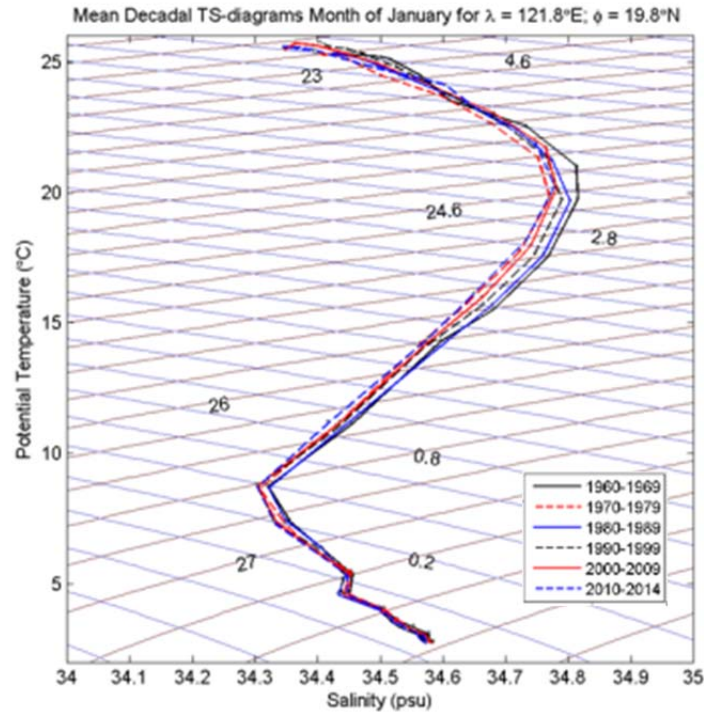


Figure 44. SMG-WOD January Mean Decadal T-S Diagram (Point E).

Figure 45 shows the oscillation of the thermocline from the lowest spiciness in 1960–1969 time period consecutively going higher to 1970–1979 to the highest spiciness in 1980–1989 and then decrease to 1990–1999 and consecutively decreasing in 2000–2009 and 2010–2014 time period. The July rainy season shows higher temperature but with a lower salinity.

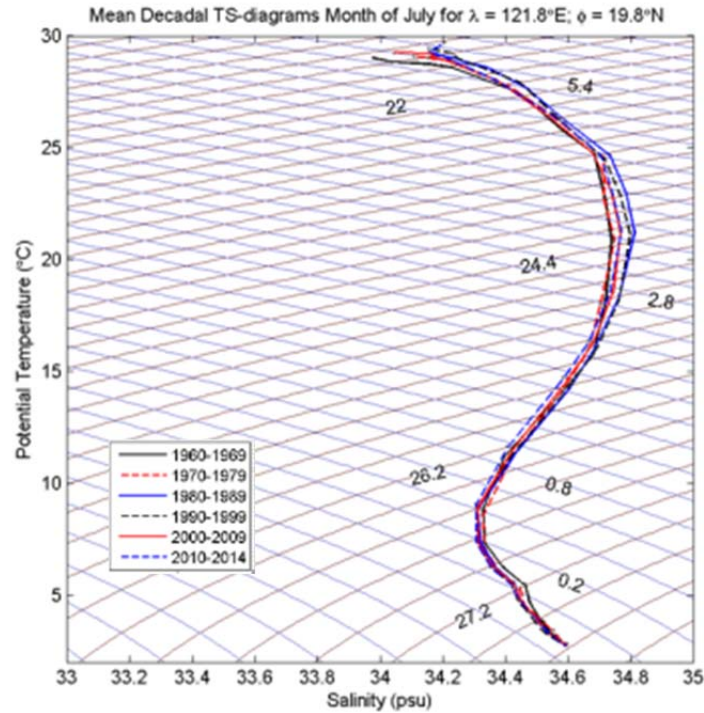


Figure 45. SMG-WOD July Mean Decadal T-S Diagram (Point E).

## 6. Point F

Figure 46 shows the oscillation of the thermocline from the highest spiciness in 1960–1969 time period going lower in 1970–1979 and 1980–1989 as the lowest, and then increasing in 1990–1999, then decreasing again in 2000–2009 but increasing again in 2010–2014 time period. The January dry season shows slightly higher salinity but with a lower temperature.

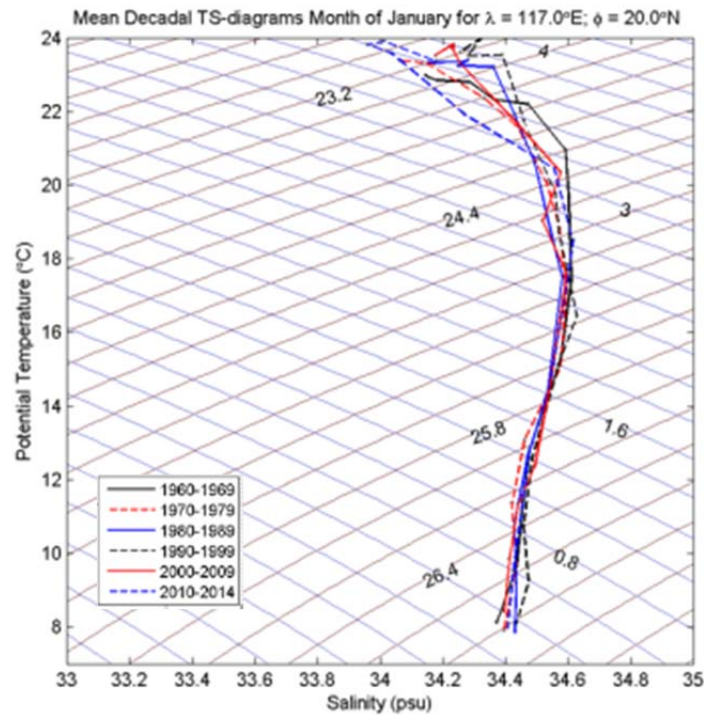


Figure 46. SMG-WOD January Mean Decadal T-S Diagram (Point F).



Figure 47 shows the oscillation of the thermocline from the lowest spiciness in 1960–1969 time period consecutively going higher from 1970–1979 to 1990–1999 and then decrease in 2000–2009, then increasing again to the highest in 2010–2014 time period. The July rainy season shows higher temperature but with slightly lower salinity.

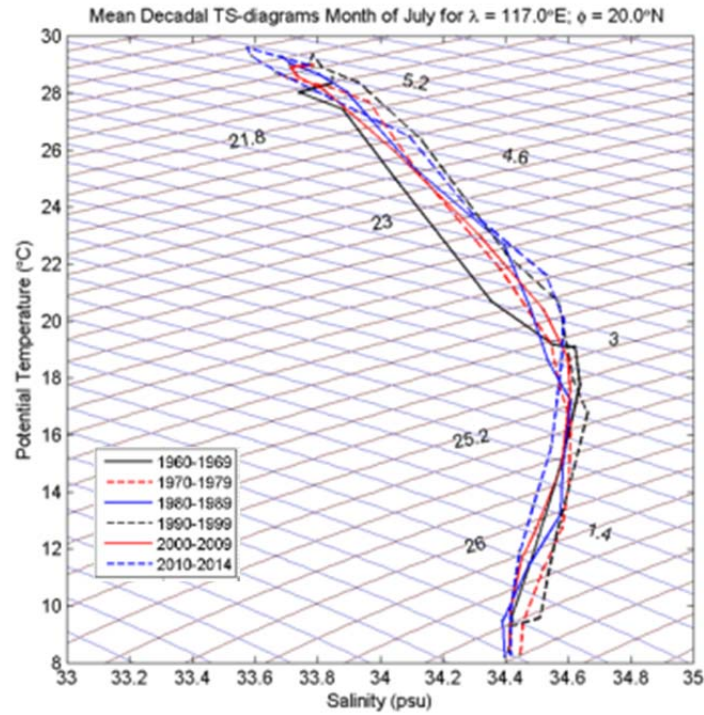


Figure 47. SMG-WOD July Mean Decadal T-S Diagram (Point F).

## 7. Point G

Figure 48 shows the oscillation of the thermocline from 1960–1969 time period going higher in 1970–1979 and then going lower in 1980–1989 to the lowest spiciness, and then going higher again in 1990–1999 to the highest spiciness, in 2000–2009 the spiciness going lower, and going higher again in 2010–2014. The January dry season shows slightly higher salinity but with a lower temperature.

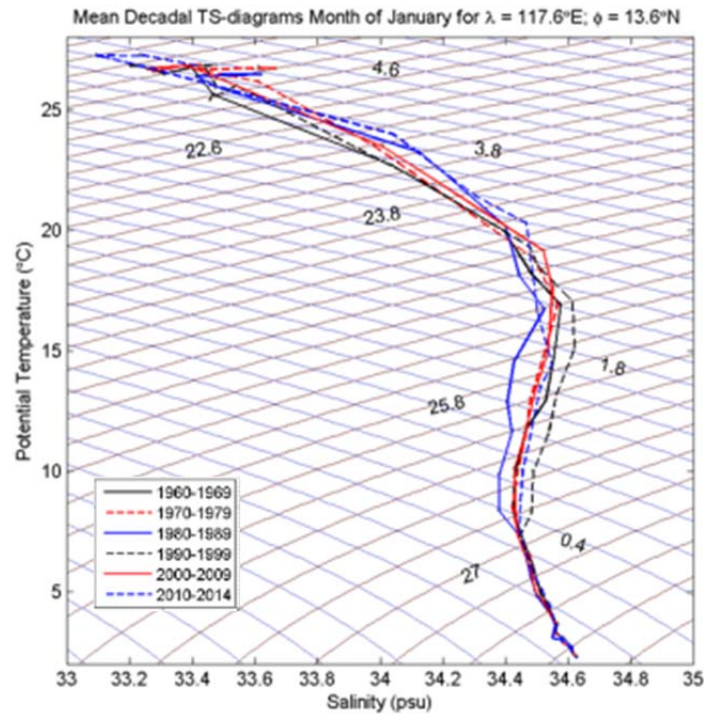


Figure 48. SMG-WOD January Mean Decadal T-S Diagram (Point G).

Figure 49 shows the oscillation of the thermocline from 1960–1969 time period, going lower in 1970–1979, then going higher in 1980–1989 to the highest spiciness, and then going lower consecutively in 1990–1999, 2000–2009 and 2010–2014 to the lowest spiciness. The July rainy season shows higher temperature but with slightly lower salinity.

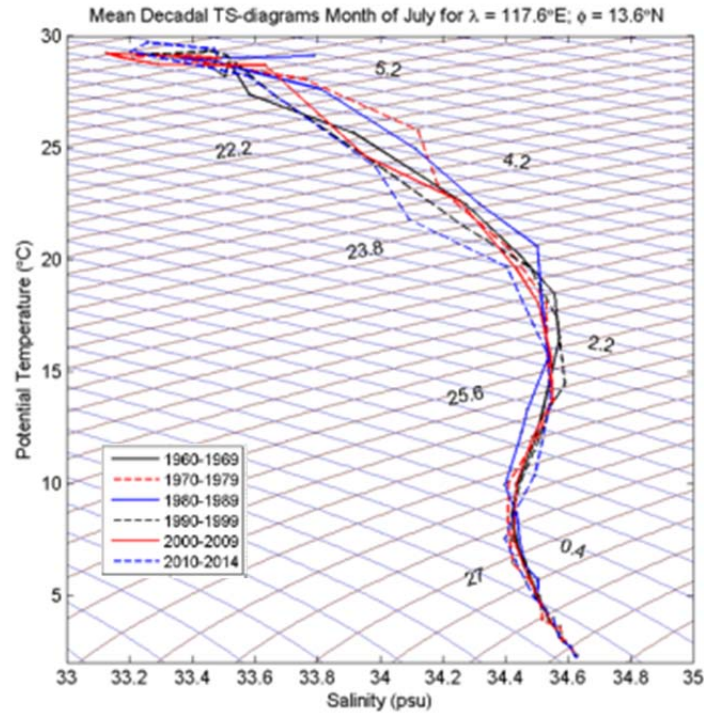


Figure 49. SMG-WOD July Mean Decadal T-S Diagram (Point G).

## 8. Point H

Figure 50 shows the oscillation of the thermocline from the lowest in 1960–1969 time period, going higher in 1970–1979, and then going lower in 1980–1989, and then going higher again in 1990–1999, going back lower in 2000–2009, then in 2010–2014 going to the highest spiciness. The January dry season shows slightly higher salinity but with a lower temperature.

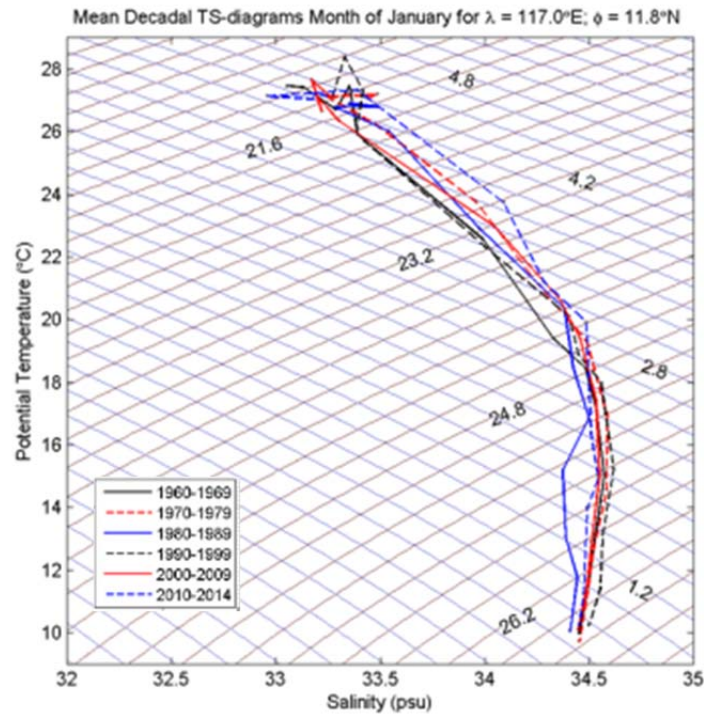


Figure 50. SMG-WOD January Mean Decadal T-S Diagram (Point H).

Figure 51 shows the oscillation of the thermocline from 1960–1969 time period going to the highest spiciness in 1970–1979, and then going lower in 1980–1989 and 1990–1999, then going higher in 2000–2009, then going back lower in 2010–2014 to the lowest spiciness. The July rainy season shows higher temperature but with slightly lower salinity.

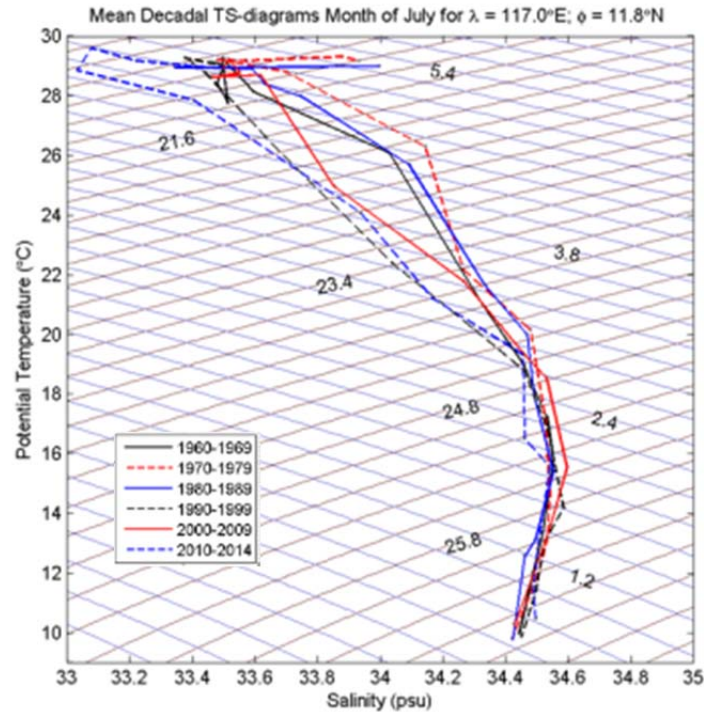


Figure 51. SMG-WOD July Mean Decadal T-S Diagram (Point H).

From the figures above, we know that the main fluctuations of temperature and salinity mainly occurred between 1970 and 2009. The spiciness is higher and the fluctuations are more regular in the Philippine Sea (point A, B, C, D and E) than in the South China Sea (point F, G and H). This can be explained by Spiciness NPTW circulating with the western Pacific Boundary current.

## **F. MEAN TRANSMISSION LOSS-GDEM**

Transmission loss has been modeled using the BELLHOP model for a 3500 Hz sound source located at 40 m and 101 evenly distributed receiver depths, along a path for maximum propagation range of 70 nm, the sound source is directed one way to 90°, except in point D to 270°, and in point H to 200° which are directed inward the research area, using GDEM monthly mean sound speed profiles. To be able to see how sound propagates in the Philippine Sea and South China Sea, this modelling will provide information on where objects can be detected. Figures 52–59 show transmission loss for January and July as the two characteristic months of the dry and rainy season to see the sound propagation difference at points A–H. For complete 12 months of GDEM mean transmission loss in each point see appendix D.

### **1. Transmission Loss Point A**

There is a surface duct formed approximately at 80 m depth in January due to a lower sea surface temperature in the dry season.

In January, sound rays propagate downward to 9000 m depth, and it creates convergence zone at the surface at approximately 65 km range and submarines can be detected at the long distances where convergence path occurs. Also, there is surface duct path near the surface and TL is about 70–85 dB, making a long range detection of a submarine possible at the surface. Between 8 km and 65 km range, it is hard to detect submarines due to very large shadow zone.

In July, sound rays propagate downward to 9000 m depth, and it creates convergence zone at the surface at approximately 65 km range. Also, there is no surface duct path found near the surface. Likewise in January in between 8 km and 65 km range is hard to detect submarines due to very large shadow zone. Point A provides high possibility to detect the submarines at long distances.



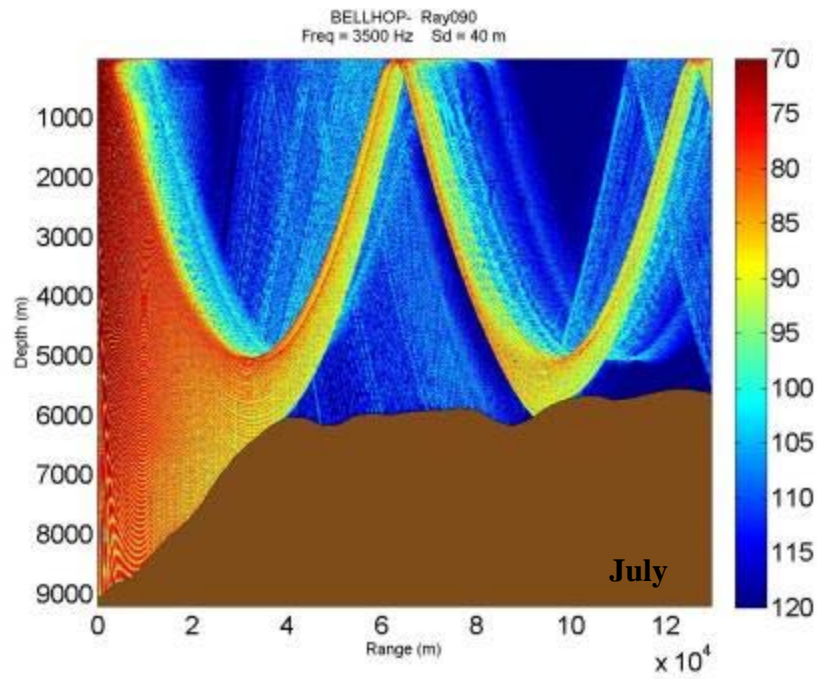
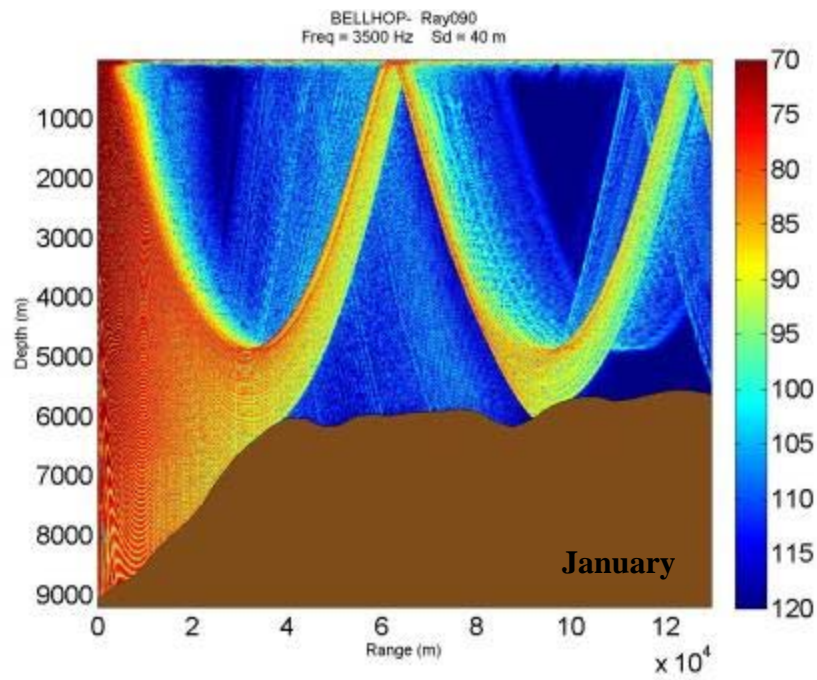


Figure 52. TL Point A.

## **2. Transmission Loss Point B**

There is no evidence that a surface duct formed in January and July. In January, sound rays propagate downward to 6000 m depth, and it creates convergence zone at the surface at approximately 60 km range and submarines can be detected at the long distances where convergence path occurs. Between 6 km and 60 km range, it is hard to detect submarines due to very large shadow zone.

In July, sound rays propagate downward to 6000 m depth, and it creates convergence zone at the surface at approximately 60 km range. Also, there is no surface duct path found near the surface. Between 6 km and 60 km range, it is hard to detect submarines due to very large shadow zone. In July, there is less TL in the ray path. Point B provides high possibility to detect the submarines at long distances.



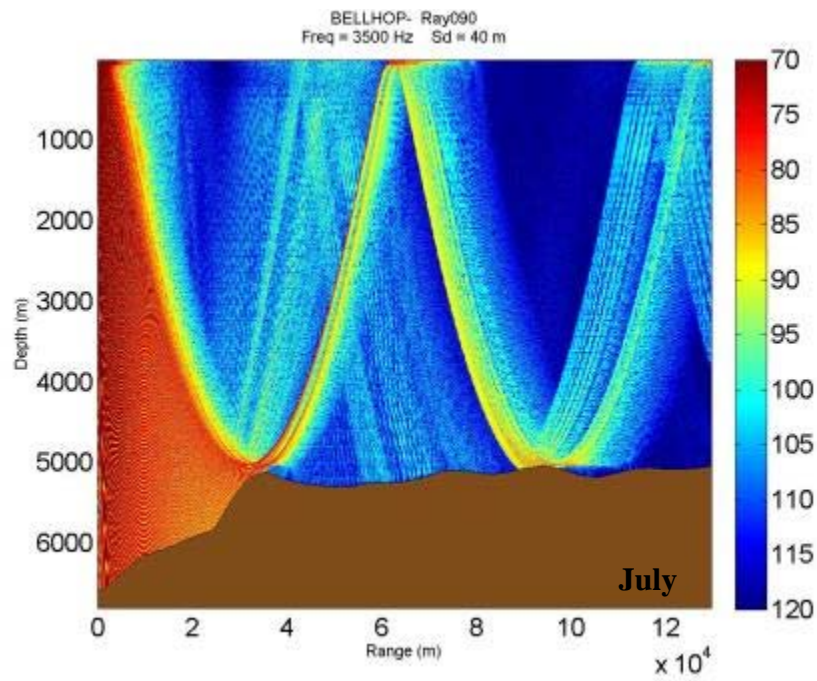
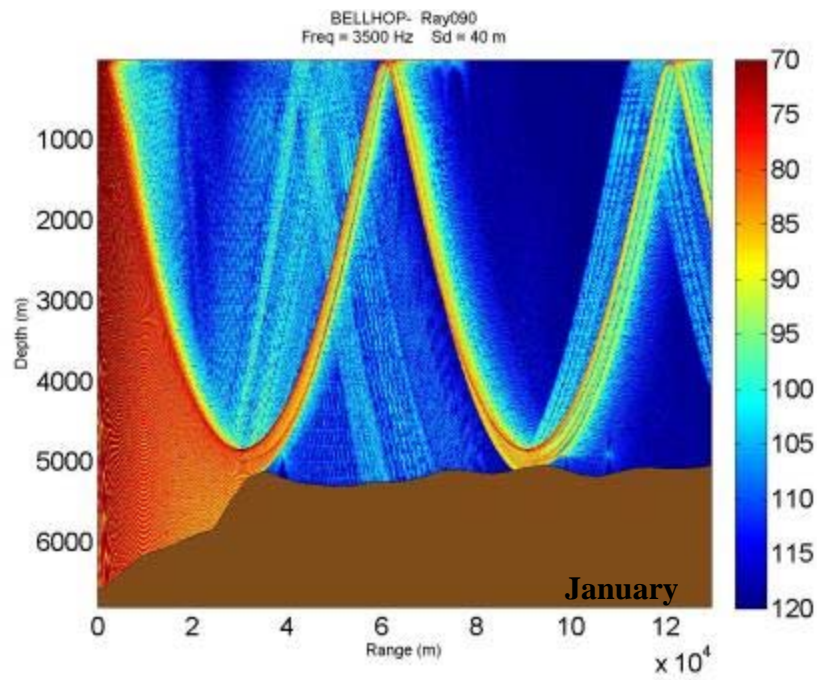


Figure 53. TL Point B.

### **3. Transmission Loss Point C**

A surface duct formed approximately at 90 m depth in January due to a lower sea surface temperature in the dry season. In January, sound rays propagate downward to 4000 m depth, and it creates convergence zone at the surface at approximately 55 km range and submarines can be detected at the long distances where convergence path occurs. Also, there is surface duct path near the surface and TL is about 70–85 dB, making a long range detection of a submarine possible at the surface. Between 8 km and 55 km range, it is hard to detect submarines due to very large shadow zone.

In July, sound rays propagate downward to 4000 m depth, and it creates convergence zone at the surface at approximately 55 km range. Also, there is no surface duct path found near the surface. Between 8 km and 55 km range, it is hard to detect submarines due to very large shadow zone. In July, more TL in the ray path. Point C provides high possibility to detect the submarines at long distances.

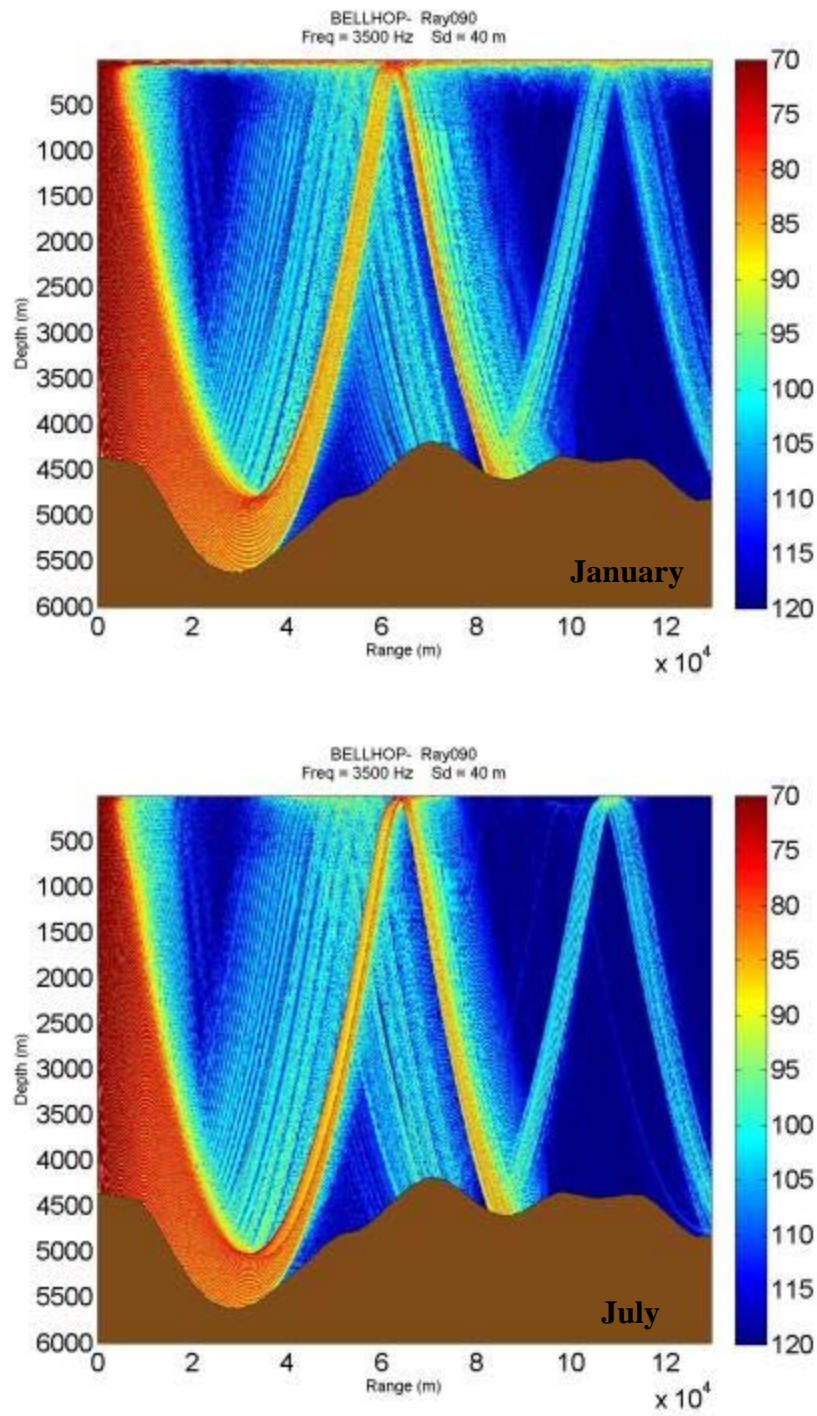


Figure 54. TL Point C.

#### **4. Transmission Loss Point D**

A surface duct formed approximately at 90 m depth in January due to a lower sea surface temperature in the dry season. In January, sound rays propagate downward to 5000 m depth, and creates convergence zone at the surface at approximately 65 km range then submarines can be detected at the long distances where convergence path occurs. Also, there is surface duct path near the surface and TL is about 60–75 dB, making a long range detection of a submarine possible at the surface. Between 10 km and 65 km range, it is hard to detect submarines due to very large shadow zone.

In July, sound rays propagate downward to 5000 m depth, and it creates convergence zone at the surface at approximately 65 km range. Also, there is no surface duct path found near the surface. Between 10 km and 65 km range, it is hard to detect submarines due to very large shadow zone. At point D, less TL in the shadow zone making it more possible to find a target, and also point D provides high possibility to detect submarines at long distances.

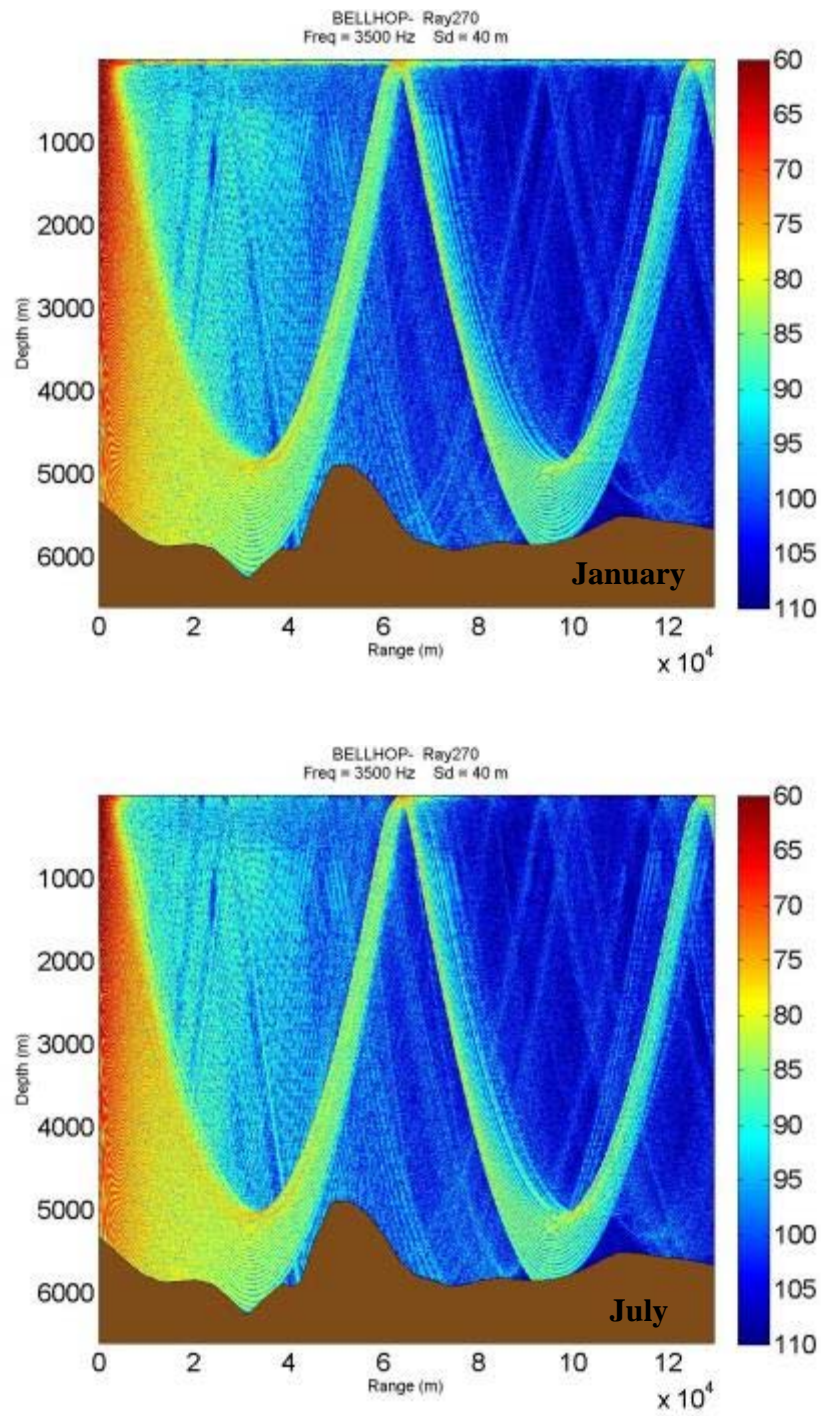


Figure 55. TL Point D.

## **5. Transmission Loss Point E**

In January, sound rays propagate downward to 1500 m depth, some refracted upward due to higher sound speed, and some bounced upward from the bottom. No convergence zones and surface ducts formed, and no shadow zone formed making it possible for detecting a target in a long range approximately to 40 km of range.

In July, sound rays propagate downward to 1500 m depth, some refracted upward due to higher sound speed, and some bounced upward from the bottom. No convergence zones and surface ducts formed, likewise in January no shadow zone formed making it possible for detecting target in a long range approximately to 40 km of range, less TL occurs in July.

The results correspond less with convergence zone expectations from mean sound speed profiles because of the seafloor shape. Point E provides high possibility to detect the submarines at long distances.



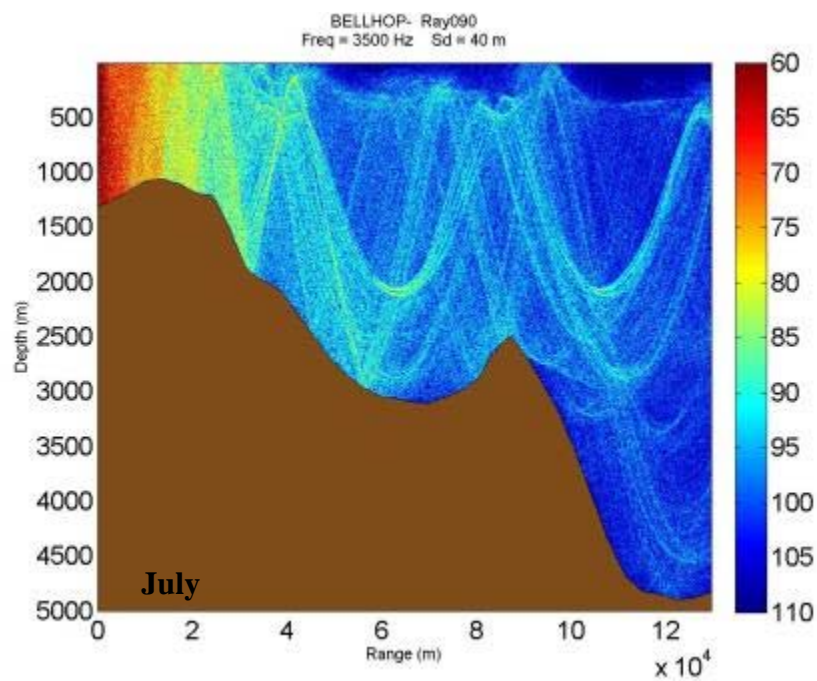
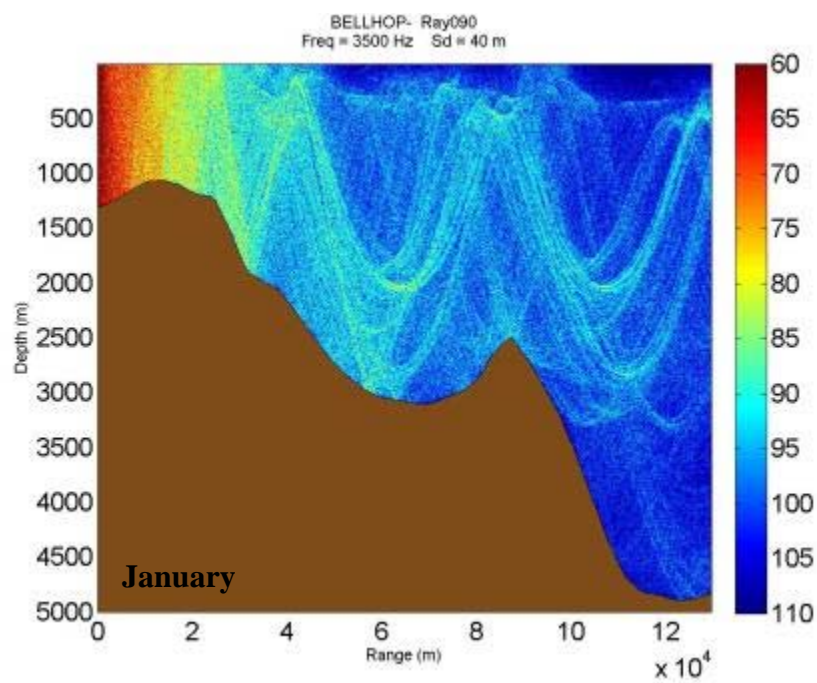


Figure 56. TL Point E.

## **6. Transmission Loss Point F**

In January, sound rays propagate downward to 1500 m depth, some refracted upward due to higher sound speed, and some bounced upward from the bottom. No convergence zones and surface ducts formed, and no shadow zone formed making it possible for detecting a target in a long range approximately to 60 km of range.

In July, sound rays propagate downward to 1500 m depth, some refracted upward due to higher sound speed, and some bounced upward from the bottom. No convergence zones and surface duct formed, likewise in January no shadow zone formed making it possible for detecting target in a long range approximately to 60 km of range, less TL occurs in July.

The results correspond less with convergence zone expectations from mean sound speed profiles because of the seafloor shape. Point F provides high possibility to detect the submarines at long distances.



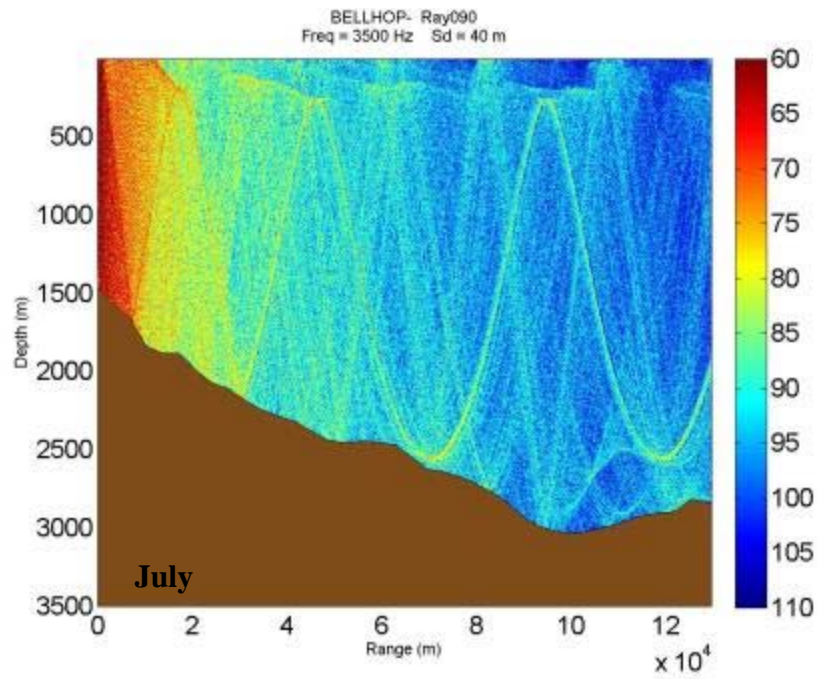
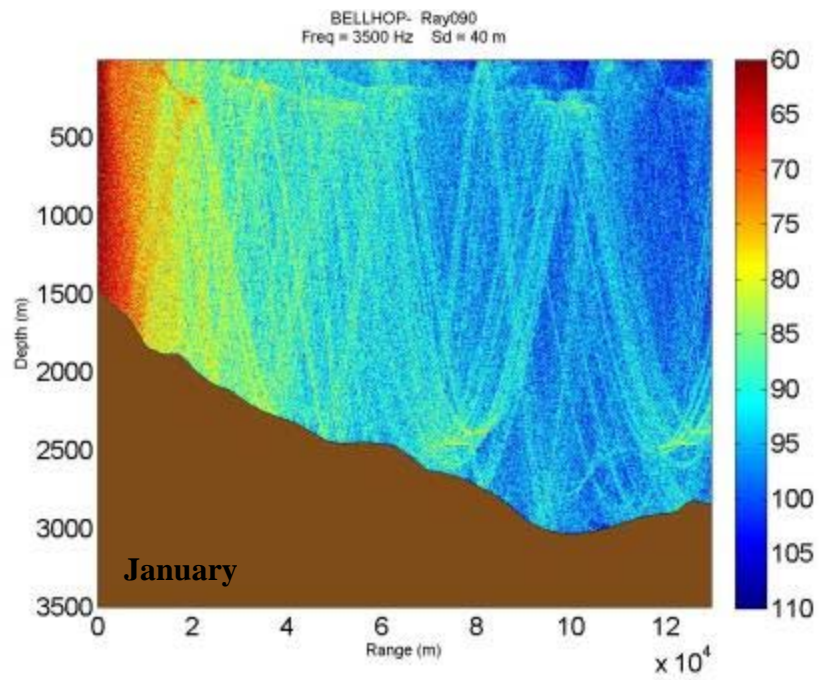


Figure 57. TL Point F.

## **7. Transmission Loss Point G**

In January, sound rays propagate downward to 4000 m depth, and it creates convergence zone at the surface at approximately 40 km range and submarines can be detected at the long distances where convergence path occurs. Between 8 km and 40 km range, it is hard to detect submarines due to large shadow zone. After 60 km of range, there is a very high TL.

In July, sound rays propagate downward to 4000 m depth, and it creates convergence zone at the surface at approximately 40 km range and submarines can be detected at the long distances where convergence path occurs. Between 8 km and 40 km range, it is hard to detect submarines due to large shadow zone. After 60 km of range, there is a very high TL yet less than in January.

The results correspond less with convergence zone expectations from mean sound speed profiles. Point G provides low possibility to detect the submarines at long distances.

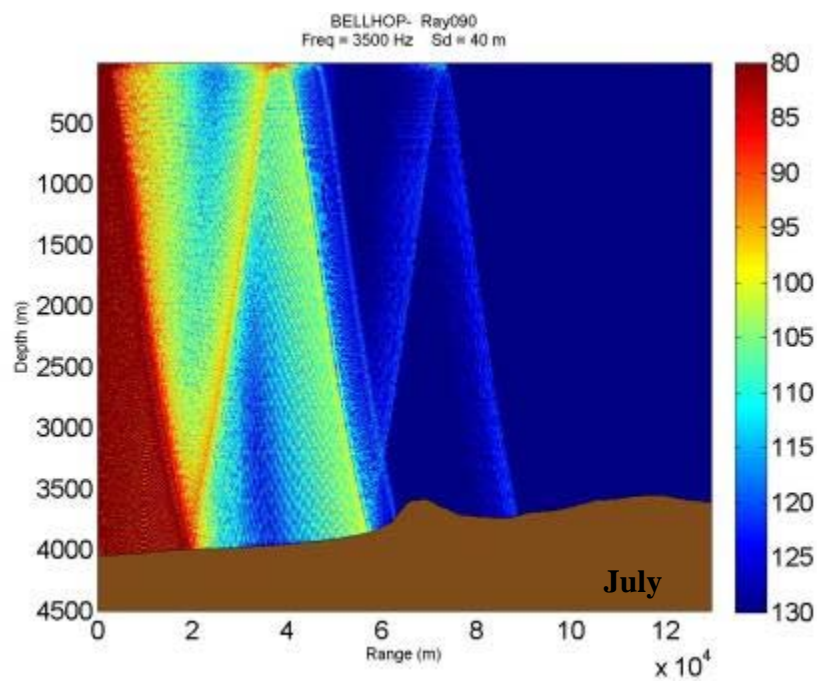
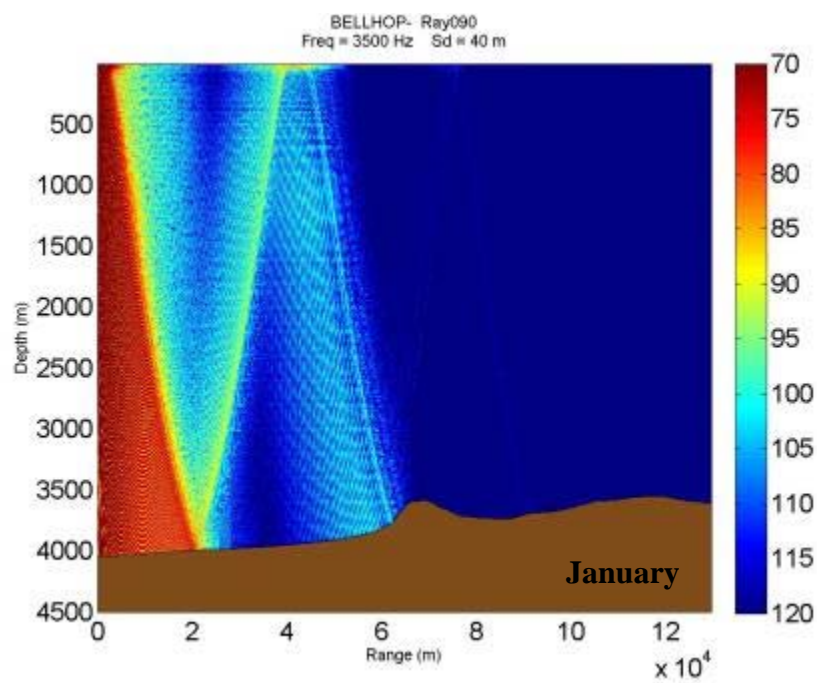


Figure 58. TL Point G.

## **8. Transmission Loss Point H**

In January, sound rays propagate downward to 50 m depth and refracted from the bottom. No convergence zones or shadow zones formed making it possible for detecting target in a long range approximately to 60 km of range. A weak surface duct at 10 meters depth due to a lower sea surface temperature exists in the dry season.

In July, sound rays propagate downward to 50 m depth and refracted from the bottom. Likewise in January no convergence zones, surface ducts or shadow zone formed making it possible for detecting target in a long range approximately to 60 km of range.

The results correspond less with convergence zone expectations from mean sound speed profiles because of the seafloor shape. Point H provides low possibility to detect the submarines at long distances.

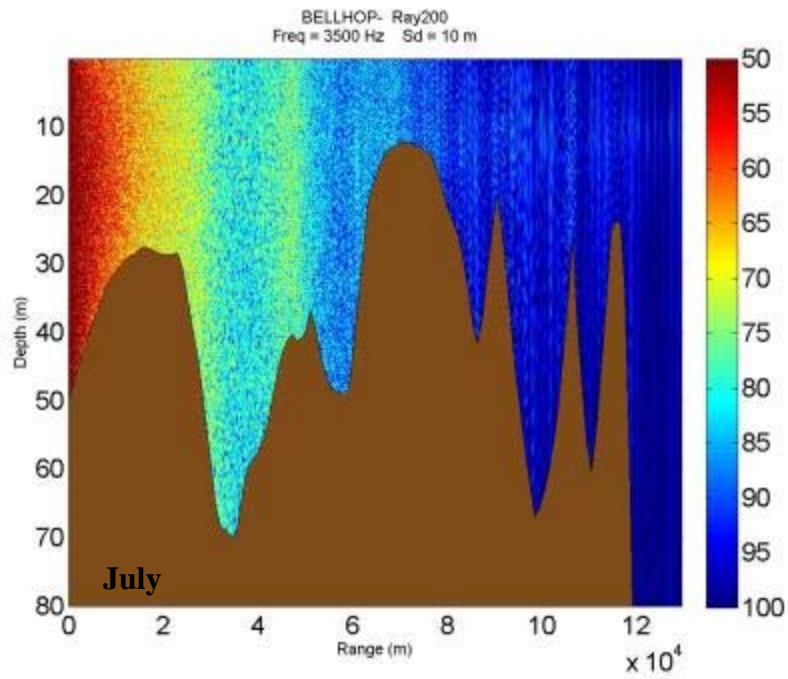
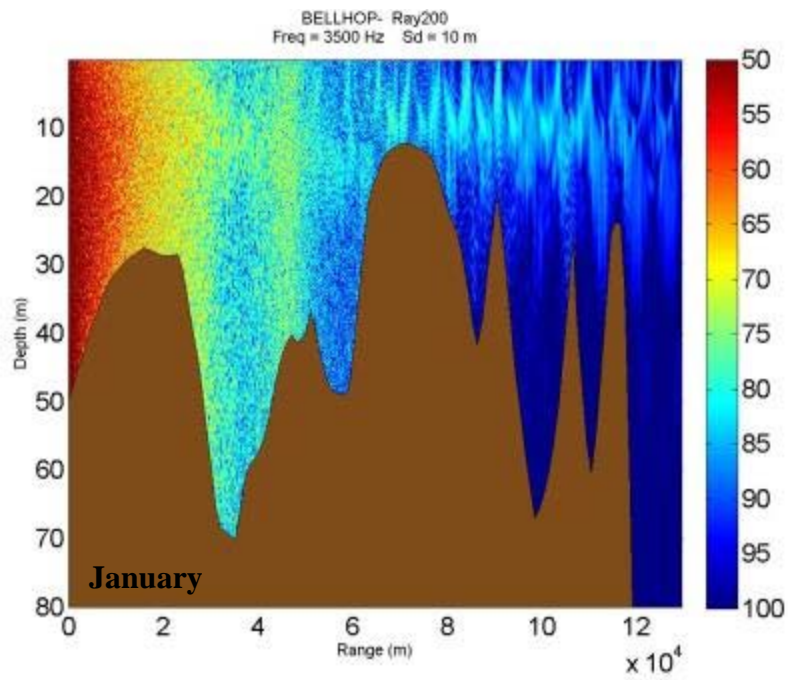


Figure 59. TL Point H.

## **G. GDEM AND SMG-WOD COMPARISON**

Differences in transmission loss were analyzed when the sound speed propagation is modeled using GDEM and SMG-WOD. The figures below show the TL profiles for two datasets, the left column for GDEM and the right column for SMG-WOD, the upper row for January and the lower row for July.

### **1. Point A**

At the point A location in January (Figure 60, upper panels), the sound propagation patterns were similar to each other. The SMG-WOD (right) exhibited a stronger surface duct propagation than the GDEM (left) along the ray path to more than 100 km of range after the convergence zone. The range of convergence zone is in agreement for about 60 km of range. However, there was a slight difference between their TLs in the shadow zones. The GDEM reflects a slightly lower TL in the shadow zones.

In July (Figure 60, lower panels), sound propagation patterns were similar to each other. The range of convergence zone is in agreement for about 60 km of range. Lower TL is modeled with SMG-WOD in shadow zones. A higher attenuation is found in GDEM deep layer. Both the datasets produced similar propagation ranges in January and July.



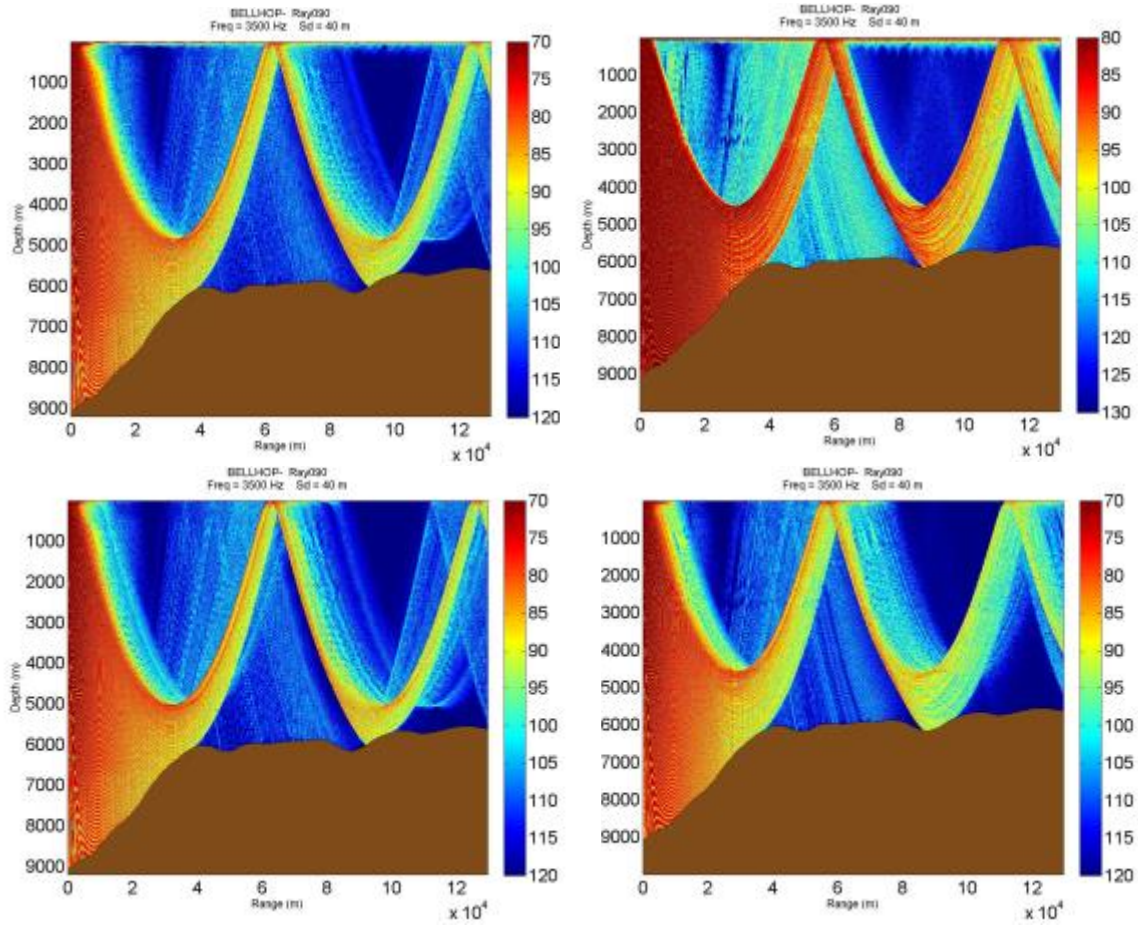


Figure 60. Point A January (upper) and July (lower).

## 2. Point B

At the point B location in January (Figure 61, upper panels), the sound propagation patterns were similar to each other. The SMG-WOD (right) have less TL in the deep layer. The range of convergence zone is in agreement for about 60 km of range. The GDEM reflects a slightly lower TL in the shadow zones, yet at the ray path the SMG-WOD have a lower TL.

In July (Figure 61, lower panels), sound propagation patterns were similar to each other. The range of convergence zone is in agreement for about 60 km of range. Lower TL is modeled with SMG-WOD in shadow zones. A higher attenuation is found in GDEM deep layer. Both the datasets produced similar propagation ranges in January and July.

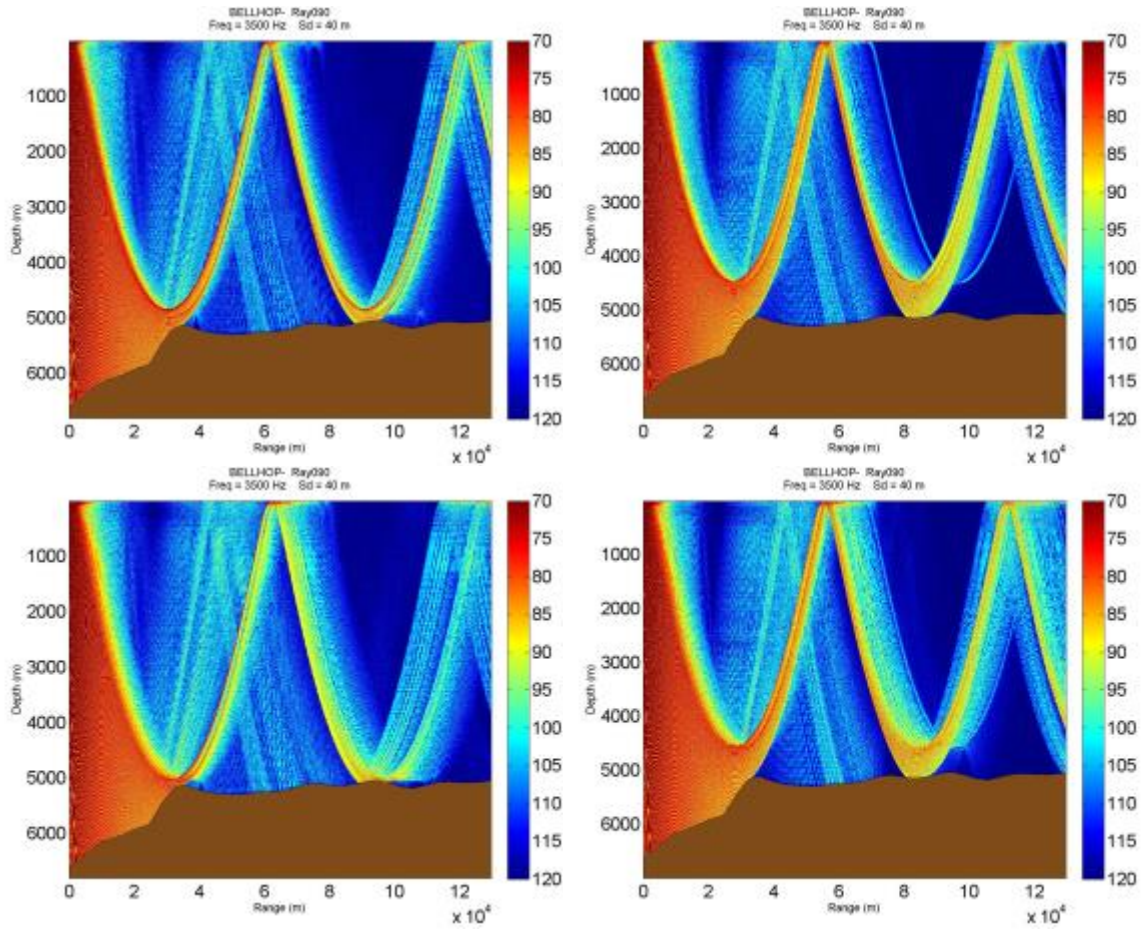


Figure 61. Point B January (upper) and July (lower).

### 3. Point C

At the point C location in January (Figure 62, upper panels), a similar pattern exists. The GDEM (left) exhibit a stronger surface duct propagation than the SMG WOD (right) along the ray path to more than 100 km of range after the convergence zone. Convergence zone is in agreement for about 60 km of range, but the SMG-WOD showed a stronger convergence zone after 60 km. The SMG-WOD reflects a lower TL in the shadow zones. In July (Figure 62, lower panels), a similar pattern is present. Convergence zone is in agreement for about 60 km of range. Lower TL is modeled with SMG-WOD in shadow zones, and a stronger convergence zone is found in the SMG-WOD model. Both the datasets produced similar propagation ranges in January and July, with less TL in the SMG-WOD model.



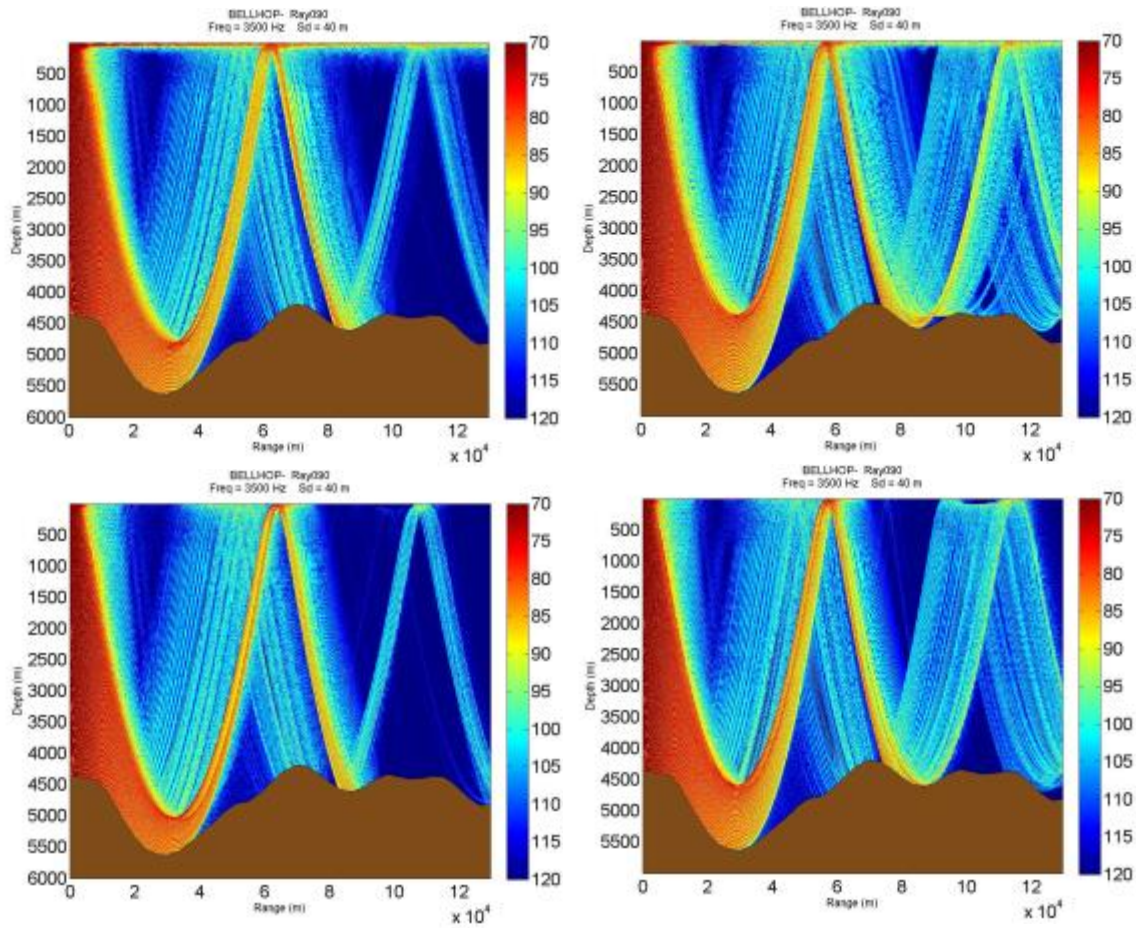


Figure 62. Point C January (upper) and July (lower).

#### 4. Point D

At the point D location in January (Figure 63, upper panels), a similar pattern exists. The SMG-WOD (right) and GDEM (left) exhibited a similar surface duct propagation. The range of convergence zone is in agreement for about 65 km of range, but the GDEM model will give a longer second convergence zone than the SMG-WOD for about 10 km of range. The GDEM reflects a slightly lower TL in the shadow zones. In July (Figure 63, lower panels), a similar pattern exists. The range of convergence zone is in agreement for about 65 km of range, but the GDEM model will give a longer second convergence zone than the SMG-WOD for about 10 km of range. Slightly lower TL is modeled with GDEM in shadow zones, and a higher attenuation is found in GDEM deep

layer. Both the datasets produced similar propagation ranges in January and July, but have a different following convergence zone range.

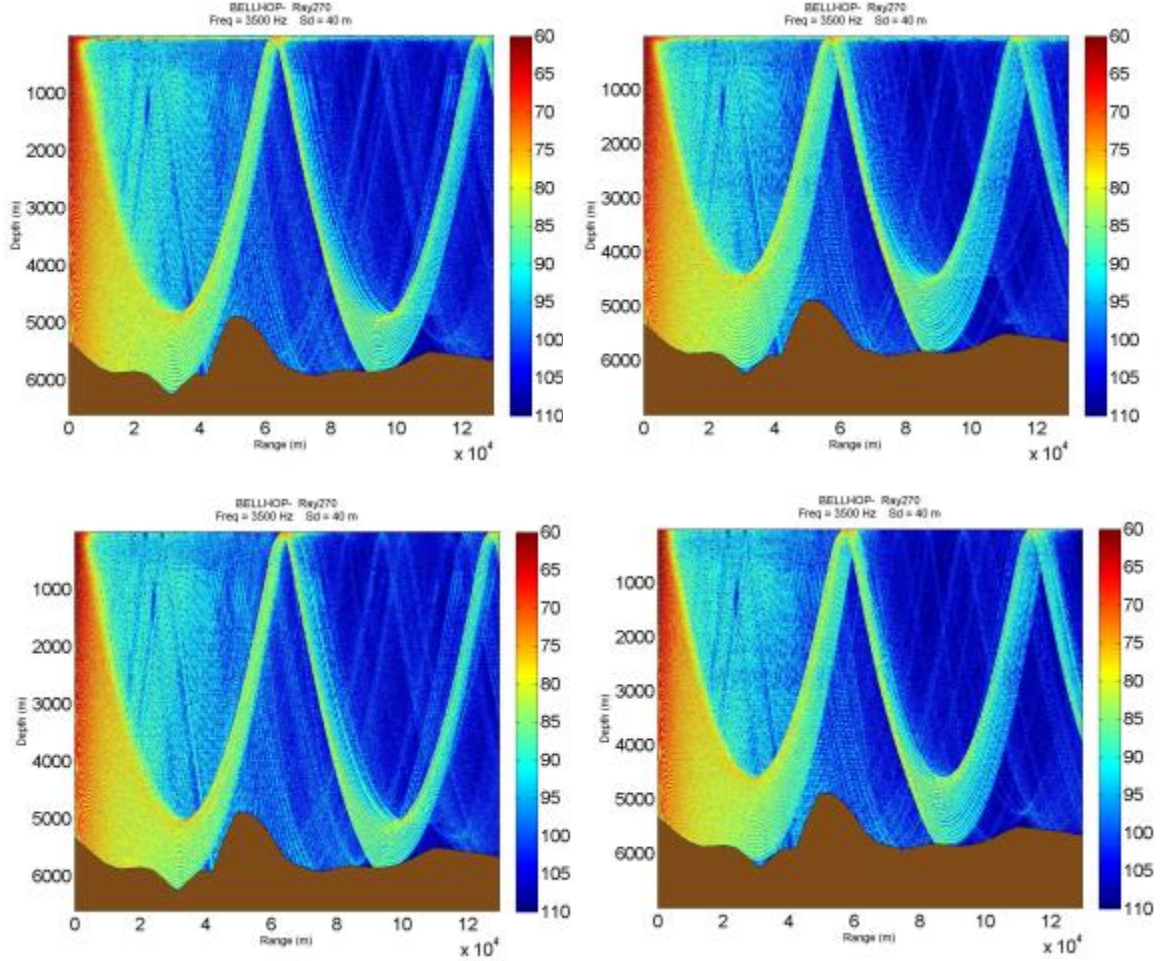


Figure 63. Point D January (upper) and July (lower).

## 5. Point E

At the point E location in January (Figure 64, upper panels), the sound propagation patterns were similar to each other with no surface duct, convergence zone, and a weak shadow zone. The propagation is more affected by the bottom bounce. The SMG-WOD reflects a slightly lower TL in the shadow zones.

In July (Figure 64, lower panels), sound propagation patterns were similar to each other but the SMG-WOD shows a stronger sound propagation or less TL than the

GDEM. A higher attenuation is found in GDEM deep layer. Both the datasets produced similar propagation ranges in January and July, but a SMG-WOD shows a stronger sound propagation.

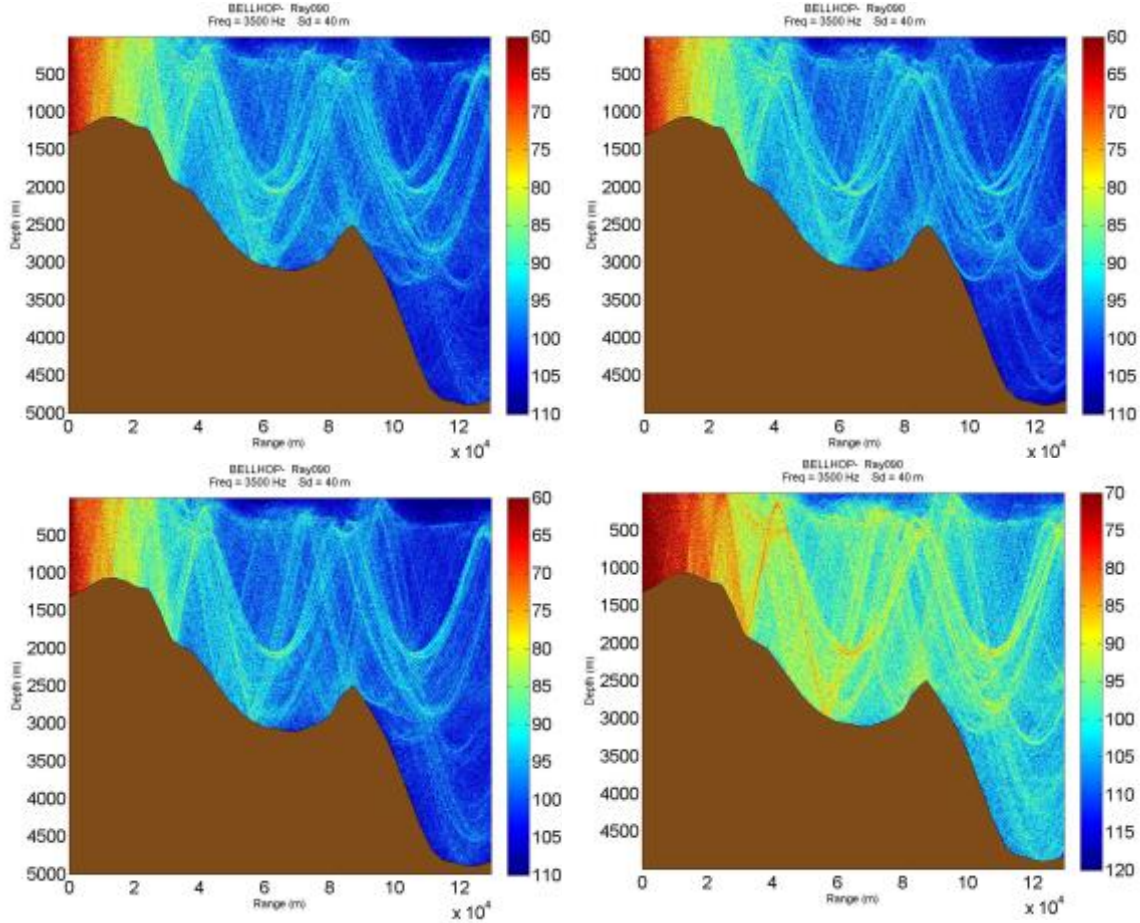


Figure 64. Point E January (upper) and July (lower).

## 6. Point F

At the point F location in January (Figure 65, upper panels), the sound propagation patterns were similar to each other with no surface duct, convergence zone, and a weak shadow zone. The propagation is more affected by the bottom bounce. The GDEM shows a lower TL in the shadow zones.

In July (Figure 65, lower panels), sound propagation patterns were similar to each other but the GDEM shows a stronger sound propagation or less TL than the GDEM.



Both the datasets produced similar propagation ranges in January and July, but GDEM shows a stronger sound propagation and more scattering along the ray path, which will enhance the detection of a target.

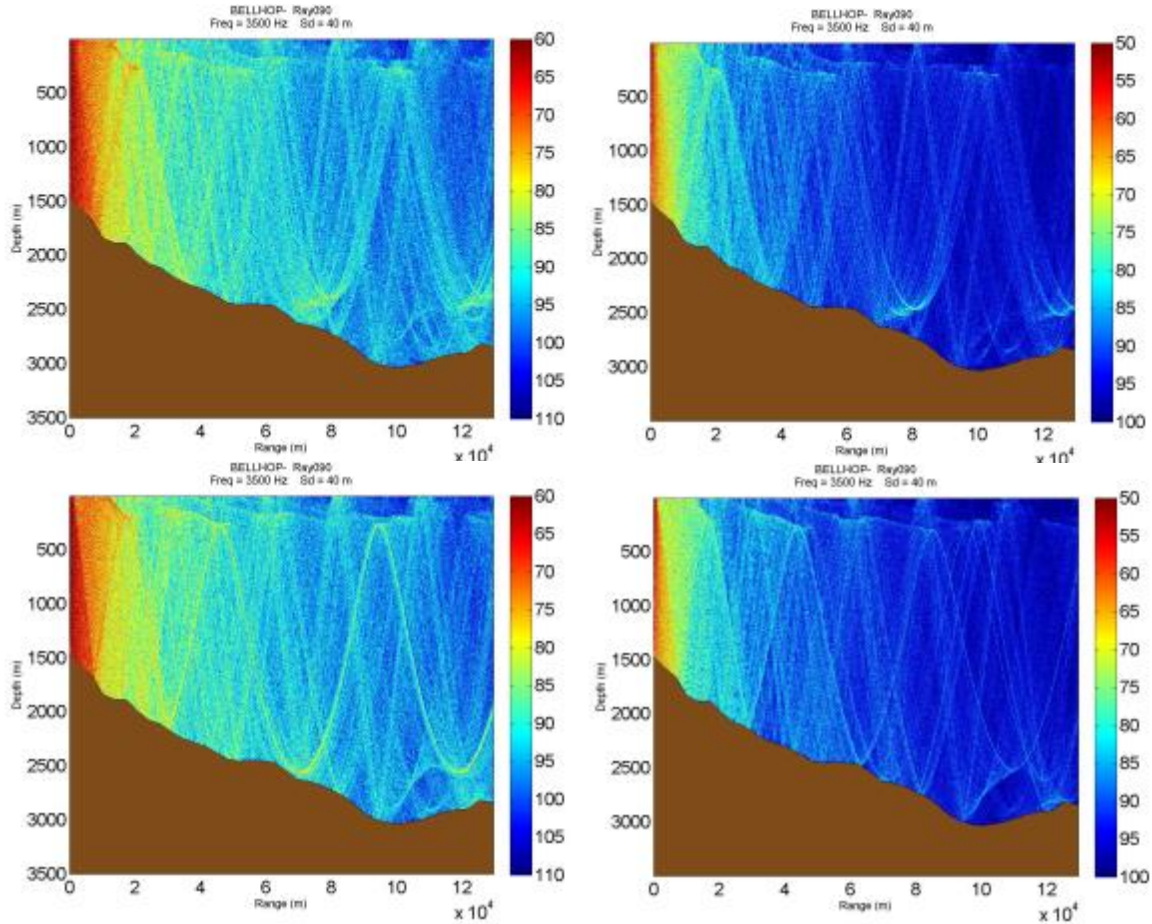


Figure 65. Point F January (upper) and July (lower).

## 7. Point G

At the point G location in January (Figure 66, upper panels), the sound propagation patterns were similar to each other. The range of convergence zone is in agreement for about 40 km of range, and after the convergence zone there is a large TL that makes the sound propagation is approximately limited to 60 km of range. The GDEM reflects a slightly lower TL in the shadow zones.

In July (Figure 66, lower panels), sound propagation patterns were similar to each other. The range of convergence zone is in agreement for about 40 km of range, and after the convergence zone there is a large TL that makes the sound propagation is approximately limited to 80 km of range. The GDEM reflects a lower TL. Both the datasets produced similar propagation pattern, with less TL in July.

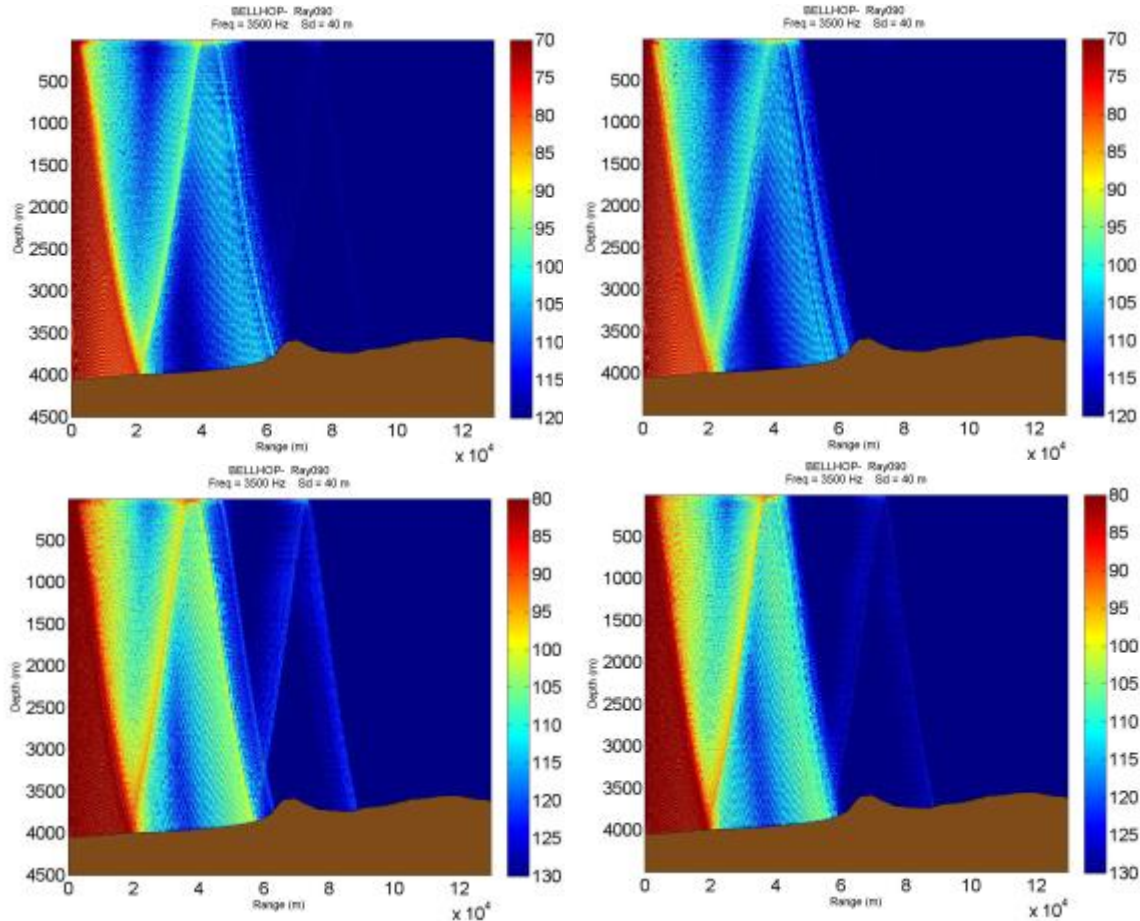


Figure 66. Point G January (upper) and July (lower).

## 8. Point H

At the point H location in January (Figure 67, upper panels), the sound propagation patterns were similar to each other with no convergence zone, and shadow zone. The propagation is more affected by the bottom bounce. The GDEM shows a lower TL, and a weak surface duct that propagate through a long distance.

In July (Figure 67, lower panels), sound propagation patterns were similar to each other but the SMG-WOD shows less TL, and a weak surface duct that propagate through a long distance. Both the datasets produced a different propagation ranges in January and July, but GDEM shows a stronger sound propagation with less TL.

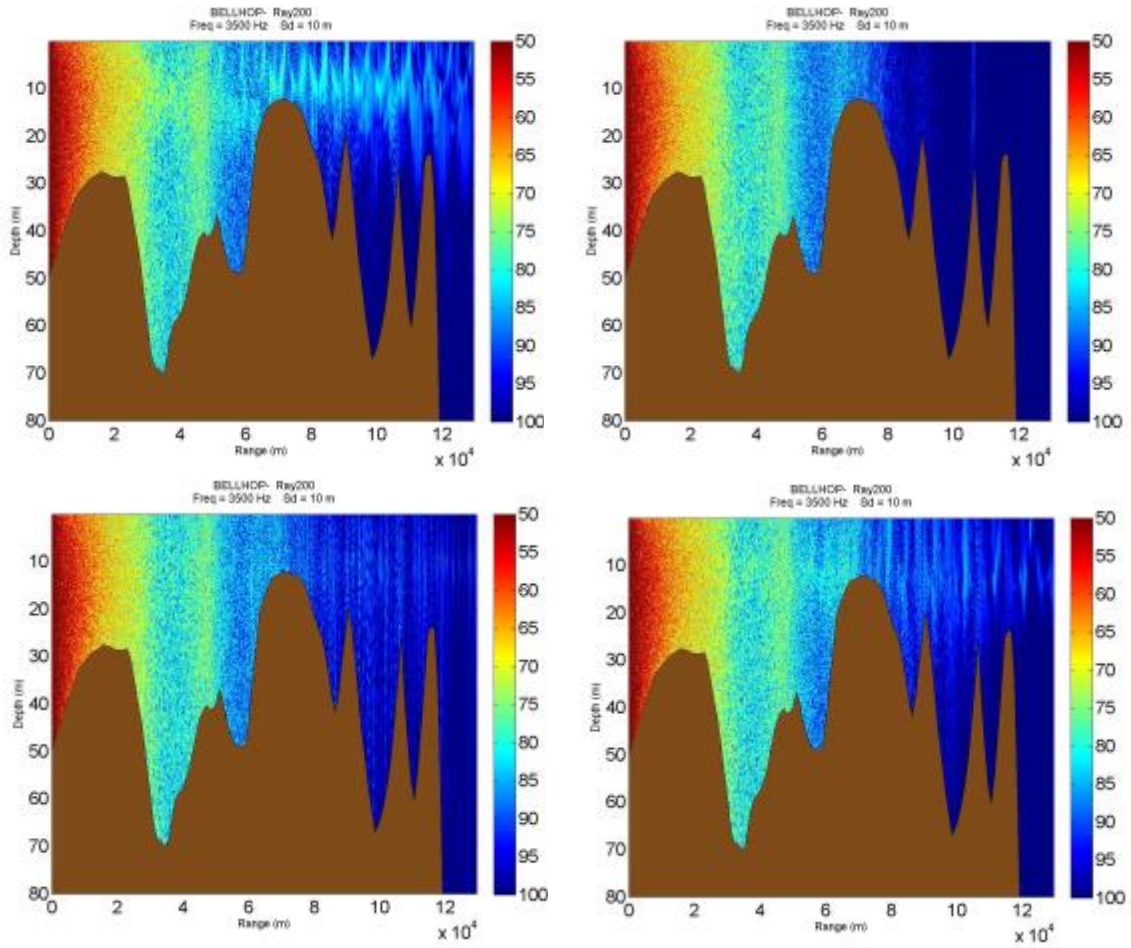


Figure 67. Point H January (upper) and July (lower).

## **V. INTERANNUAL VARIABILITY**

### **A. TIME VARIATIONS OF (T, S, SSP) PROFILES**

Temperature, salinity and sound speed profiles are described at the eight selected locations, data are obtained from the SMG-WOD dataset.

#### **1. Temperature**

Time-depth plots for SMG-WOD temperature fields for the selected points are shown in Figures 68–75. The time axis runs from 1960 to 2014 with a one-month step. Two types of temporal variability are evident in these graphs. First, significant seasonal variations exist in the upper layer at all the locations. These variations are connected to annual variability of heat fluxes, and the water column stability. The seasonal variability is modulated by interannual and decadal modes of variability. The same effects were found earlier by Kucukosmanoglu (2016) for the Mediterranean Sea but contribution of seasonal and interannual variability can be different at different locations.

At point A (Figure 68) the interannual variability exist as an anomaly from the periodic seasonal variability and mostly occurred in the thermocline layer. There were variations of a warmer temperature occurred in 1960–1967 and 1975–1978 in the intermediate layer propagating down to 1000 meters, and there were variations of colder temperature in the mixed layer between 2005 and 2008.

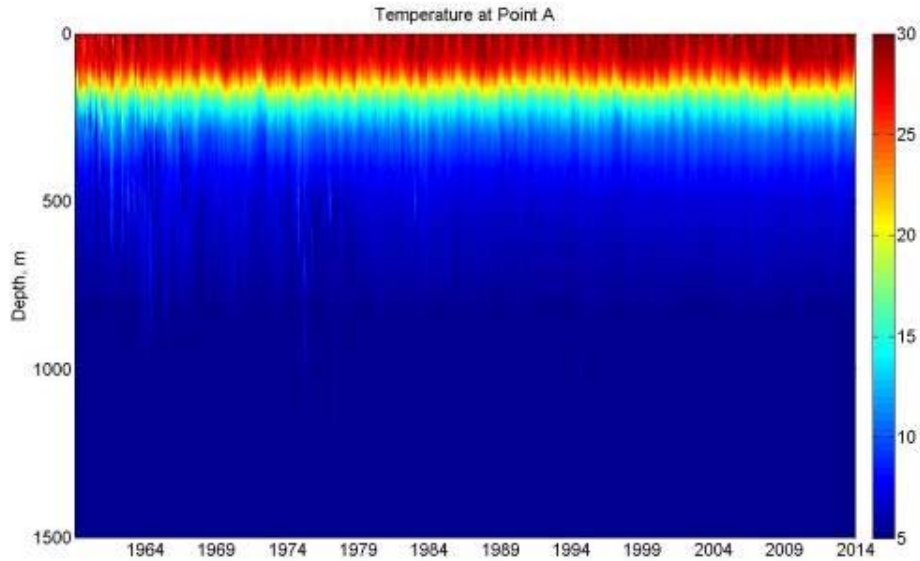


Figure 68. Temporal Variability of SMG-WOD Temperature at point A.

At point B (Figure 69), there were variations of a colder mixed layer in 1960–1964 and variations of a warmer temperature occurred in 1960–1967 and 1975–1978 in the intermediate layer propagating down to 1000 meters, and there were variations of colder temperature in the mixed layer between 2005 and 2008.

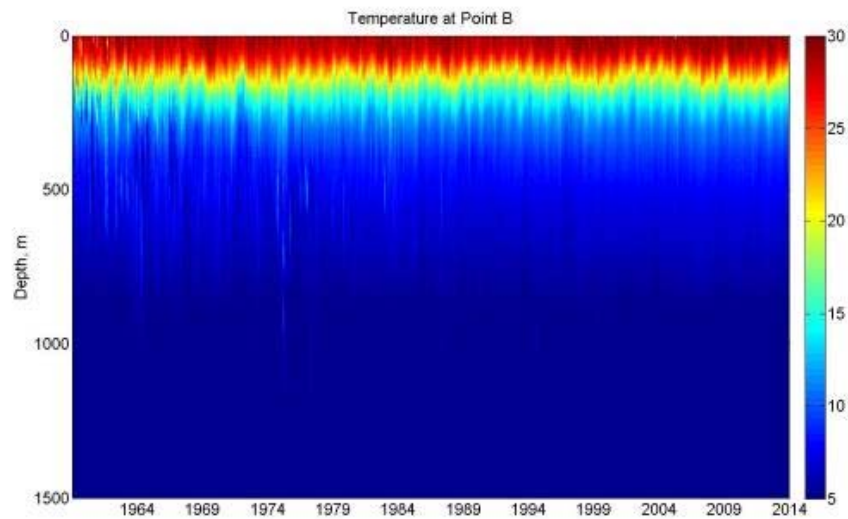


Figure 69. Temporal Variability of SMG-WOD Temperature at point B.



At point C (Figure 70), there were variations of a warmer temperature occurred in 1962–1965 and 1975–1978 in the intermediate layer propagating down to 900 meters, and there were variations of colder temperature in the mixed layer between 2005 and 2008.

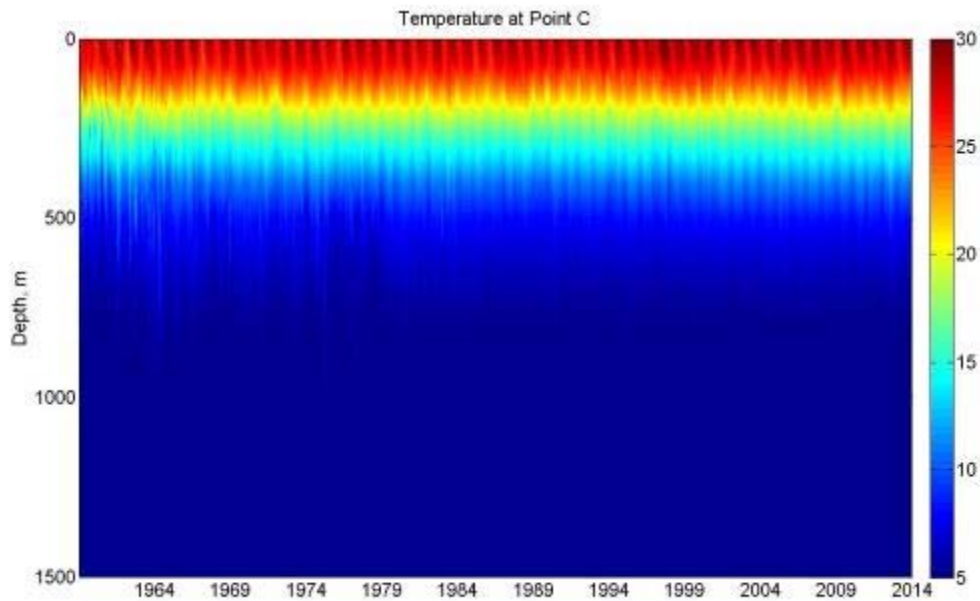


Figure 70. Temporal Variability of SMG-WOD Temperature at point C.

At point D (Figure 71), there were variations of a warmer temperature occurred in 1961–1965 propagating down to 400 meters, and there were variations of colder temperature in the mixed layer between 2005 and 2008.

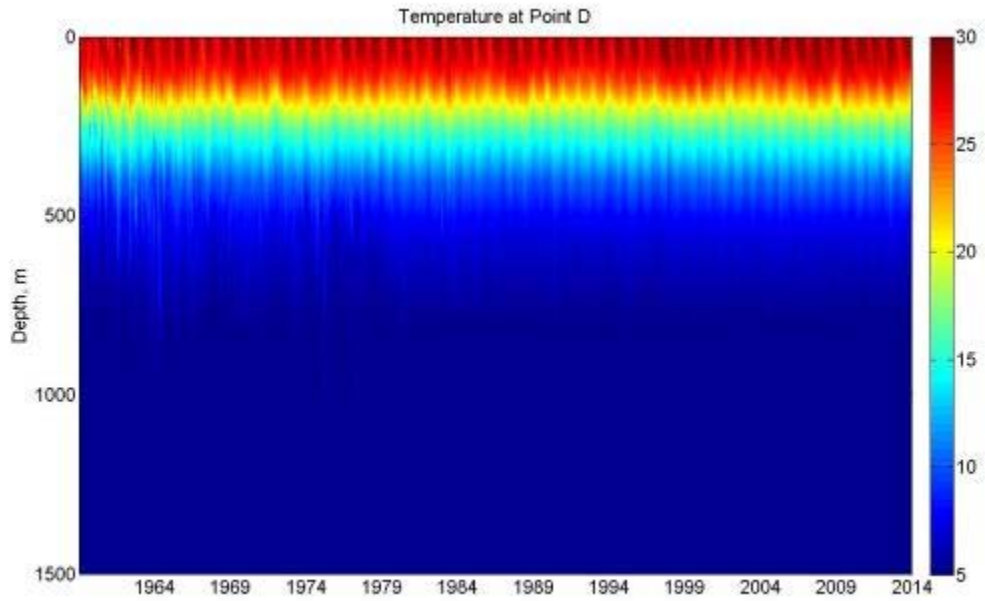


Figure 71. Temporal Variability of SMG-WOD Temperature at point D.

At point E (Figure 72), there were variations of a warmer temperature occurred in 1960–1965 at the mixing layer and in the intermediate layer propagating down to 400 meters.

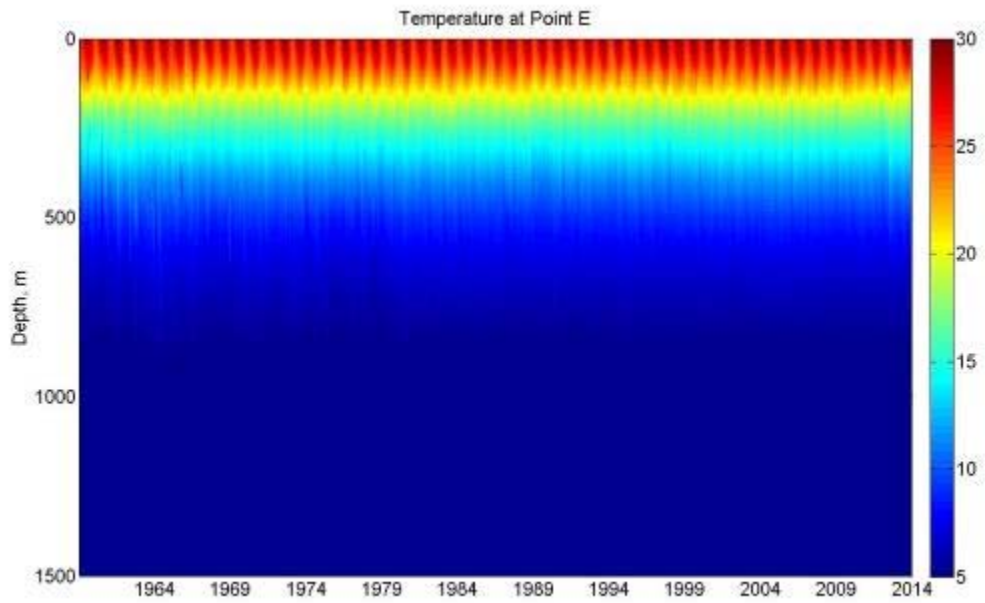


Figure 72. Temporal Variability of SMG-WOD Temperature at point E.

At point F (Figure 73), there were variations of a colder temperature at approximately 100 m depth in 1960–1963. Warmer temperature variations occurred in 1986–1989, 1998–2002 and 2010–2013 in the intermediate layer down to 400 meters.

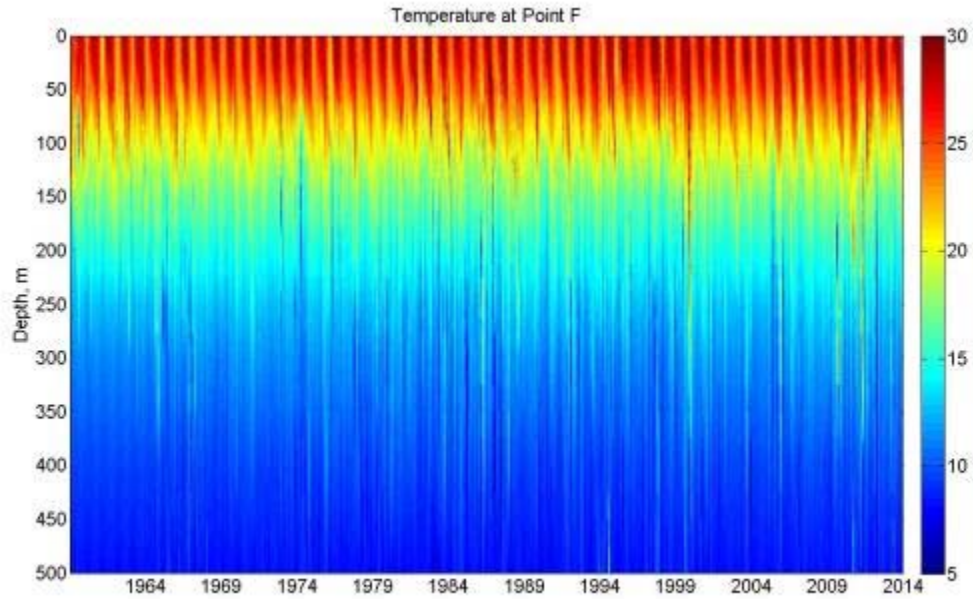


Figure 73. Temporal Variability of SMG-WOD Temperature at point F.

At point G (Figure 74), there were variations of a warmer temperature occurred in 1960–1967 and 1997–2001 in the surface layer propagating down to 300 meters and in 2009–2012 in the surface layer propagating down to 500 meters.

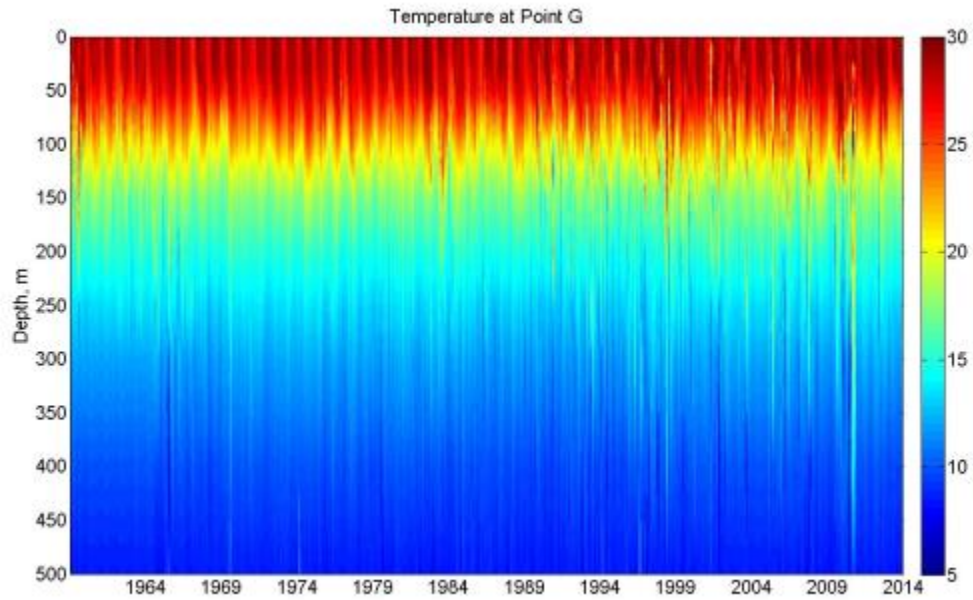


Figure 74. Temporal Variability of SMG-WOD Temperature at point G.

At point H (Figure 75), there were variations of a warmer temperature occurred in 1964–1969 and 1997–2001 in the surface layer propagating down to 200 meters and in 2009–2012 in the surface layer propagating down to 350 meters.

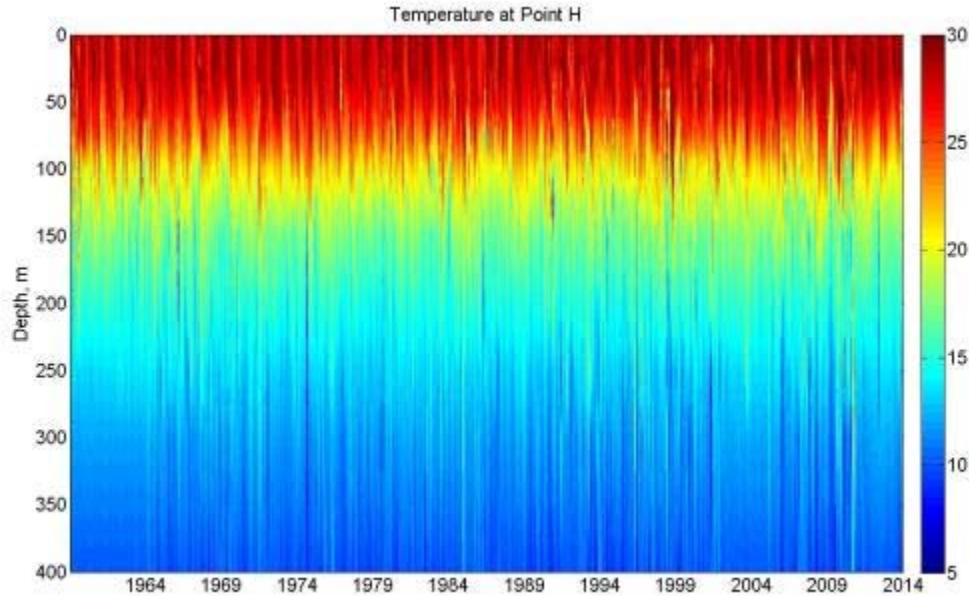


Figure 75. Temporal Variability of SMG-WOD Temperature at point H.

## 2. Salinity

Figures 76–83 show time-depth distribution of SMG-WOD salinity at the selected locations, for the time period between 1960 and 2014 with a one-month step. Just as for the temperature profiles, both seasonal and interannual modes of variability can be seen in these plots. However, the interannual variability dominates the salinity vertical distribution. This can be explained by significant variability of the Pacific Western Boundary circulation at the interannual and decadal scales (Hu et al., 2015). In addition, the formation rate and transport of the North Pacific tropical Water are also affected by the interannual modes of variability (for example, ENSO), and can change the salt content in this region. Comparison of the time-depths plots of SMG-WOD salinity also show significant spatial variability between the selected locations, as described below.

The salinity showed interannual variations between 1960 and 2014 at point A (Figure 76). The salinity variations are mostly affected by the dry and rainy season period. The interannual and decadal variability at this location seems to be synchronized with the interannual variability of temperature (Figure 68). Specifically, the salinity decreasing variations occurred in 1960–1963 through 500 m depth, and in 1985–1993 through 700 m depth.

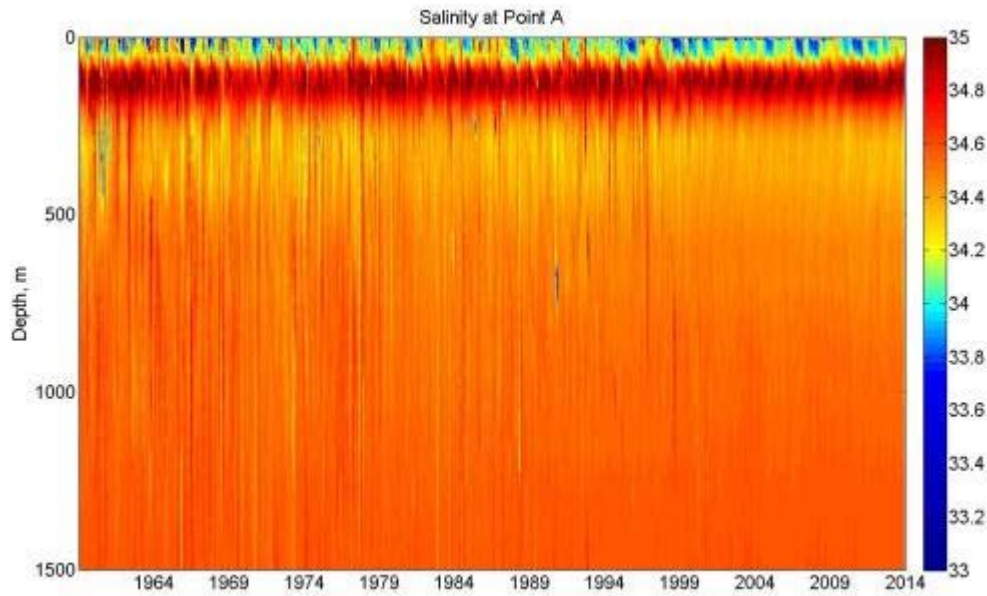


Figure 76. Temporal Variability of SMG-WOD Salinity at point A.



The salinity showed interannual variations between 1960 and 2014 at point B (Figure 77). The salinity variations are mostly affected by the dry and rainy season period. Specifically, the salinity decreasing variations occurred in 1960–1963 through 500 m depth, and in 1985–1993 through 700 m depth.

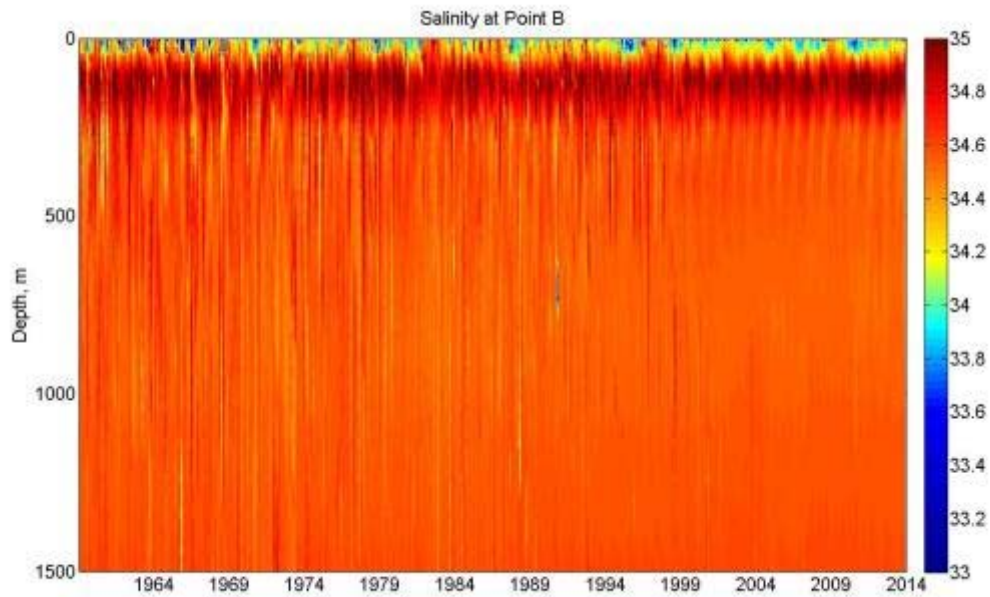


Figure 77. Temporal Variability of SMG-WOD Salinity at point B.



The salinity showed interannual variations between 1960 and 2014 at point C (Figure 78). The salinity variations are mostly affected by the dry and rainy season period. Specifically, the salinity decreasing variations occurred in 1960–1963 through 500 m depth, and in 1985–1993 through 700 m depth.

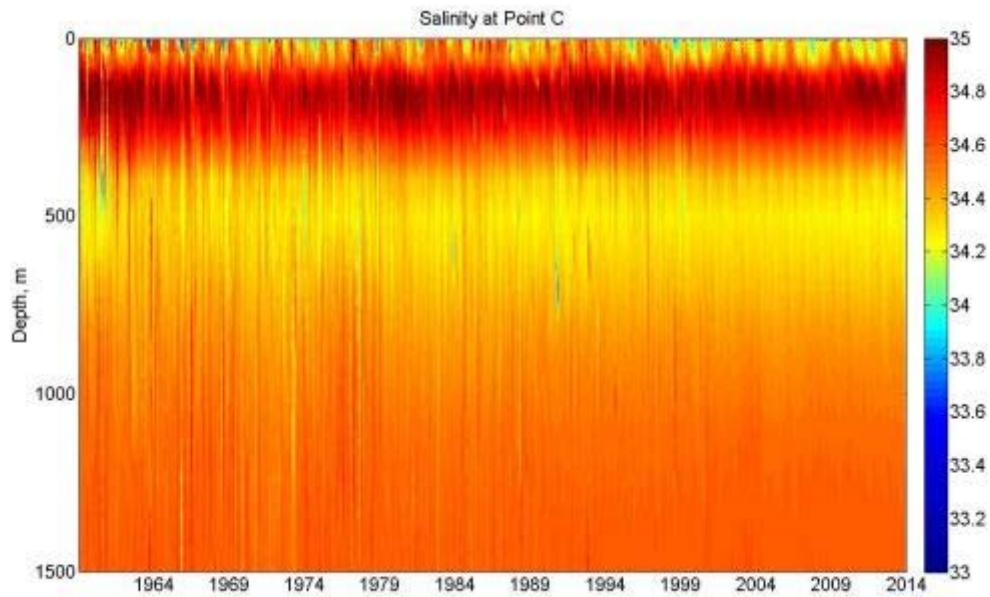


Figure 78. Temporal Variability of SMG-WOD Salinity at point C.

The salinity showed interannual variations between 1960 and 2014 at point D (Figure 79). The highest salinity occurred at approximately between 50 meters and 300 m depth, mainly caused by the NEC circulation. The salinity variations are mostly affected by the dry and rainy season periods. Specifically, the salinity decreasing variations occurred in 1961–1968 at the mixing layer through 500 m depth, and in 1979–1983 and 1999–2009 at the mixing layer.

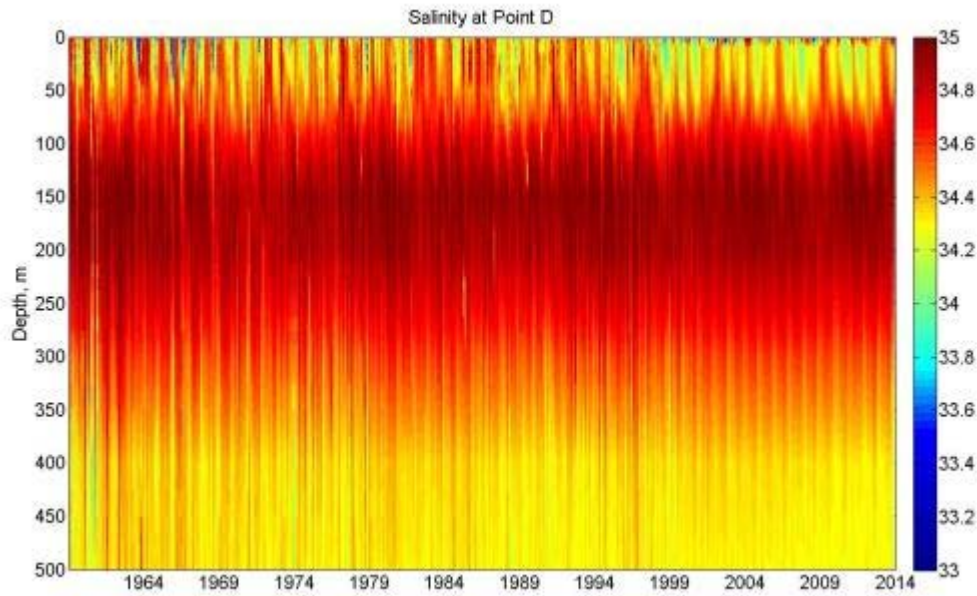


Figure 79. Temporal Variability of SMG-WOD Salinity at point D.

The salinity showed interannual variations between 1960 and 2014 at point E (Figure 80). The highest salinity occurred at approximately 10–400 meters and below 700 m depth, mainly caused by the NEC circulation. The salinity variations are mostly affected by the dry and rainy season periods. Specifically, the salinity decreasing variations occurred in 1972–1978 at the intermediate layer through 1400 m depth, and in 1962–1970 and 1999–2009 at the mixing layer.

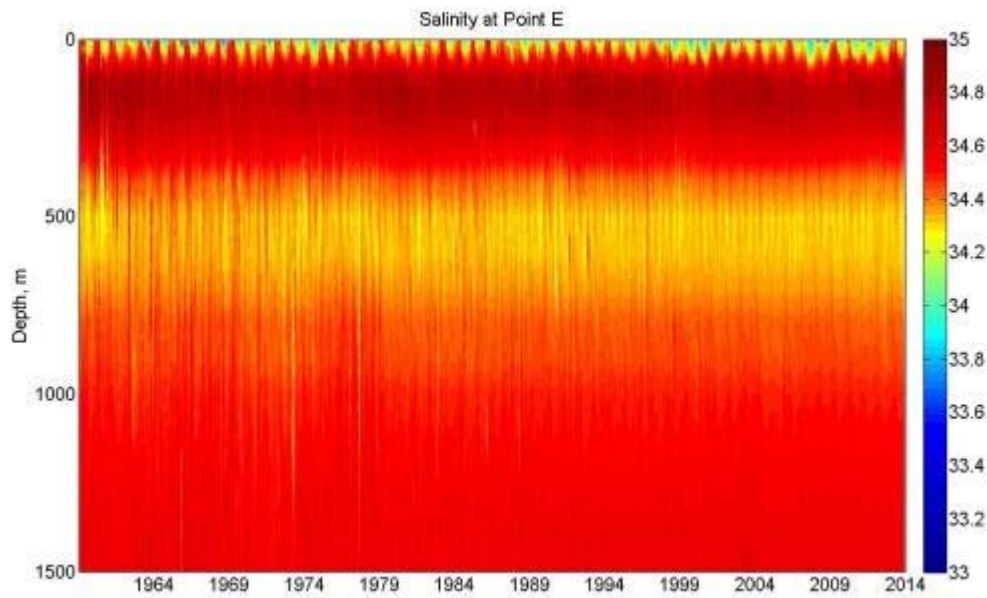


Figure 80. Temporal Variability of SMG-WOD Salinity at point E.

The salinity showed interannual variations between 1960 and 2014 at point F (Figure 81). The salinity variations are mostly affected by the dry and rainy season period. Specifically, the salinity decreasing variations occurred in 1968–1970 and 1973–1975 at the mixing layer through the intermediate layer approximately 500 m depth, and in 2008–2014 at the mixing layer. The increased salinity variations occurred in 1979–1995, 200–2002 and 2009–2012 in the intermediate layer through approximately 500 m depth.

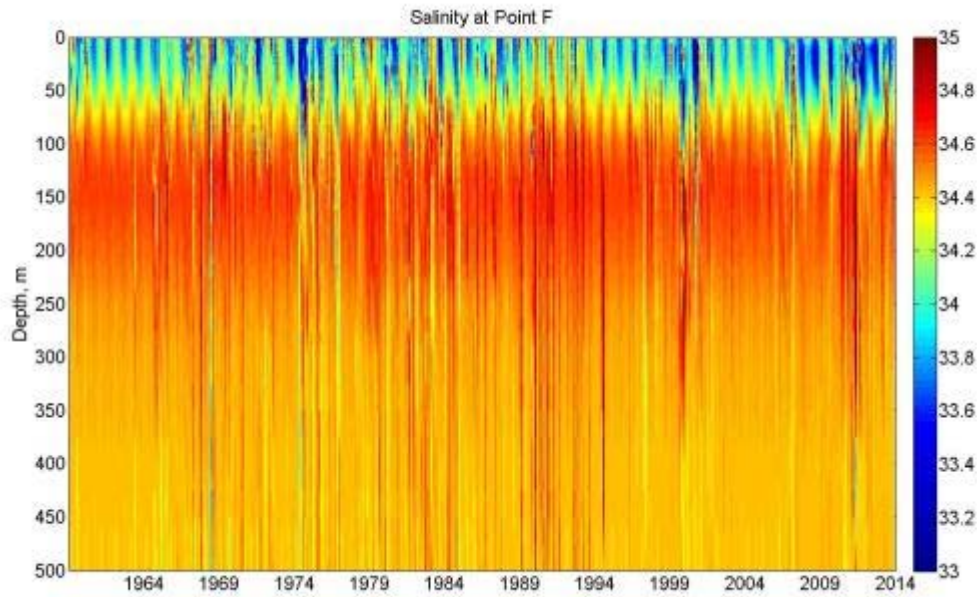


Figure 81. Temporal Variability of SMG-WOD Salinity at point F.

The salinity showed interannual variations between 1960 and 2014 at point G (Figure 82). The salinity variations are mostly affected by the dry and rainy season period. Specifically, the salinity decreasing variations occurred in 1965–1969, 1964–1979 and 2010–2012 at the mixing layer through the intermediate layer approximately 1300 m depth. The increased salinity variations are seen in 1982–1993 in the intermediate layer through approximately 1500 m depth.

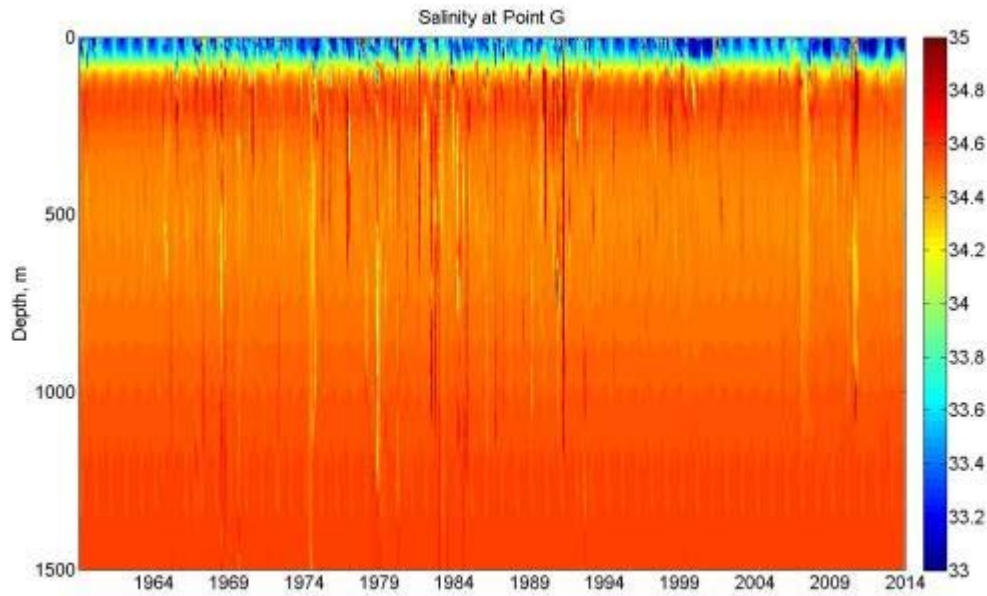


Figure 82. Temporal Variability of SMG-WOD Salinity at point G.

The salinity showed interannual variations between 1960 and 2014 at point H (Figure 83). The salinity variations are mostly affected by the dry and rainy season period. Specifically, the salinity decreasing variations occurred in 1979–1984 and 2006–2008 in the intermediate layer through approximately 400 m depth. The salinity variations increased in 1965–1994, 199–2003 and 2006–2011 at the mixing layer through in the intermediate layer through approximately 400 m depth.

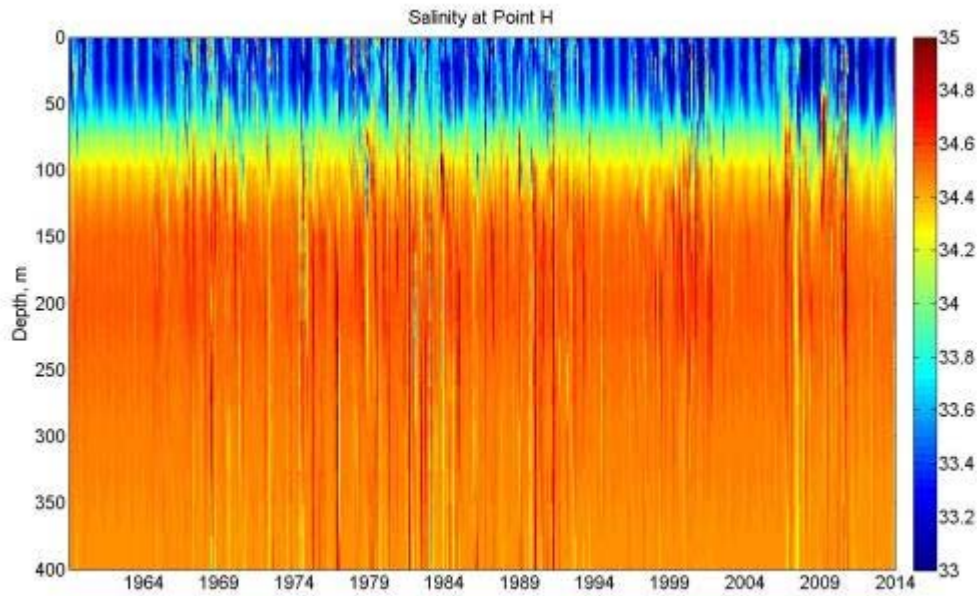


Figure 83. Temporal Variability of SMG-WOD Salinity at point H.

### 3. Sound Speed

In Figures 84–91, temporal variability of sound speed profiles is shown as calculated from the SMG-WOD temperature and salinity fields for 1960–2014 with a one-month step. Comparison of temperature and salinity shows a strong correlation with the seasonal and interannual variability for the sound speed especially at the intermediate layer to the surface.



At point A (Figure 84), the sound speed at the surface was almost same. Below a depth of 200 meters, the sound speed shows higher interannual variations. The sound speed has the increasing variations in 1960–1967 and 1975–1978 at the intermediate layer through approximately 1200 m depth. In 2005–2008, there are decreasing variations at the mixing layer. These results agreed with temperature and salinity results of Point A because both of them have significant increasing variations between 1960 and 1978.

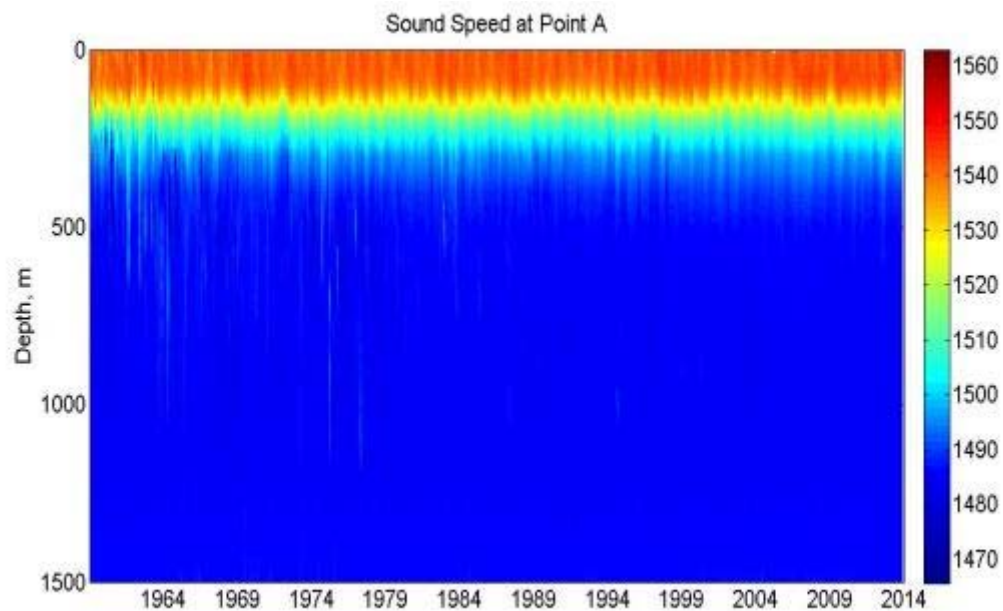


Figure 84. Temporal Variability of SMG-WOD Sound Speed at Point A.

At point B (Figure 85), the sound speed at the surface was almost same. Below a depth of 100 meters, the sound speed shows higher interannual variations. The sound speed has the decreasing variations in 1960–1967 at the mixing layer. The sound speed has increasing variations in 1960–1967 at the intermediate layer, and 1975–1978 at the intermediate layer through approximately 1200 m depth. In 2005–2008, there are decreasing variations at the mixing layer. These results agreed with temperature and salinity results of Point B because both of them have significant increasing variations between 1960 and 1978.

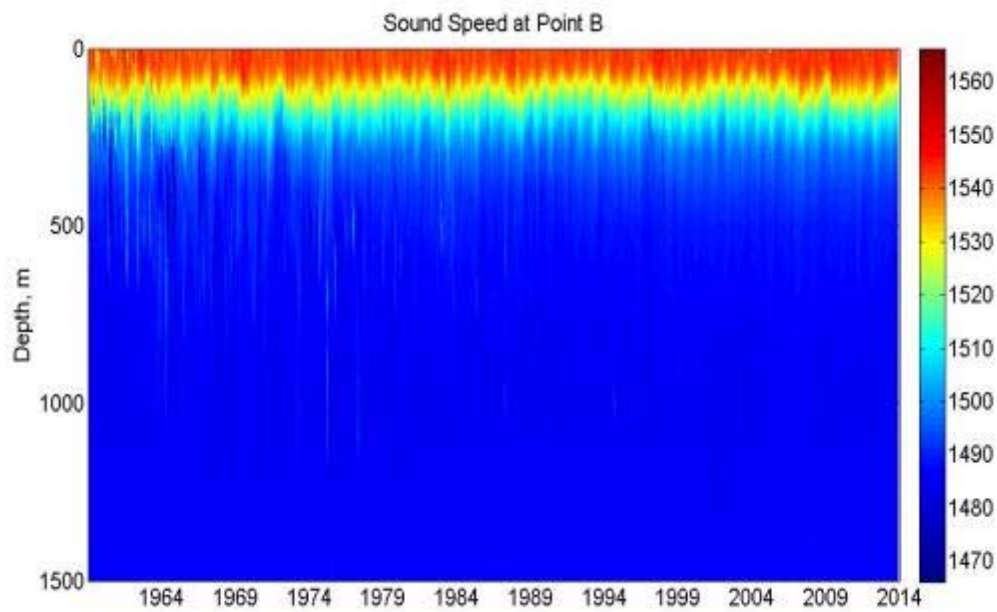


Figure 85. Temporal Variability of SMG-WOD Sound Speed at Point B.



At point C (Figure 86), the sound speed at the surface was almost same. Below a depth of 200 meters, the sound speed shows higher interannual variations. The sound speed has the increasing variations in 1962–1965 and 1975–1978 at the intermediate layer through approximately 1200 m depth, and decreasing variations in 2005–2008 at the mixing layer. These results agreed with temperature and salinity results of Point C because both of them have significant increasing variations between 1960 and 1978.

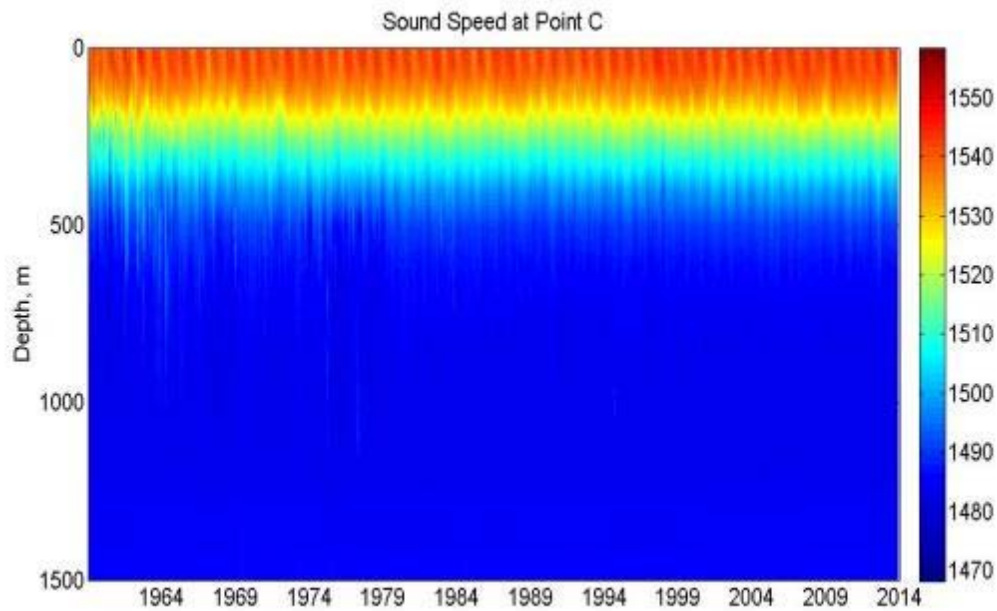


Figure 86. Temporal Variability of SMG-WOD Sound Speed at Point C.

At point D (Figure 87), the sound speed at the surface was almost same. Below a depth of 200 meters, the sound speed shows higher interannual variations. The sound speed has the increasing variations in 1961–1965 at the intermediate layer through approximately 450 m depth, and has decreasing variations in 2005–2008 at the mixing layer. These results agreed with temperature and salinity results of Point D because both of them have significant increasing variations between 1961 and 1965.

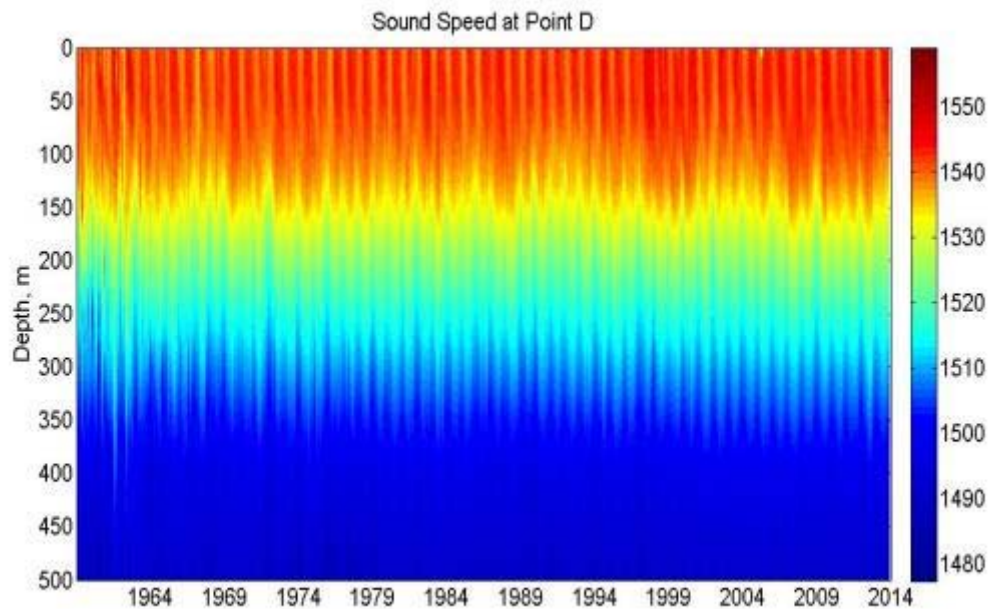


Figure 87. Temporal Variability of SMG-WOD Sound Speed at Point D.

At point E (Figure 88), the sound speed at the surface was almost same. Below a depth of 200 meters, the sound speed shows higher interannual variations. The sound speed has the increasing variations in 1962–1966 at the intermediate layer through approximately 800 m depth. These results agreed with temperature and salinity results of Point E because both of them have significant increasing variations between 1962 and 1966.

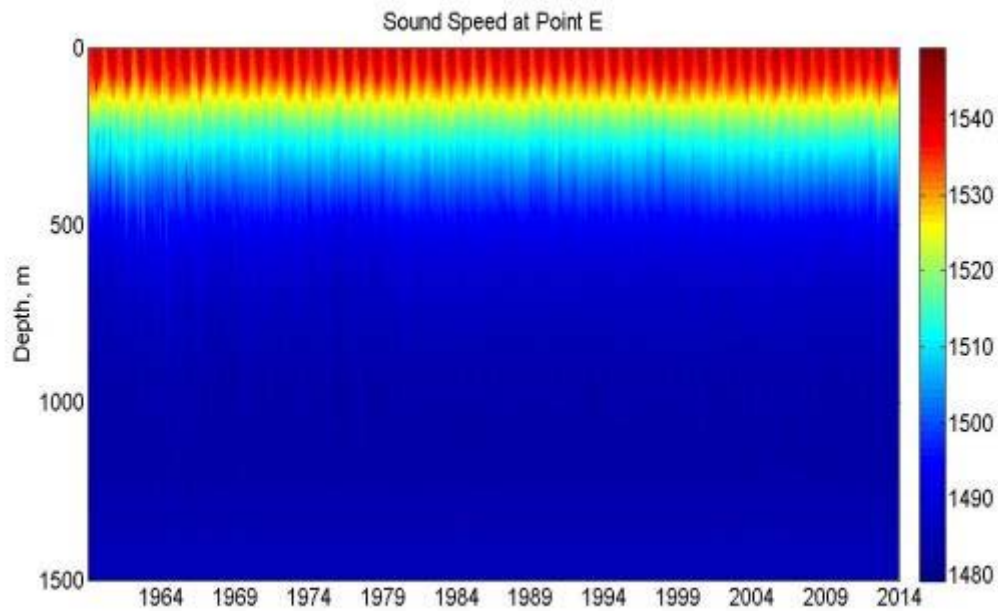


Figure 88. Temporal Variability of SMG-WOD Sound Speed at Point E.

At point F (Figure 89), the sound speed at the surface was almost same. Below a depth of 100 meters, the sound speed shows higher interannual variations. The sound speed has the decreasing variations in 1960–1963 at approximately 100 m depth, has the increasing variations in 1986–1989, 1998–2002 and 2009–2012 at the intermediate layer through approximately 500 m depth. These results agreed with temperature and salinity results of Point F because both of them have significant increasing variations between 1986 and 2013.

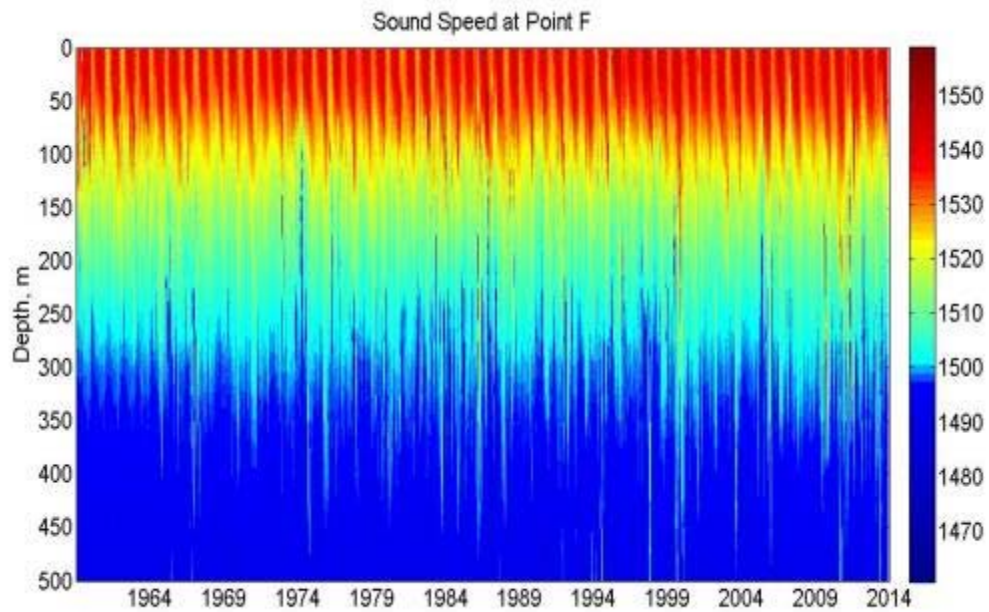


Figure 89. Temporal Variability of SMG-WOD Sound Speed at Point F.

At point G (Figure 90), the sound speed at the surface was almost same. Below a depth of 50 meters, the sound speed shows higher interannual variations. The sound speed has the increasing variations in 1960–1967, 1997–2001 and 2009–2012 at the intermediate layer through approximately 500 m depth. These results agreed with temperature and salinity results of Point G because both of them have significant increasing variations between 1960–1967 and 1997–2012.

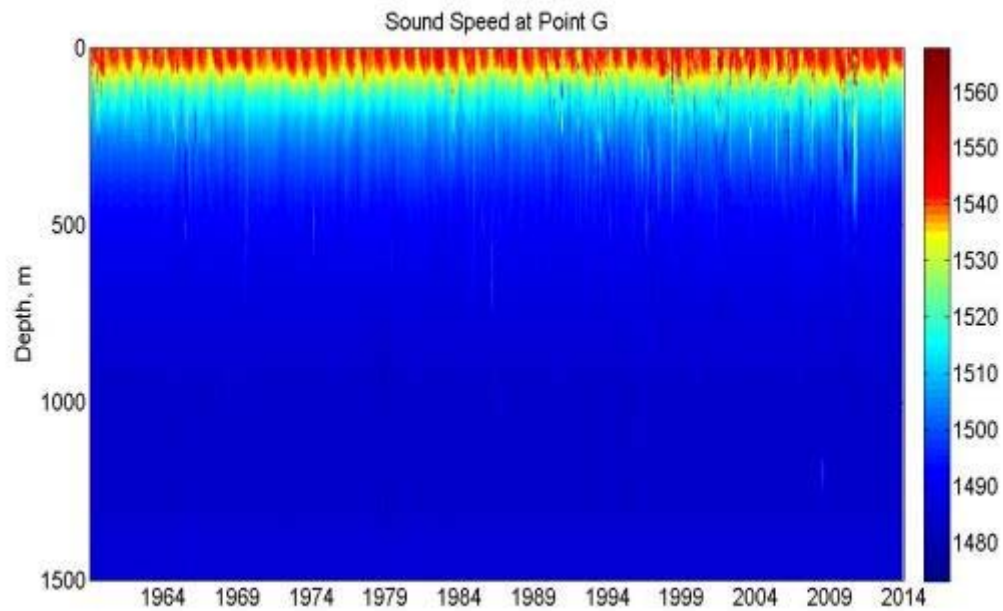


Figure 90. Temporal Variability of SMG-WOD Sound Speed at Point G.

At point H (Figure 91), the sound speed at the surface was almost same. Below a depth of 50 meters, the sound speed shows higher interannual variations. The sound speed has the increasing variations in 1964–1969, 1981–1986, 1997–2001 and 2009–2012 at the intermediate layer through approximately 400 m depth. These results agreed with temperature and salinity results of Point H because both of them have significant increasing variations between 1964–1986 and 1997–2012.

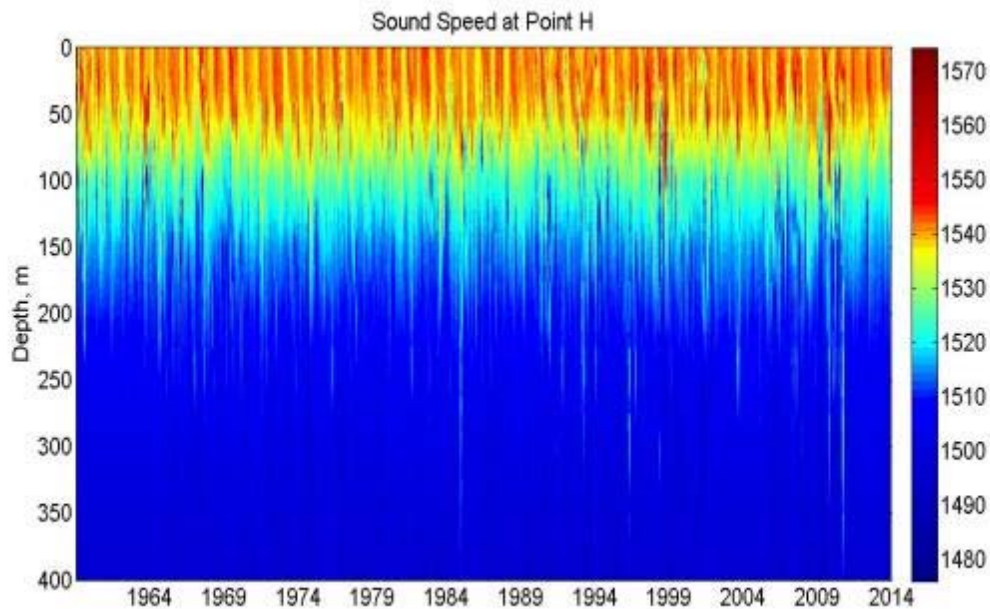


Figure 91. Temporal Variability of SMG-WOD Sound Speed at Point H.

## B. EOF ANALYSIS

The EOF analysis (Hannachi, 2004) is applied to the SMG-WOD data from 1960 to 2014, in order to analyze the interannual. Seasonal variability is larger than interannual variability as expected, thus we need to remove the seasonal variability and find the principal component (PC) of the interannual variability.

The EOFs are computed for the synoptic monthly anomaly of SSPs at the eight points in Philippine Sea and South China. Most variability is contained in the first four modes (Table 14).

Table 14. Variances of First Four EOF Modes.

Point	Mode 1 %Variance	Mode 2 %Variance	Mode 3 %Variance	Mode 4 %Variance	Cumulative Variance
A	41.18	18.9	10.26	9.74	80.08
B	42.84	18.34	11.1	8.22	80.5
C	43.34	19.59	10.58	7.1	80.61
D	40.74	20.58	10.84	8.28	80.44
E	44.08	22.02	10.42	6.1	82.62
F	55.84	17.72	10.1	5.44	89.1
G	39.14	16.87	10.42	6.49	72.92
H	46.82	20.85	10.89	6.78	85.34

Figures 92 through 99 provide Eigen values and Mode Variances of sound speed. In particular, the point A to D data needs 6–7 modes to reach 90% of variance, depending on region and depths. Points E, F and H correspond to shallower regions, and require 4–6 modes to reach 90% of variance. Point G, demands 8–9 modes to reach 90% of variance.

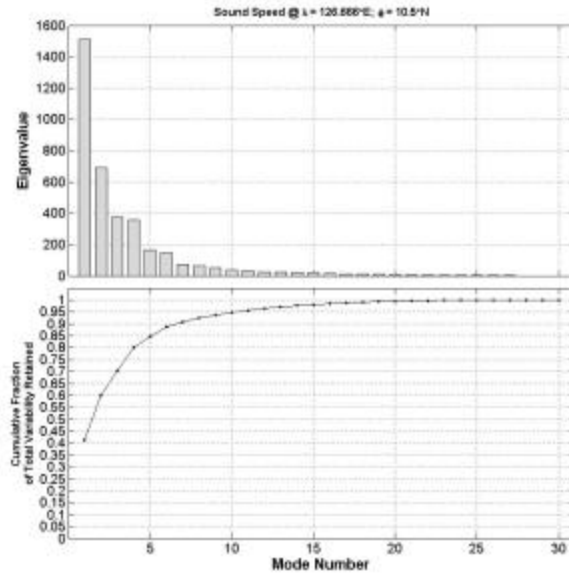


Figure 92. Point A: Eigenvalues and Mode Variance.

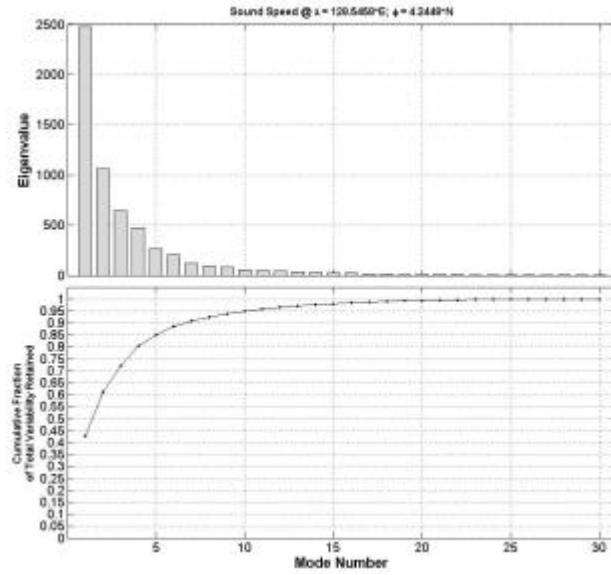


Figure 93. Point B: Eigenvalues and Mode Variance.

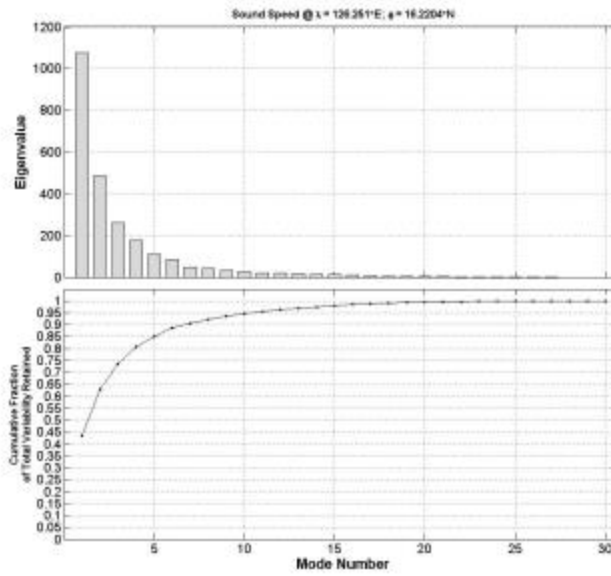


Figure 94. Point C: Eigenvalues and Mode Variance.



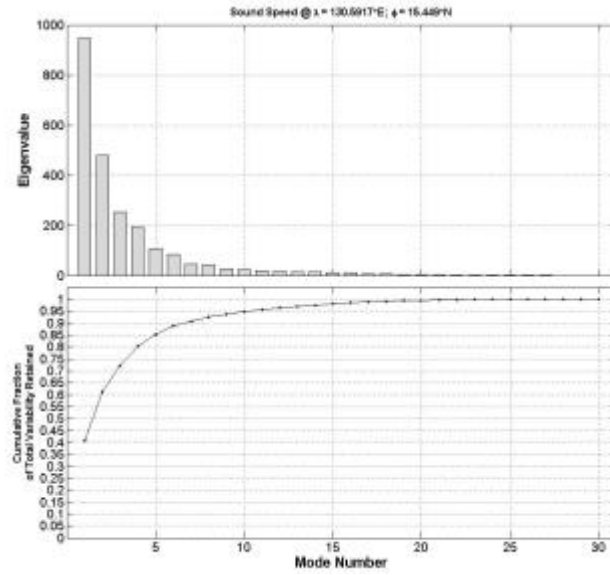


Figure 95. Point D: Eigenvalues and Mode Variance.

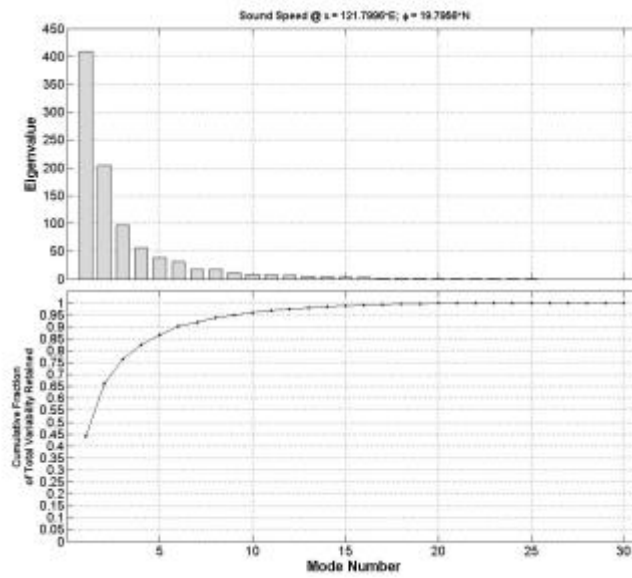


Figure 96. Point E: Eigenvalues and Mode Variance.

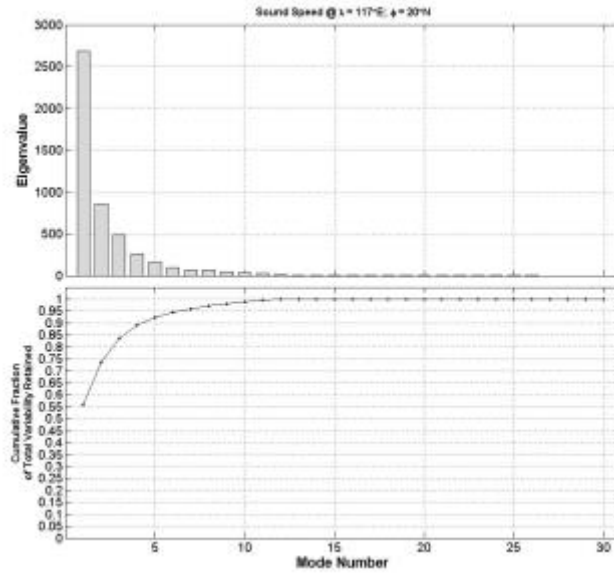


Figure 97. Point F: Eigenvalues and Mode Variance.

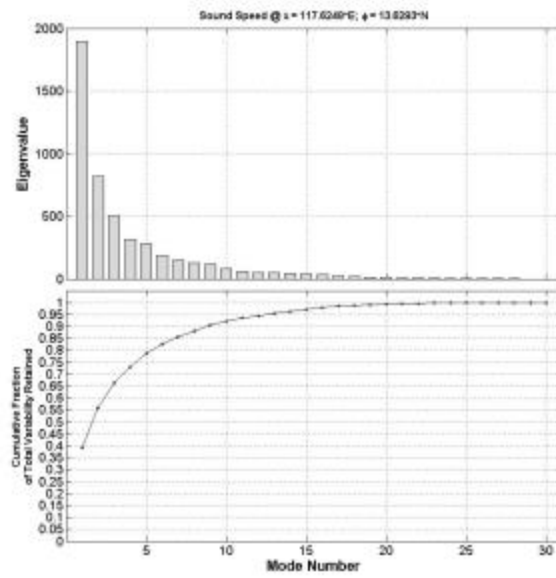


Figure 98. Point G: Eigenvalues and Mode Variance.

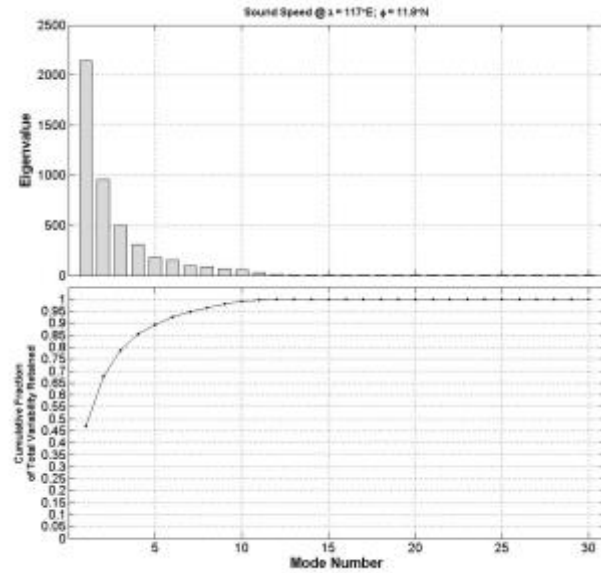


Figure 99. Point H: Eigenvalues and Mode Variance.

Figure 100–115 shows EOFs for the first four EOFs as a function of depth. Only the first four EOF are showed because they explain most of variability in the data.

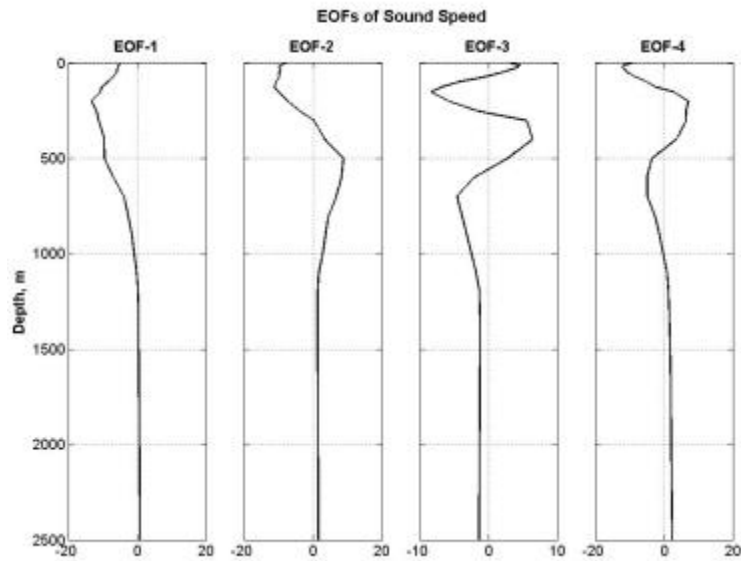


Figure 100. The First Four EOFs of Point A.

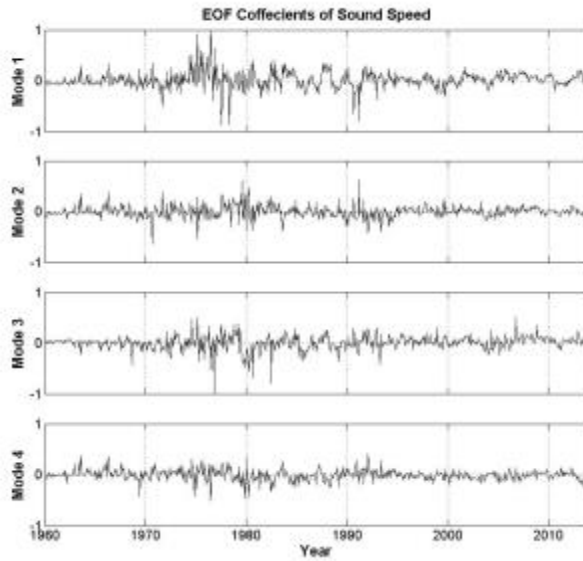


Figure 101. EOF Coefficients of Sound Speed of Point A.

To explain the sound speed temporal variation at each depth, we need to multiply the corresponding EOF at this depth and the EOF coefficient at the specific time. The results are shown in Tables 15–22.

Table 15. EOF Analysis at Point A.

Mode Number	EOF		PC		Sound Speed
	Depth	Value	Time	Value	
1	100	Negative	1970-1990 2000-2014	Positive	Decrease
	500	Negative			Decrease
	800	Negative			Decrease
	1000	Negative			Decrease
	1500	Positive			Increase
1	100	Negative	1960-1970 1990-2000	Negative	Increase
	500	Negative			Increase
	800	Negative			Increase
	1000	Negative			Increase
	1500	Positive			Decrease
2	100	Negative	1970-1990 2000-2014	Positive	Decrease
	500	Positive			Increase

Mode Number	EOF		PC		Sound Speed
	Depth	Value	Time	Value	
	800	Positive			Increase
	1000	Positive			Increase
	1500	Positive			Increase
2	100	Negative	1960-1970 1990-2000	Negative	Increase
	500	Positive			Decrease
	800	Positive			Decrease
	1000	Positive			Decrease
	1500	Positive			Decrease
3	100	Negative	1960-1970 1990-2014	Positive	Decrease
	500	Positive			Increase
	800	Negative			Decrease
	1000	Negative			Decrease
	1500	Negative			Decrease
3	100	Negative	1970-1990	Negative	Increase
	500	Positive			Decrease
	800	Negative			Increase
	1000	Negative			Increase
	1500	Negative			Increase
4	100	Negative	1960-1980 1990-2000	Positive	Decrease
	500	Negative			Decrease
	800	Negative			Decrease
	1000	Negative			Decrease
	1500	Positive			Increase
4	100	Negative	1980-1990 2000-2014	Negative	Increase
	500	Negative			Increase
	800	Negative			Increase
	1000	Negative			Increase
	1500	Positive			Decrease

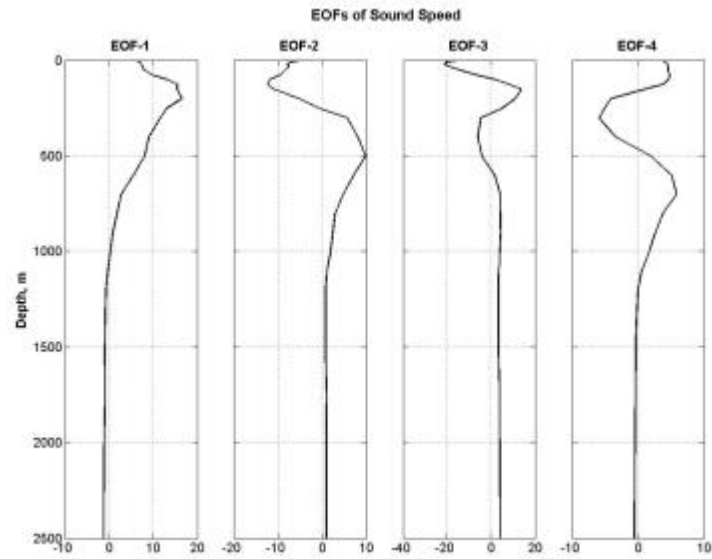


Figure 102. The First Four EOFs of Point B.

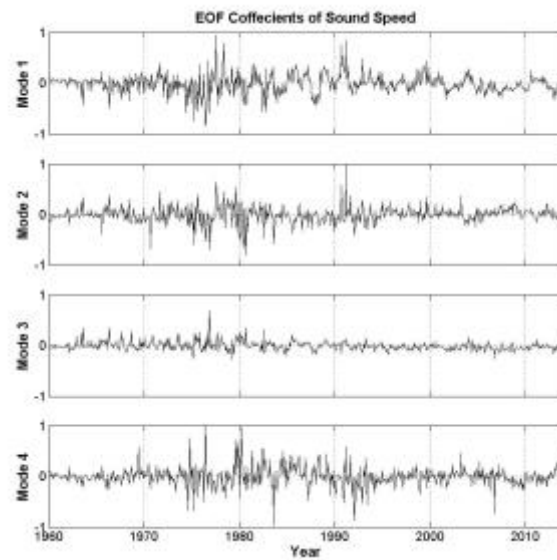


Figure 103. Coefficients of Sound Speed of Point B.

Table 16. EOF Analysis at Point B.

Mode Number	EOF		PC		Sound Speed
	Depth	Value	Time	Value	
1	100	Positive	1960-1970 1990-2000	Positive	Increase
	500	Positive			Increase
	800	Positive			Increase
	1000	Positive			Increase
	1500	Negative			Decrease
1	100	Positive	1970-1990 2000-2014	Negative	Decrease
	500	Positive			Decrease
	800	Positive			Decrease
	1000	Positive			Decrease
	1500	Negative			Increase
2	100	Negative	2000-2014	Positive	Decrease
	500	Positive			Increase
	800	Positive			Increase
	1000	Positive			Increase
	1500	Positive			Increase
2	100	Negative	1960-2000	Negative	Increase
	500	Positive			Decrease
	800	Positive			Decrease
	1000	Positive			Decrease
	1500	Positive			Decrease
3	100	Positive	1960-1990	Positive	Increase
	500	Negative			Decrease
	800	Positive			Increase
	1000	Positive			Increase
	1500	Positive			Increase
3	100	Positive	1990-2014	Negative	Decrease
	500	Negative			Increase
	800	Positive			Decrease
	1000	Positive			Decrease
	1500	Positive			Decrease
4	100	Positive	1980-1990	Positive	Increase
	500	Positive			Increase
	800	Positive			Increase
	1000	Positive			Increase
	1500	Negative			Decrease
4	100	Positive	1960-1980 1990-2014	Negative	Decrease
	500	Positive			Decrease
	800	Positive			Decrease

Mode Number	EOF		PC		Sound Speed
	Depth	Value	Time	Value	
	1000	Positive			Decrease
	1500	Negative			Increase

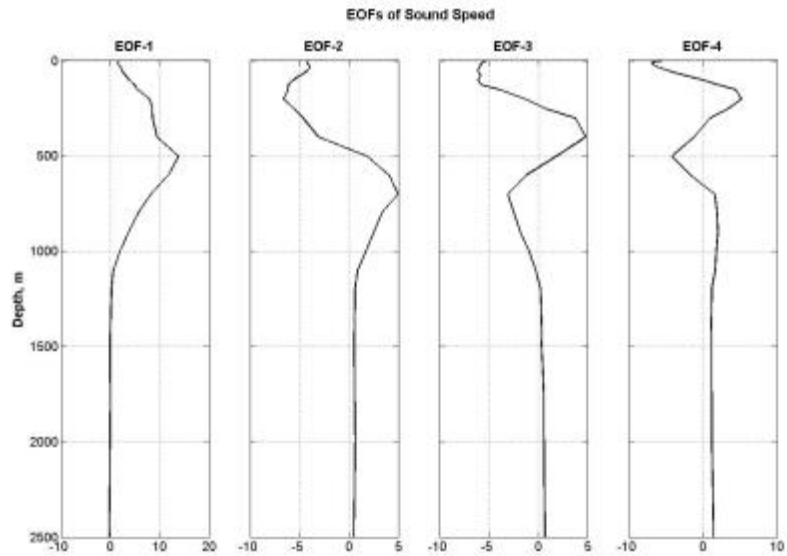


Figure 104. The First Four EOFs of Point C.

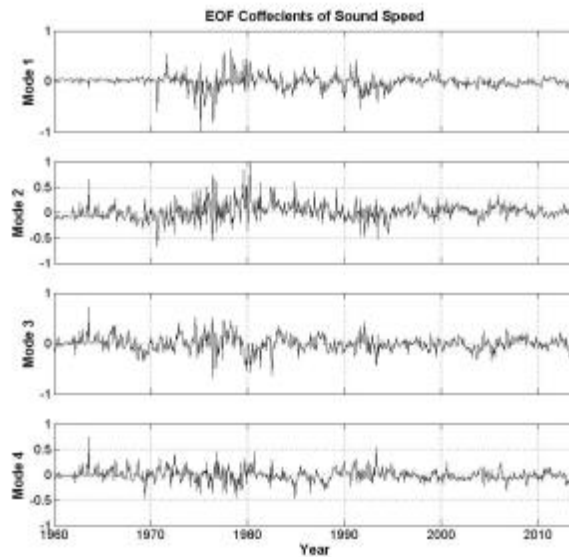


Figure 105. Coefficients of Sound Speed of Point C.



Table 17. EOF Analysis at Point C.

Mode Number	EOF		PC		Sound Speed
	Depth	Value	Time	Value	
1	100	Positive	1960-1970	Positive	Increase
	500	Positive			Increase
	800	Positive			Increase
	1000	Positive			Increase
	1500	Negative			Decrease
1	100	Positive	1970-2014	Negative	Decrease
	500	Positive			Decrease
	800	Positive			Decrease
	1000	Positive			Decrease
	1500	Negative			Increase
2	100	Negative	1970-1990 2000-2014	Positive	Decrease
	500	Positive			Increase
	800	Positive			Increase
	1000	Positive			Increase
	1500	Positive			Increase
2	100	Negative	1960-1970 1990-2000	Negative	Increase
	500	Positive			Decrease
	800	Positive			Decrease
	1000	Positive			Decrease
	1500	Positive			Decrease
3	100	Negative	1960-1980	Positive	Decrease
	500	Positive			Increase
	800	Negative			Decrease
	1000	Negative			Decrease
	1500	Positive			Increase
3	100	Negative	1980-2014	Negative	Increase
	500	Positive			Decrease
	800	Negative			Increase
	1000	Negative			Increase
	1500	Positive			Decrease
4	100	Positive	1960-1970 1990-2000	Positive	Increase
	500	Negative			Decrease
	800	Positive			Increase
	1000	Positive			Increase
	1500	Positive			Increase
4	100	Positive	1970-1990 2000-2014	Negative	Decrease
	500	Negative			Increase
	800	Positive			Decrease
	1000	Positive			Decrease

Mode Number	EOF		PC		Sound Speed
	Depth	Value	Time	Value	
	1500	Positive			

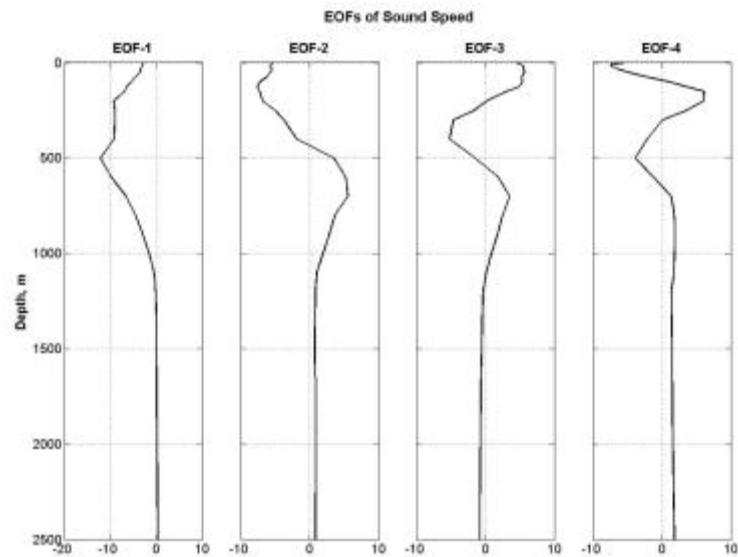


Figure 106. The First Four EOFs of Point D.

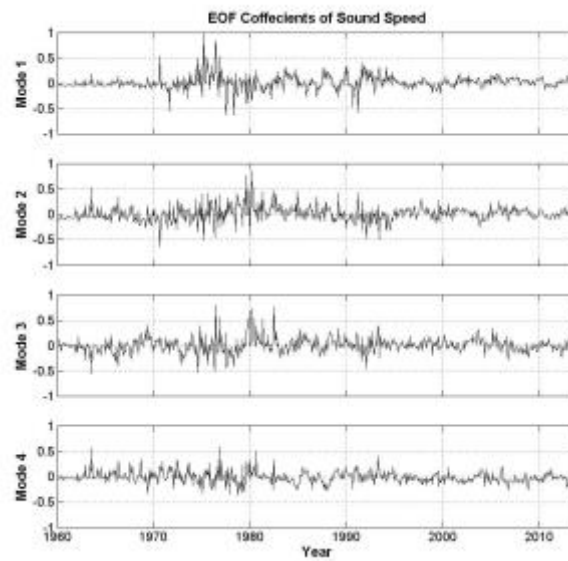


Figure 107. Coefficients of Sound Speed of Point D.

Table 18. EOF Analysis at Point D.

Mode Number	EOF		PC		Sound Speed
	Depth	Value	Time	Value	
1	100	Negative	1970-2014	Positive	Decrease
	500	Negative			Decrease
	800	Negative			Decrease
	1000	Negative			Decrease
	1500	Positive			Increase
1	100	Negative	1960-1970	Negative	Increase
	500	Negative			Increase
	800	Negative			Increase
	1000	Negative			Increase
	1500	Positive			Decrease
2	100	Negative	1970-1990 2000-2014	Positive	Decrease
	500	Positive			Increase
	800	Positive			Increase
	1000	Positive			Increase
	1500	Positive			Increase
2	100	Negative	1960-1970 1990-2000	Negative	Increase
	500	Positive			Decrease
	800	Positive			Decrease
	1000	Positive			Decrease
	1500	Positive			Decrease
3	100	Positive	1980-2014	Positive	Increase
	500	Negative			Decrease
	800	Positive			Increase
	1000	Positive			Increase
	1500	Negative			Decrease
3	100	Positive	1960-1980	Negative	Decrease
	500	Negative			Increase
	800	Positive			Decrease
	1000	Positive			Decrease
	1500	Negative			Increase
4	100	Positive	1960-1980	Positive	Increase
	500	Negative			Decrease
	800	Positive			Increase
	1000	Positive			Increase
	1500	Positive			Increase
4	100	Positive	1980-2014	Negative	Decrease
	500	Negative			Increase
	800	Positive			Decrease

Mode Number	EOF		PC		Sound Speed
	Depth	Value	Time	Value	
	1000	Positive			
	1500	Positive			Decrease

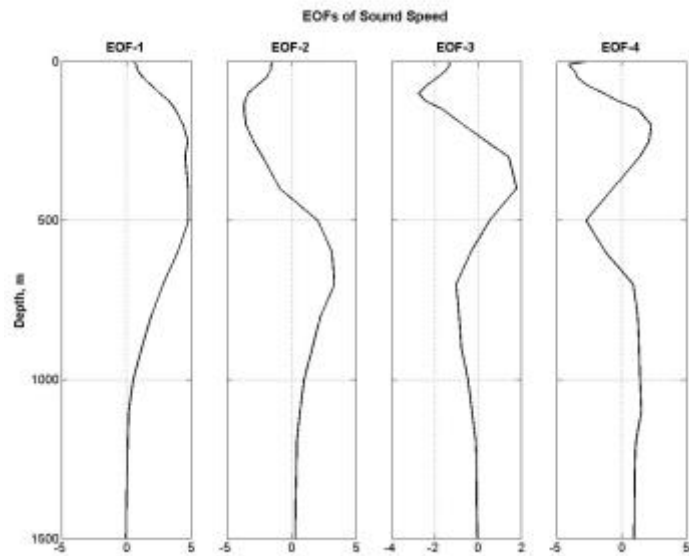


Figure 108. The First Four EOFs of Point E.

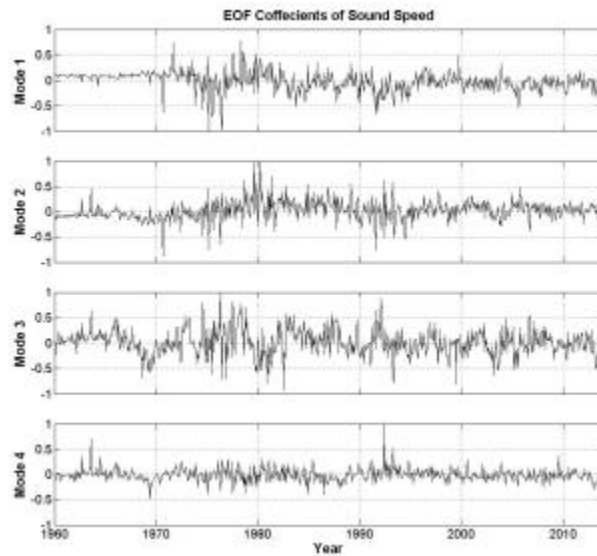


Figure 109. Coefficients of Sound Speed of Point E.

Table 19. EOF Analysis at Point E.

Mode Number	EOF		PC		Sound Speed
	Depth	Value	Time	Value	
1	100	Positive	1960-1980	Positive	Increase
	500	Positive			Increase
	800	Positive			Increase
	1000	Positive			Increase
	1500	Negative			Decrease
1	100	Positive	1980-2014	Negative	Decrease
	500	Positive			Decrease
	800	Positive			Decrease
	1000	Positive			Decrease
	1500	Negative			Increase
2	100	Negative	1980-2014	Positive	Decrease
	500	Positive			Increase
	800	Positive			Increase
	1000	Positive			Increase
	1500	Positive			Increase
2	100	Negative	1960-1980	Negative	Increase
	500	Positive			Decrease
	800	Positive			Decrease
	1000	Positive			Decrease

Mode Number	EOF		PC		Sound Speed
	Depth	Value	Time	Value	
	1500	Positive			Decrease
3	100	Negative	1960-1990	Positive	Decrease
	500	Positive			Increase
	800	Negative			Decrease
	1000	Negative			Decrease
	1500	Negative			Decrease
3	100	Negative	1990-2014	Negative	Increase
	500	Positive			Decrease
	800	Negative			Increase
	1000	Negative			Increase
	1500	Negative			Increase
4	100	Negative	1990-2000	Positive	Decrease
	500	Negative			Decrease
	800	Positive			Increase
	1000	Positive			Increase
	1500	Positive			Increase
4	100	Negative	1960-1990 2000-2014	Negative	Increase
	500	Negative			Increase
	800	Positive			Decrease
	1000	Positive			Decrease
	1500	Positive			Decrease

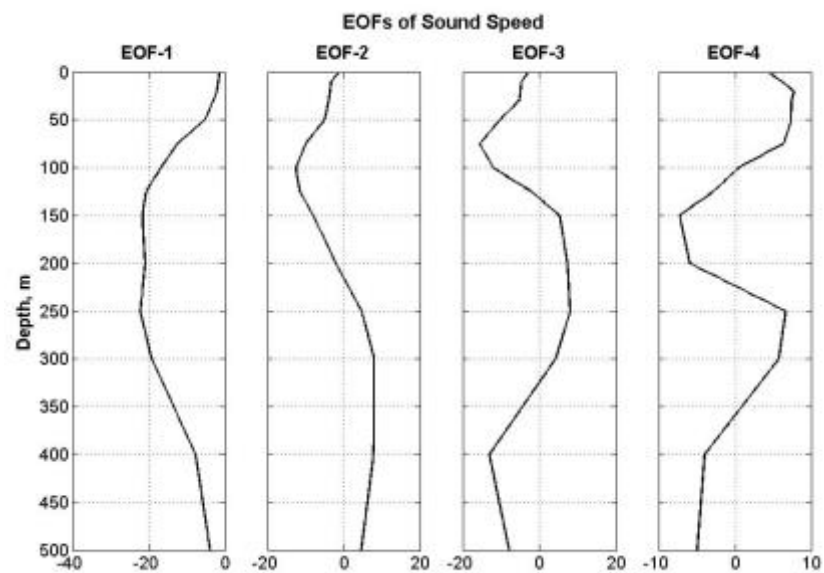


Figure 110. The First Four EOFs of Point F.

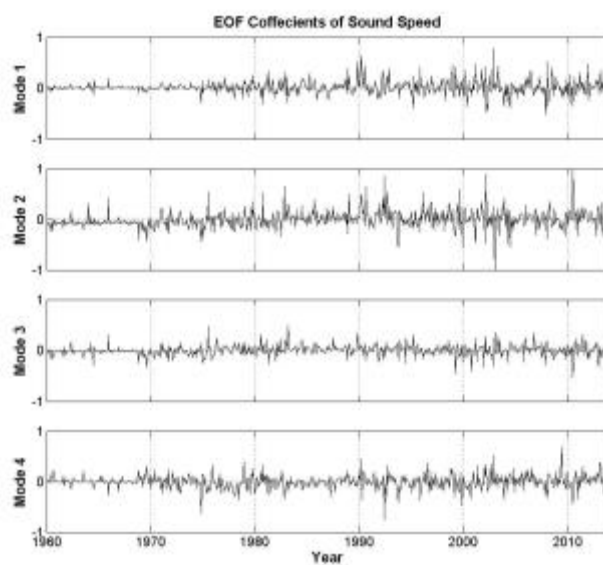


Figure 111. Coefficients of Sound Speed of Point F.

Table 20. EOF Analysis at Point F.

Mode Number	EOF		PC		Sound Speed
	Depth	Value	Time	Value	
1	50	Positive	1960-2014	Positive	Increase
	100	Positive			Increase
	200	Negative			Decrease
	400	Positive			Increase
2	50	Negative	1960-1980	Positive	Decrease
	100	Negative			Decrease
	200	Negative			Decrease
	400	Positive			Increase
2	50	Negative	1980-2014	Negative	Increase
	100	Negative			Increase
	200	Negative			Increase
	400	Positive			Decrease
3	50	Negative	1980-2000	Positive	Decrease
	100	Negative			Decrease
	200	Positive			Increase
	400	Negative			Decrease
3	50	Negative	1960-1980 2000-2014	Negative	Increase
	100	Negative			Increase
	200	Positive			Decrease
	400	Negative			Increase
4	50	Positive	1960-1970 2000-2014	Positive	Increase
	100	Positive			Increase
	200	Negative			Decrease
	400	Negative			Decrease
4	50	Positive	1970-2000	Negative	Decrease
	100	Positive			Decrease
	200	Negative			Increase
	400	Negative			Increase



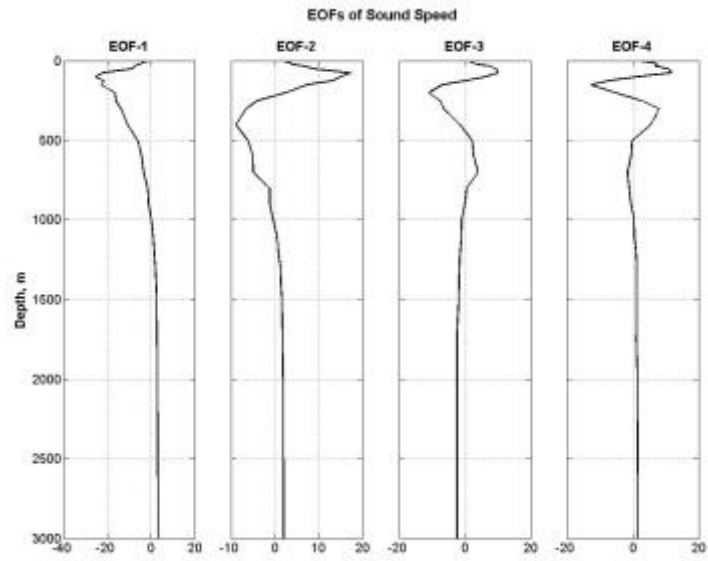


Figure 112. The First Four EOFs of Point G.

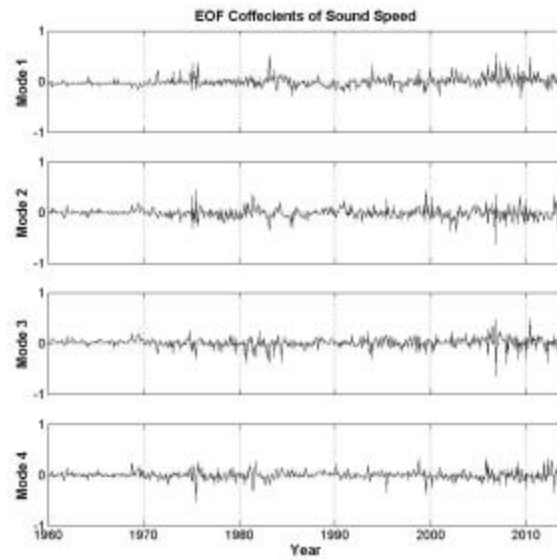


Figure 113. Coefficients of Sound Speed of Point G.

Table 21. EOF Analysis at Point G.

Mode Number	EOF		PC		Sound Speed
	Depth	Value	Time	Value	
1	100	Negative	2000-2014	Positive	Decrease
	500	Negative			Decrease
	800	Negative			Decrease
	1000	Positive			Increase
	1500	Positive			Increase
1	100	Negative	1960-2000	Negative	Increase
	500	Negative			Increase
	800	Negative			Increase
	1000	Positive			Decrease
	1500	Positive			Decrease
2	100	Positive	1960-1970	Positive	Increase
	500	Negative			Decrease
	800	Negative			Decrease
	1000	Negative			Decrease
	1500	Positive			Increase
2	100	Positive	1970-2014	Negative	Decrease
	500	Negative			Increase
	800	Negative			Increase
	1000	Negative			Increase
	1500	Positive			Decrease
3	100	Positive	1960-1970 1990-2014	Positive	Increase
	500	Positive			Increase
	800	Positive			Increase
	1000	Negative			Decrease
	1500	Negative			Decrease
3	100	Positive	1970-1990	Negative	Decrease
	500	Positive			Decrease
	800	Positive			Decrease
	1000	Negative			Increase
	1500	Negative			Increase
4	100	Positive	1960-1970 1980-2000	Positive	Increase
	500	Negative			Decrease
	800	Negative			Decrease
	1000	Positive			Increase
	1500	Positive			Increase
4	100	Positive	1970-1980 2000-2014	Negative	Decrease
	500	Negative			Increase
	800	Negative			Increase

Mode Number	EOF		PC		Sound Speed
	Depth	Value	Time	Value	
	1000	Positive			
	1500	Positive			Decrease

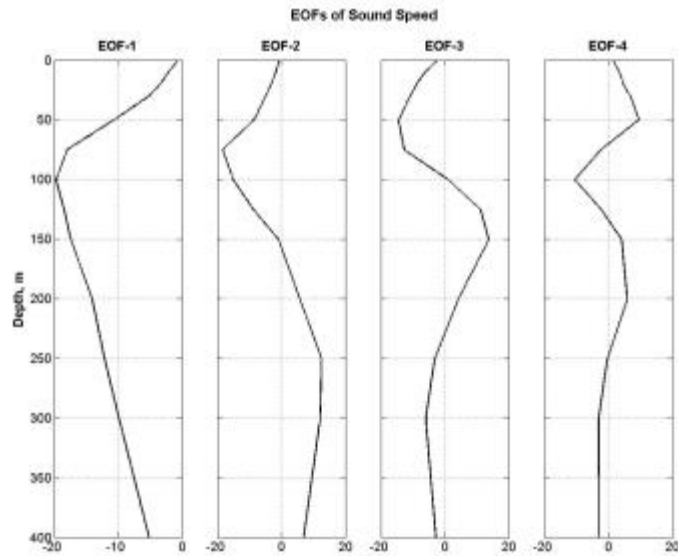


Figure 114. The First Four EOFs of Point H.

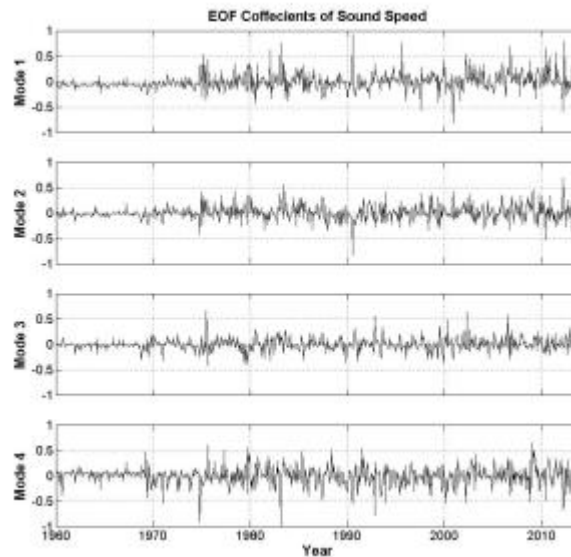


Figure 115. Coefficients of Sound Speed of Point H.

Table 22. EOF Analysis at Point H.

Mode Number	EOF		PC		Sound Speed
	Depth	Value	Time	Value	
1	50	Negative	1990-2014	Positive	Decrease
	100	Negative			Decrease
	200	Negative			Decrease
	400	Positive			Increase
1	50	Negative	1960-1990	Positive	Decrease
	100	Negative			Decrease
	200	Negative			Decrease
	400	Positive			Increase
2	50	Negative	1970-1990 2000-2014	Positive	Decrease
	100	Negative			Decrease
	200	Positive			Increase
	400	Positive			Increase
2	50	Negative	1960-1970 1990-2000	Negative	Increase
	100	Negative			Increase
	200	Positive			Decrease
	400	Positive			Decrease
3	50	Negative	1980-1990 2000-2014	Positive	Decrease
	100	Positive			Increase
	200	Positive			Increase
	400	Negative			Decrease
3	50	Negative	1960-1980 1990-2000	Negative	Increase
	100	Positive			Decrease
	200	Positive			Decrease
	400	Negative			Increase
4	50	Positive	1960-1970 1980-1990 2000-2014	Positive	Increase
	100	Positive			Increase
	200	Negative			Decrease
	400	Negative			Decrease
4	50	Positive	1970-1980 1990-2000	Negative	Decrease
	100	Negative			Increase
	200	Positive			Decrease
	400	Negative			Increase

According to EOF analysis of Point A through H, sound speed does not exhibit interannual variability below a depth of 1500 meters at Point A, B, C, D, E and G there is a high variability from 1970 to 2014. Mode 1 and mode 2 covers the majority of data.

Sound speed is faster between 1960 and 1970 for all points except point F which is slower until 1980. From 1970 to 1990 the sound speed is slower for all points except for points B, E and F. From 1990 to 2000 the sound speed is faster for all points except for point E. From 2000 to 2014 the sound speed also faster for all points, except for points B, E and H. A more detailed research is needed to find out the dynamic process that caused these differences.

### **C. TRANSMISSION LOSS DUE TO SHORT-TERM INTER ANNUAL VARIABILITY**

As earlier, January and July have been selected to represent the dry and rainy seasons. Time periods were selected according to years, which have significant interannual variability (3-7 years), then find the TL distributions by modeling the acoustic environment using the SMG-WOD database. Figures 116–124 show the comparisons due to short-term interannual variability, January at the left column and July at the right column.

# 1. Point A

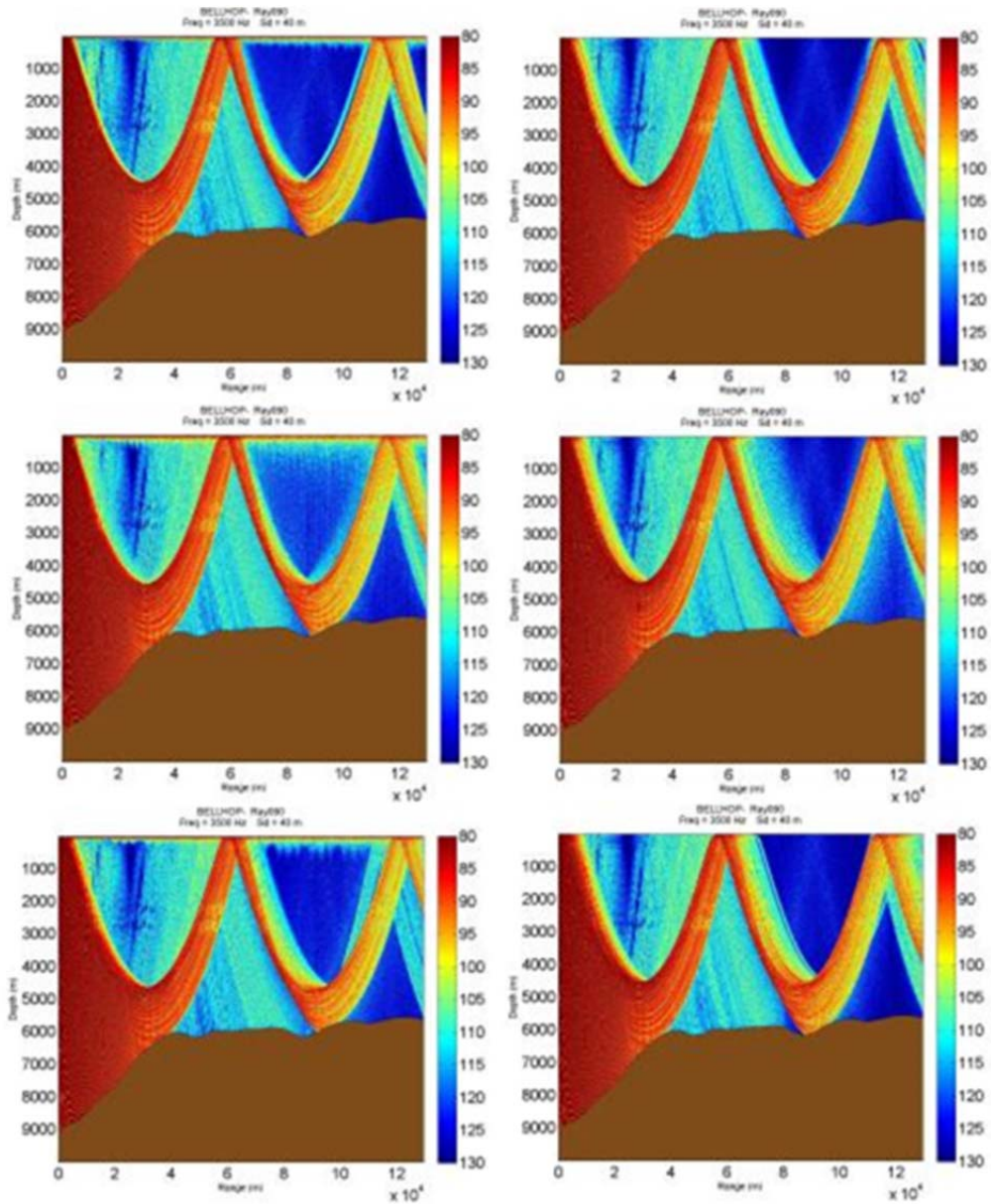


Figure 116. TL for 1960–1967 (upper panels), 1975–1978 (middle panels) and 2005–2008 (lower panels) for Point A in January (left column) and July (right column).

TL distributions in January 1960–1967 time period (upper left) has a 80 dB TL at close distances and shows surface duct propagation to distances of more than 120 km. It shows a large shadow zone and convergence zone at approximately 60 km; between the shadow zone it has 100–130 dB TL. The 1975–1978 time period (middle left) shows a

TL of 80 dB at close distances. Specifically, it exhibits a lower TL at the surface duct and in the upper ray limit of the convergence zone, and less TL at long range between the convergence zones. As compared to the 2005–2008 time period (lower left) the 1975–1978 time period has a lower TL for close ranges, and long ranges.

TL distributions in July 1960–1967 (upper right) and 2005–2008 (lower right) shows similar TL at close and long ranges, in the 2005–2008 time period shows a lower TL at long ranges. In the 1975–1978 time period has the lowest TL mainly on the long range. Also, January shows significantly more variations than July that will make January to have less TL mainly in the gap between convergence zones at long ranges.

## 2. Point B

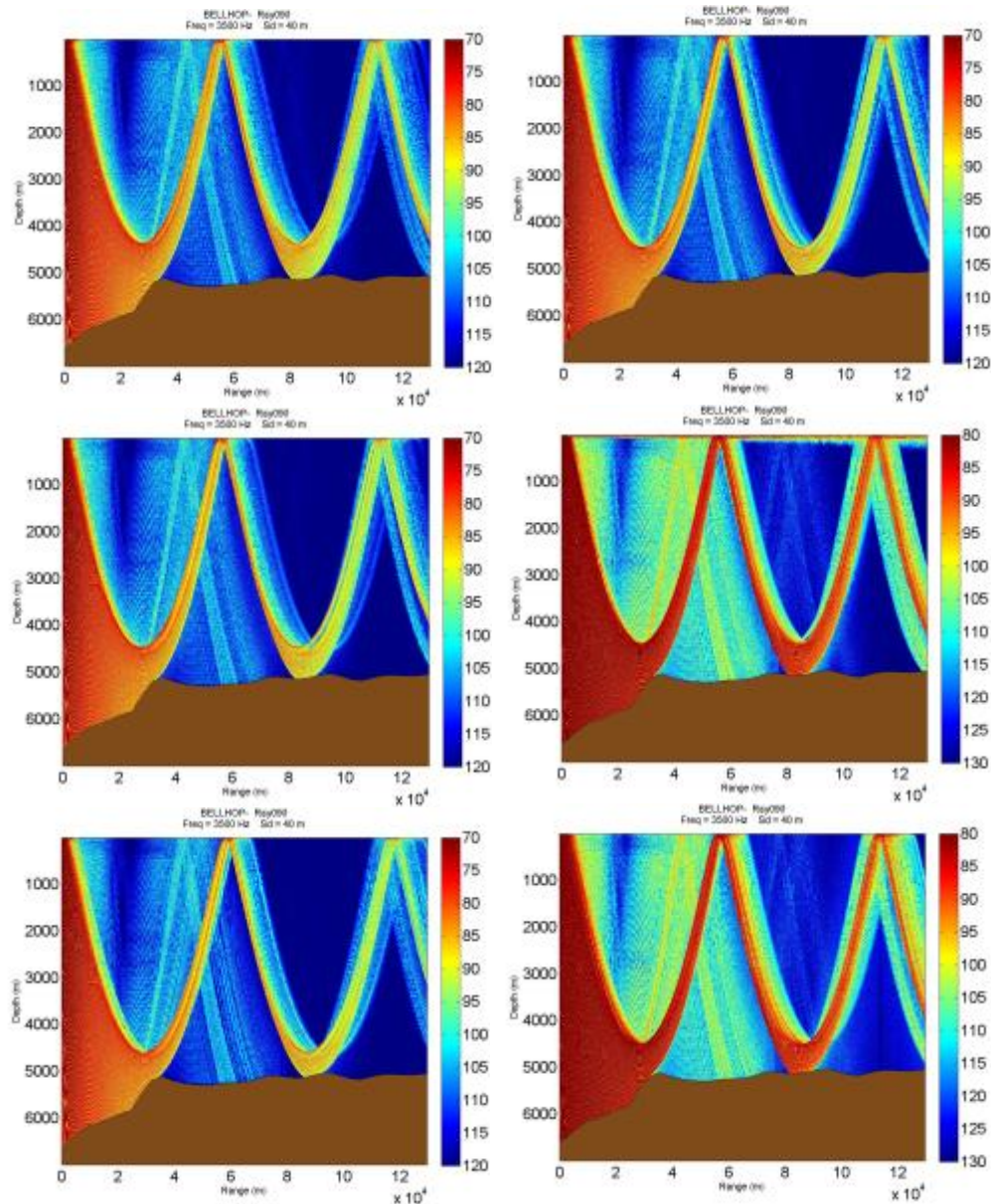


Figure 117. TL for 1960–1967 (upper panels), 1975–1978 (middle panels) and 2005–2008 (lower panels) for Point B in January (left column) and July (right column).

TL distributions in January 1960–1967 (upper left) has 70 dB TL at close distances. It shows large shadow zone and convergence zone at approximately 60 km; between the shadow zones, it has 100–130 dB TL. The 1975–1978 time period (middle left) and the 2005–2008 times period (lower left) shows similar TL pattern of 70 dB at



close distances, with less TL at long range propagation. As compared the three ray path have similar TL with the 2005–2008 has the least TL at the long-range propagation.

TL distributions in July 1960–1967 (upper right) has 70 dB TL at close distances with no surface duct and have the convergence zone at approximately 60 km. In 1975–1978 (middle right) shows a higher TL of 80dB at close distance, and have the surface duct that does not occurred in the other time period parts, with the similar distance of the convergence zones, but has less TL in the zone between the ray paths with more scatterings. In 2005–2008 (lower right) shows a higher TL of 80 dB at close distance similar with the 1975–1978 time period, but with no surface duct. In the 1960–1967 time period has the lowest TL mainly on the long range. Also, July shows significantly more variations than January that will make July to have less TL mainly in the gap between convergence zones at long ranges.

### 3. Point C

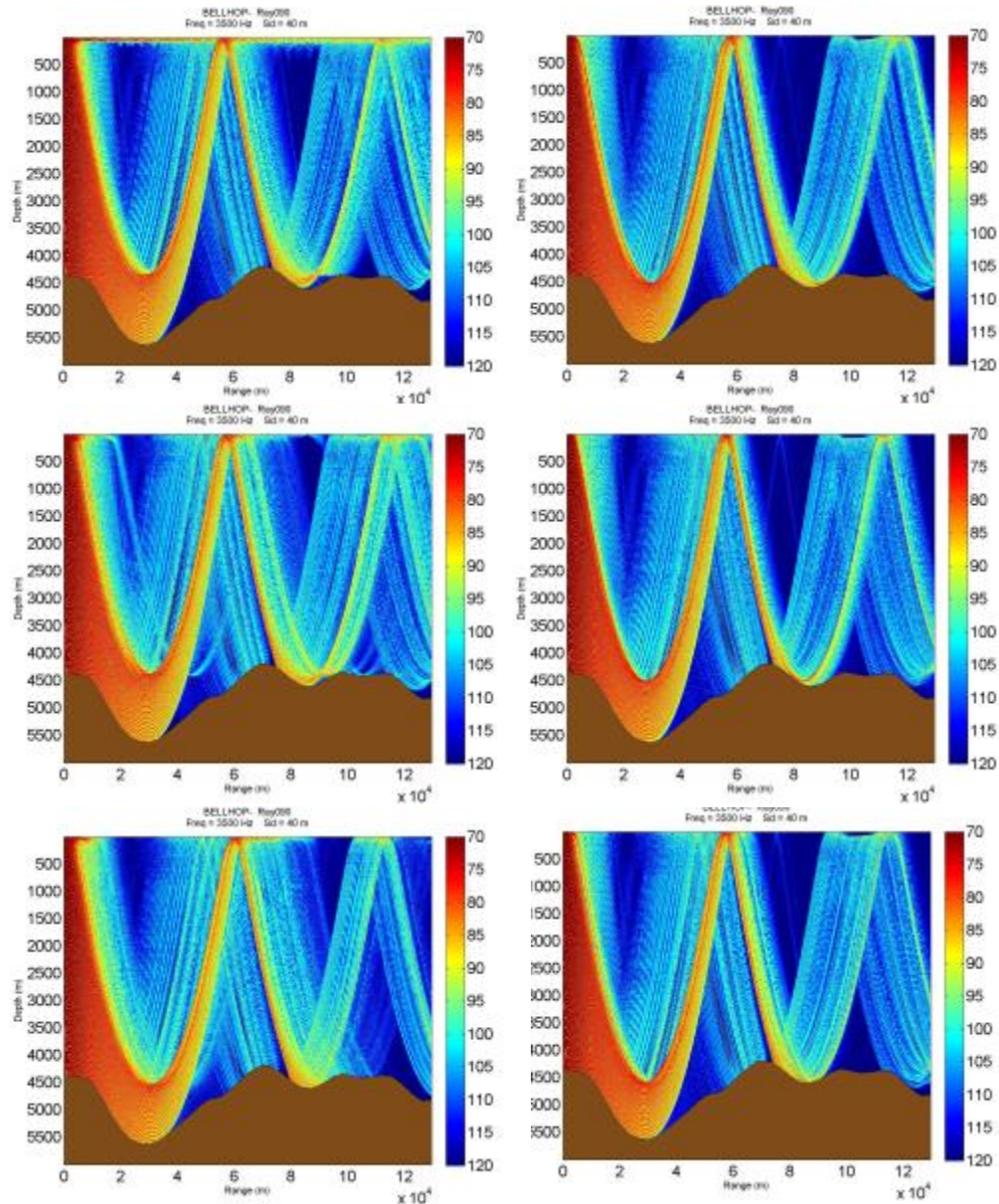


Figure 118. TL for 1962–1965 (upper panels), 1975–1978 (middle panels) and 2005–2008 (lower panels) for Point C in January (left column) and July (right column).

TL distributions in January 1962–1965 (upper left) has 70 dB TL at close distances and shows surface duct propagating to long distance more than 120 km, with TL from 70 dB to 90 dB. It shows large shadow zone and convergence zone at approximately 60 km; between the shadow zones, it has 90–120 dB TL. The 1975–1978

time period (middle left) and the 2005–2008 times period (lower left) shows similar TL pattern of 70 dB at close distances, with less TL at close and long range propagation, with no surface duct. In the 2005–2008 times period shows a weak surface duct from the convergence zone to approximately 20 km of distance. As compared the three ray path have similar TL, with the 1962–1965 has the least TL at the short and long-range propagation.

TL distributions in July 1962–1965 (upper right) has 70 dB TL at close distances with no surface duct and has the convergence zone at approximately 60 km. In 1975–1978 (middle right) and in 2005–2008 (lower right) shows a similar ray path with 70 dB TL at close distances, with no surface duct. In the 1962–1965 time period has the lowest TL mainly on the short and long distance. Also, January shows significantly more variations than July that will make January to have less TL with the occurrence of the surface duct and more scattering between the convergence zone gaps.

#### 4. Point D

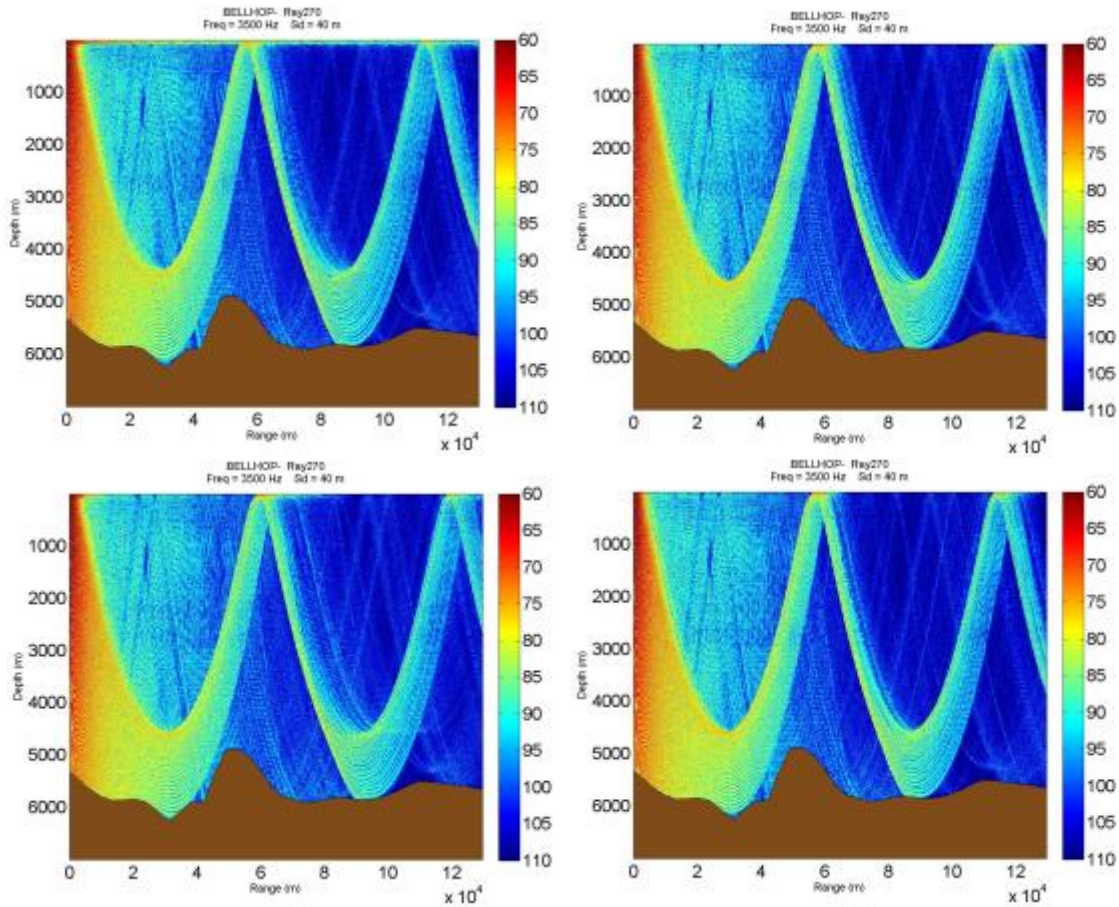


Figure 119. TL for 1961–1965 (upper panels) and 2005–2008 (lower panels) for Point D in January (left column) and July (right column).

TL distributions in January 1961–1965 (upper left) has 60 dB TL at close distances and shows surface duct propagating to long distance more than 120 km, with TL from 60 dB to 90 dB. It shows large shadow zone and convergence zone at approximately 60 km; between the shadow zones, it has 80–110 dB TL. The 2005–2008 time period (lower left) shows similar TL pattern of 70 dB at close distances, with less TL at close and long range propagation, with no surface duct. As compared the two ray path have similar TL, with the 1961–1965 has the least TL at the short and long-range propagation.

TL distributions in July 1961–1965 (upper right) has 60 dB TL at close distances with no surface duct and have the convergence zone at approximately 60 km. In 2005–2008 (lower right) shows a similar ray path with 60 dB TL at close distances, with no surface duct. In the 1961–1965 time period has the lowest TL mainly on the long distance. Also, January shows more variations than July that will make January to have less TL with the occurrence of the surface duct and more scattering between the convergence zone gaps.

## 5. Point E

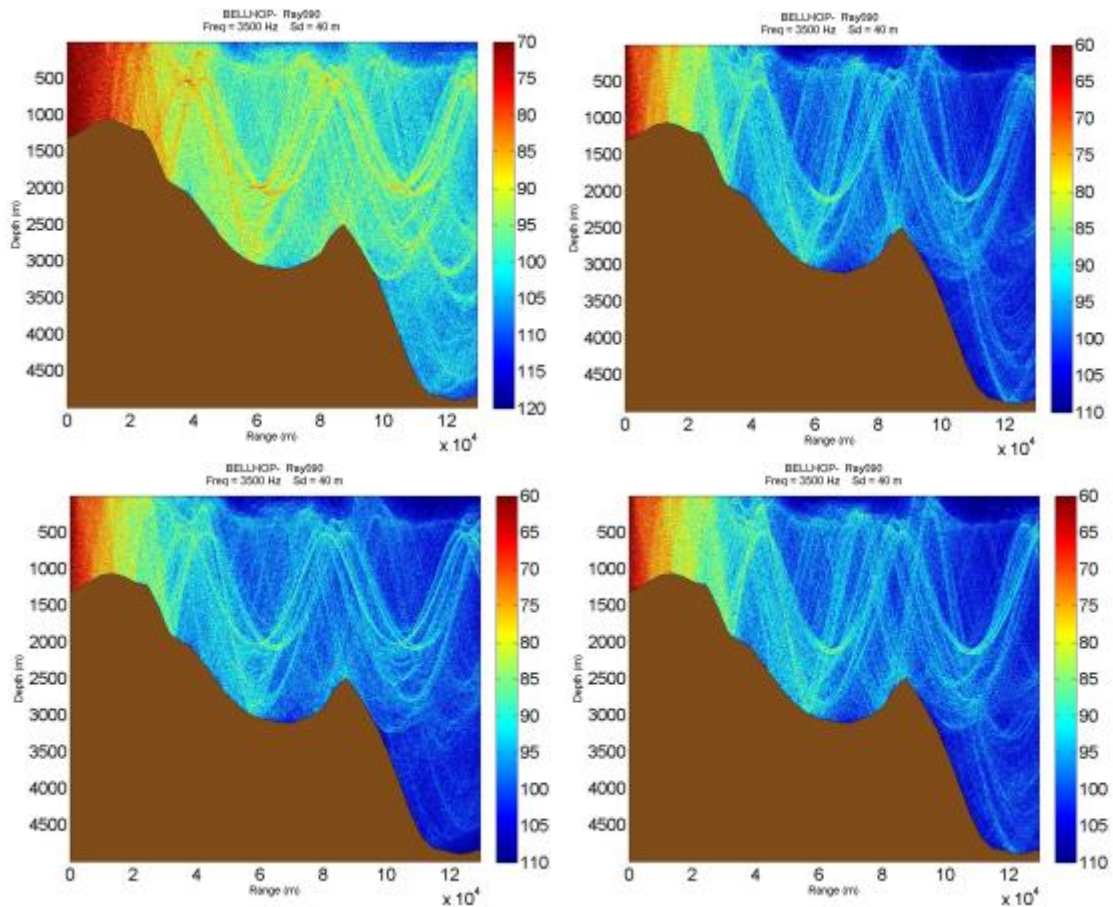


Figure 120. TL for 1962–1966 (upper panels) and 1969–1972 (lower panels) for Point E in January (left column) and July (right column).

TL distributions in January 1962–1966 (upper left) has 70 dB TL at close distances and shows refractions from the bottom seafloor through long distance, with TL from 70 dB to 100 dB. It does not show surface duct or a significant convergence zone. The 2005–2008 time period (lower left) shows similar TL pattern of 60 dB at close distances, with less variability in the sound propagation resulting less TL in the short distance but more TL in the long range propagation TL at close and long range propagation. As compared the two ray path have a different TL, with the 1962–1966 time period has the least TL at long-range propagation.

TL distributions in July 1962–1966 (upper right) has 60 dB TL at close distances with no surface duct and shows refractions from the bottom seafloor through long distance, with TL from 70 dB to 100 dB. In 2005–2008 (lower right) shows a similar ray path with 60 dB TL at close distances. In January 1962–1966 time period has the lowest TL mainly on the long distance. Also, January shows more variations than July that will make January to have less TL with the occurrence more scattering and intensification along the path.



## 6. Point F

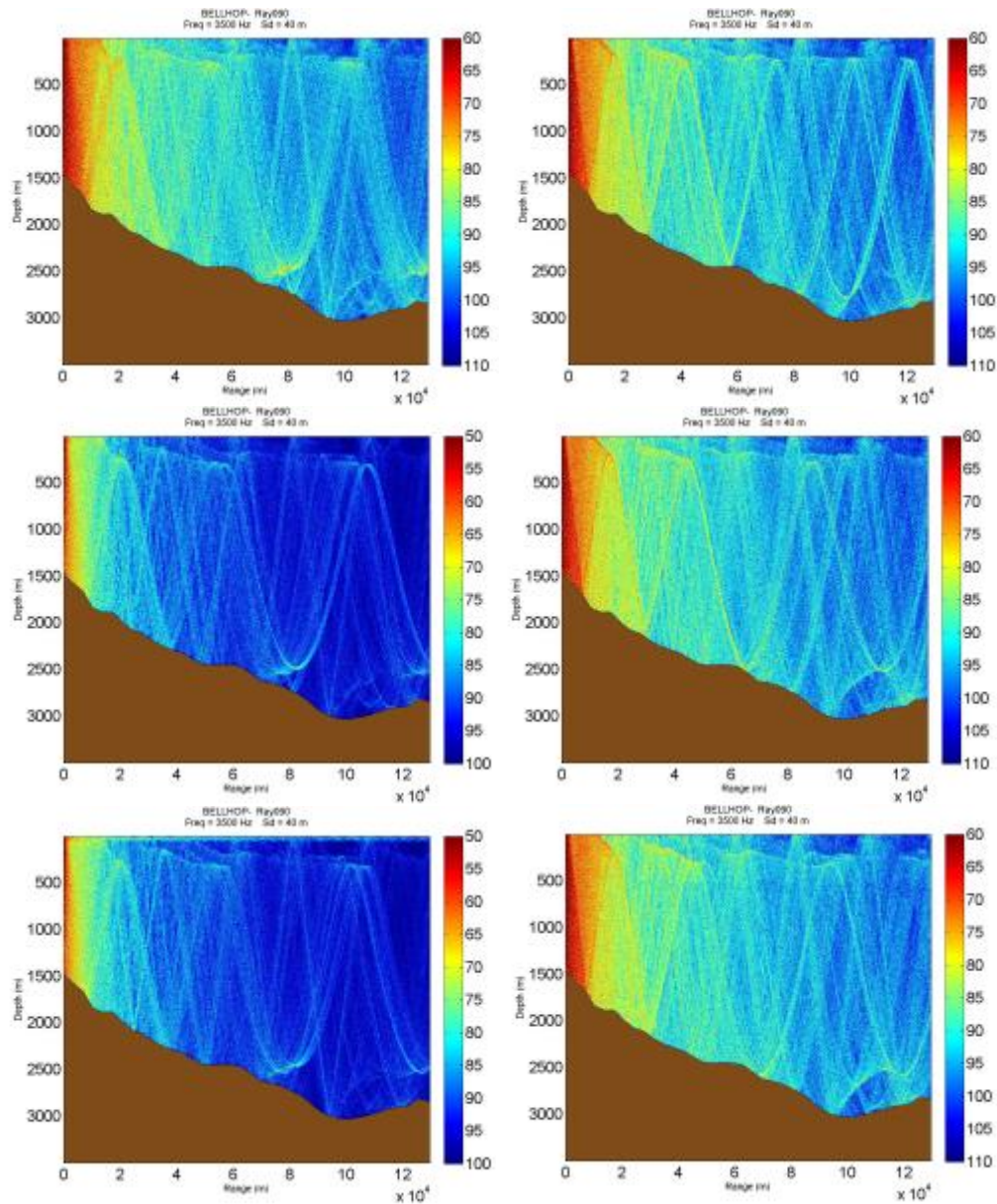


Figure 121. TL for 1960–1963 (upper panels), 1998–2002 (middle panels) and 2010–2013 (lower panels) for Point F in January (left column) and July (right column).

TL distributions in January 1962–1965 (upper left) has 60 dB TL at close distances. It does not show shadow zone and convergence zone, because it has many refractions from the bottom sea floor. The refractions help the propagation to a longer

range with TL 75 to 95 dB. The 1998–2002 time period (middle left) and the 2005–2008 times period (lower left) shows similar TL pattern but with a stronger close distance propagation with 50 dB of TL at close distances, and weaker long distance propagation with TL 75 to 100 dB. In the 2010–2013 time period we found surface duct that will enhance the sound propagation. As compared the three ray path have similar TL with the 1960–1963 time period has the least TL at the long-range propagation.

TL distributions in July 1962–1965 (upper right) has 60 dB TL at close distances. It does not show shadow zone and convergence zone, because it has many refractions from the bottom sea floor. The refractions help the propagation to a longer range with TL 75 to 95 dB. The 1998–2002 time period (middle left) and 2010–2013 times period (lower left) shows similar TL pattern but with a stronger long distance propagation with TL 75 to 95 dB. In the 1998–2002 and 2010–2013 time period has the highest TL mainly on the long range. Also, July shows significantly more variations than January that will make July to have less TL mainly at long ranges.



## 7. Point G

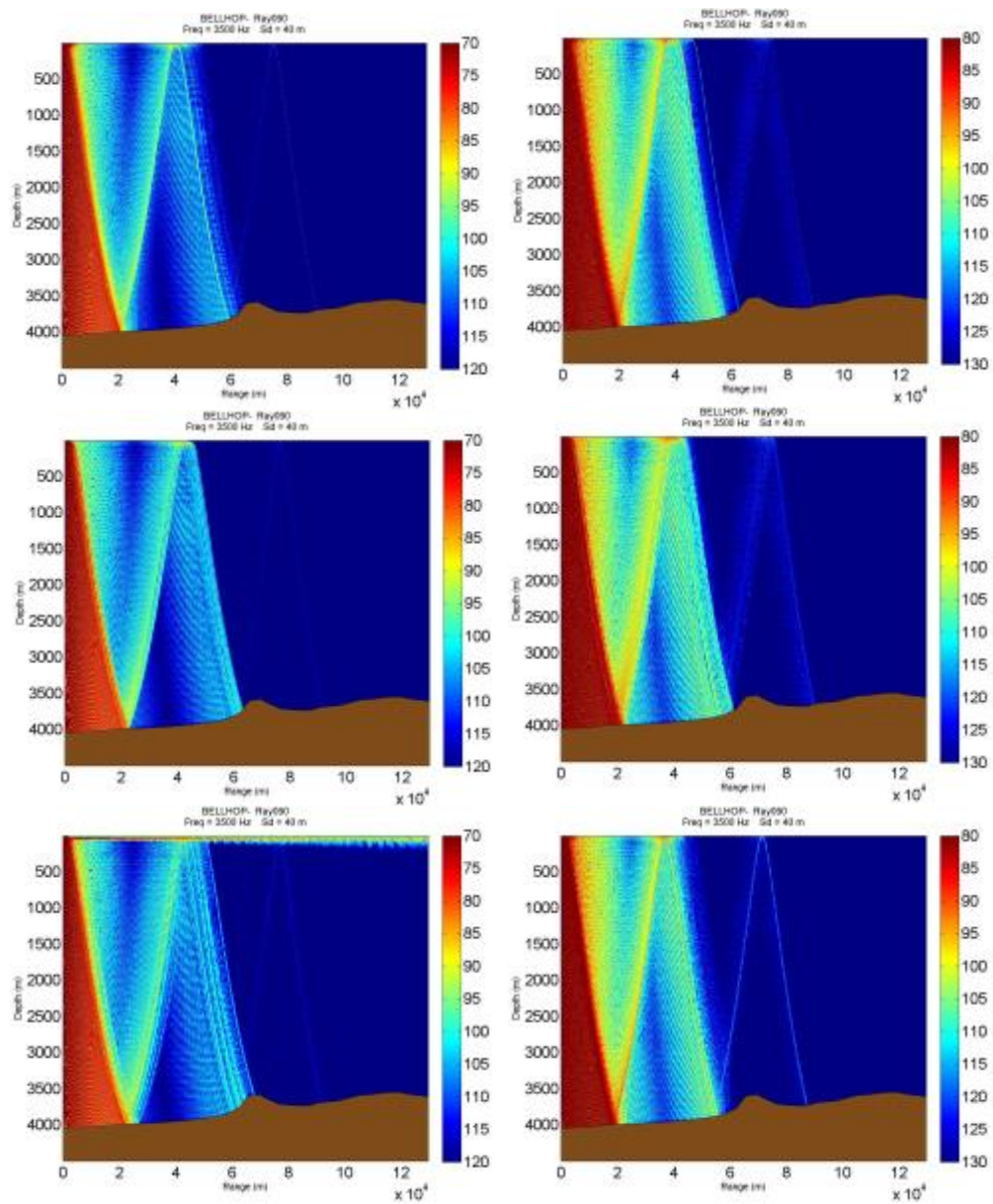


Figure 122. TL for 1960–1967 (upper panels), 1997–2001 (middle panels) and 2009–2012 (lower panels) for Point G in January (left column) and July (right column).

TL distributions in January 1960–1967 (upper left) has 70 dB TL at close distances. It shows convergence zone at approximately 40 km of distance, and after the convergence zone the TL increasing significantly from 100 dB to 120 dB. It does not show

surface duct. The 1997–2001 time period (middle left) shows similar TL pattern with the 1960–1967 time period, with slightly lower TL at the ray path after the convergence zone. In the 2009–2012 time period we found surface duct that will enhance the sound propagation at the surface layer to a long distance, in the deeper layer it has the similar pattern of TL with the 1960–1967 and 1997–2001 time period. As compared the three ray path have similar TL with the 2009–2012 time period, which has the least TL at the long-range propagation.

TL distributions in July 1960–1967 (upper right) has 80 dB TL at close distances. It shows convergence zone at approximately 40 km of distance and after the convergence zone the TL increasing significantly from 100 dB to 130 dB, with a weak sound propagation after the second convergence zone, and it does not show surface duct. The 1997–2001 time period (middle right) shows similar TL pattern with the 1960–1967 time period. In the 2009–2012 time period we found a similar TL pattern with the 1997 and 1960–1967 time period with less sound propagation spreading after the second convergence zone. In the 2009–2012 time period has the lowest TL mainly on the long range. Also, July shows more variations than January that will make July to have less TL at short and long ranges.

## 8. Point H

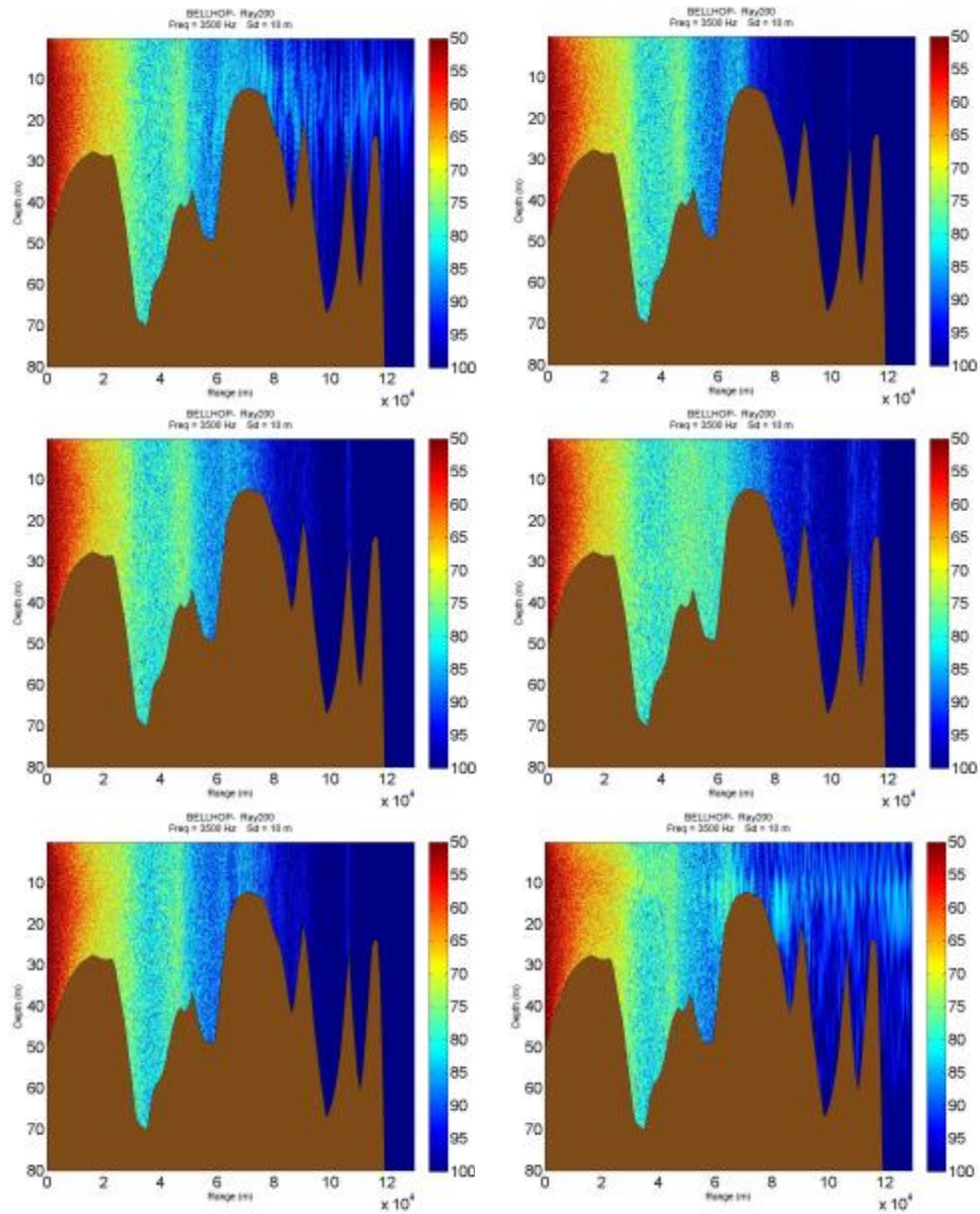


Figure 123. TL for 1964–1969 (upper panels), 1997–2001 (middle panels) and 2009–2012 (lower panels) for Point G in January (left column) and July (right column).

TL distributions in January 1964–1969 (upper left) has 50 dB TL and a weak surface duct which make the sound propagation to be longer with less TL to 85 dB. It does not have a convergence zone, because it has shallow water propagation that

obstructed by the sea floor feature. The 1997–2001 time period (middle left) and the 2009–2012 times period (lower left) shows similar TL pattern at close distances has 50 dB TL, and high TL to 100 dB at the long distances approximately more than 10 km.

The 1964–1969 time period (upper right) and the 1997–2001 time period (middle right) shows similar TL pattern at close distances has 50 dB TL. And have high TL to 100 dB at the long distances approximately more than 10 km. It does not have a convergence zone, because it has shallow water propagation that obstructed by the sea floor feature. TL distributions in July 2009–2012 (lower right) has 50 dB TL and a weak surface duct which make the sound propagation to be longer with less TL to 85 dB. In January and July have similar variations, with slightly higher variations in July that will make July to have less TL long ranges. The sea floor feature restricts the sound propagation path in the shallow water depth, and a surface duct condition will enhance the sound propagation to a longer range with less TL.

## VI. CONCLUSIONS

The main purpose of this research is to study the effect of interannual variability of temperature and salinity in the Philippine Sea and South China Sea by using Synoptic Monthly Gridded – World Ocean Database (SMG-WOD) and Generalized Digital Environmental Model (GDEM) data in the BELLHOP acoustic propagation model.

The climatological (GDEM) and multi-year (SMG-WOD) mean synoptic databases correctly reproduce the stratification of the Philippine Sea and South China Sea. The Philippine Sea shows a greater scale of variability of spiciness than the South China Sea in July (rainy season), spiciness decreases in dry season and increases in rainy season. Philippine Sea is mostly affected by the western Pacific boundary currents, which cause it to have greater spiciness with a more regular variations compared with South China Sea that is mostly affected by intrusions from the Pacific western boundary currents. In addition, there are high Spiciness values around the Philippine Sea because of the North Eastern Circulation (NEC) delivering the North Pacific Tropical Water (NPTW) and North Pacific Intermediate Water (NPIW) with high salinity and temperature.

Eight locations were selected in the Philippine Sea and South China Sea to study the spatial and environmental differences aspect which could affect the seasonal and interannual variability in our area of research. A composite analysis method was applied to separate the seasonal and the interannual variability.

The temperature profiles at all the locations shows strong seasonality due to the significant heat flux and variations of the seasonal ocean circulation, and this seasonal circulation also strongly affected by the interannual and decadal variability, especially in the western Pacific, which have the influence from El Nino Southern Oscillation (ENSO) with a range period 3 – 7 years. Variability shows that the upper layer sound speed is strongly affected by seasonal temperature, while the lower level is determined by the pressure with no significant seasonal or interannual variability. The temperature and

salinity is generally oscillating in every decade especially from 1970 to 2009 from high to low approximately about 1.0 m<sup>3</sup>/kg of spiciness.

The SMG-WOD and GDEM sound speed profiles in the area of research are generally matched to each other with some differences especially in the thermoclines. The difference is possible because of the difference in the data resolution GDEM has 78 vertical layers with 0.25 degree of horizontal resolution, SMG-WOD has 57 vertical layers with 1 degree of horizontal resolution. And also GDEM data are calculated from 1945–2014, while SMG-WOD data are calculated from 1960–2014, a significant interannual and decadal variability between the year gap can cause a biased mean.

Empirical orthogonal functions (EOF) analysis was used to identify the main patterns of the interannual variability of the sound speed profiles. The number of modes to capture the significant total variance in the area (80%) will depend on each region. Shallower area should need fewer modes to cover the variances. From the analysis only 4 modes were needed in each point to reach cumulative variance of more than 80% except for point G it will need 6 modes to cover the variances more than 80%, possibly because of the water intrusions from the Philippine archipelago, which causes more variation at point G.

The maximum sound-speed interannual variability was observed in different periods for different points. The Philippine Sea (Point A to D) has a significant variability in 1960–1967, 1975–1978 and 2005–2008, with the largest variability in 1960–1967. In the Luzon strait (Point E) which is the area between Philippine Sea and South China Sea has a significant variability in 1962–1966 and 1969–1972, with the largest variability in 1962–1966. In South China Sea (Point F to H) has a significant variability in 1960–1969, 1986–1989, 1997–2001 and 2009–2013, with the largest variability in 2009–2013.

The interannual variability detected by the EOF analysis shows that the sound speed profile shapes would be different in the same seasons for different years. In the BELLHOP acoustic propagation model the sound source located at 40 m depth and has frequency of 3500 Hz. The propagation was modeled in certain directions up to a maximum range of 70 nautical miles. TL profiles modeled from SMG-WOD multi-year

monthly average are similar with those modeled from GDEM monthly mean sound speed profiles, but some differences were found in the ray scatterings and the forming of the surface ducts, which will affect the range of propagation and the transmission loss approximately around 10 dB.

TL was modeled in eight locations in the area using the BELLHOP acoustic environment model, and certain time intervals were chosen which related to the interannual variability based on the EOF analysis. The acoustic modeling was conducted for January and July since it is the significant month for the dry and rainy season that occurs in the Philippine Sea and South China Sea.

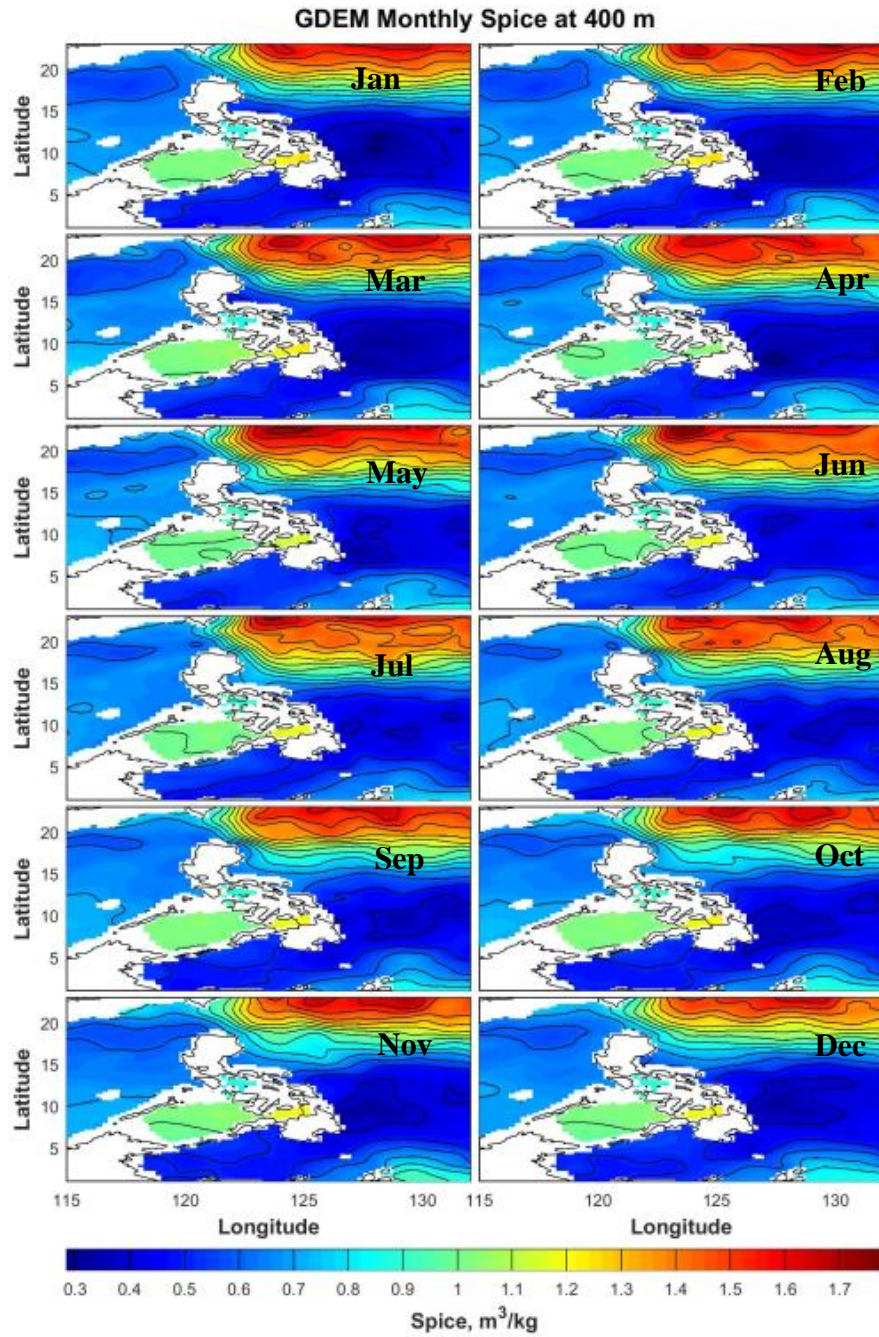
The TL shows some high interannual variability over convergence zone paths. A higher interannual variability is more significant at short distances around 5 km and less significant at longer distances. July showed slightly more interannual changes than January. Surface ducts varied in January, but in July, more scattering variations were found that will make less TL between the convergence zones. The interseasonal variability is more significant in the upper layer than the deeper layer especially in the dry season.

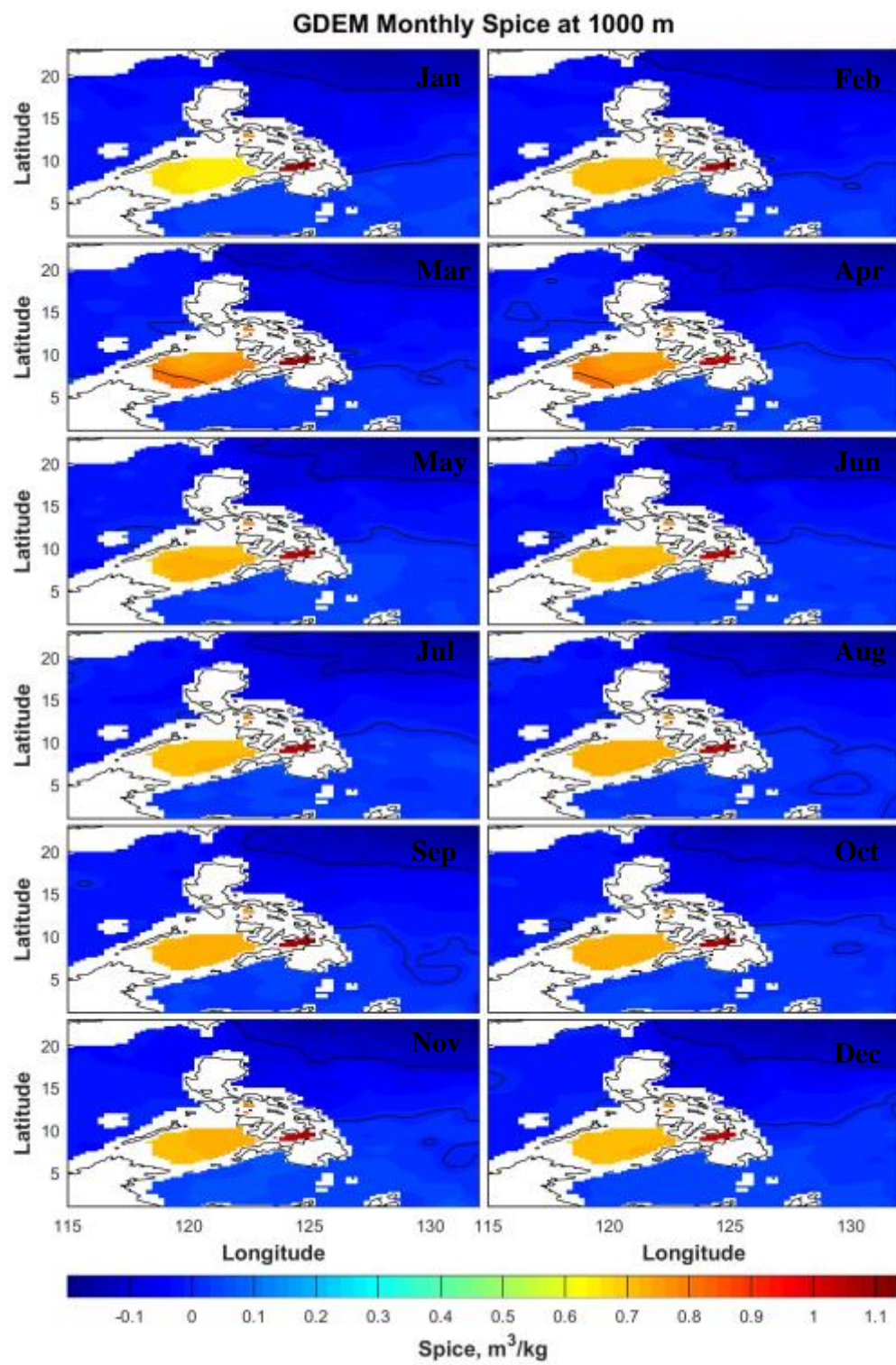
The convergence zones occur in the deep layer of the Philippine Sea and South China Sea in all seasons, except in point E, F and H which are shallower that will make the ray path to be more scattered. The surface duct will occur in the mixed layer in the dry season for deeper points because of the positive SSP gradient at the surface, supporting long distance acoustic detections. There are some differences between the GDEM and SMG-WOD to be considered for naval operations. For instance, the SMG-WOD showed less TL between the convergence zone than GDEM data, and GDEM shows a stronger (less TL) surface duct than SMG-WOD data. For submarine operations in the shadow zone, using SMG-WOD model will gives more awareness because more scattering (less TL) is shown in SMG-WOD due to interannual variability. Recommend a more detail research regarding the sound propagation variability due to significant interannual variability effect in a certain area and time, to anticipate the vulnerability in ASW.

THIS PAGE INTENTIONALLY LEFT BLANK



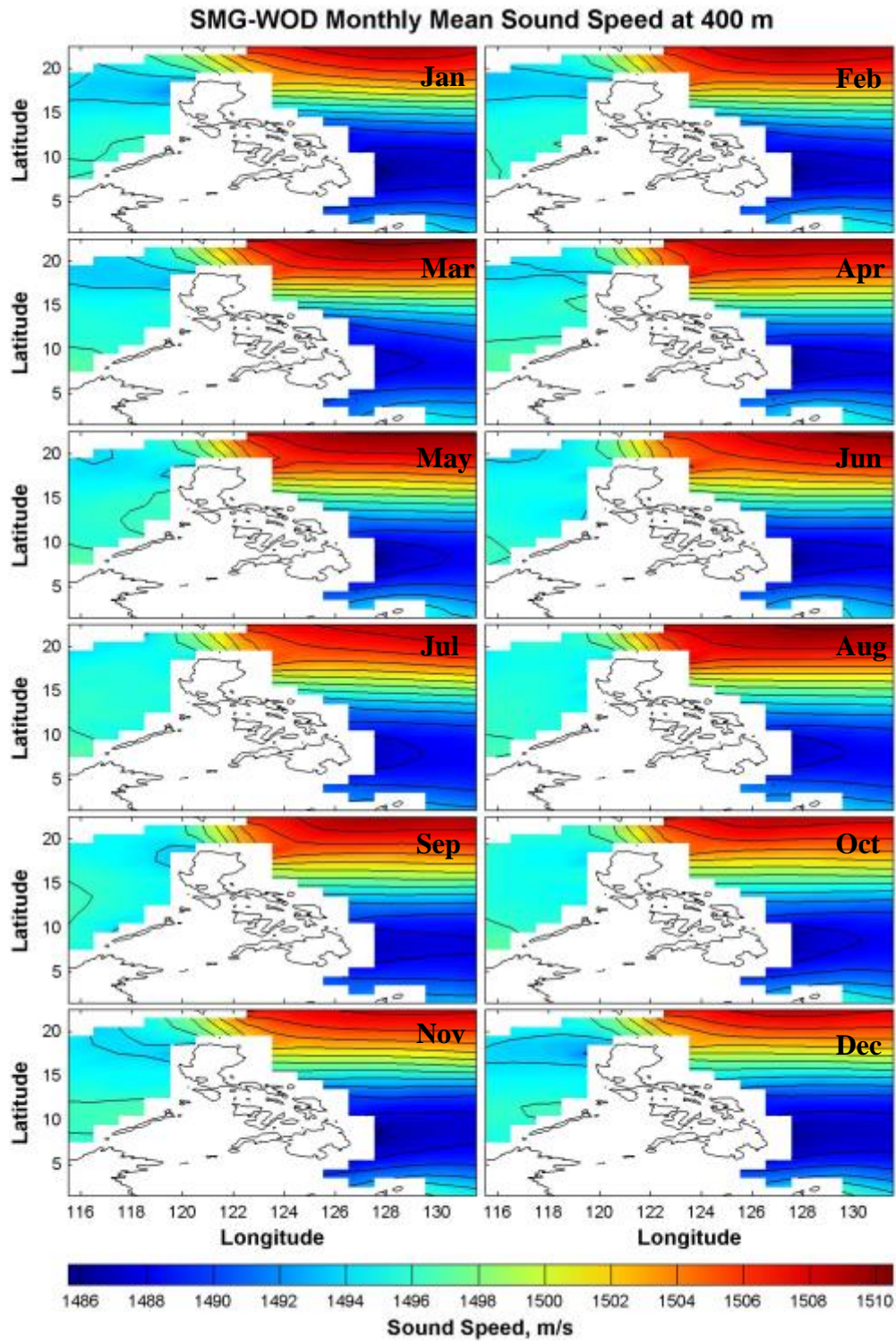
## APPENDIX. ADDITIONAL GDEM MONTHLY SPICINESS FIGURES

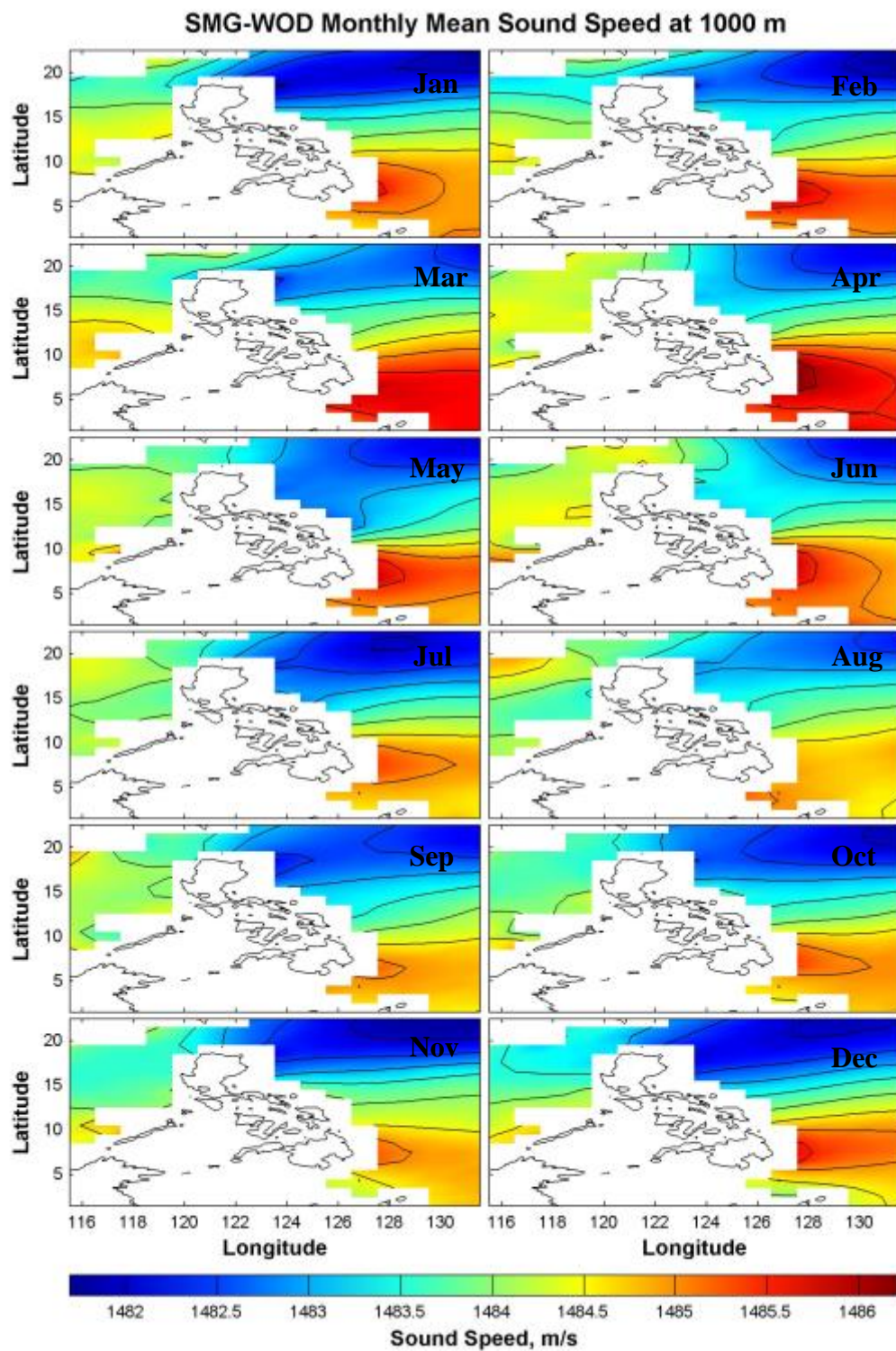






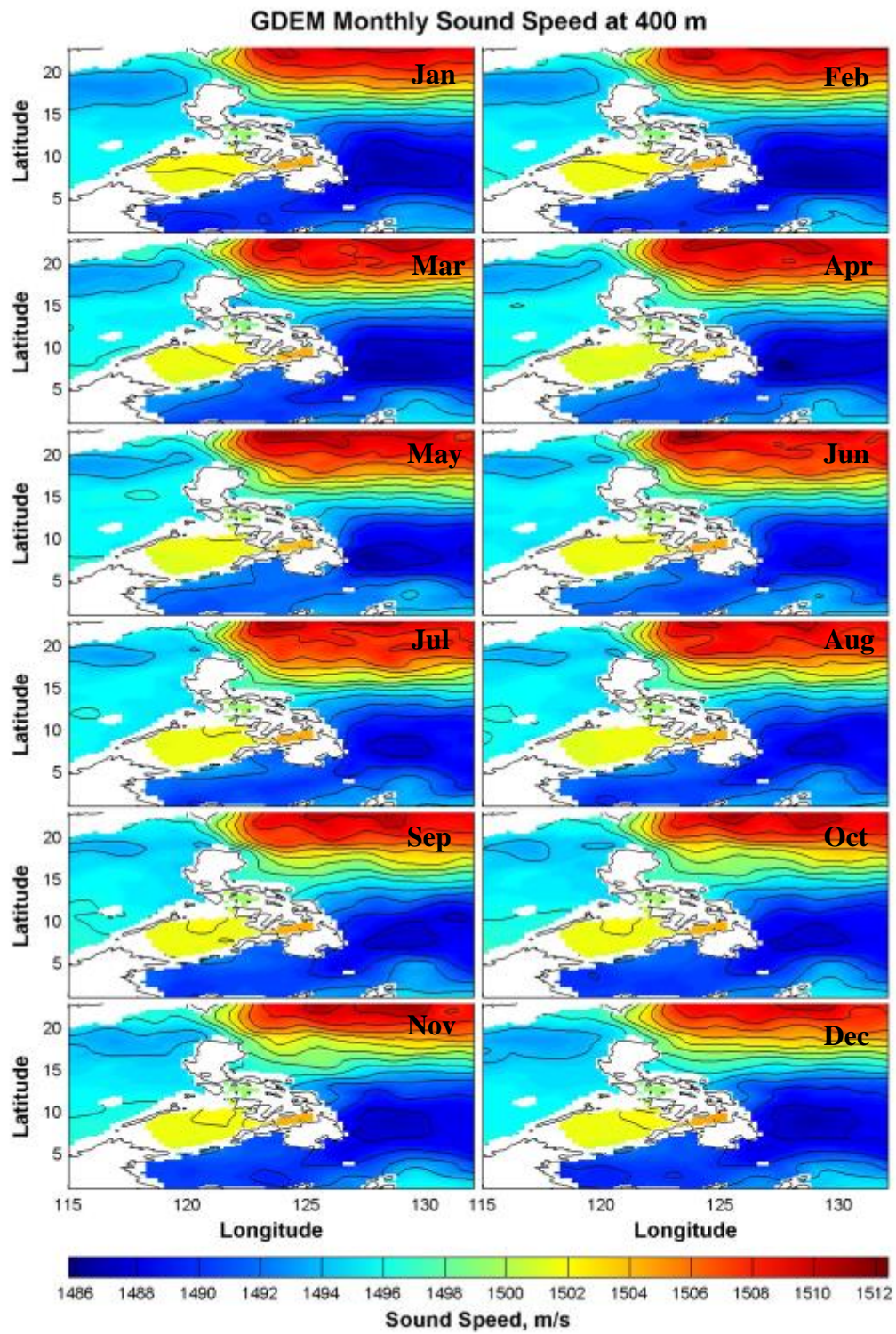
## APPENDIX B. ADDITIONAL SMG-WOD MONTHLY MEAN SOUND SPEED FIGURES

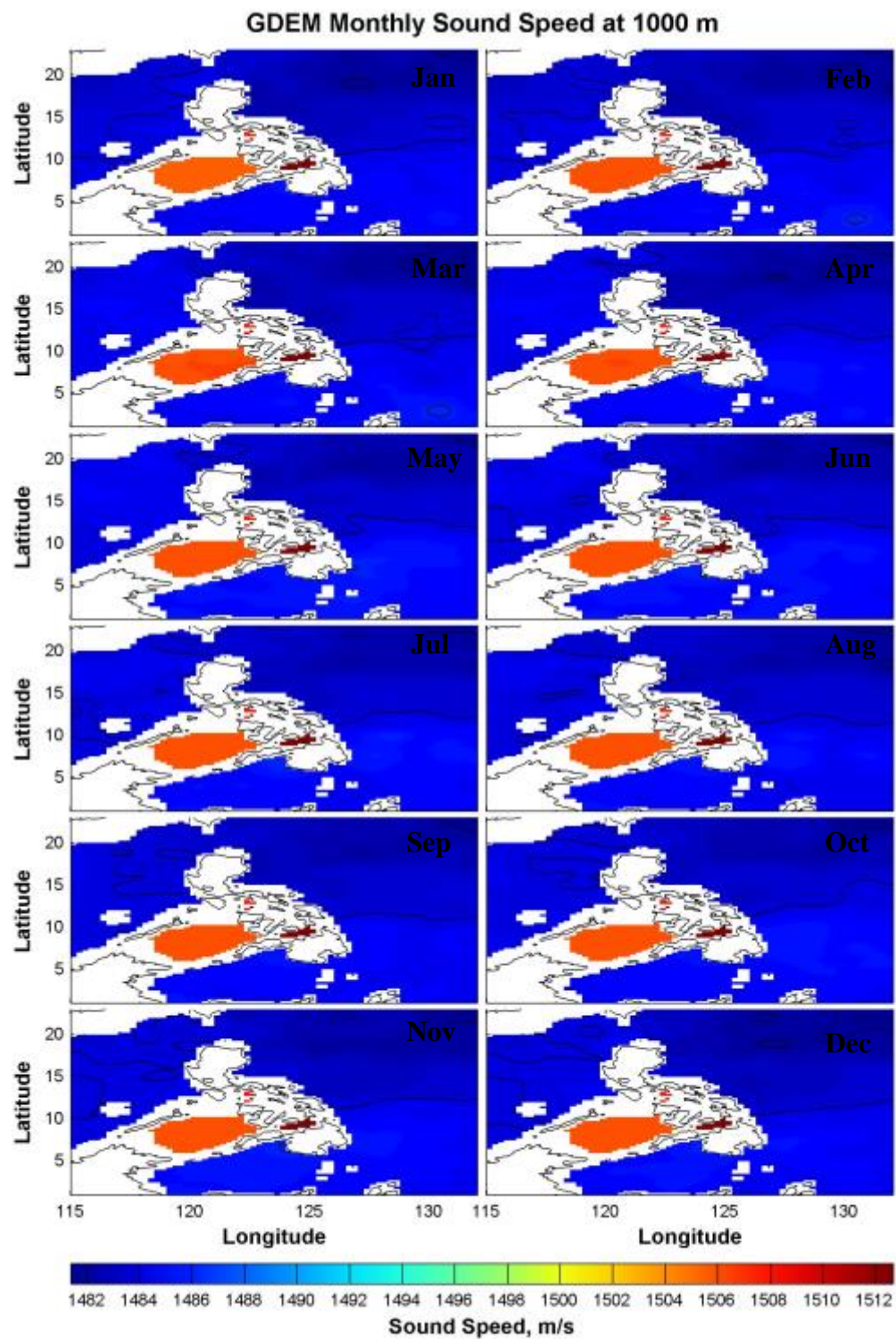






## APPENDIX C. ADDITIONAL GDEM MONTHLY SOUND SPEED FIGURES



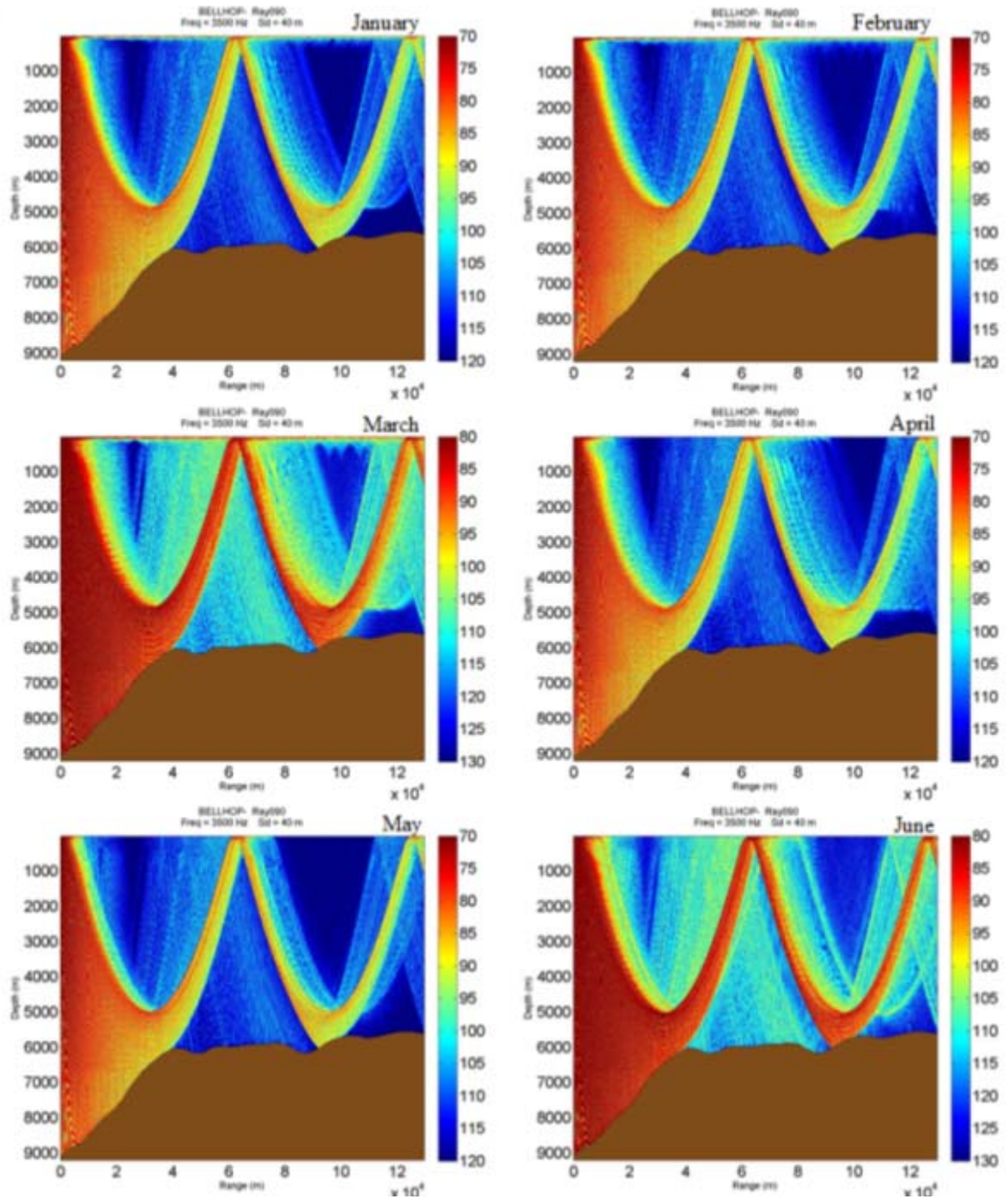


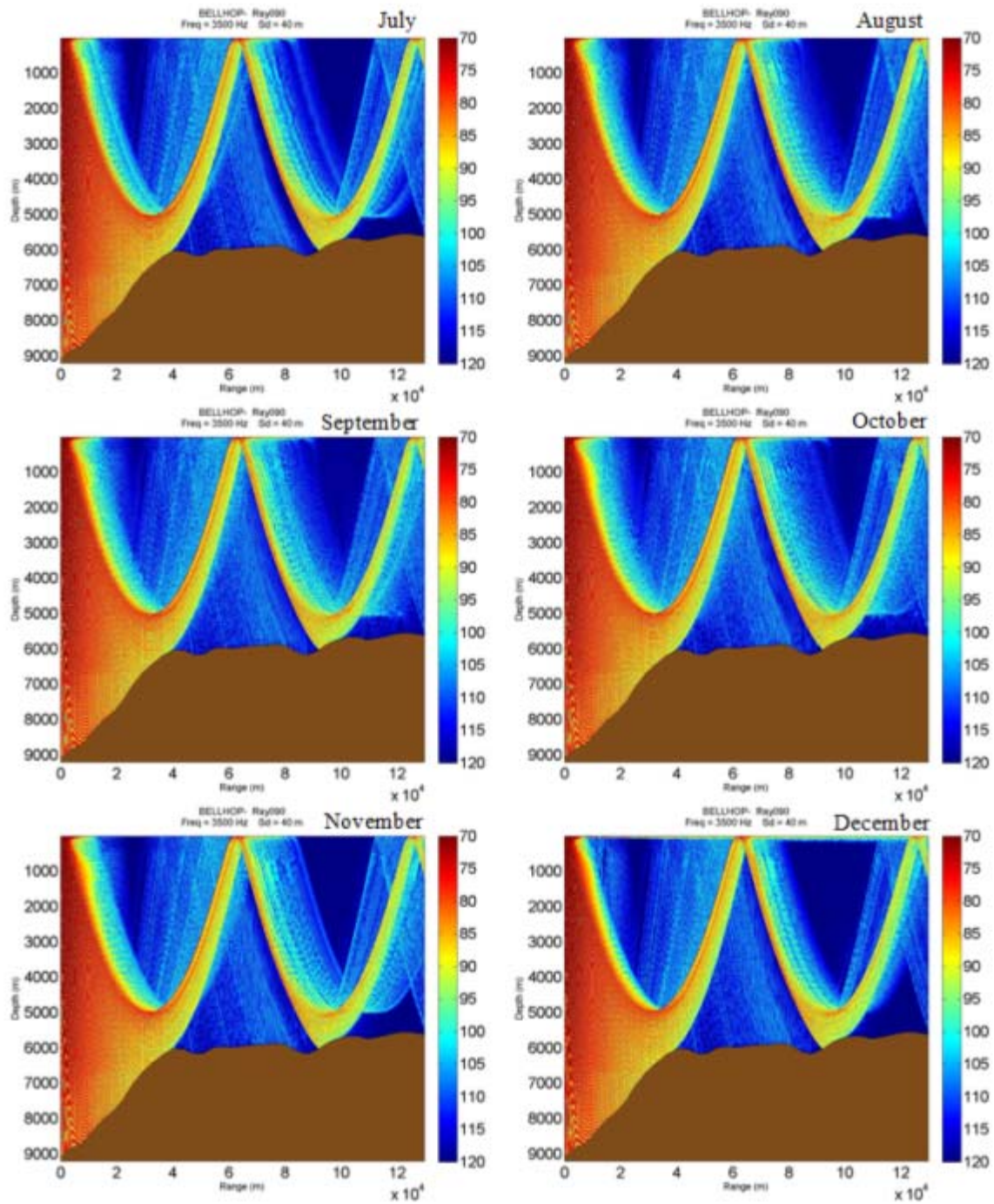


## APPENDIX D. MEAN TRANSMISSION LOSS-GDEM

Point A (126.666° E - 10.500° N)

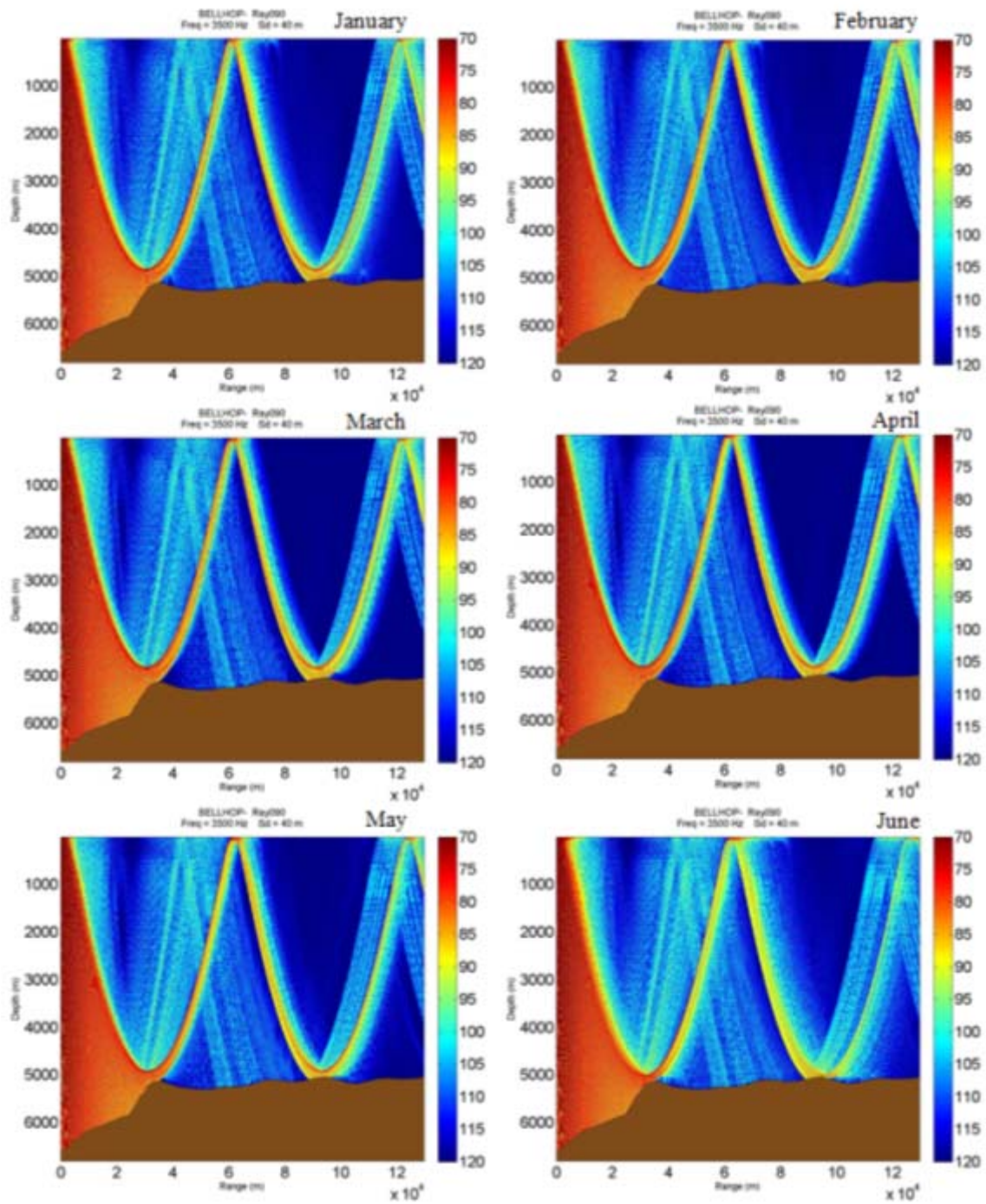
I

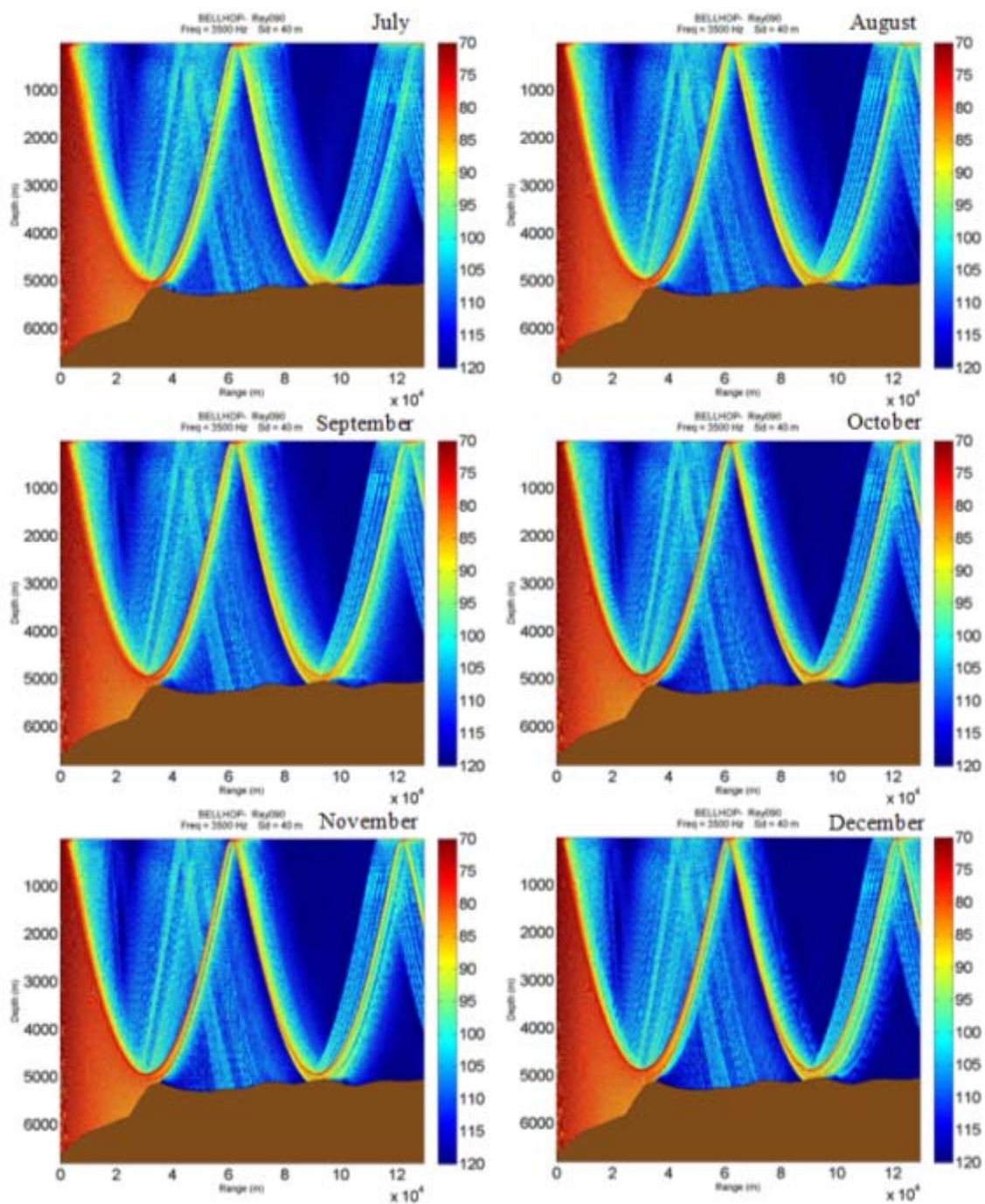






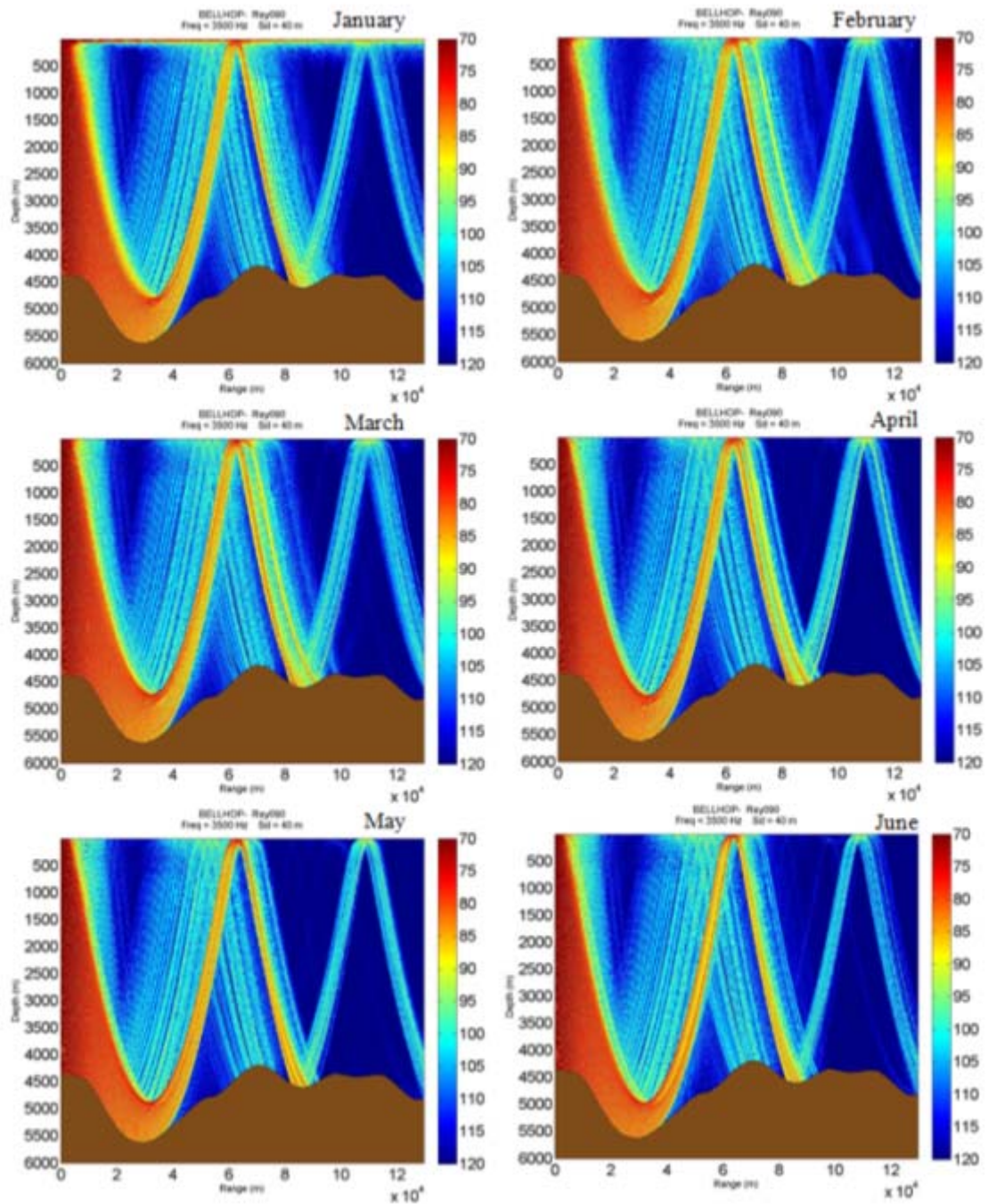
Point B ( $128.5458^{\circ}$  E –  $4.2448^{\circ}$  N)

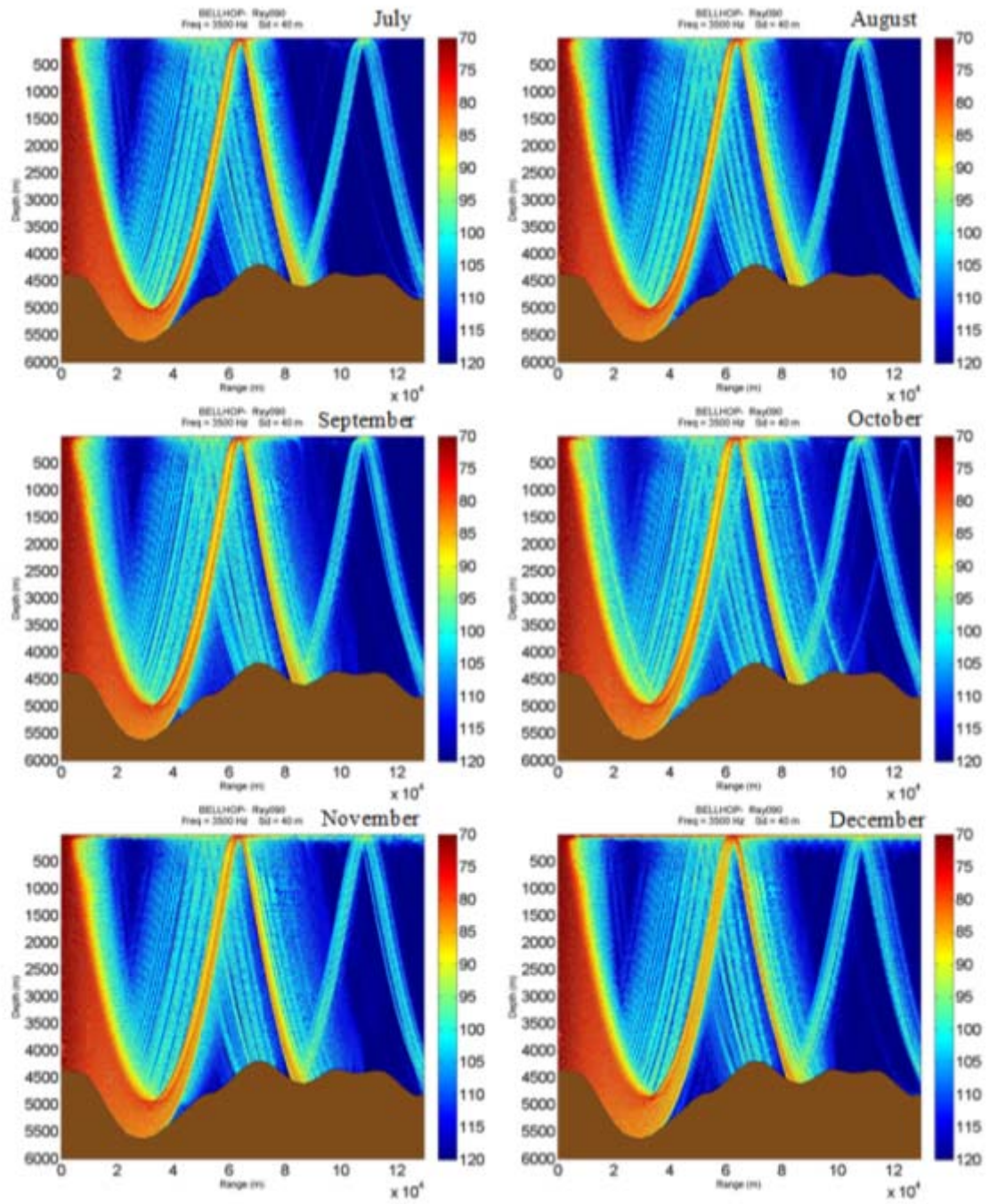






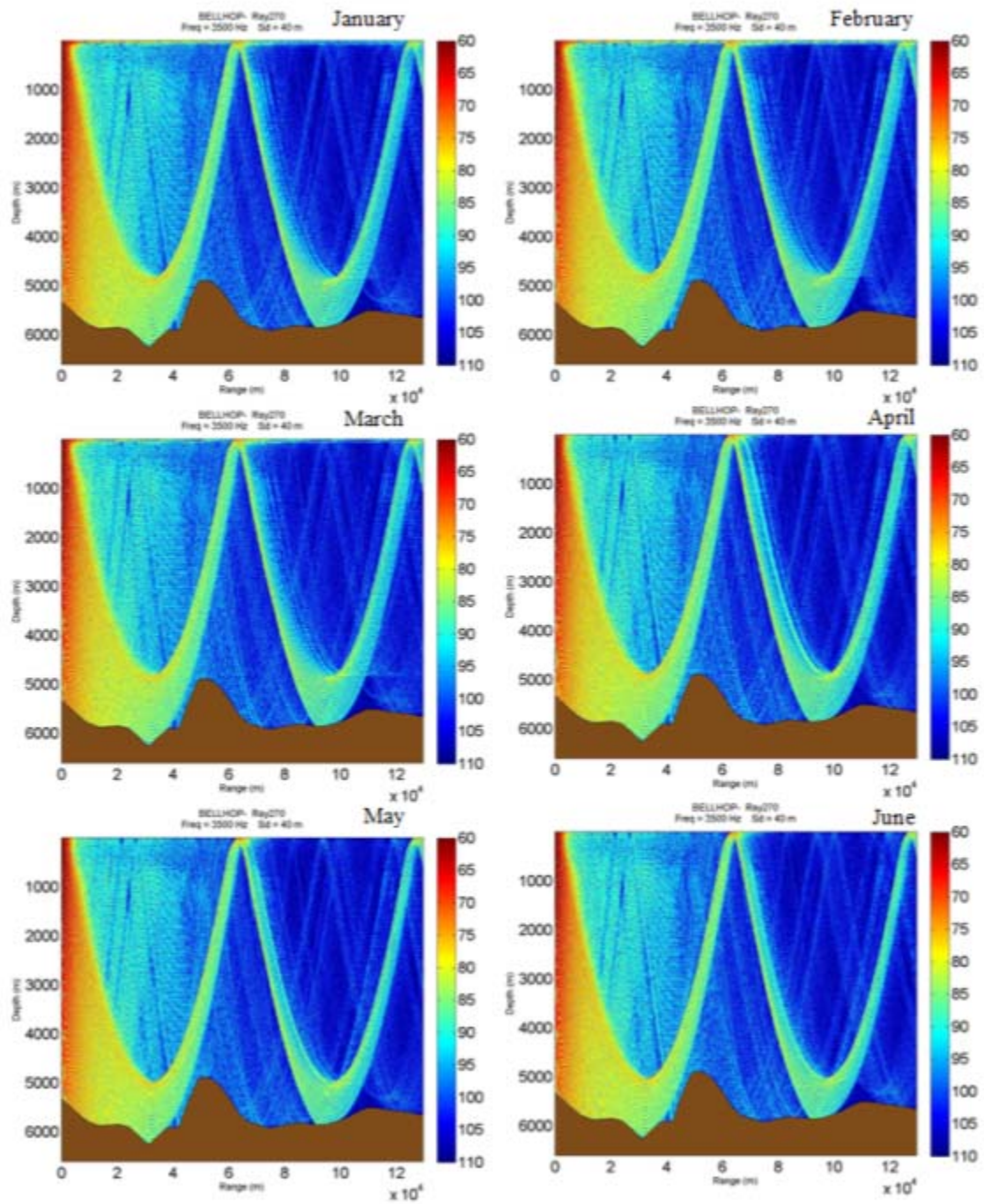
Point C (126.2510° E – 16.2204° N)

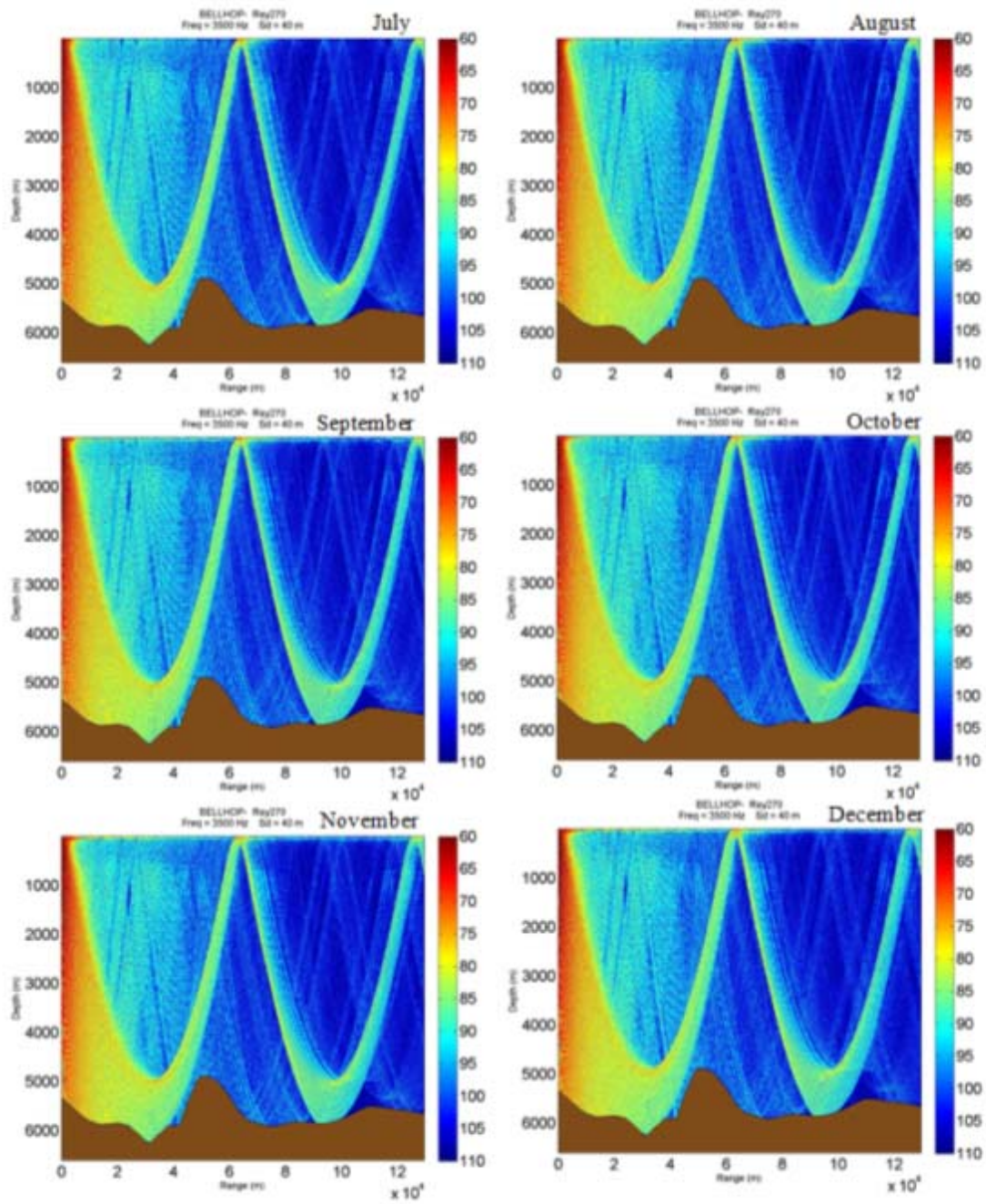




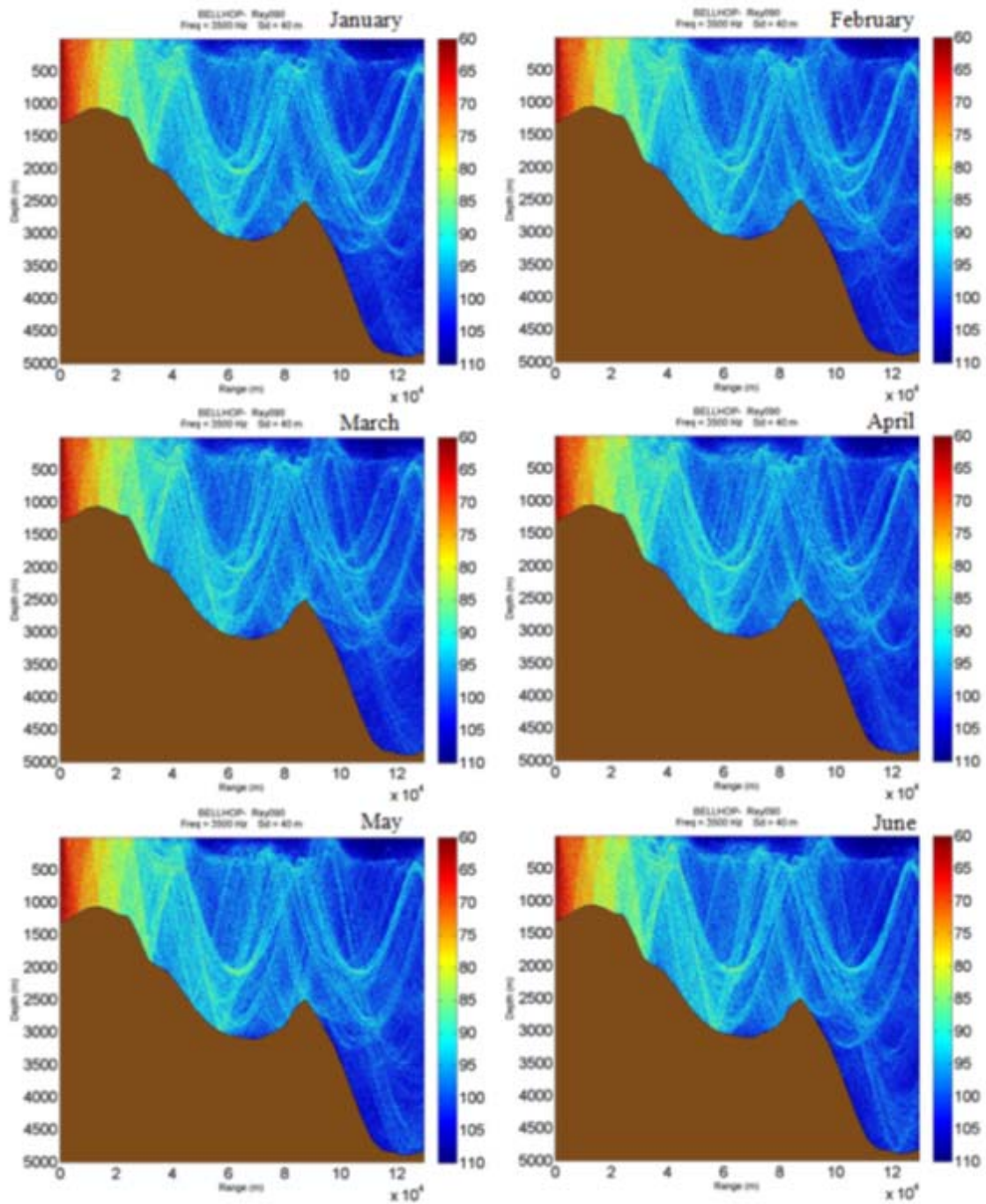


Point D (130.5917° E – 15.4490° N)

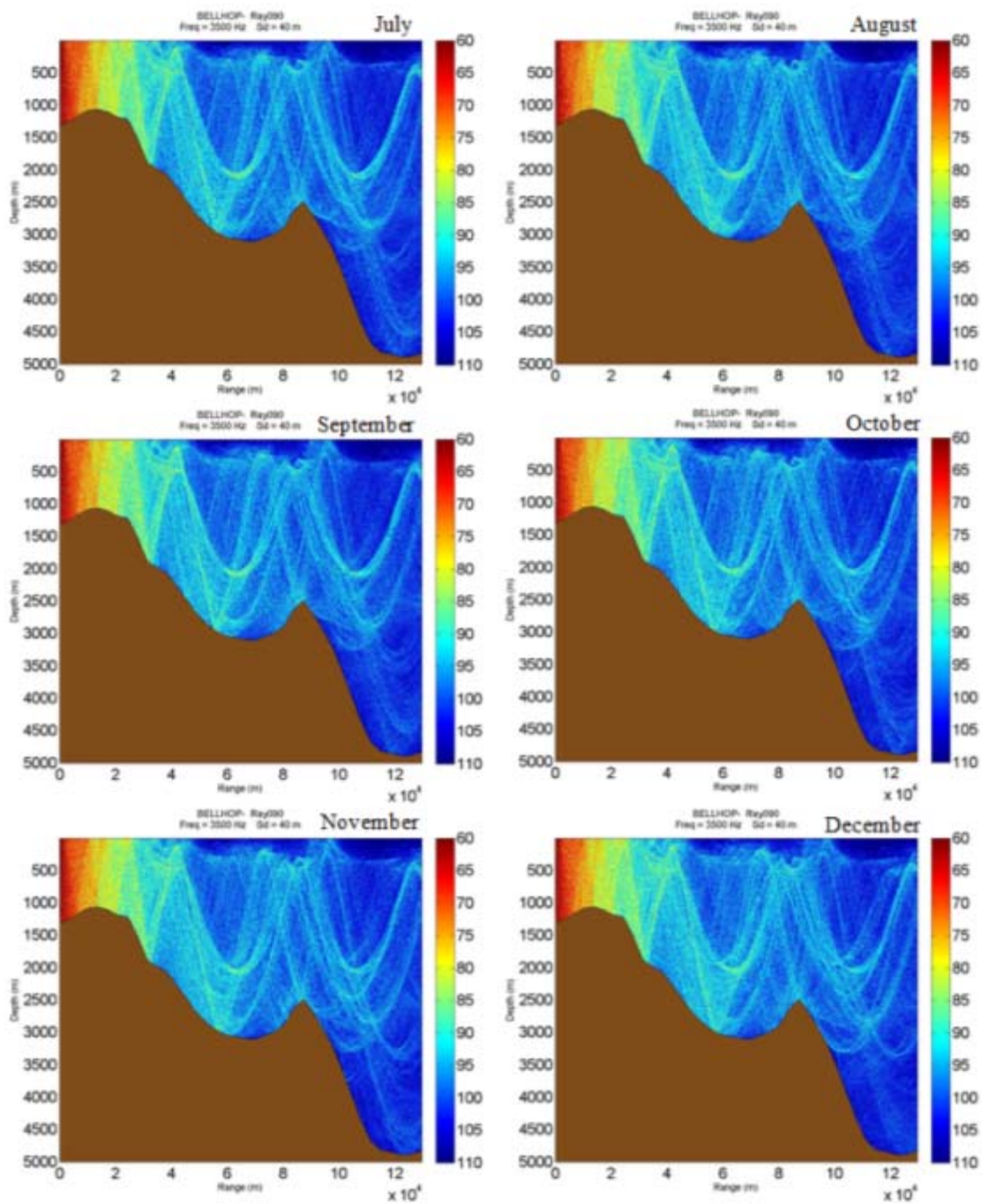




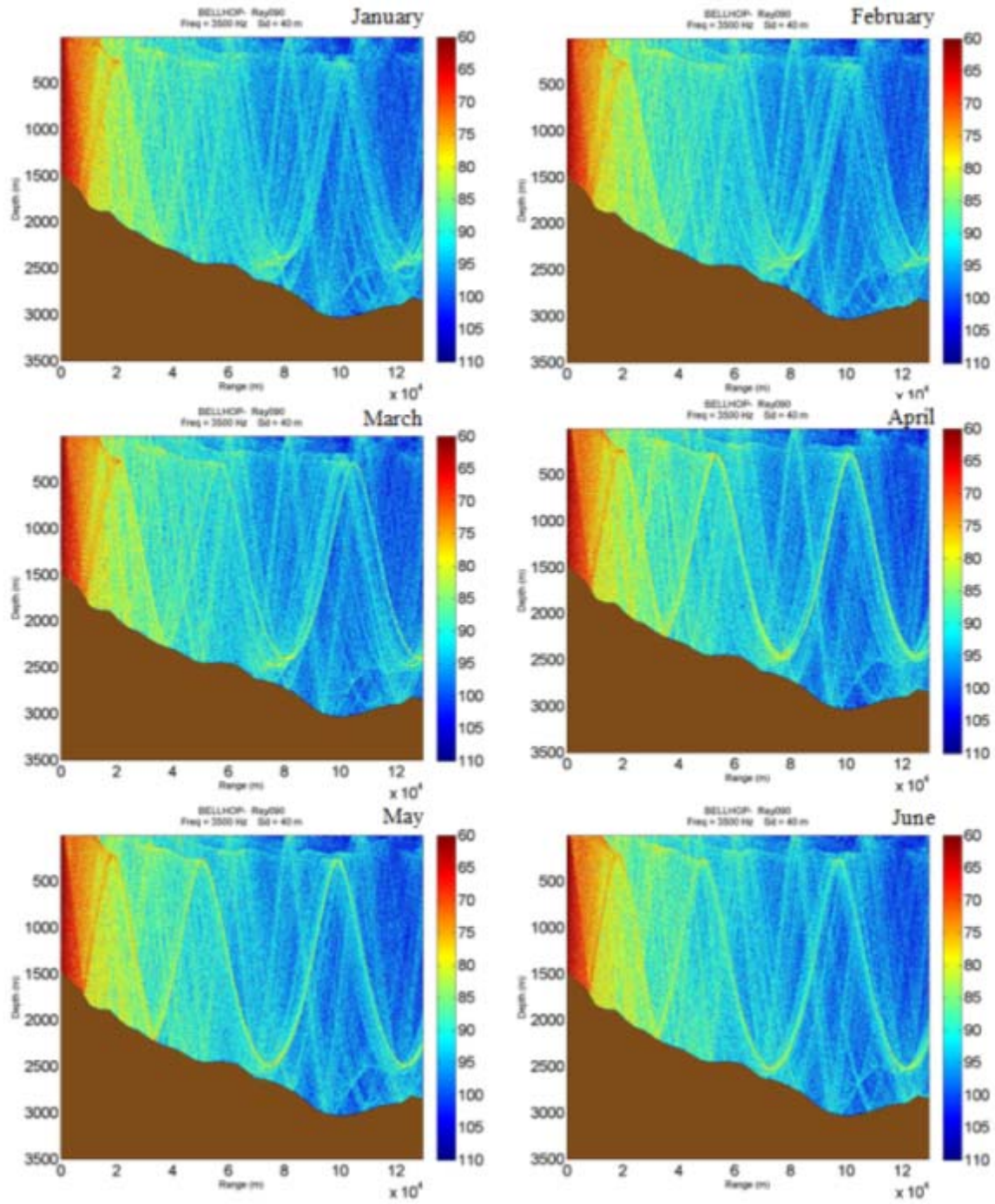
Point E (121.7996° E – 19.7956° N)

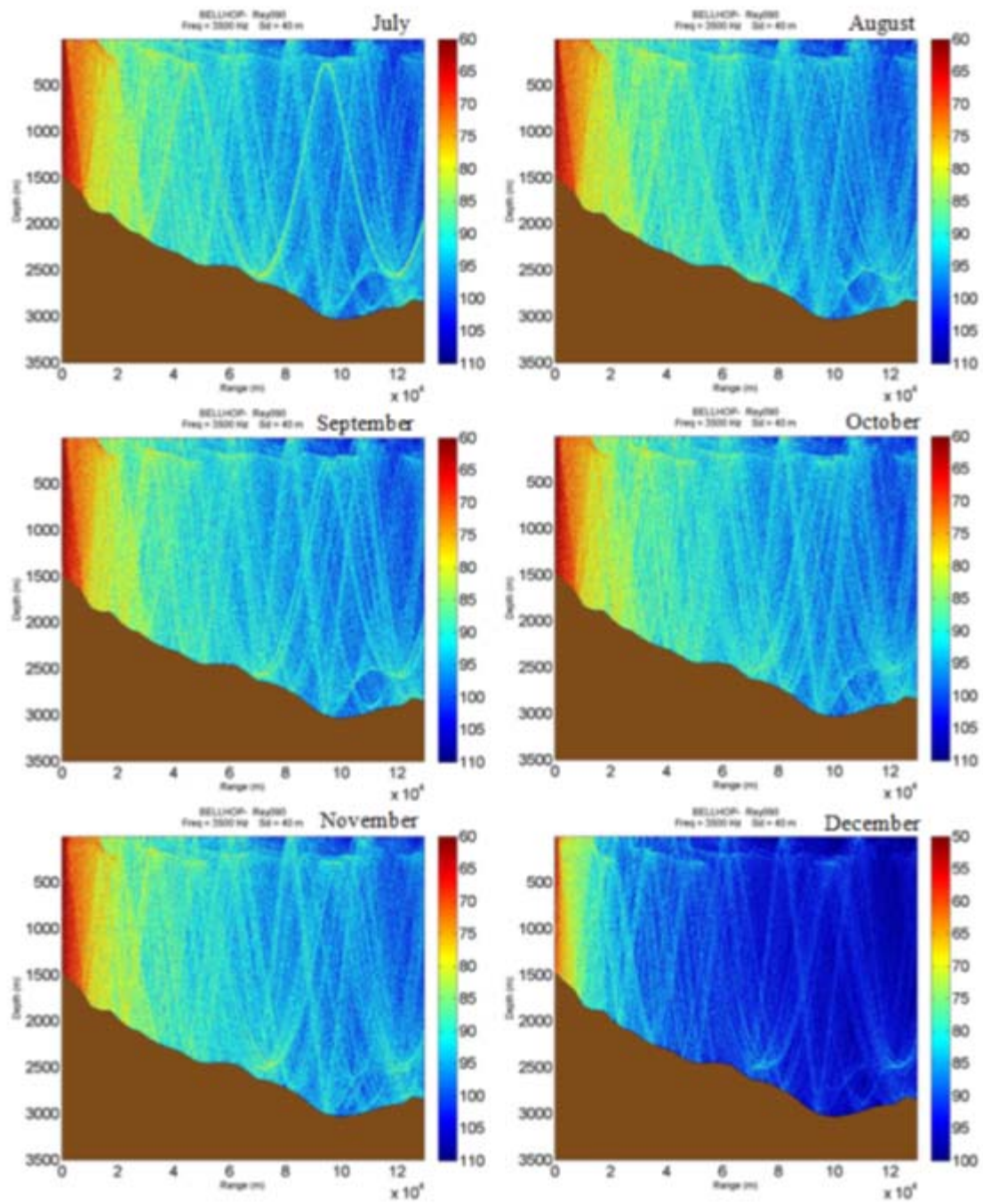






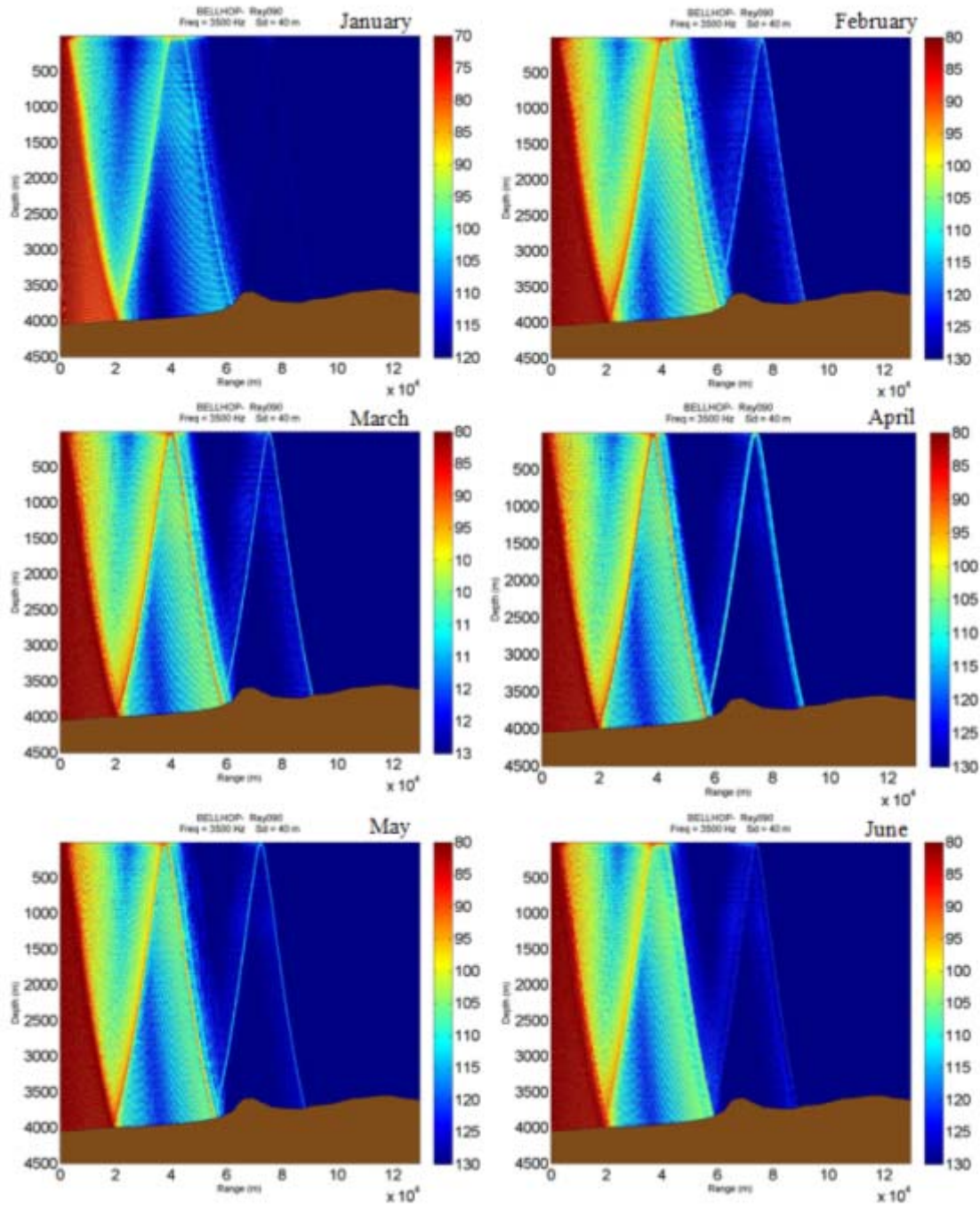
**Point F (117.0° E – 20.0° N)**

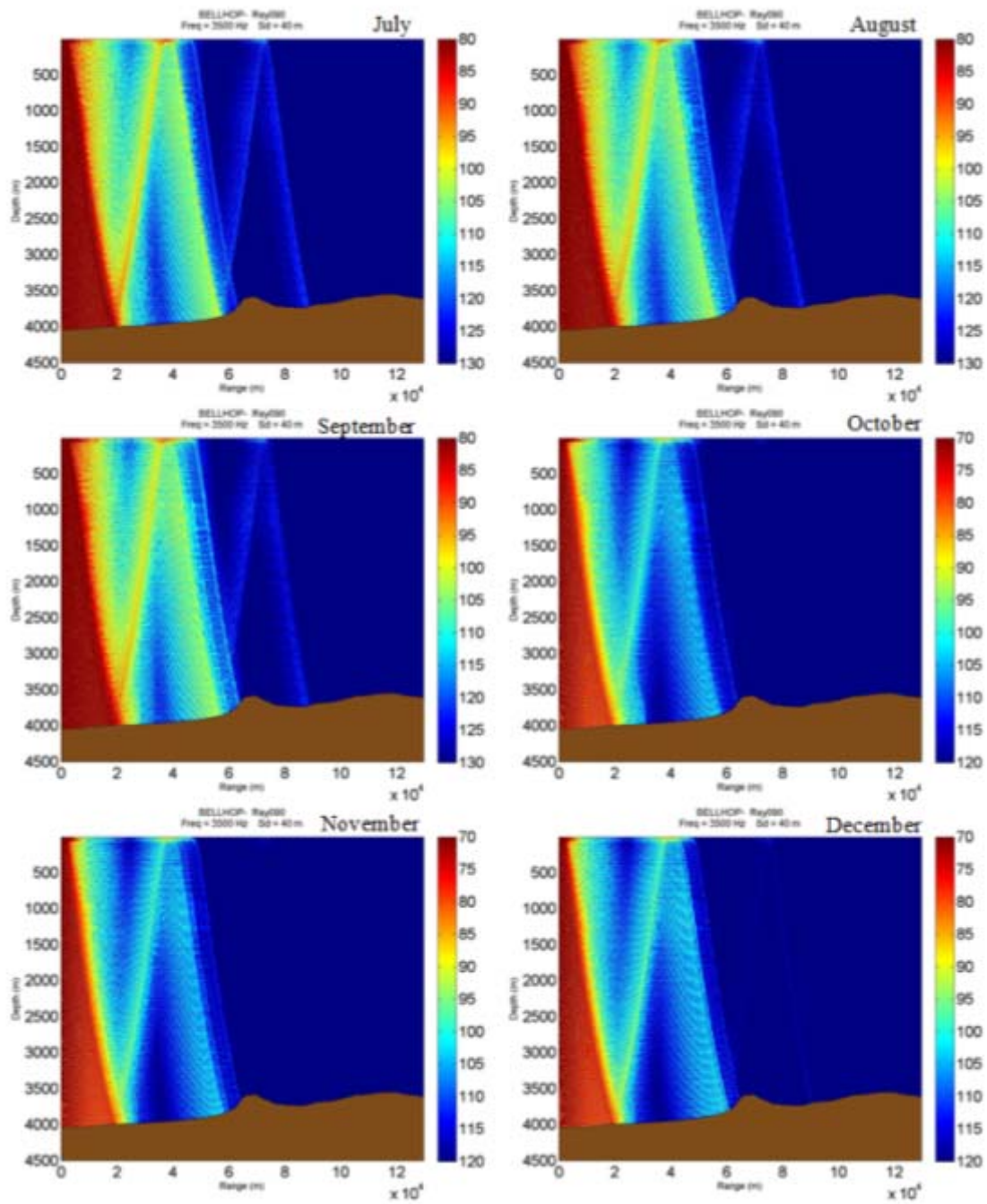




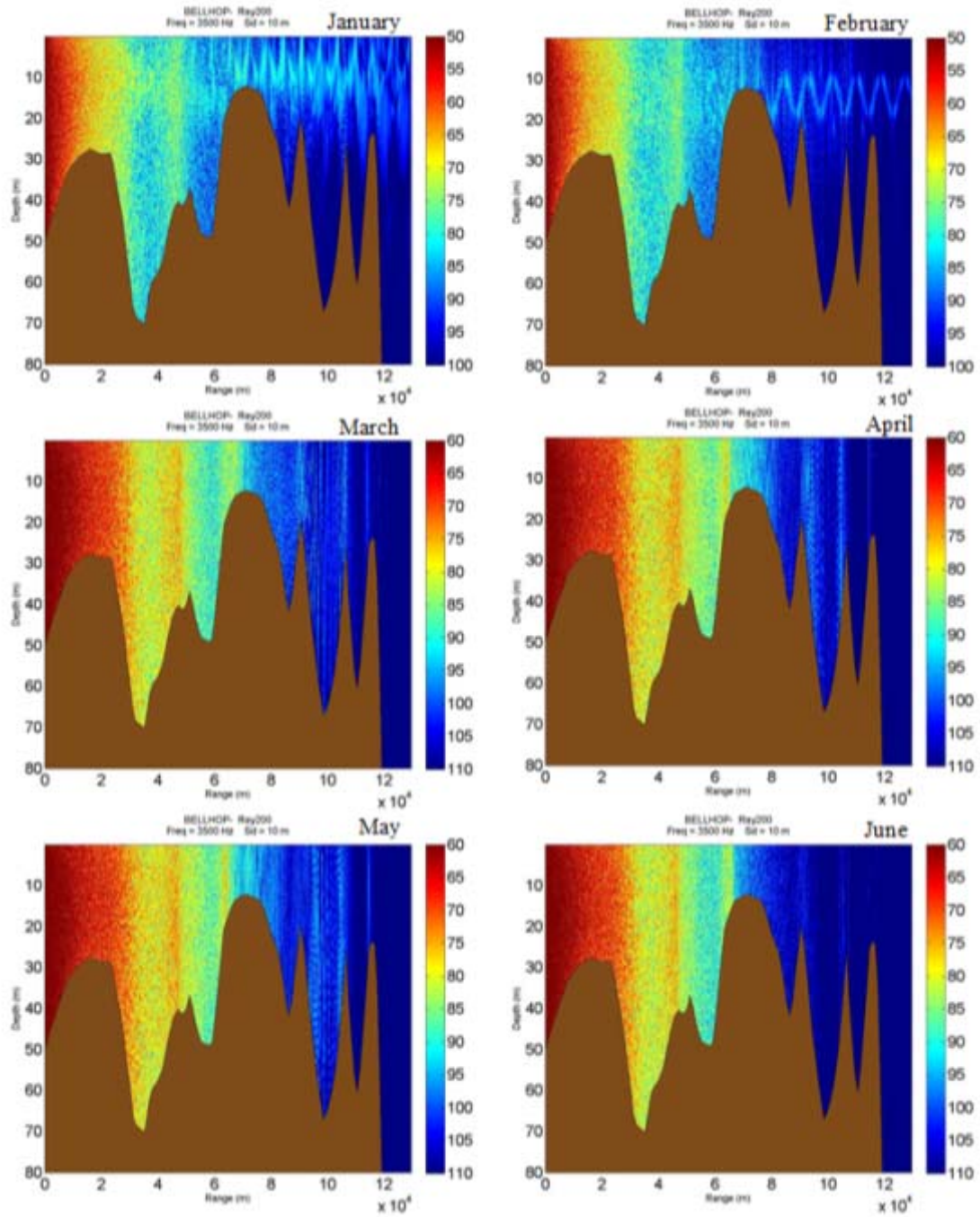


Point G (117.6248° E – 13.6293° N)

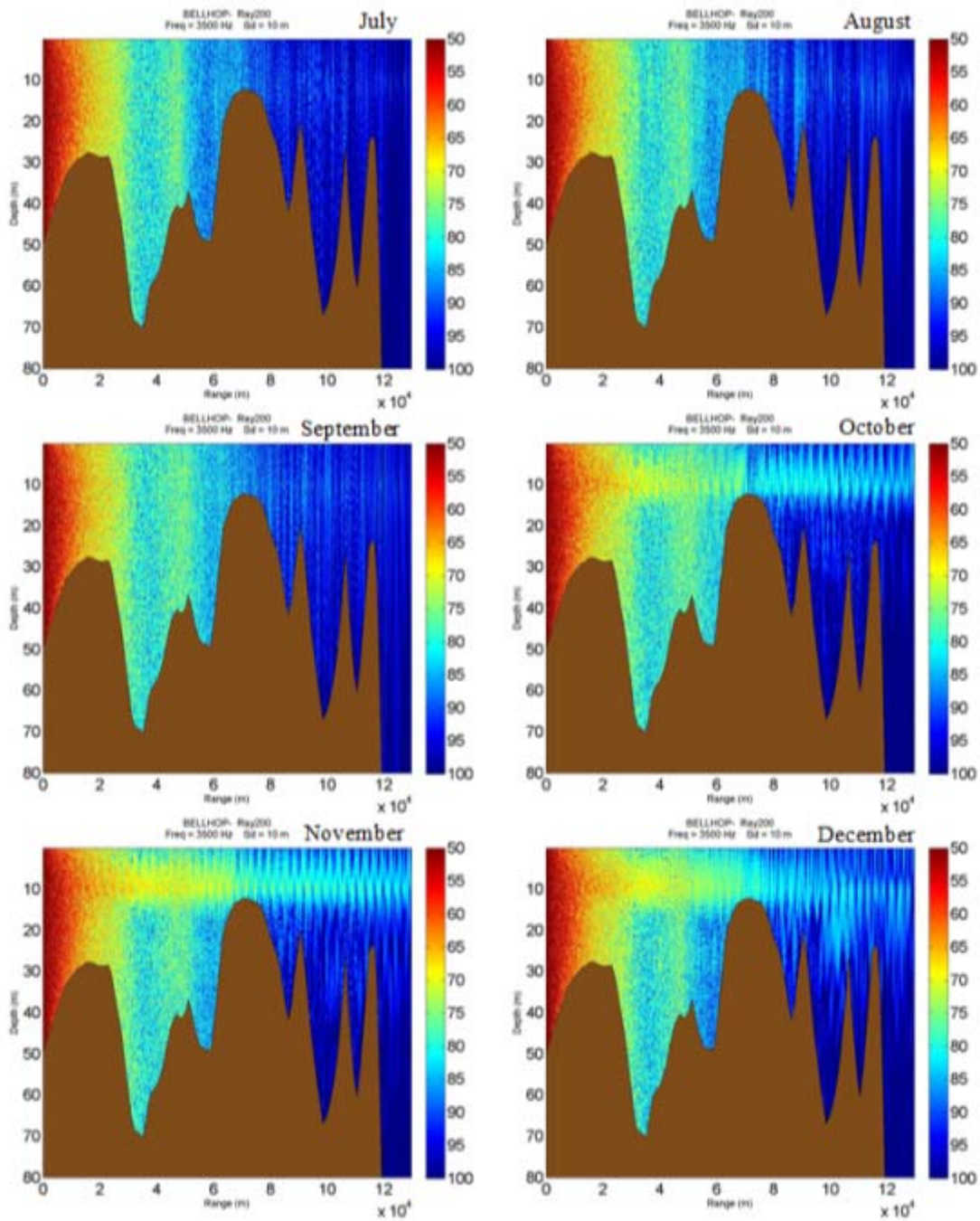




**Point H (117° E – 11.8° N)**









## LIST OF REFERENCES

- Boyer, T. P., and Coauthors, 2013: World ocean database 2013, *NOAA Atlas NESDIS*, **72**, 209 pp, doi: 10.7289/V5NZ85MT.
- Boehlert, G. W., Costa, D. P., Crocker, D. E., Green, P., O'Brien, T., Levitus, S., and Le Boeuf, J., 2001: Autonomous Pinniped Environmental Samplers: Using Instrumented Animals as Oceanographic Data Collectors. *J. Atmos. Oceanic Technol.*, **18**, 9–11.
- Carnes, M. R., 2009: Description and evaluation of GDEM-V 3.0., *Naval Research Laboratory*, NRL/MR/7330--09-9165, 1–24.
- Chen, C-T and Millero, F.J., 1977: Speed of sound in seawater at high pressures. *J. Acoust. Soc. Am*, **62**, 1129–1135.
- Chu, P. C., 2011: Global upper ocean heat content and climate variability. *Ocean Dynamics*, **61**, 1189–1204.
- Chu, P. C., and C. W. Fan, 2016a: Synoptic monthly gridded world ocean database (SMG-WOD). *Geosci. Data J.*, submitted for publication.
- Chu, P. C., and C. W. Fan, 2016b: Synoptic monthly gridded three dimensional (3D) World Ocean Database temperature and salinity from January 1945 to December 2014 (NCEI Accession 0140938). Version 1.1. NOAA National Centers for Environmental Information. Dataset. [Available online at <http://data.nodc.noaa.gov/cgi-bin/iso?id=gov.noaa.nodc:0140938>.]
- Chu, P. C., H. Tseng, C. P. Chang, and J. M. Chen, 1997: South China Sea warm pool detected in spring from the Navy's Master Oceanographic Observational Data Set (MOODS). *J. of Geophys. Research*, **102**, 15761–15771.
- Chu, P. C., L. M. Ivanov, T. P. Korzhova, T. M. Margolina, and O. M. Melnichenko, 2003a: Analysis of sparse and noisy ocean current data using flow decomposition. Part 1: Theory. *Journal of Atmospheric and Oceanic Technology*, **20**, 478–491.
- Chu, P. C., L. M. Ivanov, T. P. Korzhova, T. M. Margolina, and O. M. Melnichenko, 2003b: Analysis of sparse and noisy ocean current data using flow decomposition. Part 2: Application to Eulerian and Lagrangian data. *Journal of Atmospheric and Oceanic Technology*, **20**, 492–512.
- Chu, P. C., R. T. Tokmakian, C. W. Fan, and C. L. Sun, 2015: Optimal spectral decomposition (OSD) for ocean data assimilation, *J. of Atmos. Oceanic Tech.*, **32**, 828–841.

- Chu, P. C., Y. Chen, and S. Lu, 1998: Temporal and Spatial Variabilities of Japan Sea Surface Temperature and Atmospheric Forcings. *Journal of Oceanography*, **54**, 273–284.
- Chu, P.C., Y. C. Chen, A. Kunikaka, 2005: Seasonal variability of the Yellow Sea/East China Sea surface fluxes and thermohaline structure. *Adv in Atm Sci*, **22**, 1–22.
- Chu, P. C., Y. Q. Qi, Y. C. Chen, P. Shi and Q. W. Mao, 2004: South China Sea windwave characteristics. Part I: Validation of Wavewatch-III using TOPEX/Poseidon data. *J. Atmos. Oceanic Technol.*, **21**, 1718–1733.
- Coronas, J., 1920: The climate and weather of the Philippines 1903–1918, *Manila Observatory*, 45–61.
- DOSITS, 2017: How is sound used to find submarines?. Accessed 8 May 2017. [Available online at <http://www.dosits.org/people/defense/findsubmarines/>]
- FAS, 2017: Speed of sound in the sea. Accessed 14 May 2017. [Available online at [https://fas.org/man/dod-101/navy/docs/es310/SNR\\_PROP/snr\\_prop.htm](https://fas.org/man/dod-101/navy/docs/es310/SNR_PROP/snr_prop.htm)]
- Flament, P., 2002: A State variable for characterizing water masse and their diffusive stability: spiciness. *Progress in Oceanography*, **54**, 493–501.
- Fofonoff, N. P., 1985: Physical properties of seawater: a new salinity scale and equation of state for sea-water. *J. of Geophys. Research*, **90**, 3332–3342.
- Fukuoka, A., 1951: A study of 10-day forecast (a synthetic report), Vol. XXII, *The Geophysical Magazine*: Tokyo, 177–218.
- Hamilton, E.L., 1980: Geoacoustic modeling of the sea floor. *J. Acoust. Soc. Am.*, 1313–1340.
- Hamilton, E.L., 1982.: Bachman, R.T. Sound velocity and related properties of marine sediments. *J. Acoust. Soc. Am.*, 1891–1904.
- Hannachi, A., 2004: A Primer for EOF Analysis of Climate Data: Department of Meteorology, University of Reading, 33 pp. [Available online at <http://www.met.rdg.ac.uk/~han/Monitor/eofprimer.pdf>.]
- Hannachi, A., Jolliffe, I., T., and Stephenson, D., B., 2007: Empirical orthogonal functions and related techniques in atmospheric science: A review, *Int. J. Climatol.* **27**: 1119–1152, DOI: 10.1002/joc.1499.
- Hu, D., and Coauthors, 2015: Pacific western boundary currents and their roles in climate, *Nature Publishing*, **522**, 299–308, doi: 10.1038/nature14504 M3.

- Hu, D., and Coauthors, 2015: Pacific western boundary currents and their roles in climate, *Nature Publishing*, **522**, 299–308, doi: 10.1038/nature14504 M3.
- Jensen, F. B., W. A. Kuperman, Porter, M. B. and Schmidt, H., 2011: *Computational Ocean Acoustic: 2<sup>nd</sup> ed.*, Springer Science, 783 pp.
- Katsura, S., Qiu, B., and Schneider, N., 2013: Formation and Subduction of North Pacific Tropical Water and Their Interannual Variability, *J. Phys. Oceanogr.*, **43**, 2401–2402.
- Kilpatrick, T., N. Schneider, and E. Di Lorenzo, 2011: Generation of low-frequency spiciness variability in the thermocline, *J. Phys. Oceanogr.*, **41**, 365–377.
- Kim, H., Kimura, S., Shinoda, A., Kitagawa, T., Sasai, Y., and Sasaki, H., 2007: Effect of El Niño on migration and larval transport of the Japanese eel (*Anguilla japonica*), *ICES Journal of Marine Science*, **64**, 1387–1395, doi: 10.1093/icesjms/fsm091.
- Kucukosmanoglu, M., 2016: Inter-Annual Variability Of The Acoustic Propagation In The Mediterranean Sea Identified From a Synoptic Monthly Gridded Database as compared with GDEM, Naval Postgraduate School, 169 pp.
- Li, Y., Wang, F., Zhai, F., 2012: Interannual Variations of Subsurface Spiciness in the Philippine Sea: Observations and Mechanism. *J. Phys. Oceanogr.*, **42**, 1022–1036.
- Lorenz, E.,N., 1956: Empirical Orthogonal Functions and Statistical Weather Prediction. Technical report, Statistical Forecast Project Report 1, *Dep of Meteor, MIT*: 49.
- McDonald, C., 2016: Inter-annual variability of the acoustic propagation in the Yellow Sea identified from a synoptic monthly gridded database as compared with GDEM, Naval Postgraduate School, 161 pp.
- Medwin, H., 1975: Speed of sound in water: A simple equation for realistic parameters. *J. Acoust. Soc. Am*, **58**, 1318–1319.
- Munk, W., 1981: Internal waves and small-scale processes. In Evolution of physical oceanography, *Cambridge, MA: MIT Press*, 264–291.
- National Oceanic and Atmospheric Administration (NOAA), 2005: ENSO cycle. Accessed 24 April 2017. [Available online at [http://www.cpc.ncep.noaa.gov/products/analysis\\_monitoring/ensocycle/ensocycle.shtml](http://www.cpc.ncep.noaa.gov/products/analysis_monitoring/ensocycle/ensocycle.shtml)]
- Naval Oceanographic Office (NAVO), 2003: Database description for bottom sediment Type (U), Oceanographic and Atmospheric Master Library, OAML-DBD-86, 55pp.

- Naval Oceanographic Office (NAVO), 2006: Database description for bottom sediment type Digital Bathymetric Data Base–Variable Resolution (DBDB-V) version 5.4 (U). Oceanographic and Atmospheric Master Library, OAML-DBD-90, 55pp.
- Naval Oceanographic Office (NAVO), 2009: Database Description for the Generalized Digital Environmental Model-Variable Resolution (GDEM-V) Version 3.0.1 (U), Oceanographic and Atmospheric Master Library, OAML-DBD-72F, 39 pp.
- NOAA - NCEI, 2017: Southern Oscillation Index. Accessed 24 April 2017. [Available online at <https://www.ncdc.noaa.gov/teleconnections/enso/indicators/soi/>]
- NPL, 2000: Technical Guides-Speed of Sound in Sea-Water. Accessed 12 May 2017. [Available online at [http://www.comm-tec.com/Library/Technical\\_Papers/speedsw.pdf](http://www.comm-tec.com/Library/Technical_Papers/speedsw.pdf)]
- Obukhov, A.,M., 1947: Statistically homogeneous fields on a sphere, *Uspehi Matematicheskikh Nauk*, **2**, 196–198.
- Philippine Atmospheric Geophysical and Astronomical Services Administration (PAGASA), 2017: Climate of the Philippines. Accessed 24 April 2017. [Available online at <http://www1.pagasa.dost.gov.ph/index.php/climate/climatological-normals>]
- Porter, M. B, 2011: The BELLHOP manual and user’s guide: Preliminary draft. Heat, Light, and Sound Research, Inc. 57 pp.
- Qu, T., Mitsudera H., and Yamagata, T., 1998a: A Climatology of the Circulation and Water Mass Distribution near the Philippine Coast, *J. Phys. Oceanogr.*, **29**, 1488–1504.
- Qu, T., Mitsudera H., and Yamagata, T., 1998b: On the western boundary currents in the Philippine Sea, *Journal of Geophysical Research*, **103**, 7537–7548.
- Rodriguez, D. L., 2016: Inter-annual variability of the California current system and associated biochemical characteristics from prolonged data series, Naval Postgraduate School, 129 pp.
- Schneider, N., 2000: Decadal spiciness mode in the tropics. *Geophys. Res. Lett.*, **27**, 257–260.
- Talley, L. D., Pickard, G. L., Emery, W. J., and Swift, J. H., 2011: Descriptive Physical Oceanography, an Introduction. *Pacific Ocean*, Elsevier, 303–350.
- Tsuchiya, M., 1968: Upper Waters of the Intertropical Pacific Oceans. *Johns Hopkins Oceanographic Studies, Johns Hopkins Press*, **4**, 50pp.

United Nations Conference on Trade and Development (UNCTAD), 2011: Review of Maritime Transport. Accessed 5 May 2017. [Available online at [http://unctad.org/en/docs/rmt2011\\_en.pdf](http://unctad.org/en/docs/rmt2011_en.pdf)]

USNA, 2017: Speed of sound in the sea. Accessed 14 May 2017. [Available online at <https://www.usna.edu/Users/physics/ejtuchol/documents/SP411/Chapter4.pdf>]

THIS PAGE INTENTIONALLY LEFT BLANK

## **INITIAL DISTRIBUTION LIST**

1. Defense Technical Information Center  
Ft. Belvoir, Virginia
2. Dudley Knox Library  
Naval Postgraduate School  
Monterey, California